A 3D PRINTED PATIENT SPECIFIC *IN-VIVO* DOSIMETRY SYSTEM

by

Nicholas Lynch

Submitted in partial fulfillment of the requirements
for the degree of Doctor of Philosophy

at

Dalhousie University
Halifax, Nova Scotia
June 2024

"The final conclusion of absurdist protest is, in fact, persistence in that hopeless encounter between human questioning and the silence of the universe."

- Albert Camus, *The Rebel (1951)*

TABLE OF CONTENTS

LIST OF TABLES

LIST OF FIGURES

ABSTRACT

While radiotherapy treatments are meticulously planned, checked, and verified before the patient arrives at the clinic, once the treatment commences, there is often no direct monitoring of the radiation dose received by the patient. Improved safety and treatment accuracy for patients undergoing radiotherapy can be accomplished by using *in-vivo* dosimetry. However, most commercially available detectors are best suited to measuring radiation in a quality control and assurance setting. As a result, their designs are often too fragile, bulky, or complex for direct use on patients, limiting the routine clinical use of *in-vivo* dosimetry. This research aims to address this limitation by using 3D printing to develop a wireless radiation detector capable of addressing the clinical need for *in-vivo* dosimetry of patients undergoing radiotherapy.

A series of three manuscripts form the basis of this thesis. The first manuscript, "Characterization of Novel 3D Printed Plastic Scintillation Dosimeters," presents a methodology for the rapid fabrication of plastic scintillators with bespoke geometries and represents the first comprehensive analysis of 3D printed plastic scintillation dosimeters for radiotherapy applications. The second manuscript, "Camera-Based Radiotherapy Dosimetry Using Dual-Material 3D Printed Scintillator Arrays" demonstrates an innovative methodology for the dual-material 3D printing of bespoke arrays of plastic scintillators and establishes a procedure for the dosimetric calibration of planar array geometries. Finally, the third manuscript, "Camera Based Multipoint *In-Vivo* Dosimetry Using 3D Printed Patient-Specific Scintillator Arrays" describes the development of a patient-specific array of plastic scintillators and demonstrates its ability to measure clinical surface dose distributions wirelessly.

From the initial 3D printing of individual scintillators to the fabrication of complex patient-specific arrays, these manuscripts document the evolution of a novel detector system. This work not only makes the production of custom-designed plastic scintillators accessible but also enables the development of patient-specific radiation detectors. While the primary focus of this research is on radiotherapy applications, the potential of this technology extends to radiation detection and high-energy physics experiments, where the use of complex 3D-printed scintillation detectors is desirable.

LIST OF ABBREVIATIONS AND SYMBOLS USED

2D	**T**wo-**D**imensional
3D	**T**hree-**D**imensional
3D-CRT	**T**hree-**D**imensional **C**onformal **R**adiation **T**herapy
AAA	**A**nisotropic **A**nalytical **A**lgorithm
ABS	**A**crylonitrile **B**utadiene **S**tyrene
AXB	**A**curos **XB** Algorithm
BEV	**B**eam's **E**ye **V**iew
CAD	**C**omputer **A**ided **D**esign
CBCT	**C**one **B**eam **C**omputed **T**omography
CCD	**C**harge **C**oupled **D**evice
CERN	**C**onseil **E**uropéen pour la **R**echerche **N**ucléaire
CMOS	**C**omplementary **M**etal **O**xide **S**emi**c**onductor
CPE	**C**harged **P**article **E**quilibrium
CSDA	**C**ontinuous **S**lowing **D**own **A**pproximation
CT	**C**omputed **T**omography
DICOM	**D**igital **I**maging and **CO**mmunications in **M**edicine
DLP	**D**igital **L**ight Processing
DMLS	**D**irect **M**etal **L**aser **S**intering
DNA	**D**eoxyribo**N**ucleic **A**cid
DVH	**D**ose **V**olume **H**istogram
EM-ICCD	**E**lectron **M**ultiplying **I**ntensified **C**harge **C**oupled **D**evice
EPID	**E**lectronic **P**ortal **I**maging **D**evice

FDM	**F**used **D**eposition **M**odeling
GSL	**G**rey **S**cale **L**evel
HU	**H**ounsfield **U**nit
IAEA	**I**nternational **A**tomic **E**nergy **A**gency
ICCD	**I**ntensified **C**harge **C**oupled **D**evice
ICRP	**I**nternational **C**ommission on **R**adiological **P**rotection
IDEX	**I**ndependent **D**ual **E**xtrusion
IMRT	**I**ntensity **M**odulated **R**adiotherapy
KERMA	**K**inetic **E**nergy **R**eleased per unit **MA**ss
KeV	**K**ilo **E**lectron **V**olt
KV	**K**ilo**V**oltage
LCD	**L**iquid **C**rystal **D**isplay
LINAC	**LIN**ear **AC**celerator
MC	**M**onte **C**arlo
MeV	**M**ega **E**lectron **V**olt
MJF	**M**ulti **J**et **F**usion
MLC	**M**ulti **L**eaf **C**ollimator
MOSFET	**M**etal **O**xide **S**emiconductor **F**ield **E**ffect **T**ransistor
MTF	**M**odulation **T**ransfer **F**unction
MU	**M**onitor **U**nit
MV	**M**ega**V**oltage
OSLD	**O**ptically **S**timulated **L**uminescent **D**osimeter
PDD	**P**ercent **D**epth **D**ose

PENELOPE	**PEN**etration and **E**nergy **LO**ss of **P**ositrons and **E**lectrons
PETG	**P**oly**E**thylene **T**erephthalate **G**lycol
PLA	**P**oly**L**actic **A**cid
POPOP	1,4-Bis(5-phenyl-2-oxazolyl) Benzene
PPO	Diphenyloxazole
PSD	**P**lastic **S**cintillation **D**osimeter
PTFE	**P**oly**T**etra**F**luoro**E**thylene
PTV	**P**lanning **T**arget **V**olume
QA	**Q**uality **A**ssurance
QE	**Q**uantum **E**fficiency
ROI	**R**egion **O**f **I**nterest
RTE	**R**adiation **T**ransport **E**quation
sCMOS	**S**cientific **C**omplementary **M**etal **O**xide **S**emi**c**onductor
SLA	Stereolithography
SSD	**S**ource to **S**urface **D**istance
TCPE	**T**ransient **C**harged **P**article **E**quilibrium
TLD	**T**hermo**L**uminescent **D**osimeter
TPE	**T**hermo**P**lastic **E**lastomer
TPS	**T**reatment **P**lanning **S**ystem
UV	**U**ltra**V**iolet
VMAT	**V**olumetric **M**odulated **A**rc **T**herapy
WHO	**W**orld **H**ealth **O**rganization

α	Fine Structure Constant	Dimensionless
β	Relativistic Beta Factor	Dimensionless
Δ	Disparity	Pixels
ε	Scintillation Efficiency	Dimensionless
θ	Angle	Degrees
κ_N	Nuclear Pair Production Cross Section	m^2 or $barns \cdot atom^{-1}$
κ_E	Electronic Triplet Production Cross Section	m^2 or $barns \cdot atom^{-1}$
λ	Wavelength	m
μ_0	Vacuum Magnetic Permeability	$kg \cdot m \cdot s^{-2} \cdot A^{-2}$
μ	Linear Attenuation Coefficient	m^{-1}
μ_{en}	Mass Energy Absorption Coefficient	$m^2 \cdot kg^{-1}$
μ_{tr}	Mass Energy Transfer Coefficient	$m^2 \cdot kg^{-1}$
ρ	Density	$kg \cdot m^{-3}$
σ_C	Compton Scattering Cross Section	m^2 or $barns \cdot atom^{-1}$
σ_R	Rayleigh Scattering Cross Section	m^2 or $barns \cdot atom^{-1}$
τ	Photoelectric Cross Section	m^2 or $barns \cdot atom^{-1}$
Φ_k	Photon Fluence	m^{-2}
φ_E	Electron Energy Fluence	$MeV \cdot m^{-2}$
ϕ	Angle	Degrees
ψ_k	Photon Energy Fluence	$MeV \cdot m^{-2}$
Ω	Solid Angle	sr
ω	Angular Frequency	$rad \cdot s^{-1}$

A	Atomic Mass	kg
B	Baseline	mm
b	Impact Parameter	m
c	Speed of Light in Vacuum	$m \cdot s^{-1}$
C	Camera Principal Point	Pixels
D	Dose	Gy
D_{cav}	Dose to Cavity	Gy
D_{med}	Dose to Medium	Gy
d_n	Radial Distortion Coefficient	Dimensionless
E	Energy	MeV
$\overline{E}$	Mean Energy	MeV
E_B	Binding Energy	MeV
E_e	Electron Kinetic Energy	MeV
E_γ	Photon Energy	MeV
E_{tr}	Transferred Energy	MeV
f	Focal Length	mm
I	Excitation Energy	MeV
$\mathrm{K}B$	Birks Constant	$mm \cdot MeV^{-1}$
K_{med}	KERMA	Gy
K_{med}^{col}	Collison KERMA	Gy
K_{med}^{rad}	Radiative KERMA	Gy
L_Δ	Restricted Mass Stopping Power	$MeV \cdot cm^2 \cdot g^{-1}$

L	Path Length	m
$\bar{L}$	Mean Path Length	m
M	Translation Matrix	mm
m	Mass	kg
$m_e c^2$	Electron Rest Mass Energy	MeV
N_A	Avogadro's Number	mol^{-1}
n	Index of Refraction	Dimensionless
q	Electric Charge	C
R	Range	m
R_θ	Rotation Matrix	Dimensionless
$\bar{R}$	Mean Range	m
R_{CSDA}	CSDA Range	m
r	Radial Distance	m
r_e	Classical Electron Radius	m
S	Mass Stopping Power	$MeV \cdot cm^2 \cdot g^{-1}$
S_{col}	Collison Stopping Power	$MeV \cdot cm^2 \cdot g^{-1}$
S_{col}^{hard}	Hard Collison Stopping Power	$MeV \cdot cm^2 \cdot g^{-1}$
S_{col}^{soft}	Soft Collison Stopping Power	$MeV \cdot cm^2 \cdot g^{-1}$
S_{rad}	Radiative Stopping Power	$MeV \cdot cm^2 \cdot g^{-1}$
s	Skew Coefficient	Dimensionless
t	Time	s
v	Velocity	$m \cdot s^{-1}$

W	Mean Energy Per Ion Pair	MeV
$\boldsymbol{Z}$	Atomic Number	Dimensionless

ACKNOWLEDGEMENTS

I express my deepest gratitude to my co-advisors, Dr. James Robar, and Dr. Thalat Monajemi, for entrusting me with such a tremendous opportunity. Their collective mentorship, expertise, and collaborative spirit have greatly enriched this work. I am indebted to Dr. Monajemi for her exceptional guidance and insights. I consider myself incredibly fortunate to have had the opportunity to learn from her, and I will always be grateful for the profound impact she has had on me. I am also thankful to Dr. Robar for his advice and insightful feedback, which has been invaluable in shaping the direction of this thesis. His clinical focus and dedication to translational research have been genuinely inspiring.

I extend my heartfelt appreciation to my colleagues and friends whom I have had the pleasure of knowing throughout my studies. Your camaraderie, intellectual exchange, and shared experiences have transformed this academic pursuit into the journey of a lifetime. I am also immensely thankful to my family for their unwavering encouragement and understanding during this challenging yet rewarding period. In particular, I am profoundly grateful to my partner, Kristy Canton, for her steadfast support, patience, and sacrifices. Her unwavering belief in me has always been my greatest strength.

This thesis was only possible because of the collaboration and assistance of many people. I am sincerely thankful to all who have contributed to it.

CHAPTER 1 INTRODUCTION

1.1 PREAMBLE

Radiation safety is a key issue in radiotherapy, as such all treatments are carefully planned, checked, and verified prior to treatment. Despite this, the radiation dose received by the patient is still susceptible to errors in the overall radiotherapy process (setup, calculation, and/or transcription), with examples of misadministration's being reported worldwide[1–4]. The consequences of these mistreatments could have been prevented by directly measuring the radiation dose received by the patients during treatment. Also known as *in-vivo* dosimetry, it constitutes an essential component of radiation safety. It is recommended for all patients undergoing radiation treatments by the World Health Organization (WHO)[4], the International Commission on Radiological Protection (ICRP)[5], and the International Atomic Energy Agency (IAEA)[1].

Radiation measurement is an essential component of a radiotherapy program, and many detectors already exist for this purpose[6]. However, most detectors are best suited to measuring radiation in a quality control and assurance setting, i.e., in the absence of a patient. Consequently, the design of most detectors is such that they are either too rigid, fragile, bulky, or cumbersome to use directly on patients, limiting the routine clinical use of *in-vivo* dosimetry[7]. Some detectors are still designed to perform *in-vivo* measurements, such as radiochromic film[8], optically stimulated luminescence dosimeters (OSLDs)[9], and metal-oxide-semiconductor field-effect transistors (MOSFETs)[10]. Although these detectors enable *in-vivo* and real-time monitoring of patients, their routine use in clinics remains excessively cumbersome[7]. Therefore, it is desirable to have a simple real-time detector system capable of monitoring the intensity and position of the radiation beam, thus allowing treatment verification for every patient[7,11,12].

In addition to safeguarding against significant errors, routine real-time *in-vivo* dose measurement would provide dosimetric data that could be linked directly to patient clinical outcomes (e.g., local control and side effects/morbidity). It is well known that modern radiotherapy treatment planning systems (TPS) do not accurately predict dose in the superficial layers of skin[13]. Discrepancies of 10% - 30% between simulated and measured surface doses have been reported[14–16]. As a result, uncertainties in skin dose can lead to dose underestimation,

particularly in cases necessitating high therapeutic skin doses[17] or in skin toxicity , with reactions ranging from mild erythema to brisk moist desquamation[18]. Therefore, to improve treatment accuracy and mitigate toxicity, it is desirable to measure skin dose for these patients *in-vivo*. However, for such dose measurements to be clinically practical, the detector must not only conform to the exterior surface of the patient but require minimal setup time.

The overarching objective of this research is the creation of a patient-specific radiation detector capable of meeting the current clinical demand for routine real-time *in-vivo* dosimetry in radiation therapy[7,19]. As illustrated in Fig. 1.1, the detector system consists of a 3D printed array of plastic scintillators designed to adapt to the exterior surface of the patient. The light emitted by the array during treatment is then measured using a stereoscopic arrangement of cameras positioned within the treatment room. The array's light output is correlated to dose through pretreatment dosimetric calibration, facilitating real-time comparison between the patient's received dose and the planned dose distribution during treatment.

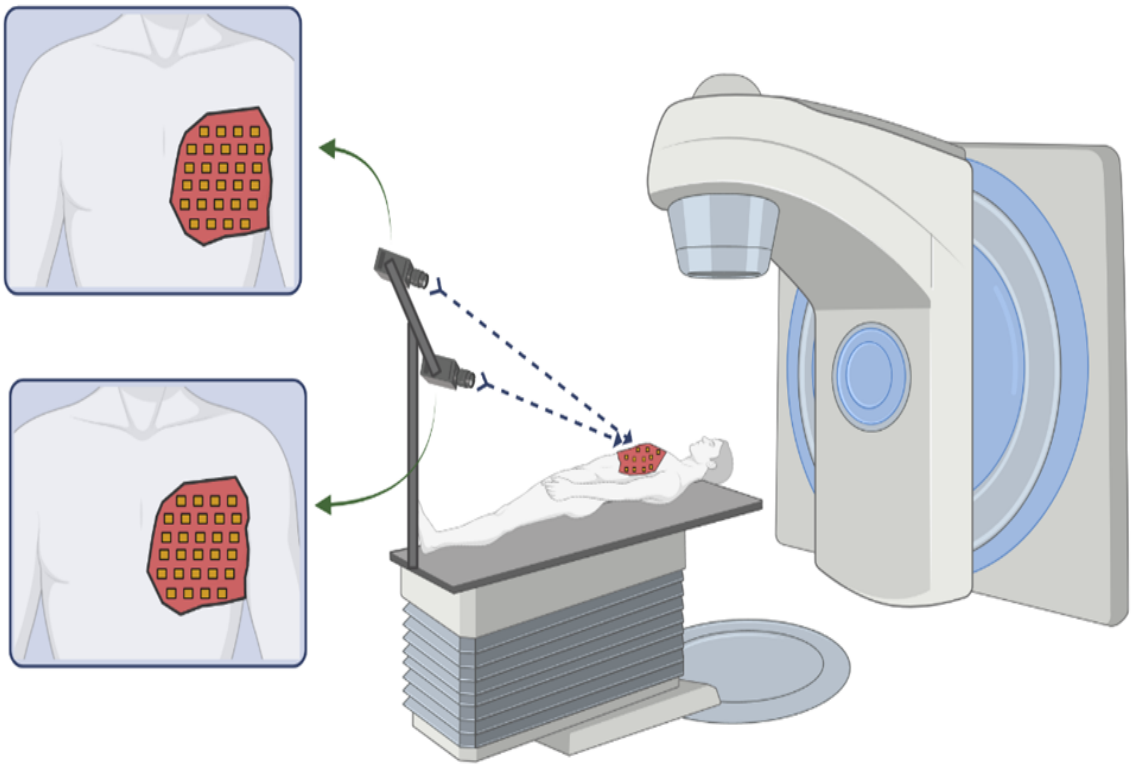

Figure 1.1: Schematic drawing of the skin-surface scintillator conforming to the patient surface, as well as the treatment unit gantry and stereoscopic camera system positioned at the foot of the treatment couch[20].

1.2 RADIATION THERAPY

Radiation therapy uses high doses of ionizing radiation to kill cancer cells and reduce tumor size. Ionizing radiation either directly interacts with the deoxyribonucleic acid (DNA) of cancerous cells to cause damage or indirectly through the generation of free radicals inside the cell. This damage can lead to cell death or hinder the ability of the cancer cells to divide.

External beam radiation therapy is the main form of radiation therapy, where an X-ray or electron beam is generated by a treatment unit known as a linear accelerator (LINAC). Section 2.1.1 contains an expanded description of particle beam generation in clinical LINACs. To treat a tumor, the LINAC directs multiple radiation beams, or arcs of beams, which converge upon the target (e.g., the tumor volume). The LINAC gantry (Fig 1.2), rotatable through 360^{0}, allows for various incident beam angles, and an internal collimation system can be used to shape the radiation field. In C-arm linear accelerators, such as the Varian TrueBeam system (Varian Medical Systems, Inc., Palo Alto, CA), this collimation system is comprised of two sets of orthogonally placed opposing tungsten jaws and a multi-leaf collimator (MLC). The MLC is comprised of two opposed banks of individually motor-controlled tungsten leaves.

Radiotherapy selectively targets cancer cells while attempting to spare surrounding healthy tissues. External beam radiotherapy employs various beam arrangements and collimation techniques. The simplest is 3D Conformal Radiation Therapy (3D-CRT), where multiple radiation beams are collimated to align with the target's projection at each beam angle. This process creates a 3D dose distribution that closely matches the tumor's shape[21]. More advanced fixed-angle dose delivery techniques, such as Intensity-Modulated Radiation Therapy (IMRT), use multiple static beams of varying intensity levels. IMRT employs dynamic beam shaping using the MLC to customize the dose intensity across the tumor volume[22]. IMRT was expanded from fixed fields to continuously rotating arcs known as volumetric modulated arc therapy (VMAT)[23]. VMAT allows for the continuous adjustment of the radiation dose delivery as the treatment gantry rotates around the patient. This dynamic modulation optimizes dose conformity and reduces treatment time compared to traditional IMRT[24].

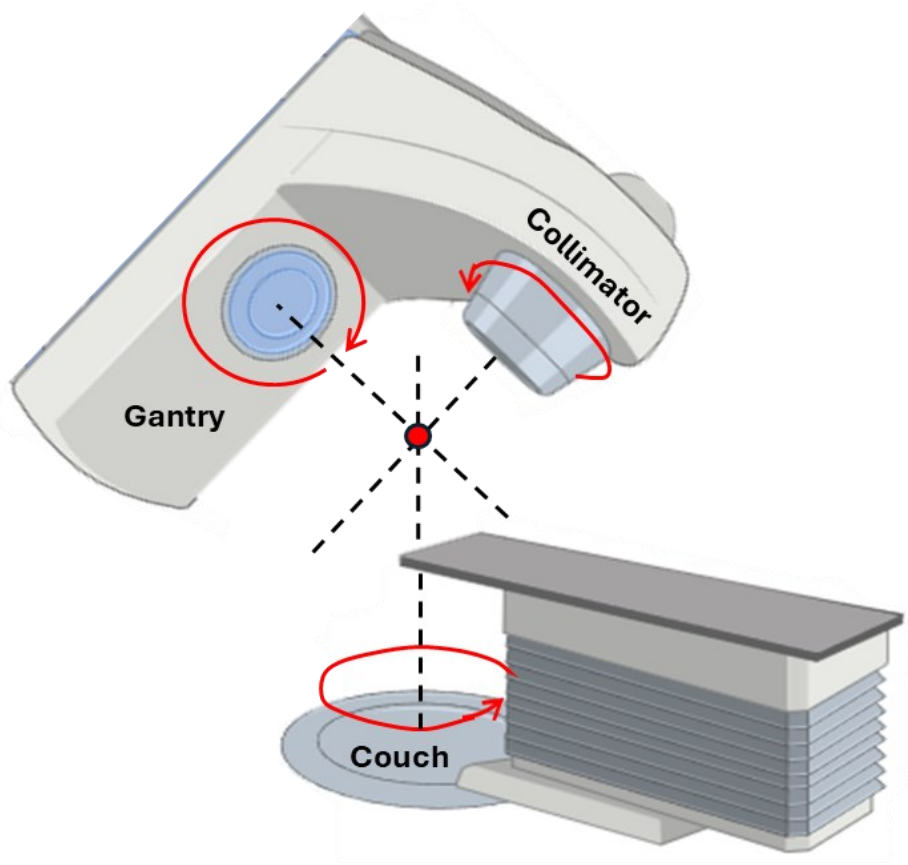

Figure 1.2: Illustration of LINAC geometry and rotation axes with the machine isocenter depicted in red.

To calculate the absorbed dose to the patient (i.e., the energy absorbed per unit mass in tissue), modern radiotherapy systems use volumetric imaging data to create a 3D representation of the patient, voxel by voxel. The primary imaging data set used for treatment planning is a Computed Tomography (CT) scan. A CT dataset provides the most accurate model of the patient for dose computation, as there is a one-to-one relationship between CT number and electron density. A typical CT volume comprises 50 to 200 axial images, with a voxel matrix dimension of 512 x 512 and a slice thickness ranging from 0.625 to 5 mm[21].

1.3 *IN-VIVO* DOSIMETRY

There exist numerous variables involved in external beam radiotherapy treatment planning; these include mechanical variables related to collimating and positioning the beam, radiation-related variables associated with the intensity profile of the beam produced by the LINAC, and patient-related variables, such as the patients shape and position relative to the

beam. Delivery of radiotherapy treatment with high spatial and dosimetric accuracy requires all these variables to be within tolerance. Before patients arrive at the clinic for radiation therapy, treatments are carefully planned, checked, and verified. However, pretreatment dose verification cannot catch errors related to patient geometry or beam delivery during the actual treatment[25]. Consequently, variations in patient position, anatomical changes, or inadvertent deviations in treatment unit performance may introduce errors in radiation dose delivery.

In 2020, Ruiz et al. gave a formal definition of *in-vivo* dosimetry for use in the context of external beam radiotherapy treatments[19]:

"IVD is a radiation measurement that is acquired while the patient is being treated, containing information related to the absorbed dose in the patient. This definition implies that an IVD system must be able to capture errors due to equipment failure, errors in dose calculation, patient positioning errors, and patient anatomy changes."

In radiotherapy, *in-vivo* dosimetry serves two primary purposes: measuring the dose to sensitive structures that are difficult to calculate (e.g., eyes, gonads, or skin) and verifying the delivered dose to enhance treatment accuracy and minimize the risk of dose errors[26]. I*n-vivo* dosimetry has been shown to detect a variety of potential treatment errors[27,28]:

i) Positioning differences between treatment planning and delivery (e.g., source-to-surface distance, beam geometry, isocenter, table angle.)
ii) Treatment machine error (e.g., Changes in the dose delivered per monitor unit, beam parameters out of tolerance (flatness, symmetry), improper rotational rate for arc therapy.)
iii) Human errors in data generation, data transfer, and treatment setup (e.g., incorrect setting of beam energy or monitor units, incorrect alignment of wedge filter or other treatment accessory, selected treatment data for the wrong patient.)
iv) Errors in entrance dose calculation by the TPS.

Geometric misses due to improper positioning are the most frequently occurring treatment error[27].

The dosimetric impact of a given treatment error is unique for each case, influenced by factors such as the proportion of affected fields, the volume mistreated, and the number of treatment fractions administered before the error was detected. Generally, a significant

systematic error is one leading to a deviation of 5% or more from the intended dose, surpassing what is referred to as the tolerance level[26,28]. The IAEA recommends halting treatment if the tolerance level is exceeded by a factor of 2 or more (i.e., > 10%) until the cause of the error has been identified[26].

1.4 *IN-VIVO* DETECTORS

As previously discussed, most detectors are best suited to measuring radiation in the absence of a patient. Despite this, some detectors can still perform *in-vivo* surface dose measurements. In most cases, this involves the placement of one or more-point dosimeters on the patient. The dosimeters measure the absorbed dose and allow the practitioner to subsequently read out this measured dose for comparison to planned values. These detectors include:

I. **Thermoluminescent Dosimeters (TLDs):** These dosimeters provide dose at a discrete point. TLD crystals (e.g., lithium fluoride doped with magnesium or titanium) store accumulated charge and are annealed with heat to provide a retrospective measurement of the absorbed dose.

II. **Optically Stimulated Luminescent Dosimeters (OSLDs):** These dosimeters also provide dose at a point and typically contain an Al_2O_3:C crystal. Following irradiation, OSLDs are placed into an optical reader and stimulated with light, allowing a retrospective readout of the absorbed dose.

III. **Metal Oxide Field Effect Transistors (MOSFETs) or Photodiodes:** These are small, solid-state detectors that may be placed on the surface of the patient. Absorption of ionizing radiation produces a detectable charge (or current), which can be related to the absorbed dose. These detectors allow for real-time dosimetry at a single point and are generally directly connected to readout electronics.

IV. **Point Scintillators:** Point scintillators are composed of a near water equivalent plastic scintillator material. Under irradiation they produce light which is generally transmitted via optical fiber to a photodetector. Following calibration to dose, scintillators permit retrospective or real-time readout of the absorbed dose at a point.

The accuracy of the various point detectors in *in-vivo* surface dose measurement is dependent on the accuracy of their calibration, the beam geometry, the total dose being

measured, and the baseline used for comparison (e.g., ion chamber, TPS calculation or Monte Carlo simulation). Difficulty in positioning the detector on the patient and uncertainty in its placement can also substantially impact the measured-to-planned dose agreement of point detectors[29]. Various studies using OSLDs, TLDs, MOSFETs, diodes and scintillators for surface dose measurements have demonstrated individual differences of as little as 1%-2% to as much as 20%-30% of the corresponding reference dose[14,29–37].

While point detectors offer dosimetric measurements at specific locations, a notable drawback is their inability to provide information about the dose distribution across a broader surface area. This limitation, coupled with the need for retrospective dose measurements or the use of numerous wires on the patient, imposes practical constraints on the maximum number of points that can be effectively measured. Finally, point detectors may perturb the dose due to the presence of readout electronics or the use of high atomic number detector materials[29].

To address these limitations, some detector systems have been developed that can perform *in-vivo* dose measurements over the patient's surface.

I. **Radiochromic Film:** A thin layer (~20 μm) of colorless radiosensitive dye is contained between two transparent layers of plastic, typically Mylar or polyester. Exposure to ionizing radiation initiates a polymerization reaction that darkens the film. Following a fixed development time, the amount of film darkening can be determined using an optical scanner, allowing for a retrospective measurement of the absorbed dose.

II. **Cherenkov Dosimetry:** Cherenkov radiation is emitted when charged particles travel through a medium at a speed greater than the phase velocity of light in that medium and occurs in tissues exposed to radiotherapy treatment beams. Cherenkov imaging provides real-time high-resolution imaging of surface dose distributions. However, conversion of the measured Cherenkov light intensity to absolute dose is impacted by the optical properties of the patient's tissue, currently limiting its ability to provide quantitative dosimetric data[38,39].

Finally, there exists a class of *in-vivo* detector system which does not perform dose measurements on the surface of the patient but attempts to reconstruct planar 2D or 3D dose distributions within the patient.

I. **Transmission Dosimetry:** This method involves capturing the spatial intensity of x-rays passing through the patient during treatment using an Electronic Portal Imaging Device (EPID) coupled to the LINAC. Using CT imaging to determine the anatomical shape and composition of the patient, the dose absorbed within the patient can be inferred using either forward or back projection algorithms. *In-vivo* transmission dosimetry is capable of preventing potential treatment errors[40–42]. Although computationally intensive, it can be performed in real-time for IMRT but gantry angle-dependent reconstruction limits its current application for VMAT[40,43,44]. However, dose differences in the plane of the EPID do not always directly correlate with those in the patient due to the non-water-equivalent response of the detector[7,19,41]. This requires detailed vendor specific models of EPID response or empirical/model-based corrections for accurate dosimetry[45]. The response of the EPID detector also drifts overtime due to radiation damage[45].

In-vivo Cherenkov and transmission dosimetry have both demonstrated the potential to prevent treatment errors resulting from differences in patient positioning, human error, and large deviations in treatment machine performance[25,40,46,47] However, additional research is required to provide quantitative dosimetric data that can be accurately correlated with the dose received by specific structures. This includes linking Cherenkov dosimetry to the dose received by the patient's skin and transmission dosimetry to the dose deposited in the 3D volume of the patient. Recent papers highlight the need for improved technology for the routine implementation of *in-vivo* dosimetry in radiation therapy[11,19]. Currently, no feasible methods exist for providing *in-vivo* dose measurement over the patient's surface during radiotherapy treatment delivery.

Point scintillators overcome many of the challenges faced by other *in-vivo* detectors. Their water equivalence ensures dose deposition in the detector is equivalent to tissue, the scintillation light they produce is proportional to the absorbed dose, they do not suffer from dose rate dependence and can be readout in real-time. However, like other point detectors, their application in *in-vivo* dosimetry is hindered as the placement of numerous point detectors

on the patient is cumbersome, challenging to position accurately and adds extra time to treatment delivery. The proposed detector system aims to address this current limitation of point scintillators by using 3D printing to produce a conformal array of plastic scintillators for performing dosimetric measurements on the surface of the patient. The detector can be read out wirelessly, alleviating the need to place numerous wires on the patient, and could be done so in real-time. Its conformal design would also reduce positioning errors and remove the need to adhere hundreds of point detectors to the patient prior to treatment.

1.5 FDM 3D PRINTING OF RADIATION DETECTORS

The following excerpts have been modified and reproduced with permissions (Appendix A.1) from: "Camera-based radiotherapy dosimetry using dual-material 3D printed scintillator arrays" by Nicholas Lynch, James L Robar, Thalat Monajemi, 2023, *Medical Physics,* 50(3):1824-1842 (doi: 10.1002/mp.16167). Copyright 2023 by John Wiley and Sons. It differs only from the original text in additions for clarity and the inclusion of studies released following its publication.

"3D printing is classified as an additive manufacturing technique as the material is added in layers. In this way users can rapidly create complex shapes that would otherwise be difficult, costly and time consuming to produce by current forming and molding techniques. The lowest-cost and most common 3D printing method is Fused Deposition Modeling (FDM). FDM 3D printing functions by heating and extruding thermoplastic filament one layer at a time to additively produce 3D structures.

Currently, it is possible to print using a range of filaments, including those that are carbon fiber-infused, conductive, magnetic, wood-filled, metal-filled, glass fiber reinforced and flexible. This broad range of available materials and the potential of combining their various mechanical/electrical properties into a single 3D printed design makes FDM an attractive option for fabricating patient-specific devices in radiotherapy. 3D printing has already been shown suitable for the fabrication of phantoms, immobilization devices, boluses, brachytherapy applicators, and other patient-specific radiotherapy treatment accessories[48]. The use of individualized patient-specific devices has also been shown to improve treatment delivery, device conformity, patient comfort and cost-effectiveness while minimizing unnecessary treatment toxicity[48].

Despite numerous beneficial applications of 3D printing in radiotherapy and its continued development for the fabrication of miniaturized, low-cost sensors, there has been a sparsity of investigation into its potential to produce radiation detectors[49]. This has been partly due to the challenges encountered when attempting to print designs that incorporate multiple materials with distinctly different properties (insulating/conductive, rigid/flexible, etc.). Even when using commercially designed dual-material FDM 3D printers the quality and consistency of multi-material prints are not guaranteed. Problems with material-material adhesion, material mixing, and clogging of the print nozzles often result in poor print quality, low print success rates, and reduced dimensional accuracy[50–53]. This is particularly the case when printing with thermoplastic filaments doped with additional materials such as metal, wood, glass, and carbon fiber."

"Despite the challenges, the development of radiation detectors for radiotherapy specific applications may benefit from FDM 3D printing, but this has only been pursued recently. The feasibility of using FDM 3D printing for the fabrication of radiation detectors was initially demonstrated in 2018[54]. A 3D printed drift tube composed of polylactic acid filament (PLA), P5 gas (95% Argon, 5% Methane) and a stainless-steel anode was used for the detection of cosmic ray muons. While the 3D printed detector was not fully composed of 3D printed parts it established FDM 3D printing as a potential avenue for radiation detector development.

In 2019, FDM 3D printing was used to produce a planar ionization chamber array using conductive polylactic acid (cPLA) and insulating components made of acrylonitrile butadiene styrene (ABS)[52]. The array possessed a spatial resolution of 5 x 7 mm^2 and had a detector volume of 96 mm^3. The rectangular array elements were measured using leads connected to an electrometer and delivered comparable performance (within 2%) to a PTW diode detector under reference conditions. Continued development has improved array spatial resolution to 4 x 4 mm^2 and reduced detector volume to 28 mm^3 [55].

Finally in October of 2022 the CERN 3D Printed Detector (3DET) project demonstrated a 3 x 3 matrix of plastic scintillator cubes (1 cm^3) optically separated by a white reflector material that had been entirely FDM 3D printed[56]. Using optical fibers and silicon photomultipliers the scintillation light yield produced by cosmic ray muons was investigated. Results indicate that the 3D printed scintillator matrix produced a sufficient signal-to-noise

ratio in response of cosmic muons with minimal optical crosstalk between adjacent matrix elements."

1.6 3D PRINTING OF PLASTIC SCINTILLATORS

Scintillators are materials that produce photons in the visible spectrum in response to the passage of charged and uncharged particles. Scintillating materials are commonly used in particle detectors due to their ease of manufacture, relatively low cost, and good timing resolution. The term "plastic scintillator" refers to a scintillating material in which a primary fluorescent emitter, called an organic fluor, is suspended in a solid polymer matrix. They can be classified into either binary systems composed of scintillating material (primary fluor) incorporated into a solvent (e.g., liquid solution of p-terphenyl in toluene) or ternary systems made of two scintillating materials (primary fluor and wavelength shifter (secondary fluor)) incorporated in a solvent (e.g., plastic solution of p-terphenyl and POPOP in polystyrene)[57].

Plastic scintillators are typically manufactured over several days using a thermal polymerization process and shaped into the desired form using molding or casting[58]. Scintillators produced using this method usually have regular geometric shapes (e.g., slabs, cylinders, or fibers). Adding an initiator can shorten the polymerization time, but production within a single day remains challenging[59–63]. However, the growing adoption of 3D printing for rapid prototyping applications has generated interest in applying this process to overcome the current constraints of plastic scintillator fabrication.

In 2014, researchers at the Hebrew University of Jerusalem produced the first study of plastic scintillators fabricated using 3D printing[64]. Using a UV polymerizable acrylic monomer and resin-based stereolithography (SLA) 3D printing, researchers were able to print scintillators doped with different fractions of scintillating and wavelength shifting materials (e.g. 2,5-Diphenyloxazole, (PPO), 1,4-Bis(5-phenyl-2-oxazolyl) benzene (POPOP), and Naphthalene). SLA 3D printing is an additive manufacturing process that works by focusing a UV laser onto a vat of photopolymer resin to solidify it layer by layer. The resulting scintillators possessed a scintillation efficiency of 28.0% that of the commercial polyvinyl toluene-based plastic scintillator EJ-204.

Researchers from the Department of Nuclear Engineering at Hanyang University in Seoul, South Korea, have also been actively developing resin-based 3D printable plastics scintillators.

They have produced a series of publications that build on previously mentioned work and investigate various additional chemical formulations for an acrylic-based plastic scintillator[58,65–67]. In particular, a new wavelength shifter, ADS086BE, was added instead of the conventional POPOP. This work resulted in the development of a UV-curable photopolymer capable of functioning as a scintillating material[65]. Using Digital Light Processing (DLP) 3D printing (which, like SLA 3D printing, uses UV light to cure layers of photopolymer resin sequentially), the researchers were able to fabricate plastic scintillators that possessed a light output performance 67.0% that of the commercial polystyrene-based plastic scintillator BC-408[65]. Subsequently, these researchers have produced their 3D printed scintillators in a variety of different geometries with the goal of facilitating dosimetric measurements for the Gamma Knife® Icon[68,69].

A CERN-led 3DET collaboration, has been engaged in developing Fused Deposition Modeling (FDM) 3D-printed scintillators. To additively create 3D structures, FDM 3D printing works by heating, extruding, and depositing thermoplastic filaments one horizontal layer at a time. In 2020, the group reported on the development of a flexible plastic scintillating filament for FDM 3D printing[70]. It was created by doping polystyrene with 2% by weight of p-terphenyl, 0.05% by weight of POPOP, and 5% by weight of the plasticizer biphenyl. The subsequent 1 cm^3 FDM 3D printed scintillators demonstrated that heating did not significantly reduce the scintillator's transparency. Their light yield was comparable to scintillators produced from identical material via casting and molding techniques.

1.7 CAMERA BASED SCINTILLATION DOSIMETRY

In scintillation dosimetry, plastic scintillators are often used as point detectors and referred to as plastic scintillation dosimeters (PSDs). PSDs are a class of radiation detector that overcomes many of the limitations of other detector systems. When properly calibrated, the amount of scintillation light produced is proportional to the absorbed dose. Their water equivalence, dose rate independence, energy independence in the MV energy range, and stability make them excellent candidates for the dosimetry of clinical electron and photon beams[71]. PSDs have been used in routine beam characterization work, small-field dosimetry[72–74], and *in-vivo* dosimetry[75–77].

However, as previously discussed, they are commonly read out using an optical fiber coupled to a photodetector. While this method can provide insight into the scintillator's behavior, such a setup is unsuitable for routine multi-point *in-vivo* dosimetry, as placing hundreds of optical fibers on the patient during treatment delivery would be prohibitively cumbersome. This limitation has spurred investigations into alternative methods of scintillator readout, with the use of CCD and CMOS cameras emerging as a novel and promising approach. This has been an active area of research at the Université Laval for over a decade and is widely documented in the literature[75,78–80]. The following consists of a summary of the group's specific works that are of interest to this investigation. This work both applies and builds on the methodology employed by these investigators.

In 2008, Archambault et al. investigated the effects of ionizing radiation on CCD cameras, noting that it strongly alters the collected images and, therefore, limits quantitative image analysis[81]. The purpose of the work was to characterize the radiation-induced noise and develop filtration algorithms to restore image quality. Results indicated that the median of a time series of images produces the best filtration and minimal image distortion.

Robertson et al. then performed a systematic study in 2014 to characterize the optical artifacts affecting the measurement accuracy of camera-based liquid scintillation detector systems and to develop correction methods[82]. The optical artifacts addressed were photon scattering, refraction, camera perspective, vignetting, lens distortion, the lens point spread function, stray radiation, and noise in the camera. The proposed correction methods effectively mitigated the artifacts, increasing the average gamma analysis pass rate for the tested proton pencil beam from 66% to 98% (gamma criteria 2%/2 mm).

Finally, in 2021, Cloutier et al. published two papers on the development of a deformable scintillation dosimeter consisting of an array of 19 scintillating fibers embedded inside a cylindrical elastomer matrix[83,84]. Using a stereoscopic camera arrangement, appropriate camera calibration, and computer vision techniques, simultaneous position tracking and scintillator dose measurements were performed. The detector was capable of acquiring deformation vector fields with a precision of 0.3 mm and dose measurements within 1% of treatment planning system calculation under reference conditions.

1.8 RESEARCH OBJECTIVES

This work aims to develop a detector capable of fulfilling the unmet clinical need for accessible, routine, and real-time *in-vivo* dosimetry for patients undergoing radiotherapy[7,19]. The presented work makes a distinctive contribution, deviating from the previously discussed studies in Chapter 1, by leveraging the unique capabilities of dual-material FDM 3D printing. This research not only facilitates the fabrication of customized, high-resolution plastic scintillator arrays with user-defined geometries but also paves the way for expanding the application of 3D printing in radiotherapy to detector fabrication. This thesis presents the evolution of a novel detector system and consists of a series of three manuscripts, each addressing a key research objective.

1.8.1 Characterization of Novel 3D Printed Plastic Scintillation Dosimeters

Presented in Chapter 3, this manuscript represents the first comprehensive analysis of 3D-printed plastic scintillation dosimeters for radiotherapy applications. By leveraging the FDM 3D printing process, this work provides a methodology for producing 3D-printed plastic scintillators with the required dimensional accuracy, clarity, and light yield to function as effective radiation dosimeters. It includes establishing the basic dosimetric properties of 3D printed scintillators and quantifies the dependence of their signal on 3D printing parameters. This work demonstrates that 3D-printed scintillators possess many of the same dosimetric properties as commercially available scintillators and make excellent dosimeters. Such characteristics are an essential prerequisite for the detector material of the proposed dosimetry system.

1.8.2 Camera-Based Radiotherapy Dosimetry Using Dual-Material 3D Printed Scintillator Arrays

Presented in Chapter 4, this manuscript demonstrates the capability of dual-material 3D printing to fabricate scintillator arrays with complex geometries. It introduces methods for overcoming known challenges with dual-material 3D printing and accounts for/mitigates scintillator-specific print issues. It also provides an image processing algorithm capable of correcting various optical artifacts, facilitating wireless array readout using a single camera. This study establishes a correlation between scintillator light output and absorbed dose for simple

array geometries and demonstrates the ability of calibrated arrays to perform accurate dose measurements of radiotherapy treatment plans.

1.8.3 Camera based Multipoint *In-Vivo* Dosimetry Using 3D Printed Patient Specific Scintillator Arrays

Presented in Chapter 5, this manuscript showcases the ability of FDM 3D printing to produce patient-specific plastic scintillator arrays. This study demonstrates a unique dosimetric calibration method employing 3D printing and stereoscopic imaging. When compared to Monte Carlo simulated doses, measurements performed with a calibrated patient-specific scintillator array were within 5%-10%. This is comparable to other point detectors used for *in-vivo* surface dose measurements, such as MOSFETs, OSLDs, TLDs, and Diodes. Despite this, the patient-specific array calibration remains too clinically impractical to implement routinely. Overcoming this challenge is essential for harnessing the full potential of the detector system to provide practical and routine clinical *in-vivo* dosimetry.

The second chapter of this thesis discusses the theoretical concepts related to particle interactions, radiation dosimetry, scintillator physics, and other concepts/research methods used to accomplish the work presented. The sixth chapter concludes the thesis by summarizing the key findings of the manuscripts and hypothesizing about future work.

CHAPTER 2 BACKGROUND AND METHODS

This thesis aims to develop a novel 3D-printed radiation detector capable of performing *in-vivo* surface dose measurements during external photon beam radiotherapy treatments. As such, it is critical to understand the type of particle interactions that may take place within the detector. This chapter begins by first discussing the source of therapeutic radiation in photon beam radiotherapy, the LINAC, and how its produced photon beam interacts with attenuating materials (biological tissues, artificial phantoms, radiation detectors, etc.). During irradiation by an external photon beam, the signal produced inside the detector results from numerous particles of varying trajectories depositing energy within the detector material. However, the relationship between the energy deposited in the detector and the patient's absorbed dose depends on various detector-specific variables, including the detector's physical dimensions and material properties (homogeneity, atomic composition, electron density). Therefore, this chapter will then discuss the general aspects of measuring and calculating the absorbed dose in materials irradiated by photon beams, known as photon beam dosimetry. It will then discuss additional dosimetric characteristics specific to this investigation's chosen detector material, plastic scintillators. Finally, this chapter will address aspects of the hardware and computational methods used in experimental dosimetry and in this research.

2.1 PHOTON BEAM GENERATION AND INTERACTIONS

This section will discuss the process of photon beam generation in clinical linear accelerators and the details of photon interactions pertinent to the energy range used in external photon beam radiotherapy.

2.1.1 Photon Beam Generation

Photon beams are generated in clinical linear accelerators through the bremsstrahlung interactions of high-energy electrons as they strike a high atomic number target[85]. The details of electron interactions are covered in section 2.2. Although the specifics of photon beam generation can differ between LINAC models and vendors, this study exclusively focuses on the dosimetry of photon beams produced using the Varian TrueBeam LINAC. Consequently, the specifics of LINAC photon beam generation will be discussed here in the context of the Varian TrueBeam system.

Initially, electrons are generated within a gridded electron gun via thermionic emission from a heated cathode[85]. Unlike a traditional X-ray tube, a gridded electron gun incorporates a third element, the control grid, which is positioned between the cathode and anode[86]. This metal grid, close to the cathode, generates an electric field opposing that of the anode[86]. The application of voltage to the grid enables precise control over the quantity of electrons emitted from the plate, rendering the LINAC capable of achieving variable dose rates[86].

These electrons are then accelerated using microwaves through a series of evacuated resonance cavities called the accelerator waveguide. The process begins with the generation of microwave power using a klystron or magnetron. Microwave power is then directed to the accelerator waveguide using a series of small, pressurized pipes filled with sulfur hexafluoride insulating gas[85]. Two ceramic windows, which are transparent to microwaves, separate the pressurized pipes from the microwave generator and accelerator waveguide. As the microwave power propagates through the waveguide, it induces an alternating electric field. The timing of the electron injection is synchronized with the alternating field such that the electrons experience a force in the forward direction[85]. The initial cavities are of varying sizes and are designed to bunch and accelerate the electrons. The subsequent cavities are of equal size and maintain the electrons at constant velocity. As the electrons travel down the length of the accelerator, they gain energy reaching relativistic velocities, with a 2 MeV electron moving at 98% the speed of light[85].

As shown in Fig 2.1, the electron beam leaving the accelerator then passes through an evacuated bend magnet, which deflects the beam approximately 270^{o} [85]. This process provides additional focusing of the spread of energies in the electron beam and results in a small focal spot when it strikes the tungsten X-ray target. The spatial distribution of high energy photons that emerge from the target is strongly forward peaked. A conical metal (copper or tungsten) flattening filter is employed to achieve a more uniform distribution for treatment purposes[85]. This filter selectively absorbs more photons from the intense central axis of the beam than from its periphery, thereby flattening the initially peaked distribution. Following this, the beam is collimated using two sets of orthogonally placed opposing tungsten jaws and an MLC comprised of two opposed banks of individually motor-controlled tungsten leaves. The collimation process ensures the photon treatment field's uniformity and conforms it to the desired shape for radiotherapy treatment.

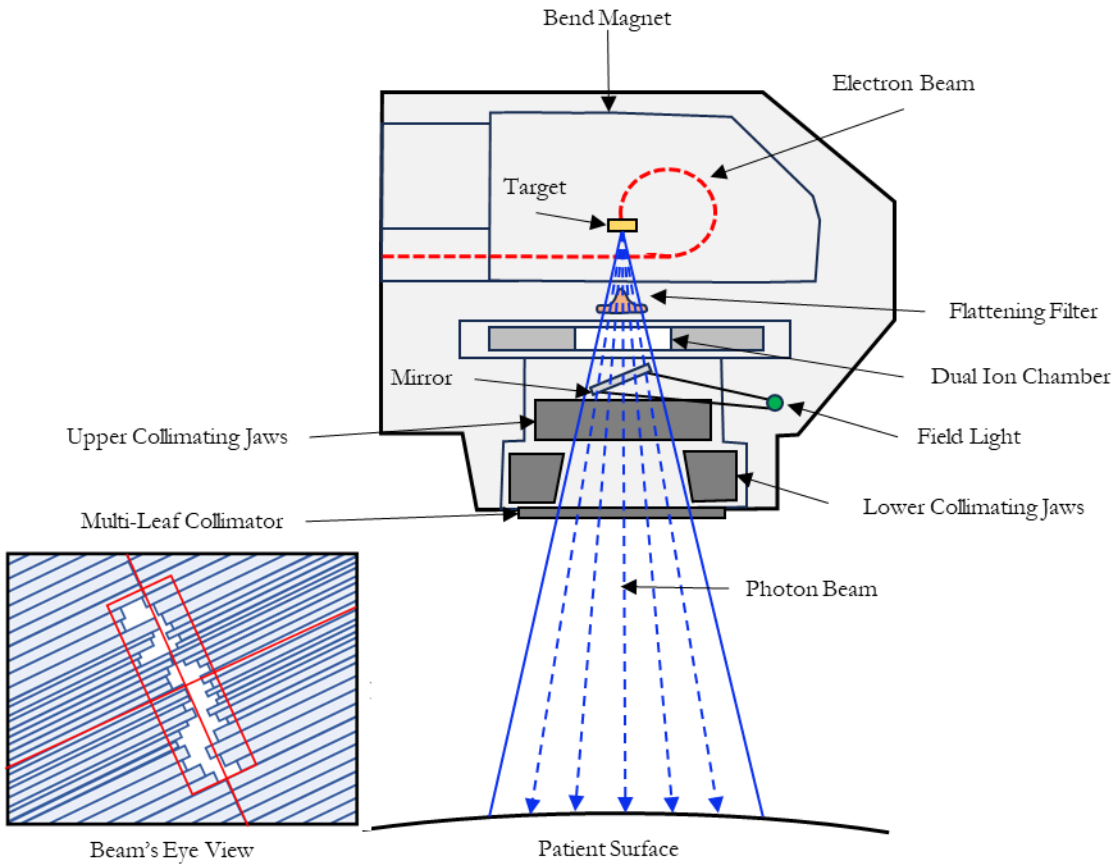

Figure 2.1: Illustrated cross section of the LINAC treatment head showing the main components and their geometric relationship to each other. Modified and reproduced with permissions from Karzmark[85] (Appendix A.2).

2.1.2 Photon Interactions in Matter

Photons are indirectly ionizing radiation, meaning they deposit their energy in an absorbing medium via a two-step process. First, the energy is transferred to light-charged particles (electrons and positrons), and then the energy is deposited in the medium by the now energetic charged particles.

An incident photon may interact with an absorbing medium through many possible mechanisms dependent on the photon energy and atomic number of the absorbing material, as shown in Fig 2.2. These interactions may be with nuclei of the absorbing medium or with orbital electrons. Of the numerous known interactions, five are of principal interest in medical physics as they govern the attenuation and scattering of photon beams by tissues and the energy transfer of photons to light-charged particles. These are The Photoelectric Effect (τ),

Compton Scattering (σ_C), Rayleigh Scattering (σ_R), Nuclear Pair Production (κ_N), Electronic Triplet Production (κ_E).

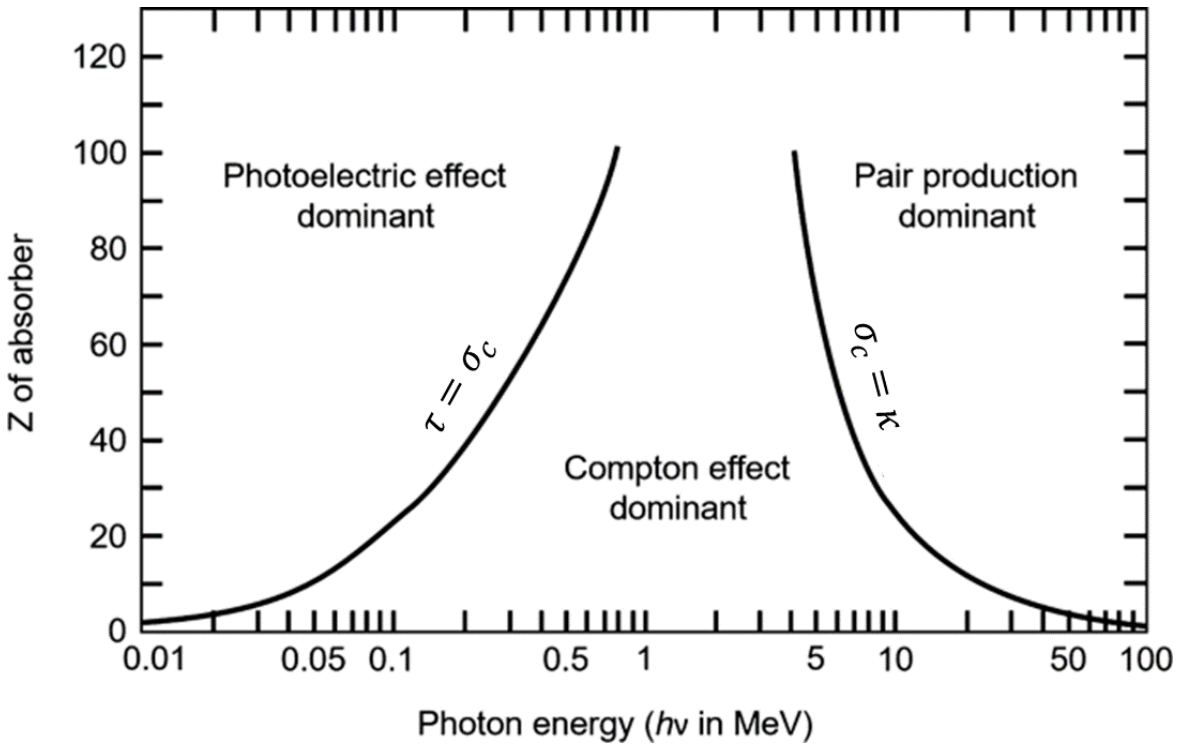

Figure 2.2: Relative importance of each photon interaction mechanism as a function of atomic number and photon energy. Lines indicate where interactions are of equal dominance. Reproduced with permissions from Tan[87] (Appendix A.4).

2.1.2.1 The Photoelectric Effect

The Photoelectric effect describes the interaction of an incident photon with a tightly bound orbital electron of an absorber atom, resulting in the ejection of an energetic photoelectron (Fig 2.3). In this case, a tightly bound electron is considered one that has a binding energy (E_B) comparable to the energy of the incident photon (E_γ). The photoelectric effect cannot occur unless $E_\gamma > E_B$ with the probability of interaction increasing the closer E_γ is to E_B[88,89]. However, at $E_\gamma = E_B$ the interaction probability drastically decreases, resulting in what is known as the characteristic absorption edge[88,89]. These sharp discontinuities occur whenever the binding energy of a given electron shell is exceeded, and a new pathway for photoexcitation becomes energetically possible.

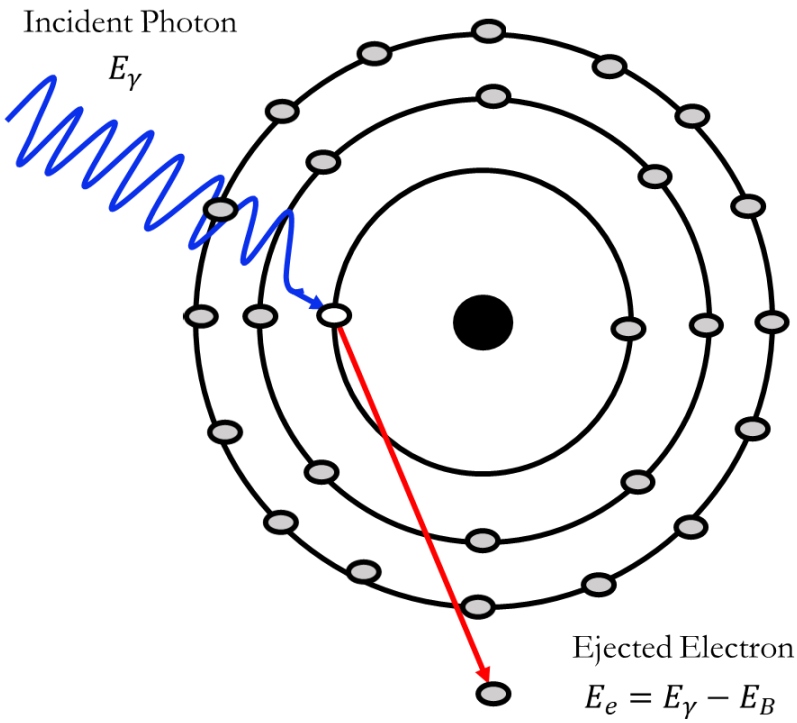

Figure 2.3: Illustration of photon undergoing a photoelectric interaction with tightly bound orbital electron.

In the energy range of interest in medical physics, interactions with the k-shell electrons play a dominant role. Photons give up 100% of their energy in interactions with tightly bound electrons, particularly in high Z materials[88,89]. About 80% of all photoelectric interactions occur within the k shell, with the remaining 20% with less tightly bound higher shell orbital electrons[88,89]. Following the interaction, the ejected photoelectron's kinetic energies (E_e) and angular distribution depends on E_γ. At low photon energies (~10 keV), photoelectrons tend to be emitted at angles close to 90^0, however, as photon energy increases the emission peak migrates progressively towards more forward angles[88,89].

The probability of photoelectric interaction is governed by the total photoelectric cross-section, which can be approximated as[89],

$$\tau = \frac{8}{3}\pi {r_e}^2 \sqrt{32}\alpha^4 Z^5 \left(\frac{m_e c^2}{E_\gamma}\right)^{\frac{7}{2}} \quad (1)$$

where r_e is the classical electron radius, and α is the fine structure constant. The photoelectric effect rapidly decreases in significance with increasing photon energy. The dependence of the

photoelectric effect on Z and E_γ results in the photoelectric effect acting as a significant contributor to photon beam attenuation for low photon energies in tissues[88,89].

2.1.2.2 Compton Scattering

Compton scattering describes the interaction of a photon with energy E_γ and a loosely bound orbital electron of an absorber atom. An electron is defined as loosely bound if the incident photon energy is much greater than the electron's orbital binding energy E_B. During a Compton interaction, the incident photon collides with the orbital electron, losing energy in the process (Fig 2.4). The photon is scattered from its original trajectory now with energy $E_\gamma{}'$ and a free electron (also called the Compton recoil electron) with kinetic energy E_e is produced. The distribution of the incident photon energy between the resulting recoil electron and the scattered photon is a function of the initial photon energy and scattered photon angle (θ).

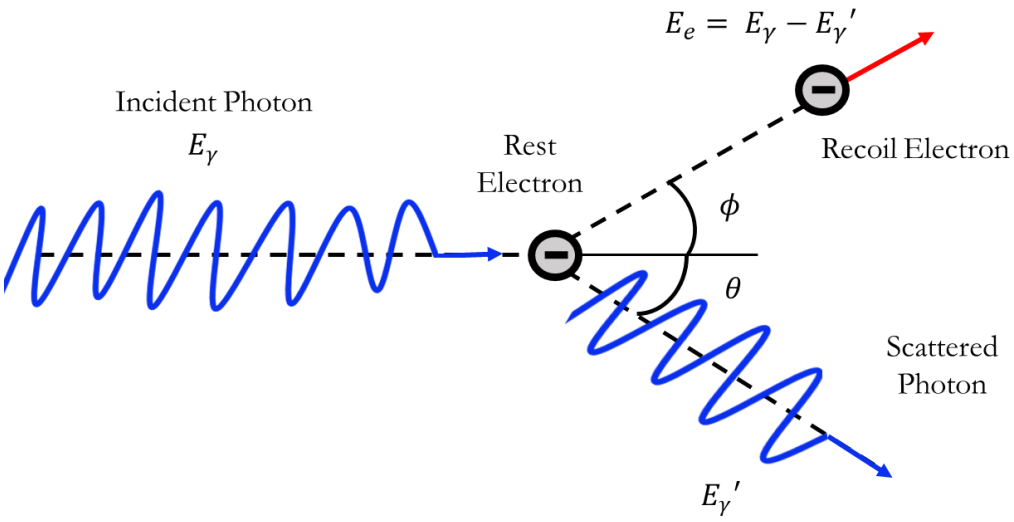

Figure 2.4: Illustration of photon undergoing Compton scattering with loosely bound orbital electron.

The distribution of the Compton scattered photons and recoil electrons is of interest in medical physics as Compton scattering is the predominant mode of photon interaction with tissue in the radiotherapy energy range (20 keV to 20 MeV)[88,89]. At low incident photon energies (~10 keV), the assumption of a loosely bound orbital electron breaks down, and electron binding energy affects the Compton cross-section[88,89]. However, this occurs in an energy region where the photoelectric effect is the dominant photon interaction process, so binding corrections are generally ignored[88,89].

The Klein-Nishina formula gives the differential cross-section for an incident photon scattered by a single loosely bound orbital electron[88,89].

$$\frac{d\sigma_C}{d\Omega} = \frac{1}{2} {r_e}^2 \left(\frac{{E_\gamma}'}{E_\gamma}\right)^2 \left[\frac{{E_\gamma}'}{E_\gamma} + \frac{E_\gamma}{{E_\gamma}'} - \sin^2(\theta)\right] \tag{2}$$

The formula describes the scattering of low-energy photons (visible light) and high-energy photons (X-rays or gamma rays). At low energies, the wavelength shift becomes negligible (no energy loss), and the Klein-Nishina formula reduces to the classical Thomson expression for elastic photon scattering[88,89].

$$\frac{d\sigma_{Th}}{d\Omega} = \frac{1}{2} {r_e}^2 [1 + \cos(\theta)^2] \tag{3}$$

Therefore, at low energies, the Klein-Nishina formula shows a symmetrical relationship with the scattering angle, i.e., it is just as probable for the photon to scatter in the forward direction as backward. However, as the incident photon energy increases, photon scattering becomes increasingly forward directed. This leads to the characteristic "peanut" shaped angular scattering distribution characteristic of Compton scattering, plotted in Fig 2.5.

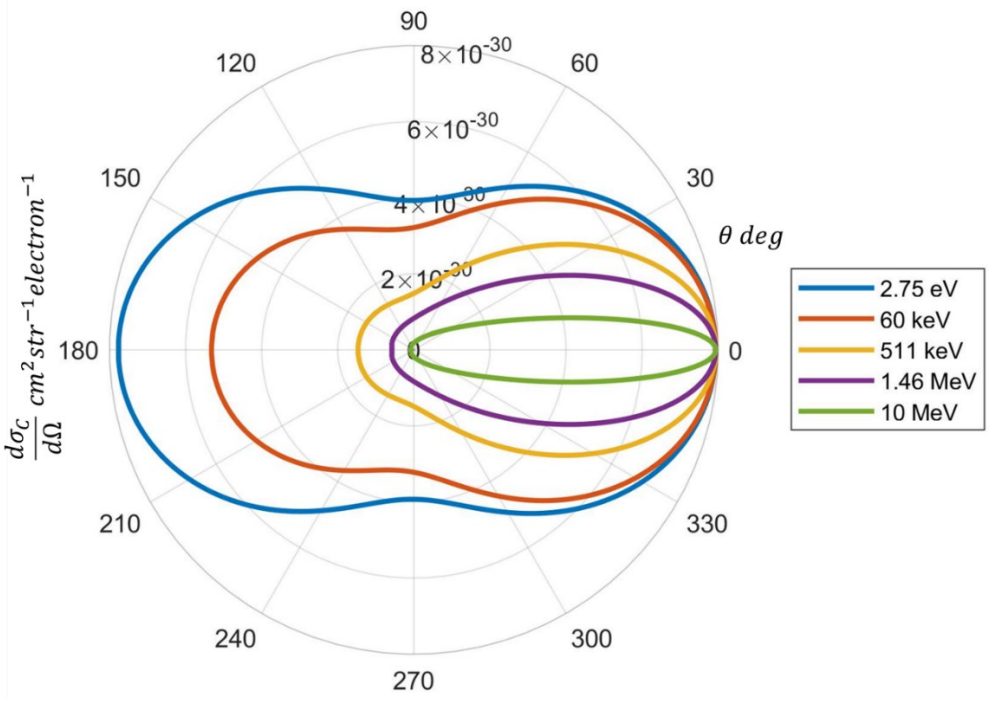

Figure 2.5: Polar plot of the differential Compton cross-section as a function of scattering angle (Eq. 2) for various incident photon energies, plotted using MATLAB.

The probability of Compton scattering is governed by the total Compton scattering cross-section, which is determined by the integral of the corresponding differential cross-section over all solid angles[90].

$$\sigma_C = Z2\pi {r_e}^2 \left(\frac{1+k}{k^2} \left[\frac{2(1+k)}{1+2k} - \frac{\ln(1+2k)}{k} \right] + \frac{\ln(1+2k)}{2k} - \frac{1+3k}{(1+2k)^2} \right) \quad (4)$$

where k is,

$$k = \frac{E_\gamma}{m_e c^2} \quad (5)$$

Compton scattering is approximately independent of the atomic number (Z), and as photon energy increases, it initially becomes more prominent and then decreases.

2.1.2.3 Rayleigh Scattering

In practice, most elastic photon scattering occurs with electrons bound in atoms rather than free electrons (Thomson scattering). This is known as Rayleigh scattering. In Rayleigh scattering, the whole atom is considered to absorb the transferred momentum, and the energies of the incident and scattered photon are the same. No energy is transferred to electrons in Rayleigh scattering, and the recoil energy imparted to the atom is small, resulting in a small photon scattering angle[88,89]. As a result, Rayleigh scattering plays no role in radiation dosimetry but is important for imaging as scattering adversely affects image quality. The differential cross-section for Rayleigh scattering is given as[88,89],

$$\frac{d\sigma_R}{d\Omega} = \frac{{r_e}^2}{2}(1+\cos^2\theta)\{F(x,Z)\}^2 \quad (6)$$

where $F(x,Z)$ is a complicated function called the atomic form factor, which is a measure of the scattering amplitude of a wave by an isolated atom and x is the momentum transfer variable given as[88,89],

$$x = \frac{\sin\left(\frac{\theta}{2}\right)}{\lambda} \quad (7)$$

where θ is the photon scattering angle and λ is the wavelength of the incident photon. At high photon energies (> 1 MeV), Rayleigh scattering is confined to only small angles for all

absorbers[88,89]. However, the angular distribution becomes broader at low energies, particularly for high Z absorbers[88,89].

While the total Rayleigh scattering cross-section may exceed the total Compton scattering cross-section at low energies, both are very small compared to the photoelectric cross-section[88,89]. Even at very small incident photon energies, the Rayleigh scattering component of the attenuation is small and amounts to only a few percent of the total[88,89]. Therefore, Rayleigh scattering is often ignored in radiation transport calculations.

2.1.2.4 Nuclear Pair Production

Pair production, also called "materialization", is an example of mass-energy equivalence in which a high-energy incident photon (> 1.02 MeV) interacts with the Coulomb field of an absorber nucleus (Fig 2.6). This interaction produces and subsequently ejects a pair of light-charged particles (an electron and a positron). This interaction can only occur in the vicinity of a Coulomb field in order to satisfy the simultaneous need for conservation of energy, charge, and angular momentum[88,89]. Unlike the other photon interactions, such as the photoelectric effect and Compton scattering, pair production exhibits a clear threshold energy below which the interaction is energetically impossible. The energy threshold for pair production is 1.02 MeV or $2m_ec^2$ [88,89].

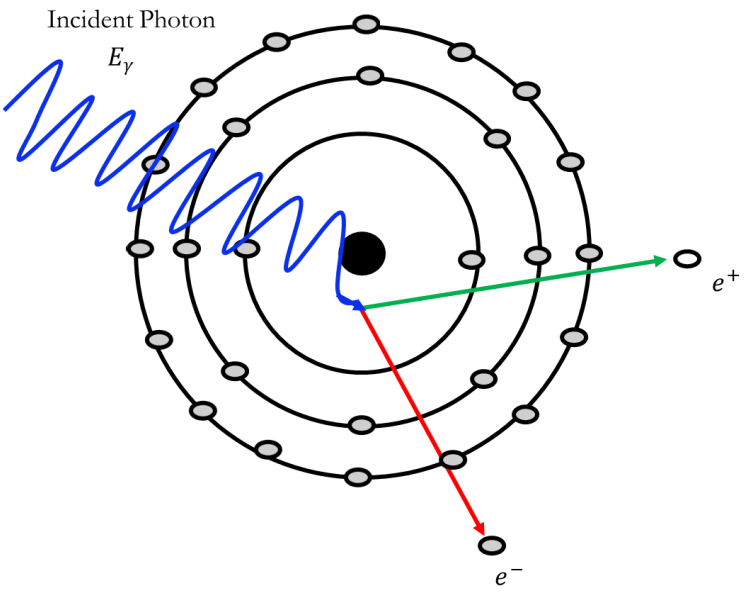

Figure 2.6: Illustration of high energy photon undergoing pair production in the presence of an atomic nucleus.

The probability of a pair production interaction is governed by the total pair production cross-section as described by the Maximon equation, which can be approximated as follows[90],

$$\kappa_N = Z^2 \alpha {r_e}^2 P(k, Z) = Z^2 \alpha {r_e}^2 \left[\frac{28}{9}\ln(2k) - \frac{218}{27} \ldots\right] \quad (8)$$

where $P(k, Z)$ is a complicated function of the incident photon energy and the absorber's atomic number. Within the radiotherapy energy range, the probability of pair production interactions first increases rapidly with incident photon energy above the 1.02 MeV threshold and then saturates. Pair production depends approximately on the square of the atomic number (Z^2).

The positron and electron do not necessarily receive equal kinetic energy following pair production. In pair production, a variety of kinetic energy distributions are possible, except extreme cases where one charged particle would receive all available energy and the other none[88,89]. Similarly, the angular distribution is a complex function of the incident photon energy and the atomic number of the absorber. However, with increasing incident photon energy, the distribution of charged particles becomes more forward peaked[88,89].

As the resulting positrons slow down in the absorbing medium via Coulomb interactions with orbital electrons, they undergo annihilation. Annihilation can occur either in flight or at rest. If annihilation occurs at rest, the positron will collide with an orbital electron, producing two photons with kinetic energy $E_\gamma = 511\ keV$ emitted in opposite directions, approximately 180° from each other[88,89]. With a lower probability (~2%), annihilation can occur in flight[88,89]. In flight, annihilation may result in the production of either one or two photons depending on whether the interacting orbital electron is tightly bound or loosely bound, respectively. The resulting annihilation photon or photons can leave the interaction site with various possible energies and emission angles depending on the incident positron's kinetic energy.

2.1.2.5 Electronic Triplet Production

Like nuclear pair production, electronic triplet production refers to the materialization of an electron-positron pair during the interaction of a high-energy photon with a Coulomb field (Fig 2.7). However, triple production differs in that it occurs with the Coulomb field of an orbital electron, not an atomic nucleus. As an orbital electron provides the Coulomb field, it

also acquires significant kinetic energy to conserve momentum, resulting in the ejection of three particles (two electrons and one positron) from the interaction site[88,89].

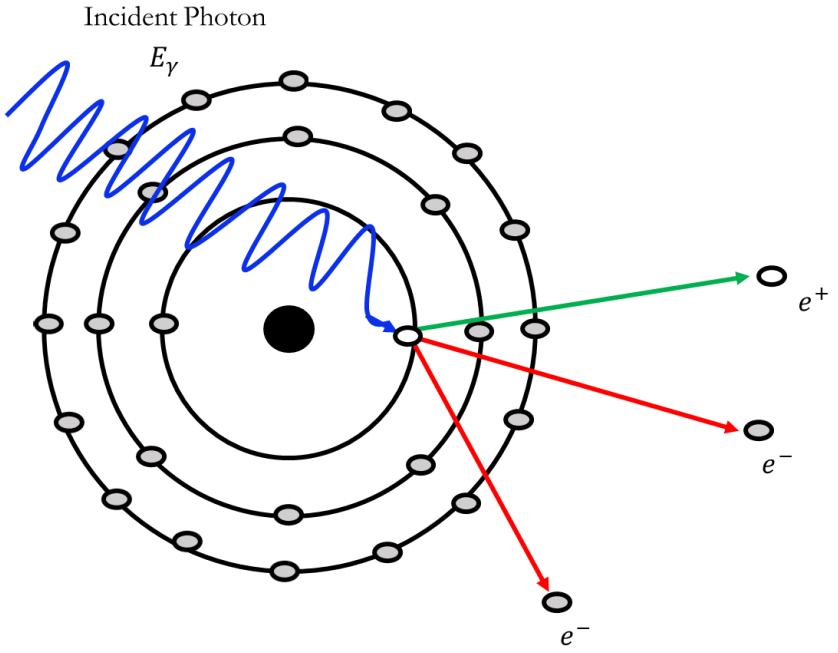

Figure 2.7: Illustration of high energy photon undergoing triplet production in the presence of an orbital electron.

As with pair production, triplet production exhibits a clear threshold energy. The energy threshold for triplet production is 2.04 MeV or $4m_ec^2$ [88,89]. In this case, $2m_ec^2$ is required for materialization, and the remaining $2m_ec^2$ is distributed as kinetic energy to the three charged particles. At the triplet production threshold, the three light-charged particles (two electrons and a positron) carry one-third of the kinetic energy available for particle recoil[88,89]. For energies above the threshold, the kinetic energy of each charged particle becomes a complex function of the incident photon energy[88,89].

The probability of a triple production interaction is governed by the total triplet production cross-section as described by the Borsellino-Ghizzetti equation, which can be approximated as follows[90],

$$\kappa_E = Z\alpha {r_e}^2 P(k,Z) = Z\alpha {r_e}^2 \left[\frac{28}{9}\ln(2k) - \frac{218}{27} \ldots\right] \quad (9)$$

where $P(k, Z)$ is a complicated function of the incident photon energy and absorber's atomic number.

It is worth noting that the cross-section for pair production is proportional to Z^2 while the cross-section for triplet production is proportional to Z. Generally, for high Z materials, the triplet cross-section is approximately 1% of the pair production cross-section[88,89]. However, its relative importance increases to 5%-10% for low Z materials (Z<10)[88,89]. Triplet production is always less probable than pair production as the threshold energy for triplet production is twice that of pair production.

2.1.3 Mass Attenuation Coefficient

When photons interact with an absorbing material, attenuation occurs. Both the material the beam travels through and the beam's energy impact this process. The main interactions involved in photon beam attenuation are the photoelectric effect, Compton Scattering, pair production, and triplet production, each described by its corresponding interaction cross-section. The total photon interaction cross-section per atom can be obtained by adding together the cross-sections of the various possible interaction mechanisms in the medium[88,89].

$$\sigma_{tot} = \tau + \sigma_R + \sigma_C + \kappa_N + \kappa_E \tag{10}$$

The mass attenuation coefficient $(\frac{\mu}{\rho})$ then describes how a material attenuates a beam of photons and is given as[88,89],

$$\frac{\mu}{\rho} = \frac{N_A}{A}[\sigma_{tot}] = \frac{1}{MFP} \tag{11}$$

where ρ is the mass density of the absorber material, N_A is Avogadro's Number, A is the atomic mass of the absorber material and MFP is the mean free path of the incident photons. The mass attenuation coefficient represents the fraction of primary photons removed from the beam per unit distance over medium density[88,89]. It is the macroscopic equivalent of the total interaction cross-section per atom.

There are two other attenuation coefficients relevant to medical physics:

i) Mass Energy Transfer Coefficient $\left(\frac{\mu_{tr}}{\rho}\right)$

This refers to the amount of energy transferred from the primary beam to charged particles in the medium per unit distance over medium density[88,89]. This relates to the energy transferred to charged particles traveling a certain distance.

ii) Mass Energy Absorption Coefficient $\left(\frac{\mu_{en}}{\rho}\right)$

This refers to the amount of energy absorbed by the medium from the primary beam per unit distance over medium density[88,89]. This relates to local energy deposition. It is also related to the mass-energy transfer coefficient by[88,89],

$$\frac{\mu_{en}}{\rho} = \frac{\mu_{tr}}{\rho}(1 - \bar{g}) \tag{12}$$

where $\bar{g}$ is the average fraction of secondary electron energy lost in radiative interactions.

2.2 ELECTRON INTERACTIONS

As previously discussed, within the energy range used for photon radiotherapy, Compton scattering is the predominant interaction mechanism and results in the production of numerous electrons within the irradiated medium. By nature of their electric charge, electrons interact with the medium through fundamentally different mechanisms than photons. Consequently, the dose deposition process of a clinical photon beam would be incomplete without discussing the interactions undergone by these secondary electrons. For brevity, this section will specifically address electron interactions while implicitly referring to positrons, acknowledging that the subsequent discussion applies to both.

2.2.1 Mass Stopping Power

Electrons set in motion by photon interactions undergo many interactions as they travel through an absorbing medium. These interactions alter the electron's trajectory within the medium, resulting in kinetic energy loss. The mean free path of an electron in the radiotherapy energy range in tissue is 10^{-5} g/cm^2 [21]. As electrons traverse an absorber, their energy loss is dependent on the characteristics of the medium. The energy loss per unit of path length by a charged particle in an absorbing medium is referred to as the linear stopping power[88,89]. The mass stopping power in units of $MeV \cdot cm^2 \cdot g^{-1}$ is then,

$$S = -\left(\frac{1}{\rho}\right)\frac{dE}{dx} \tag{13}$$

For electrons traversing an absorbing material, two competing mechanisms contribute to their energy loss per unit path length. They are the radiation stopping power (S_{rad}) and the collision stopping power (S_{col}). Therefore, the total stopping power for an electron traveling through an absorber is often expressed as[88,89],

$$S_{tot} = S_{rad} + S_{col} \tag{14}$$

In the radiotherapy energy range, electron interactions in tissue are primarily governed by the collision stopping power, with the radiative stopping power being comparatively small[88,89].

2.2.1.1 Radiation Stopping Power

Radiation stopping power refers to the energy loss of an electron through inelastic Coulomb interactions with the atomic nuclei of the absorbing material. During these interactions a portion of the electron's kinetic energy is radiated away in the form of photons (Fig 2.8). This emitted radiation is often referred to as braking radiation or bremsstrahlung, and it is the primary mechanism of photon production in medical imaging and radiotherapy. In bremsstrahlung, an incident electron interacts with the Coulomb field of a nucleus and is scattered from an initial energy state E_1 to a state E_2 with the energy difference given to a photon of energy E_γ.

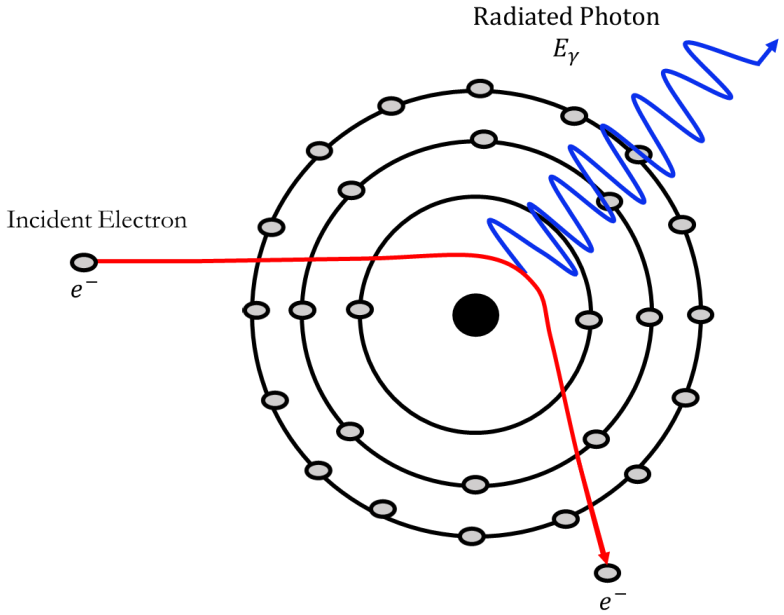

Figure 2.8: Illustration of high energy electron undergoing a bremsstrahlung interaction near the atomic nucleus of an absorber atom.

The relativistic generalization of the Larmor formula provides the total power radiated by a relativistic electron as it is decelerated or accelerated[91],

$$P = \frac{\mu_0 q^2 \gamma^6}{6\pi c}\left(a^2 - \left|\frac{\vec{v} \times \vec{a}}{c}\right|^2\right) \tag{15}$$

where $\vec{a}$ is the electron's acceleration vector, $\vec{v}$ is the electrons velocity vector, q is its charge, and γ is defined as[91],

$$\gamma = \frac{1}{\sqrt{1-\beta^2}} \tag{16}$$

where β is the ratio of the particle's velocity v to the speed of light c. The γ factor dependence results in the radiated power increasing drastically as the electron's velocity approaches the speed of light.

In the case of uniform forward motion, the power radiated per solid angle Ω is[91],

$$\frac{dP}{d\Omega} = \frac{\mu_0 q^2 a^2}{16\pi^2 c}\left(\frac{\sin^2\theta}{(1-\beta\cos\theta)^5}\right) \tag{17}$$

where θ is the angle between the observer and the particle's motion. This equation indicates that moving electrons do not radiate energy in a spherically symmetric manner. For electrons traveling at relativistic velocities, the β factor constricts the fields in the direction of motion, and the field expands in the directions perpendicular to motion.

The rate of radiative photon production by electrons traveling through an absorber is given by the Bethe-Heitler equation in units of [88,89],

$$S_{rad} = \alpha {r_e}^2 Z^2 \left(\frac{N_A}{A}\right) E_{tot} B_{rad} \tag{18}$$

where $E_{tot} = E_e + m_e c^2$ is the total electron energy and B_{rad} is a slowly varying function of the electron's total energy and the absorber's atomic number. The radiation stopping power (S_{rad}) is proportional to absorber's atomic number and the incident electron's total energy.

2.2.1.2 Collision Stopping Power

The collision stopping power refers to the energy loss of electrons through interactions with atomic electrons of the absorbing material. It can be subdivided into two components based on the incident electrons impact parameter b [88,89].

$$S_{col} = S_{col}^{soft} + S_{col}^{hard} \tag{19}$$

As shown in Fig 2.9, when an incident electron passes within a distance b of an orbital electron, it imparts a portion of its momentum. In soft collisions, the momentum transfer is small, resulting in electrons undergoing multiple small-angle deflections as they traverse the medium[88,89]. On the other hand, hard collisions result in large momentum transfers and energy losses for electrons that increase with increasing energy[88,89]. Hard collisions result in the ionization of absorber atoms through the ejection of orbital electrons and involve large scattering angles[88,89].

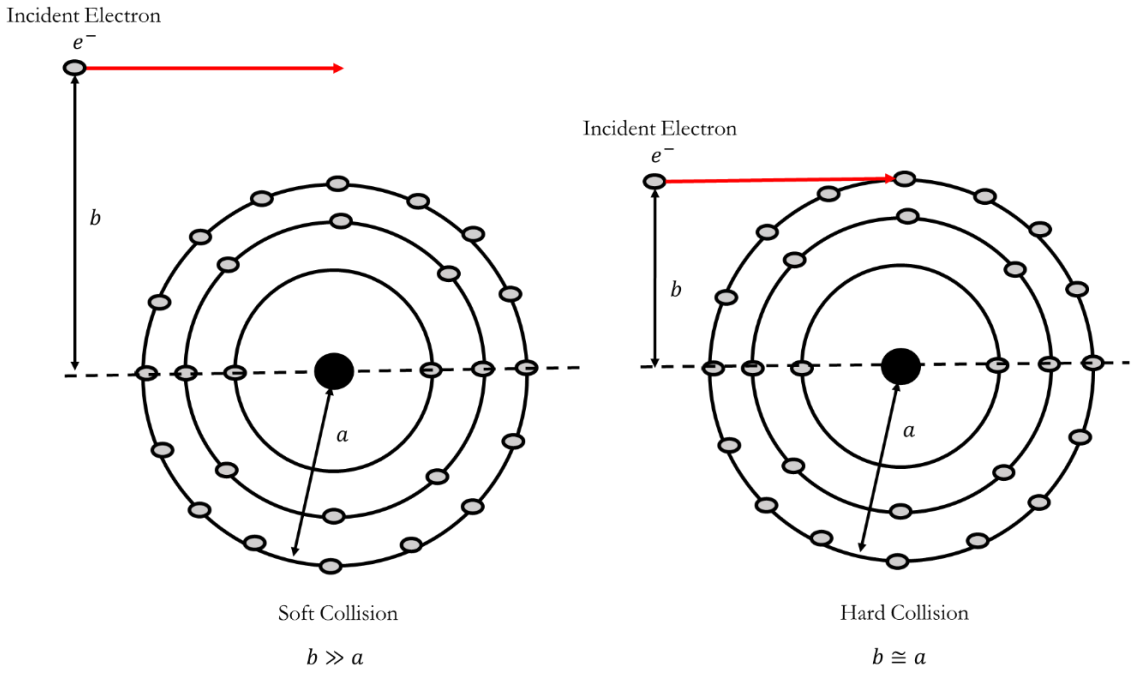

Figure 2.9: Illustration of the hard and soft electron interactions which comprise collision stopping power.

The collision stopping power for electrons was originally described mathematically by the Bethe–Bloch formula and has since been updated to include corrections for electron

interactions at low energies. The complete collision stopping power formula is given in ICRU report 37 as[92],

$$S_{col} = 2\pi r_e^2 \frac{Z}{A} N_A \frac{m_e c^2}{\beta^2}\left[ln\left(\frac{E_e^2}{I^2}\right) + \ln\left(1+\frac{\mathrm{T}}{2}\right) + F^{\pm}(\tau) - \delta(\beta) - 2\frac{C(\beta)}{Z}\right] \quad (20)$$

where T is[92],

$$\mathrm{T} = \frac{E_e}{m_e c^2} \quad (21)$$

The mean excitation energy I corresponds to the minimum amount of energy that can be transferred on average to an absorber atom in a Coulomb interaction between an incident electron and an orbital electron. $F^{\pm}(\tau)$ represents a correction function added to account for the difference in charge between electrons and positrons. The material polarization correction δ accounts for the density effect in condensed materials. Finally, $\frac{C(\beta)}{Z}$ represents the shell correction, which accounts for low-energy electron interactions. In this case, low-energy electrons are those whose energy is comparable to the binding energy of orbital electrons.

The important feature of the collision stopping power formula for high-energy electrons (electrons whose energies are substantially larger than that of the orbital electron binding energies of absorber nuclei) is its proportional relationship with the number of electrons per unit mass $\left(\frac{Z}{A}\right)$ and the mean excitation energy I of the absorbing medium. Both terms result in a considerable decrease in the collision stopping power as a function of atomic number.

2.2.2 Continuous Slowing Down Approximation

As previously discussed, electron scattering in biological tissues is pronounced. In the process of slowing down, a typical electron undergoes 10^5 - 10^6 collisions with the surrounding medium[93]. Electrons also undergo significant kinetic energy loss, losing as much as 50% of their kinetic energy during ionizing collisions[88].

This process results in electrons following complex paths through an absorbing medium (Fig 2.10). As electrons move through the absorber, they ionize atoms and deposit varying amounts of energy along their path. As electrons progressively lose energy, their velocity decreases, and as a result, their β ratio also decreases. The collision stopping power increases

drastically as electron energy decreases, with peak energy loss occurring when the electrons come to a complete stop[88,89].

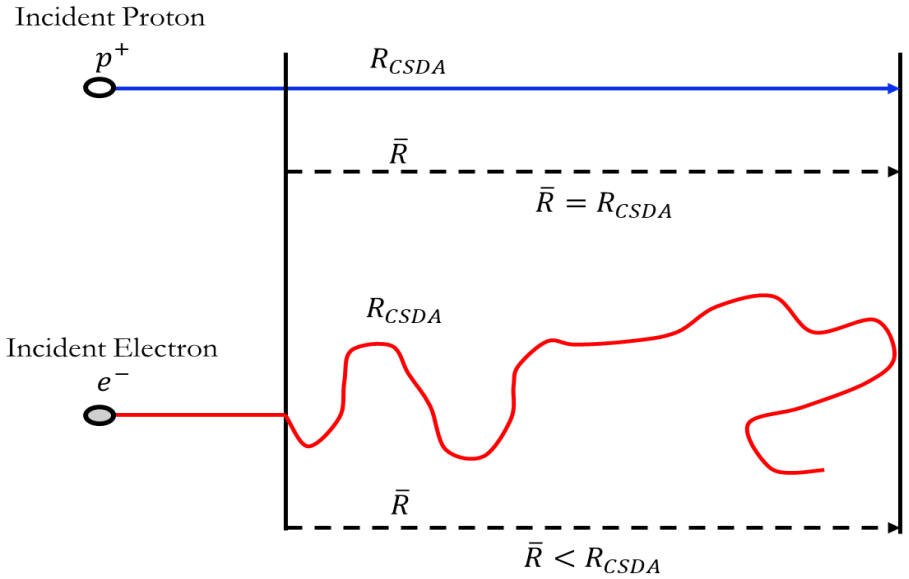

Figure 2.10: Illustration of the difference in CSDA range and trajectory of electrons and protons as they traverse an absorbing medium. Modified and reproduced with permissions from Podgorsak[88] (Appendix A.5).

The stopping of electrons occurs due to many statistically distributed collisions. Given the variability in the number of collisions required to stop an electron, a distribution of electron ranges emerges, referred to as straggling. While the magnitude of energy loss in each interaction depends on the type, the continuous slowing down approximation (CSDA) describes the electron's kinetic energy loss as they traverse an absorber as gradual and continuous. The CSDA range is given by[88,89],

$$R_{CSDA} = \int_0^{E_{ei}} \frac{dE}{S_{tot}(E)} \tag{22}$$

where E_{e_i} is the electron's initial kinetic energy, this calculated quantity signifies the mean path length along the electron's trajectory. Importantly, it does not necessarily represent the electron's maximum penetration depth in the absorbing medium.

2.3 PHOTON BEAM DOSIMETRY

This thesis exclusively addresses the dosimetry of photon radiotherapy treatments using a variety of water equivalent and solid-state detectors. As such, this section will focus on the dosimetry of photon beams, excluding additional consideration of other types of charged and uncharged particle beams such as neutrons, electrons, and protons. Dosimetry involves precisely measuring and calculating absorbed doses in diverse materials. While radiation interactions with matter are fundamentally random, in radiotherapy, where numerous particles are present over extended time periods, radiation interactions can be approximated by expectation values[88,89].

2.3.1 KERMA and Absorbed Dose

Photons impart energy to the medium in a two-step process. First, energy is transferred from the photon to the medium. Then, secondary energetic charged particles (electrons and positrons) are set in motion and travel some distance from the interaction site. The Kinetic Energy Released Per Unit Mass, also known as KERMA (K), is the ratio of the mean energy transferred by photons ($\bar{E}_{tr}$) to secondary charged particles in an absorbing medium of mass dm[88,89],

$$K = \frac{d\bar{E}_{tr}}{dm} = E\ \Phi_{med} \left(\frac{\mu_{tr}}{\rho}\right)_{med} = \bar{E}_{tr}\ \Phi_{med} \left(\frac{\mu}{\rho}\right)_{med} \tag{23}$$

where E is the incident photon energy, and Φ_{med} is the photon fluence. KERMA is expressed in units of energy per mass, J/kg or Gray (Gy).

For photons, KERMA has two distinct components[88,89],

$$K_{med} = K_{med}^{Col} + K_{med}^{Rad} \tag{24}$$

The primary component, collision KERMA (K_{Col}), arises from secondary electrons and positrons depositing their energy through collisional interactions with the orbital electrons of the absorbing medium. These secondary charged particles can also generate uncharged radiation through their own interactions, such as bremsstrahlung or annihilation photons. This second component is known as radiation KERMA (K_{Rad}).

As charged particles traverse an absorbing medium, they gradually lose kinetic energy. The mean energy imparted ($\bar{E}$) to a volume of matter with mass dm by charged particles is referred to as the absorbed dose D and is defined as[88,89],

$$D = \frac{d\bar{E}}{dm} \tag{25}$$

and is also subsequently measured in units of Gy. Absorbed dose relates to the energy lost by electrons along their tracks, whereas KERMA relates the energy given to secondary electrons at the point of liberation.

As high-energy photons penetrate a medium, collision KERMA initially peaks at the surface before gradually decreasing (Fig 2.11). On the other hand, in the superficial region, the absorbed dose is characterized by the buildup of charged particle dose. This accumulation reaches its maximum at a specific depth known as d_{max}, where the depth in the medium is equal to the average forward range of the secondary electrons liberated by the incident photon beam. Beyond d_{max}, both the absorbed dose and the collision KERMA curves begin to decrease and transition into a proportional regime.

The absorbed dose is equivalent to the collision KERMA only if the energy entering the volume is equal to the energy leaving the volume, a condition known as Charged Particle Equilibrium (CPE)[88,89].

$$D_{med} \overset{CPE}{\longleftrightarrow} K_{med}^{Col} \tag{26}$$

While CPE may be approached, achieving a perfect equilibrium throughout the entire volume is complicated due to photon attenuation and the influence of scattered radiation[88,89]. As a result, CPE can only be approximated in regions close to and following d_{max}. This proportional regime is referred to as transient charged particle equilibrium (TCPE).

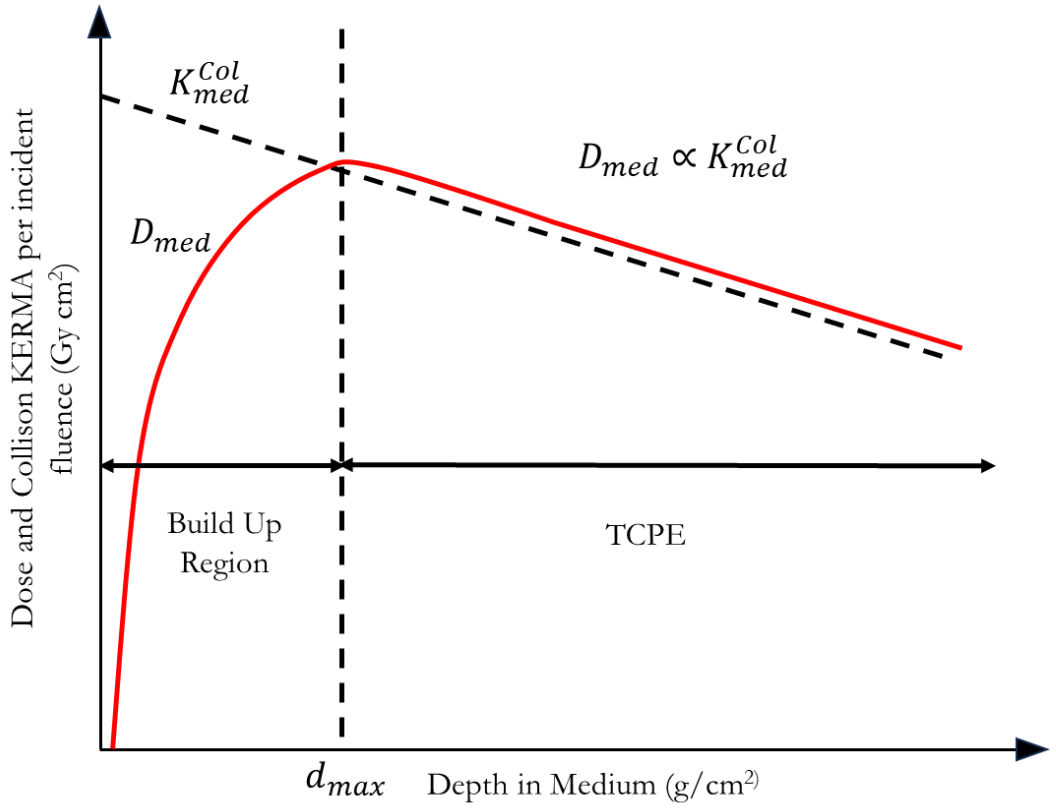

Figure 2.11: Illustration of the collision KERMA and absorbed dose variation with depth in a medium under irradiation by a high-energy photon beam. Modified and reproduced with permissions from Kumar[94] (Appendix A.6).

2.3.2 Charged Particle Equilibrium

The concept of CPE is an approximation that establishes a link between the absorbed dose and collision KERMA. CPE exists for a given volume V_1 when each charged particle of a specific type and energy leaving the volume is counterbalanced by a particle of the same type entering the volume[88,89]. For an external photon beam, CPE exists in the non-stochastic limit for V_1 if the following conditions are satisfied by the encompassing volume V_2[88,89],

i) Homogeneous atomic composition of the medium.

ii) Homogeneous density of the medium.

iii) Negligible photon attenuation within the medium.

iv) Absence of inhomogeneous electric or magnetic fields.

v) The minimum distance separating the boundaries of V_1 and V_2 is greater than the maximum range of the secondary charged particles.

At CPE, the energy absorbed by the medium equals the energy transferred to secondary charged particles within that medium. Consequently, for a monoenergetic photon beam, the absorbed dose in the medium under CPE can then be expressed as[88,89],

$$D_{med} = K_{med}^{Col} = E\,\Phi_{med}\left(\frac{\mu_{en}}{\rho}\right)_{med} \tag{27}$$

For a photon fluence spectrum, such as in the case of clinical MV photon beams, this expression becomes[88,89],

$$D_{med} = K_{med}^{Col} = \int_0^{k_{max}} \mathrm{E}_k\,[\Phi_k]_{med}\left(\frac{\mu_{en(k)}}{\rho}\right)_{med} dk \tag{28}$$

forming the foundation of photon dosimetry theory.

As previously discussed, while CPE may be approached, achieving a perfect equilibrium throughout the entire volume is hindered by photon attenuation and the influence of scattered radiation[88,89]. TCPE specifically refers to a temporary balance between the rate of energy loss by charged particles and the local collision KERMA observed in regions close to and following d_{max}[88,89]. Another more general term is Partial Charged Particle Equilibrium (PCPE), which denotes a localized equilibrium. PCPE is contingent on specific conditions or confined to distinct regions within an irradiated medium.

2.3.3 Cavity Theory

A radiation dosimeter typically consists of two major components. The radiation-sensitive volume that produces the dosimeter signal is known as the cavity, and the component that defines and contains the cavity is known as the wall. The dosimeter cavity produces a signal that is converted to dose to the cavity (D_{cav}). Cavity theory provides several expressions, known as the cavity integrals, that can be used to convert D_{cav} to the absorbed dose D_{med}. As shown in Fig. 2.12, they are applied based on the cavity's size, which is determined by the magnitude of the cavity's diameter compared to the range of secondary charged particles released through photon interactions[88,89].

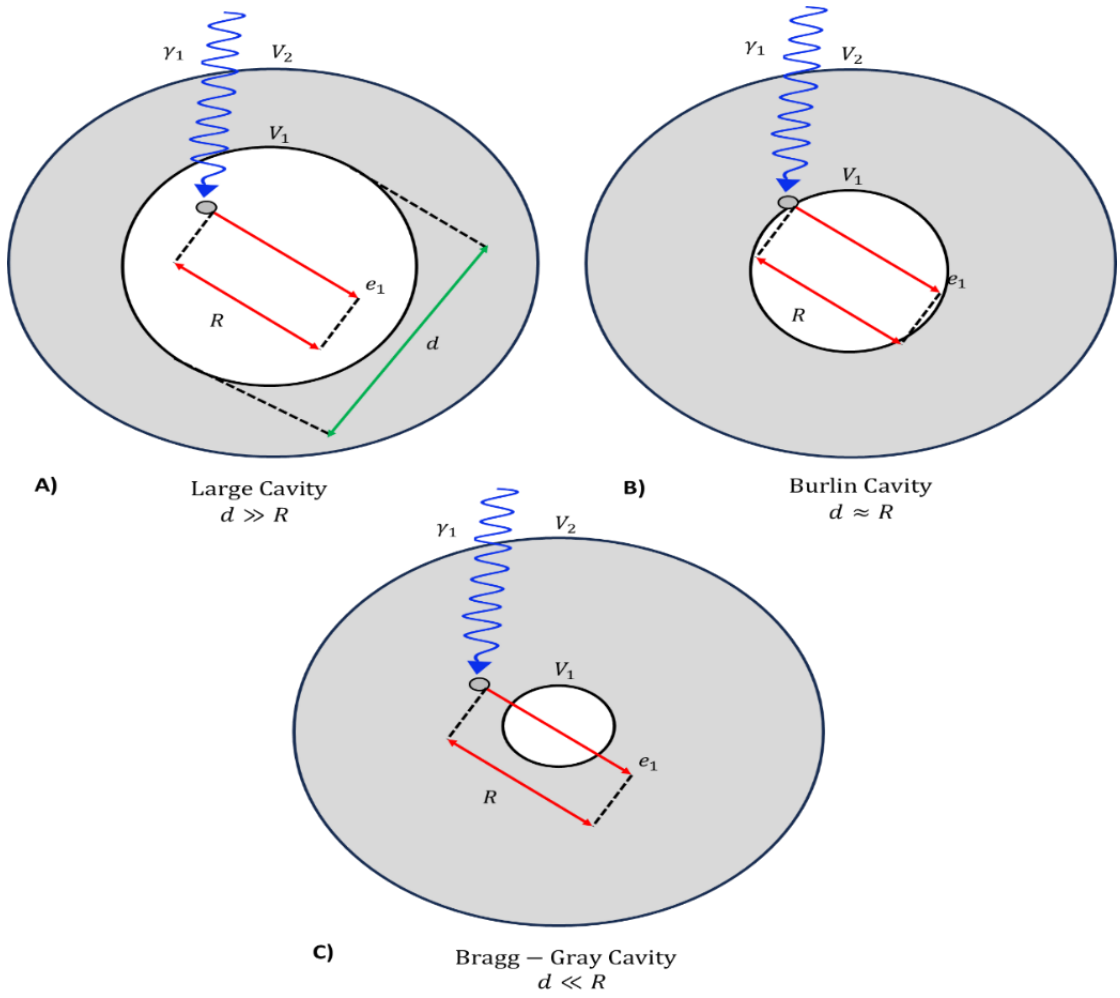

Figure 2.12: Illustration of the various cavity sizes governed by cavity theory **A)** large cavity, **B)** Burlin cavity and **C)** Bragg-Gray cavity where R is secondary electron range and d is the diameter of the corresponding cavity. Modified and reproduced with permissions from Podgorsak[88] (Appendix A.7).

2.3.3.1 Large Size Cavities

A large detector is defined as one with a diameter d, which is large compared to the range R of the secondary electrons[88,89]. At MV energies, photon beams generate secondary electrons with ranges up to several centimeters[89]. As a result, no detector exhibiting large cavity behavior can be constructed that possesses the necessary spatial resolution[65]. However, at kV energies the electron ranges are two orders of magnitude smaller[89] and large cavity detectors are used extensively in codes of practice for kV photon energies[95,96].

In the case of kV photons, due to the limited range of their secondary charged particles, photons that liberate electrons within the cavity are said to deposit their dose locally within the detector[88,89]. Therefore, large cavities detect photons, and the absorbed dose D_{cav} in the detector material is related to the photon energy fluence in the material under PCPE by[88,89],

$$D_{cav} = \int_0^{k_{max}} \mathrm{E}_k \left[\Phi_k\right]_{cav} \left(\frac{\mu_{en(k)}}{\rho}\right)_{cav} dk = \int_0^{k_{max}} (\psi_k)_{cav} \left(\frac{\mu_{en(k)}}{\rho}\right)_{cav} dk \qquad (29)$$

Provided the photon energy fluence ψ_k within the detector is negligibly different from that present in the undisturbed medium at the position of the detector, the dose to the medium can be determined by using the ratio of the spectrum averaged mean mass energy absorption coefficients[88,89].

$$\frac{D_{med}}{D_{cav}} = \frac{\left(\frac{\bar{\mu}_{en)}}{\rho}\right)_{med}}{\left(\frac{\bar{\mu}_{en)}}{\rho}\right)_{cav}} \qquad (30)$$

where[88,89],

$$\left(\frac{\bar{\mu}_{en)}}{\rho}\right) = \frac{\int_0^{k_{max}} \psi_k \left(\frac{\mu_{en(k)}}{\rho}\right) dk}{\int_0^{k_{max}} \psi_k dk} \qquad (31)$$

2.3.3.2 Bragg-Gray and Spencer-Attix Cavities

A detector is considered a Bragg-Gray cavity if its diameter d is much less than the range of secondary electrons produced within the surrounding medium[88,89]. In this case, D_{cav} is deposited solely by incident secondary charged particles generated in the surrounding irradiated medium, with photon interactions within the volume considered negligible[88,89]. This condition is only satisfied in the case of MV photon beams as a significant number of photon interactions occur inside the cavity at lower energies[88,89]. Bragg-Gray cavities, therefore, sense electrons as opposed to photons, and the absorbed dose D_{cav} in the detector material is related to the electron energy fluence in the material under PCPE by[88,89],

$$D_{cav} = \int_0^{E_{max}} (\varphi_E)_{cav} \left(\frac{S_{Col(E)}}{\rho}\right)_{cav} dE \qquad (32)$$

Provided the electron energy fluence φ_k within the detector is negligibly different from that present in the undisturbed medium at the position of the detector, the dose to medium can be determined by using the ratio of the spectrum averaged mean mass collision stopping powers[88,89].

$$\frac{D_{med}}{D_{cav}} = \frac{\left(\frac{\bar{S}_{Col}}{\rho}\right)_{med}}{\left(\frac{\bar{S}_{Col}}{\rho}\right)_{cav}} \tag{33}$$

Bragg-Gray cavity theory relies on the following assumptions[88,89],

i) CPE/TCPE/PCPE exists within the cavity.
ii) All secondary electrons that deposit dose within the cavity are themselves generated within the surrounding medium.
iii) The secondary electron spectrum is unchanged by the presence of the cavity.
iv) Delta rays (energetic electrons created inside the cavity due to the interactions of secondary electrons) deposit dose locally (i.e. within the cavity).

The contradictory assumptions of the Bragg-Gray theory make it only an approximate solution[88,89]. The Spencer-Attix formulation attempts to resolve the issues of the Bragg-Gray theory by introducing the concept of restricted mass collision stopping power ($\frac{L_\Delta}{\rho}$). The restricted mass collision stopping power uses a cut-off energy Δ, which removes the requirement that all secondary electrons created in the cavity deposit their energy locally[97]. Electrons with energy $< \Delta$ are assumed to deposit their energy where created whereas electrons with energy > Δ dissipate their energy through the CSDA[97]. The absorbed dose D_{cav} in a Spencer-Attix cavity is then[88,89],

$$D_{cav} = \int_{\Delta}^{E_{max}} \left(\varphi_E^{\delta}\right)_{cav} \left(\frac{L_{\Delta(E)}}{\rho}\right)_{cav} dE + \left[\left(\varphi_{\Delta}^{\delta}\right)_{cav} \left(\frac{S_{\mathrm{Col}(\Delta)}}{\rho}\right)_{cav} \Delta\right] \tag{34}$$

where φ_E^{δ} is now the energy spectrum of all electrons including the secondary electrons generated within the cavity. The second term contained within the square brackets represents the track end term, and it approximates dose deposited locally by electrons with energy less than Δ. Provided the secondary electron spectrum is unchanged by the presence of the cavity,

the dose to the medium can be determined by using the ratio of the spectrum averaged mean restricted mass collision stopping powers[88,89].

$$\frac{D_{med}}{D_{cav}} = \frac{\left(\frac{\bar{L}_{\Delta}}{\rho}\right)_{med}}{\left(\frac{\bar{L}_{\Delta}}{\rho}\right)_{cav}} \tag{35}$$

The Spencer-Attix formulation is in widespread use in codes of practice for the dosimetry of MV photon beams[97].

2.3.3.3 Burlin Cavities

The previous sections discussed the two limiting cases: one where the detector cavity is small compared to the range of secondary electrons and one where it is large. However, many practical situations involve detectors that do not fall into either category. In a small cavity, the absorbed dose is delivered by secondary electrons traversing the cavity. In contrast, in large cavities the absorbed dose is delivered by electrons generated and stopped within the cavity. In the intermediate case, the absorbed dose comes from both secondary electrons traversing the cavity and electrons generated from photon interactions within the cavity. Therefore, Burlin theory combines aspects of both Spencer-Attix and large cavities theories, using a combination of the restricted mass collision stopping power ratio and the ratio of mass energy absorption coefficients[88,89].

$$\frac{D_{med}}{D_{cav}} = d\left(\frac{\left(\frac{\bar{L}_{\Delta}}{\rho}\right)_{med}}{\left(\frac{\bar{L}_{\Delta}}{\rho}\right)_{cav}}\right) + (1-d)\left(\frac{\left(\frac{\bar{\mu}_{en)}}{\rho}\right)_{med}}{\left(\frac{\bar{\mu}_{en)}}{\rho}\right)_{cav}}\right) \tag{36}$$

Burlin cavity theory introduces a weighting parameter d to determine the ratio of large vs small cavity contributions to a given intermediate-sized cavity. d represents the fraction of the dose deposited in the cavity by electrons generated outside the cavity and is given as[88,89],

$$d = \frac{\left(1 - e^{\beta L}\right)}{\beta L} \tag{37}$$

where β is the effective absorption coefficient, and L is the mean path length traveled by the electrons as they traverse the cavity. The value of d tends toward one for small cavities and approaches zero for large cavities.

Burlin theory has had success in calculating ratios of absorbed dose for some types of intermediate cavities[98–100]. However, like the Bragg-Gray and Spencer-Attix cavity theories, the Burlin cavity theory neglects secondary-electron scattering effects[88,89]. This leads to significant disparities in cavity dose compared to experimental findings, particularly in high atomic number materials[101–103]. Monte Carlo simulations comparing absorbed dose in the cavity to absorbed dose in the medium as a function of cavity size have also demonstrated that using a single weighting parameter is too simplistic and that additional terms are necessary[104]. Due to these limitations, in contemporary practice, modeling of the energy deposition in intermediate-sized detector cavities is achieved through Monte Carlo simulations instead of Burlin cavity theory[105,106].

2.3.4 Average Energy per Ion Pair (W)

Particle interactions with a medium create ion pairs in gases or electron-hole pairs in solids. The total number of ion pairs created is proportional to the energy deposited in the medium[88,89]. Therefore, a significant quantity in radiation dosimetry is the average energy required to produce an ion pair in a given medium W, as these ions enable the determination of absorbed dose by radiation detectors. W is an average over the many ionizations caused by an incident particle and encompasses secondary electron generation and subsequent intermolecular processes[88,89]. W is defined as[88,89],

$$W = \frac{E}{N_{ion}} \tag{38}$$

where E is the total energy deposited in the material, and N_{ion} is the total number of ion pairs produced in the material. Solid-state detectors like TLDs, OSLDs, MOSFETs, and diodes produce a large number of electron-hole pairs per interaction due to the narrow energy gap between the valence and conduction bands of semiconductors[66]. The values of W for semiconductors are also influenced by temperature and crystal impurities[66].

2.4 SCINTILATION DOSIMETRY

Scintillation dosimetry has been extensively investigated for small field dosimetry[72–74], real-time *in-vivo* dosimtery[75–77] , surface dosimetry [37,107], brachytherapy [108–111], and quality assurance[112] in radiotherapy. The technique leverages water-equivalent organic materials called plastic scintillators, which emit light in response to ionizing radiation. This section will discuss the physical mechanism of scintillation light production in organic scintillators, the characteristics of the emitted scintillation light, and the basic properties of PSDs.

2.4.1 Physics of Organic Scintillators

The response of an organic molecule to excitation by ionizing radiation depends on the nature of the molecule and the type/energy of the ionizing particle. In the case of conjugated and aromatic organic molecules (also called organic fluors), following excitation, they emit light. Organic scintillators are either composed entirely of these organic fluors or are a combination of an organic fluor integrated into a solvent[57]. Organic scintillators can be classified into three categories based on their composition[57]:

i) **Unitary Systems:** Pure organic crystals such as Anthracene ($C_{14}H_{16}$)

ii) **Binary Systems:** Scintillating material incorporated into a solvent, such as a liquid solution of p-terphenyl in toluene.

iii) **Ternary Systems:** Two scintillating materials (primary scintillator and wavelength shifter) are incorporated into a solvent, such as p-terphenyl and POPOP in polystyrene.

The term “plastic scintillator" generally refers to an organic scintillating material consisting of a ternary system composed of a primary fluorescent emitter and wavelength shifter suspended in a solid polymer matrix[57].

As shown in Fig 2.13, as a charged particle such as an electron passes through an organic scintillator, it transfers some of its energy to the surrounding polymer matrix (in this case, polystyrene molecules). The energy from the charged particle's interaction is initially absorbed by nearby polystyrene molecules, resulting in excitation. Excited molecules can then transfer their extra energy to other molecules in close proximity through a non-radiative transfer process called excitation diffusion[57]. Excitation diffusion allows the energy received from the

initial excitation to spread to several other molecules, increasing the scintillation response[57]. The energy transferred to the surrounding molecules eventually diffuses through the polymer matrix and reaches a fluorescent emitter. Through a resonance phenomenon known as Förster Resonance Energy Transfer (FRET), the energy is again transferred non-radiatively to the primary fluorescent emitter, which undergoes excitation/de-excitation and emits an ultraviolet photon[57]. To make the emitted light visible, a second component shifts the light wavelength from ultraviolet to visible.

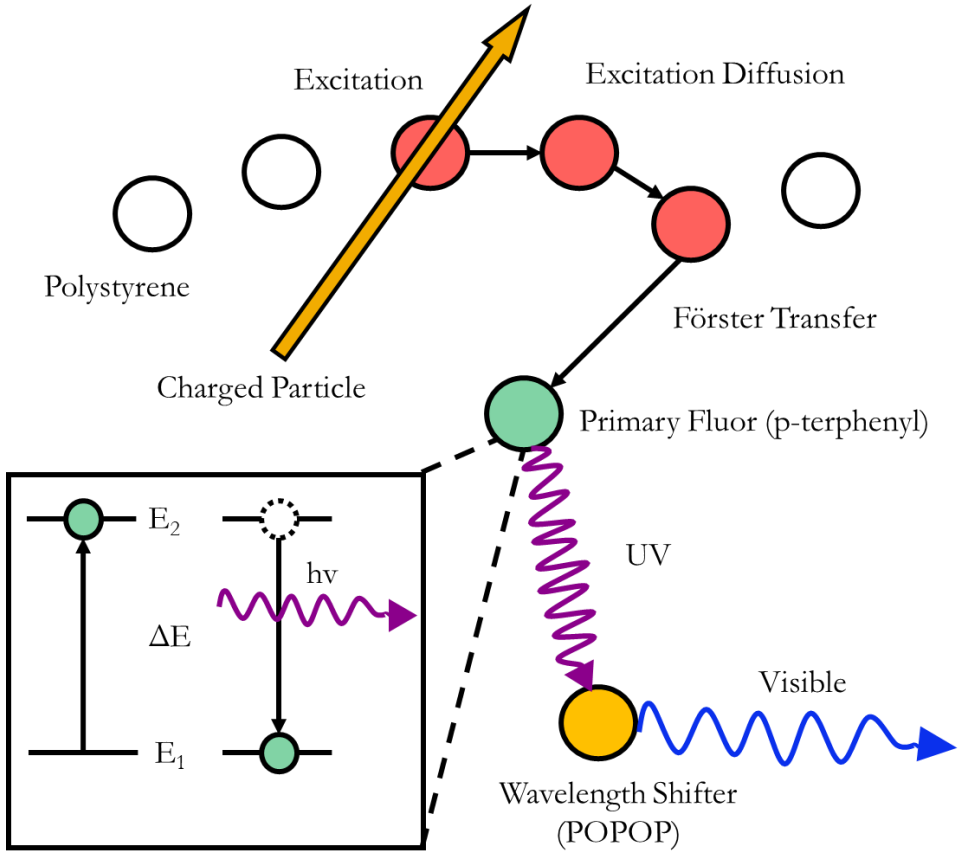

Figure 2.13: Illustration of the scintillation production mechanism in a ternary plastic scintillator material.

2.4.2 Scintillation Light Emission

Only a small portion of the energy absorbed by the scintillator is converted into light, the rest is dissipated non-radiatively in a process known as quenching (see 2.4.3). The absolute scintillation efficiency characterizes the degree of conversion. The scintillation efficiency (*S*) is defined as the fraction of energy initially deposited in the material and the amount used to

produce scintillation light[57]. Anthracene has a scintillation efficiency of 5%, while plastic scintillators have light yields of around 40% - 65% that of Anthracene[57].

Scintillation light is composed of both a fast and slow component that arises from de-excitations involving different molecular electronic states[57]. The fast component of scintillation light (τ_F) refers to the initial, rapid emission of light that occurs within a very short timeframe after ionizing radiation interacts with the scintillator material. Pure organic crystals such as Anthracene are considered instant light emitters, while plastic scintillators need a finite amount of time for their scintillation light to reach a maximum[57]. This time τ_R, is on the order of $10^{-9}\ s$[57]. The fast component typically has a very short decay time, often in the nanosecond range, meaning that the emitted light reaches its maximum intensity and then rapidly decreases. The fast component results from the excitation of molecular singlet states and provides information about the initial energy deposition of the incident radiation[57].

The slow component of scintillation light (τ_s) refers to a delayed emission of light that occurs after the fast component has decayed. It has a longer decay time, on the order of hundreds of nanoseconds, and results from the excitation of molecular triplet states[57]. The fraction of the fast and slow components depends on the nature of the incident ionizing particle. Heavier particles (protons, neutrons, α particles, etc.) with large specific energy loss result in a greater density of triplet states along the particles track, increasing the contribution of the slow component[57]. As a result, it is possible to recognize the type of particle that deposited its energy within a scintillator-based detector by the shape of the emitted scintillation light pulse.

2.4.3 Quenching

In the context of organic scintillators, quenching refers to a phenomenon where the scintillation process is inhibited, resulting in a reduction in the amount of light emitted. However, despite decades of research in scintillator response, there is still no comprehensive description of the physical mechanism of quenching for organic scintillators[57]. It is thought to be the result of several competing mechanisms:

i) **Saturation:** As the energy deposition density in a region of the scintillator increases, all scintillation centers become excited, and additional energy deposition in that region does not yield more scintillation light[59,113].

ii) **Self-absorption:** Organic scintillators absorb a portion of the scintillation light produced. If self-absorption becomes significant, the amount of light that escapes the scintillator is reduced[57].

iii) **Temperature Effects:** Scintillation is temperature dependent, and thermal energy can disrupt the scintillation process and reduce the amount of light produced[114].

iv) **Chemical Quenching:** Impurities or contaminants in the scintillator material can quench scintillation. These impurities can capture excited electrons, preventing them from participating in the scintillation process[57].

While many more complex models exist, the fit to experimental data and the mathematical simplicity of Birks' law make it the model of choice for experimental investigations of scintillation quenching[57]. Birks' law is a semi-empirical model that only considers unimolecular quenching[57]. It is based on the rationale that the primary excitation of the scintillator molecules is quenched due to the presence of a high density of ionized and excited molecules[59].

Birks' law states that in the MeV energy range, the scintillation light yield per unit path length ($\frac{dL}{dx}$) for an organic scintillator is related to the specific energy loss of the charged particle ($\frac{dE}{dx}$), and the scintillation efficiency (ε)[113].

$$\frac{dL}{dx} = \varepsilon\left(\frac{dE}{dx}\right) \tag{39}$$

The scintillation efficiency is a property of the scintillating material and represents the fraction of energy released as scintillation photons over the energy deposited within the scintillator. However, below 100 keV, the response of organic scintillators deviates from linearity becomes a more complex function[113],

$$\frac{dL}{dx} = \frac{\varepsilon\left(\frac{dE}{dx}\right)}{1 + \mathrm{K}B\left(\frac{dE}{dx}\right)} \tag{40}$$

where $B\left(\frac{dE}{dx}\right)$ is the specific density of excited and ionized molecules, and K is the probability of quenching. The product of $\mathrm{K}B$ is known as the Birk's coefficient and is given as 0.126 mm/MeV for polystyrene based scintillators[115].

2.4.4 Cherenkov Radiation

When plastic scintillators are irradiated, their observed light signal is not solely composed of scintillation light. As discussed in section 2.3.1.1, when an energetic charged particle traverses through a dielectric medium, it radiates photons. If the charged particle begins to travel through the medium faster than the velocity of light in that medium, the radiated photons form spherical wavefronts, which are seen as originating from the charged particle[88,89]. These spherical wavefronts begin to overlap and constructively interfere. This results in a cone-shaped light signal known as Cherenkov radiation (Fig 2.14).

The Cherenkov radiation produced by an incident particle of energy E is emitted at a characteristic angle θ given by[57],

$$\theta = \cos^{-1}\left(\frac{1}{n\beta}\right) = \cos^{-1}\left(\frac{1}{n\sqrt{1-\left[\frac{1}{\left(\frac{E}{m_o c^2}\right)+1}\right]^2}}\right) \tag{41}$$

where n is the index of refraction of the material the particle is traveling through, $m_o c^2$is the rest mass of the charged particle.

In contrast to fluorescence, Cherenkov radiation is continuous throughout the visible spectrum and does not exhibit spectral peaks. The number of emitted photons of a given wavelength produced per unit path length is given by the Frank-Tamm formula[57],

$$\frac{\mathrm{dN}}{dx} = 2\pi\alpha q^2\left(1-\frac{1}{\beta^2 n^2}\right)\frac{1}{\lambda^2}\,d\lambda \tag{42}$$

Cherenkov radiation exhibits a broad wavelength distribution covering the entire visible light spectrum, with its peak intensity found in the ultraviolet to blue spectral range[57].

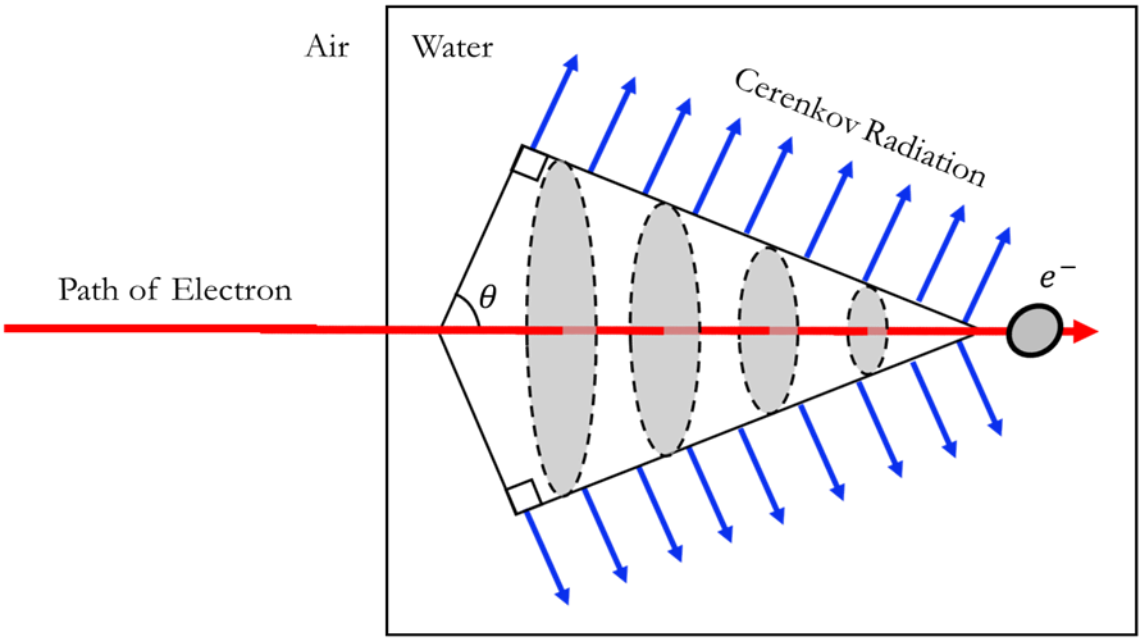

Figure 2.14: Illustration of the Cherenkov radiation produced by a high-energy electron traversing a water volume. Modified and reproduced with permissions from Beddar[57] (Appendix A.8).

2.4.5 Scintillator as Burlin Cavities

Prior to the widespread use of Monte Carlo simulations to determine the absorbed dose, it was necessary to know if a scintillating detector volume behaved as a small cavity (Bragg-Gray cavity), a large cavity, or lay somewhere between these extremes. The dose deposited in a Burlin cavity composed of a scintillator can be expressed as[98],

$$\frac{D_{sci}}{D_{med}} = d\left(\frac{\bar{S}_{Col}}{\rho}\right)_{med}^{sci} + (1-d)\left(\frac{\bar{\mu}_{en)}}{\rho}\right)_{med}^{sci} \tag{43}$$

Experimental investigations have shown that in the case of plastic scintillators measuring 3.0 mm by 4.0 mm (113 mm³) and 1.0 mm by 4.0 mm (12.6 mm³), the application of cavity theory depends on the energy range[98]. For radiation within the diagnostic energy range (<250 keV), the d parameter approaches zero and enables a large cavity approximation. For energies exceeding 20 MeV, the d parameter approaches one and enables a small cavity approximation. In the intermediate energy range used in radiation therapy, the d parameter falls between zero and one, justifying the use of Burlin cavity theory for scintillators.

2.4.6 Basic Properties of Plastic Scintillation Dosimeters

In scintillation dosimetry, plastic scintillators are often used as single-point water equivalent detectors and are referred to as plastic scintillation dosimeters (PSDs). The collision stopping power and angular scattering power of PSDs closely resemble those of water in the radiotherapy energy range [98,116], and radiation interacts with PSDs in a manner analogous to its interaction with water. As a result, CPE is not required, and no correction factor is needed to convert the dose deposited in the detector to the dose that would be deposited in water.

In addition to their water-equivalence, PSDs possess many desirable detector properties:

i) **Linear Dose Response:** The dose deposited in a PSD is linearly proportional to the light signal produced.

ii) **Dose Rate Independence:** PSDs maintain consistent response regardless of the rate at which the radiation dose is delivered.

iii) **Energy Independence:** Above a threshold of approximately 200 keV, PSDs possess an energy-independent response[98,117]. PSDs can therefore be used in radiation beams of different energies and types (photon or electron) as well as at different depths without additional correction factors.

iv) **High Spatial Resolution:** PSDs possess high spatial resolution with typical sizes of 0.5mm - 1 mm in diameter and 2 mm – 3 mm in length[73].

However, like every detector PSDs possess limitations and their effectiveness depends on the type of measurement being performed:

i) **kV Energy Dependence:** Below a threshold of approximately 200 keV, PSDs possess an energy dependent response due to quenching[98,117].

ii) **Cherenkov Light Contamination:** Besides scintillation light, Cherenkov light is produced inside the PSDs and the optical fibers typically used to measure them (section 2.4.7). It introduces unwanted background noise and has necessitated the development of a myriad of Cherenkov removal techniques in an effort to isolate the scintillation signal and improve dosimetric accuracy (section 2.4.8).

2.4.7 Optical Fibers

PSDs are generally measured using an optical fiber coupled to a photodetector. Optical fibers are dielectric waveguides that transmit light using total internal reflection. In scintillation dosimetry, they are cylindrical and composed of a transparent water-equivalent core (either plastic or silica glass) surrounded by a cladding material[57]. The refractive index of the core material is always higher than that of the cladding material, allowing total internal reflection to occur within the core.

The primary loss factor in optical fibers is attenuation caused by Rayleigh scattering, and losses increase with increasing fiber length[57]. Losses can also occur at the coupling points between the optical fiber and the PSD due to misalignments or rough surfaces causing increased reflection. These effects can be mitigated by polishing the fiber ends, uniformly splitting the fiber using a fiber cutter, and applying optical indexing gel at the coupling points to reduce surface reflectance.

2.4.8 Cherenkov Filtration

As discussed in section 2.4.4, Cherenkov radiation is generated when electrons exceed the phase velocity of light in that material. When an optical fiber is irradiated with a high-energy photon beam, secondary electrons generate Cherenkov radiation within the core. While the Cherenkov signal correlates with dose, it is a source of noise in scintillation dosimetry.

Various methods have been developed to remove the optical fibers' Cherenkov contribution from the measured scintillation signal. The earliest method involved a dual fiber approach, where two fibers were irradiated side by side, one detecting the signal from a scintillating element and the other the fiber signal under identical irradiation conditions[98,117]. The fiber signal can then be subtracted from the scintillator's measured light output to isolate the scintillation signal. However, this method necessitates using two sensors side by side, limiting its application in regions with a high dose gradient[118].

An alternative approach involves using time domain filtering based on the difference in scintillator and Cherenkov decay times[119–121]. Pulse gating techniques are applied to determine when Cherenkov radiation production terminates and to integrate the subsequent exponential decay of the scintillation light. However, it was found that short LINAC beam pulses (measured in ns rather than ms) were required to prevent saturation of the scintillation signal

from excessive dose absorption per pulse[122]. Although this method efficiently isolates the scintillation contribution, it has not been pursued further for plastic scintillation dosimetry as the short pulse times required are not achievable with many clinical LINACs[122].

Finally, Cherenkov removal techniques that exploit the differences between the scintillator and Cherenkov emission spectra have been developed[123,124]. These techniques are based on the rationale that when measurements are made using a PSD and optical fiber the measured signal is a linear superposition of scintillation (S), fluorescence (F), and Cherenkov (C) signals.

$$T = aF + bC + dS \tag{44}$$

Using the unit-area normalized spectra of C, F, and S and a least squares fitting method, the coefficients a, b, and d that best match the total observed spectrum T can be found. The total scintillation signal (area under the dS spectrum) is then assumed to be proportional to the absorbed dose in the scintillator. Spectral techniques are clinically preferable as they require a single probe, and their performance is comparable to the background subtraction method in terms of dose reproducibility and ability to remove Cherenkov radiation[118]. This method was subsequently extended to a more general and robust multispectral formalism that permits the measurement of multiple scintillators along the same optical fiber[108,125–127].

2.5 RESEARCH METHODS

2.5.1 Monte Carlo Simulation

Monte Carlo algorithms are numerical solution methods that involve random simulation. They are commonly employed in medical physics to simulate the atomic-level interactions of various particles (such as photons, electrons, positrons, neutrons, and protons) as they traverse a medium.

2.5.1.1 Radiation Transport

The radiation transport of electrons in a small homogenous volume is described by the integrodifferential linear Boltzmann Radiation Transport Equation (RTE) given as[21],

$$\frac{1}{v}\frac{\partial \Psi_e}{\partial t} + \boldsymbol{\Omega} \cdot \nabla \mathrm{N}_e + \sigma_e \Psi_e = \iint \Psi'_e \left(\frac{d^2\sigma_e}{dE'd\boldsymbol{\Omega}'}\right) dE'd\boldsymbol{\Omega}' + \mathrm{Q} \tag{45}$$

where directionality is given in spherical coordinates by $\boldsymbol{\Omega}$ and v is the incident electron velocity. Ψ_e is the angular fluence and N_e is the angular density of electrons with direction $\boldsymbol{\Omega}$ and energy E at a point in the medium. $\Psi_e{}'$ is the angular fluence of electrons scattered from a direction $\boldsymbol{\Omega}'$ and energy E' to a direction $\boldsymbol{\Omega}$ and energy E. σ_e is the macroscopic electron interaction cross section, it is analogous to the photon mass attenuation coefficient and has units of cm^{-1} [21]. Finally, Q represents the rate of electron production from other sources.

This problem is challenging to solve, particularly in the case of external beam calculations which include collisions between multiple particles (photons, electrons, and positrons). Most solutions, even for simple homogenous geometries, require multiple simplifying assumptions[128]. However, as previously discussed, particles interact with atoms of the medium through various competing mechanisms, each governed by different interaction cross-sections. Additionally, when many particles are incident on an absorbing medium, a large number of interactions occur, and those interactions are governed by probability distributions[88,89]. Therefore, Monte Carlo algorithms address radiation transport by direct stochastic simulation of the individual interactions experienced by numerous primary particles.

Monte Carlo based radiation transport simulations involve several sequential steps to accurately model particle interactions and dose deposition:

i) A particle is created by simulation of the LINAC itself or selected from a source phase space (section 2.5.1.2). It possesses energy and travels along a vector determined by random weighted probability.
ii) The distance to the particle's next interaction is randomly assigned based on the linear attenuation coefficient of the material through which the particle is traveling.
iii) Particle tracing techniques (Section 2.5.1.3) transport the particle to its designated interaction site.
iv) The type of interaction occurring is randomly sampled from known interaction probabilities weighted by the particle's type and energy.
v) The chosen interaction is then simulated encompassing various aspects, including energy deposition, scattering phenomena, and potential release of additional particles for subsequent tracking.

vi) These steps are iteratively repeated until the particle's energy is below a threshold energy, at which point the remaining energy is deposited locally as dose.

This process generates a highly accurate approximation of the dose deposited within a given voxel of the simulation. As this method relies on random sampling of interactions that adhere to probability law, Monte Carlo simulations necessitate a source of pseudorandom numbers. As a result, random noise is also inherently present in this process. Achieving a simulation accuracy within ±1% typically requires approximately 104 histories (simulated particle interactions) per voxel[89].

2.5.1.2 Phase Spaces

While it is possible to simulate the entire radiation therapy delivery process, from the initial impact of accelerated electrons on the target to the dose delivered to the patient, it is very inefficient[128]. This is because only a small fraction of the simulated electrons produce histories that progress beyond the accelerator and reach the patient. Simulation efficiency can significantly be improved by first transporting particles through the patient-independent structures of the LINAC and then storing the information for later use. This compilation of data is commonly referred to as a phase space file.

A phase space refers to a multidimensional space whose dimensions correspond to the properties of particles at a specific place and time (Fig. 2.15). A single point in phase space represents each particle. The dimensions of the phase space can correspond to various properties such as position (x, y, z), momentum (p_x, p_y, p_z), energy and direction (E, θ, φ), or other possible degrees of freedom. Additionally, time can be considered either as a coordinate or be treated as an independent variable.

In medical physics, phase space files often serve as input data for Monte Carlo simulations and contain information about the particles produced (photons, electrons, and positrons) within a LINAC or by another radiation source. These files are available from various sources, including the IAEA and LINAC vendors for a variety of different beam energies. They are all scored above the accelerator's collimation structure, allowing them to be subsequently collimated to the desired shape for a given simulation.

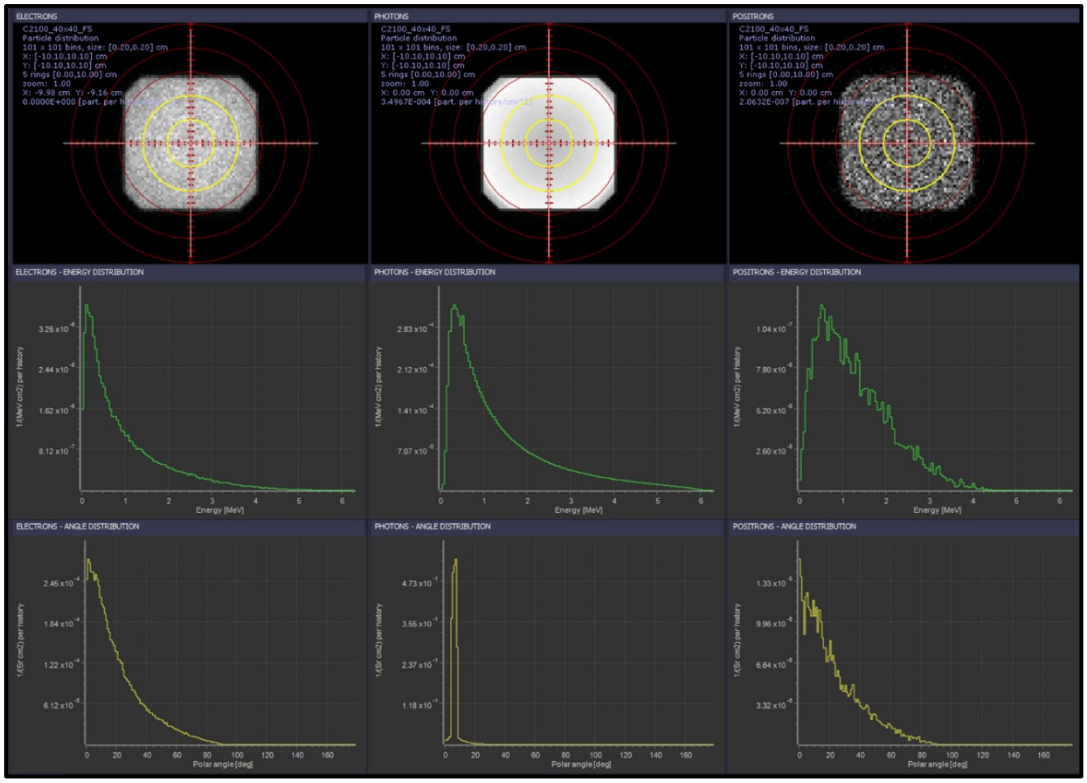

Figure 2.15: Screenshot of PRIMO software analysis for the first 10 000 particles of a Varian Truebeam 6MV phase space file used for Monte Carlo simulations. Panels demonstrate the spatial, energy and angular distribution of the electrons, positrons, and photons contained in the phase space.

2.5.1.3 Particle Tracing and Boundary Crossing

Monte Carlo simulations use particle tracing algorithms to model the trajectory of particles as they traverse and interact with various materials. A track is generated for each particle originating at the radiation source and represents the path the particle will follow through the material. The track is then traced through the material using straight-line segments between interaction sites[129]. In Monte Carlo simulations the step size then refers to the minimum distance a particle travels between consecutive interactions.

In the case of inhomogeneous media, the particles also traverse the boundaries between different materials, each potentially possessing distinctly different properties (electron density/atomic number). For Monte Carlo simulations performed in medical physics, the boundary interfaces between different media are also assumed to be sharp (no diffusion of chemical species) and passive (no surface excitation or transition radiation)[130]. When a particle

encounters a material boundary, it is stopped there, and the simulation resumes with the interaction properties of the new material. For voxelized geometries such as a CT scan of a patient or anthropomorphic phantom, the step size is limited to the voxel size due to voxel-by-voxel changes of HU value[131]. This procedure is consistent with the Markovian property of the transport process, ensuring that a particle's current interaction probability depends solely on its preceding state[129]. Leveraging this property, the generation of a particle history can be stopped at an arbitrary state (any point along its track), and the simulation can resume from this point without introducing bias[129].

2.5.1.4 Variance Reduction Techniques

Variance reduction techniques in Monte Carlo are statistical methods that improve the efficiency of simulations without affecting the accuracy of the physics and ensure that estimates remain unbiased. A myriad of variance reduction techniques exist, and the specific implementation varies based on the Monte Carlo code used[128]. This section will only briefly discuss the conceptual basis of the variance reduction techniques relevant to the Monte Carlo investigations performed for this work.

i) **Particle Splitting:** Particle splitting involves dividing a single simulated particle into multiple replicas to enhance the probability of interactions taking place[128]. A particle entering the CT volume is split into several copies given by a splitting factor S, and each is simulated sequentially. This process is designed to favor the flux of radiation towards the region of interest and restrict the radiation that moves away from the region. This technique is particularly beneficial when using pre-calculated phase spaces with a fixed number of primary particles. Splitting the primary particles enables the simulation of a greater number of interactions, diminishing the statistical uncertainty without the need to perform multiple repeated simulations[128].

ii) **Russian Roulette:** Tracking secondary electrons resulting from photon splitting can be time-consuming[128]. Therefore, photon splitting is often accompanied by Russian roulette, which selectively eliminates electrons by terminating their transport based on a certain survival probability[128]. Russian roulette and splitting are reciprocal techniques. If a particle with original weight w is split into n particles, applying Russian roulette

with a survival probability of $\frac{1}{w_n}$ would restore the weight of the surviving particles to its original value.

iii) **Condensed History Electron Transport:** As previously discussed, electron scattering in biological tissues is pronounced. In the process of slowing down, a typical electron undergoes 10^5 - 10^6 collisions with the surrounding medium[93]. However, most of these interactions do not result in significant energy losses or drastically change the electrons' trajectory. The condensed histories approach, rather than simulating each individual interaction of an electron with the medium, separates these soft interactions from hard interactions where significant energy loss occurs. The process involves grouping many discrete, small momentum transfer collisions into a single virtual large-effect interaction, which occurs within a step of predetermined size (E_{step})[93]. By condensing the history of electrons, computational efficiency is significantly enhanced, making it feasible to simulate a greater number of particles within a reasonable timeframe[93].

2.5.1.5 PENELOPE Monte Carlo Code

PENetration and Energy Loss of Positrons and Electrons (PENELOPE) is a versatile Monte Carlo code, capable of simulating particles with energies ranging from as low as 50 eV up to a maximum of 1 GeV[129]. The University of Barcelona originally developed the code to simulate electron and positron interactions at low energies[130]. PENELOPE is written in FORTRAN and comprises a series of subroutine packages (or modules) invoked from a main steering program[129].

PENELOPE simulates coupled electron-photon transport in homogeneous regions separated by sharp and passive boundaries[129]. PENELOPE creates a demarcation between high and low-energy particles based on user-defined energy thresholds[129]. Bremsstrahlung interactions, which result in the creation of photons or electrons set in motion at energies above the threshold, are treated discretely and transported analogously to primary particles. Particles with energies below the threshold are accounted for using the CSDA. The particle cut-off energies for the PENELOPE Monte Carlo code are as follows[129]:

i) Electrons: 10 - 500 keV

ii) Photon: 10 and 50 keV

iii) E_{step} Range: 2 – 5 mm

In PENELOPE, users have the flexibility to manually select these cut-off energies according to the specific demands of their application. The values chosen represent a tradeoff between the detail of secondary particle tracking required and the total simulation time. For the purposes of this investigation, which uses the PENELOPE based PRIMO Monte Carlo software (section 2.5.1.6), the electron and photon cut-off energies have been preset to 200 keV and 50 keV, respectively[132].

2.5.1.6 PRIMO Software

PRIMO is a Monte Carlo software used to simulate a wide range of Varian and Elekta LINACS, including their electron applicators and multi-leaf collimators[133]. PRIMO has been extensively validated for the simulation of clinical IMRT and VMAT radiotherapy treatment plans[134–136]. It has also been used clinically for beam commissioning and independent dose verification[137,138]. This software combines a comprehensive graphical interface with simulation processes based on the PENELOPE Monte Carlo code. The overall structure of the modules which comprise PRIMO is shown in Fig. 2.16.

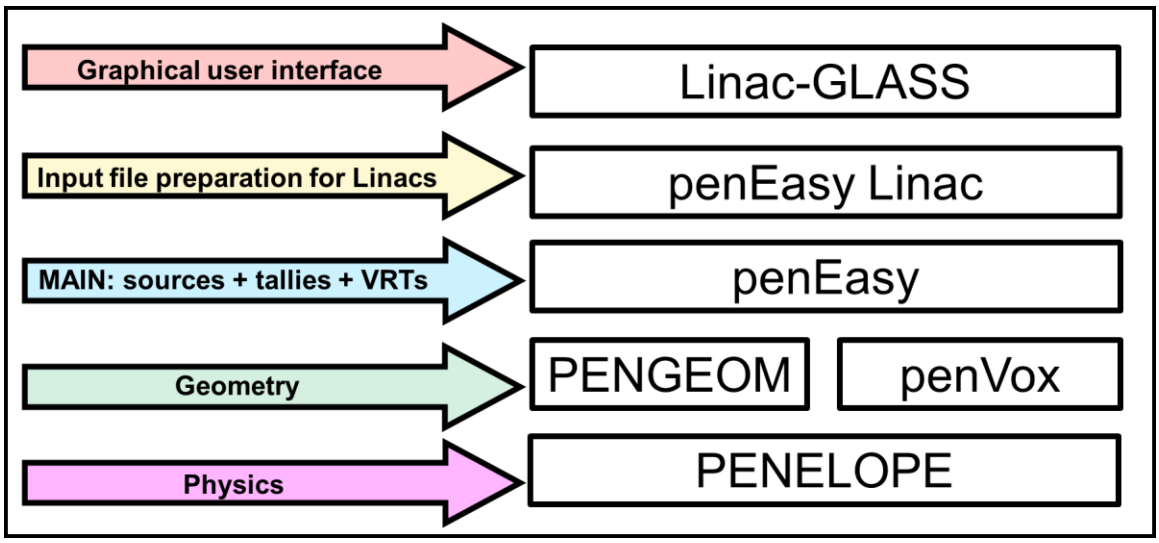

Figure 2.16: Illustration of the hierarchy of software modules that comprise the PRIMO Monte Carlo software.

PRIMO allows the simulation of the dose distribution in the patient without requiring detailed prior knowledge of the Monte Carlo method or the inner operation of a LINAC. All plan-specific parameters, including the planning geometry, dose delivery method, field arrangement, and MLC positions, can all be directly exported from the TPS and imported directly into PRIMO for simulation or analysis. The source of primary particles can be stored in a phase-space file or generated directly from various preconfigured LINAC models.

The simulation process can be delineated into three distinct stages. Initially, a phase space file is generated using one of the preconfigured LINAC models available in the PRIMO software. However, in the case of systems like the VARIAN TrueBeam LINAC, where vendor-provided geometry is unavailable, the simulation can be initiated using a phase space file supplied by the vendor. In the second stage, the interactions of all particles generated in the preceding stage with the LINAC jaws, MLC, and the airspace between the phantom (or patient) are simulated. In the third stage, interactions between particles and the phantom (or patient) are simulated, with the geometry provided by either a homogenous slab phantom or a patient CT scan. Segments can be executed individually or together with variance reduction techniques, number of particles to simulate, and CPU cores to use selected beforehand.

Once the simulation is complete, PRIMO provides dose results in units of eV/g per simulated history, reflecting the microscopic energy transfer to individual atoms or molecules along the particle track. Converting these dose values per history into absorbed dose in Gy for a given voxel of the simulation geometry requires a conversion factor, as Gy represents the macroscopic average dose over a given volume. This can be achieved by comparing the PRIMO simulated dose for a defined geometry to either a measured dose at the same point or a calculated dose by a TPS. Following conversion, the dose distribution profiles determined in the third stage can be compared with other calculated doses or experimental data. PRIMO provides both graphical and numerical tools for the comprehensive analysis of dose distributions, facilitating a thorough evaluation of the simulated dose delivery (Fig 2.17).

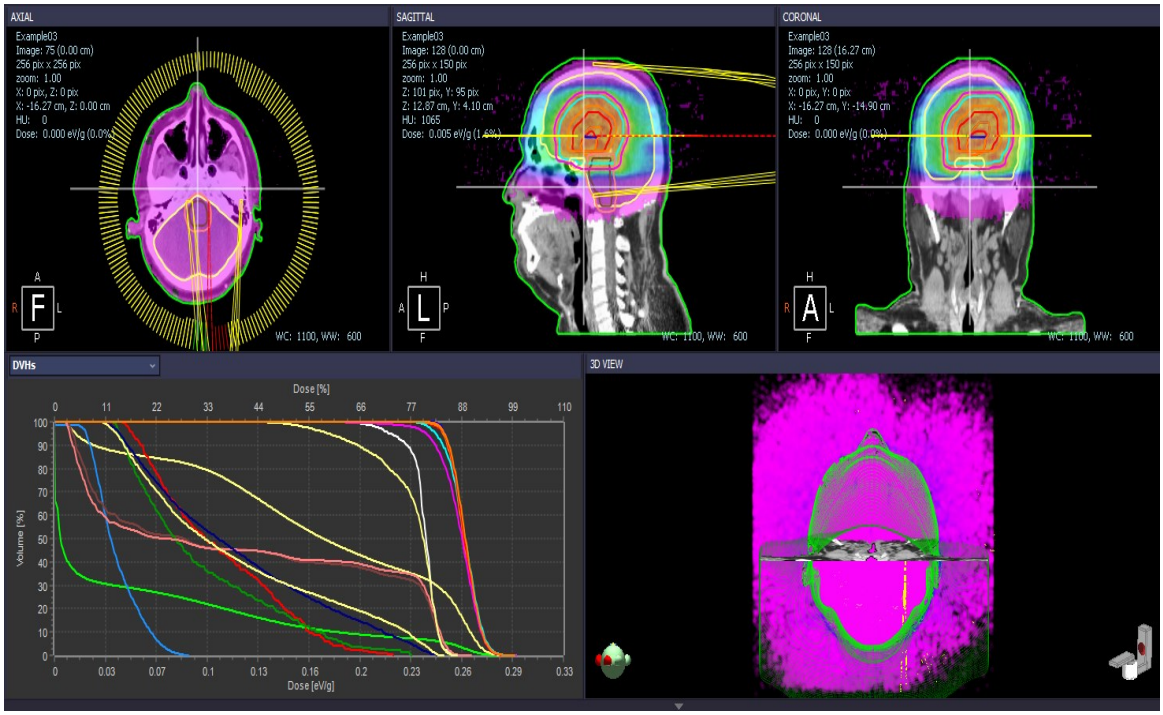

Figure 2.17: Screenshot of PRIMO software analysis for Monte Carlo simulated dose distribution of an example treatment plan. provided by developer.

2.5.2 Acuros XB Computational Dose Calculation

Numerical solutions to the Boltzmann RTE can be obtained using stochastic (Monte Carlo) or deterministic methods. Deterministic numerical methods approximately solve the RTE by discretizing both the position and the angular variables that specify the direction of radiation[139]. This method has been commercialized in the Varian Acuros XB (AXB) Treatment Planning Algorithm. It was initially proposed as an alternative to Monte Carlo simulation as a means of producing accurate dose distributions with a substantially reduced calculation time for clinical treatment planning applications[140,141].

The AXB algorithm assumes that both charged particles created during pair production are electrons and that Bremsstrahlung photons produced by electron interactions within the patient deposit their dose locally[21]. The Boltzmann RTE equation, including the modifications to improve calculation speed and account for electron and photon interactions, is given by the Fokker–Planck approximation[21],

$$\boldsymbol{\Omega}\cdot\nabla\Psi_e+\sigma_e\Psi_e-\frac{\partial S_{rad}}{\partial E}\Psi_e+\iint\Psi_\gamma{}'\left(\frac{d^2\sigma_{\gamma e}}{dE'd\boldsymbol{\Omega}'}\right)dE'd\boldsymbol{\Omega}'$$

$$+\iint \Psi_e{}'\left(\frac{d^2\sigma_{ee}}{dE'd\boldsymbol{\Omega}'}\right)dE'd\boldsymbol{\Omega}' = Q_e \tag{46}$$

As in the Condensed History Electron Transport technique used for Monte Carlo simulations, AXB separates electron collisions into large and small energy losses, the latter of which is described by the CSDA[21]. AXB employs a transport cut-off for electrons below 500 keV and photons below 10 keV[142,143]. When a particle's energy falls below the cut-off energy, it is presumed to deposit all its remaining energy at that point.

The AXB algorithm discretizes the particle energy and angle into intervals using a grid-based numerical solution method called the method of discrete ordinates[21]. In the discrete ordinate's method, the full solid angle is divided into several discrete angular intervals, and the continuous direction variable is replaced by a discrete set of direction vectors[21]. This process transforms the scattering integrals into sums. The equation is then computed using this discrete information to derive a simulated dose distribution in the treatment planning system.

Since the release of the AXB algorithm, many planning studies have investigated the efficiency and accuracy of the discrete ordinates method for solving the RTE[142,144–146]. These studies have found AXB's dose prediction ability to be comparable to Monte Carlo (~2%) and superior to other clinical dose calculation methods, such as the Anisotropic Analytical Algorithm (AAA), particularly in heterogeneous media. However, AXB's solution to the RTE is approximate, its energy and angle discretization can result in a loss of accuracy compared to fully stochastic Monte Carlo solutions[21].

2.5.3 FDM 3D Printing

3D printing is an additive manufacturing technique that fabricates objects by depositing material layer by layer (Fig 2.18). A variety of 3D printing techniques exist, including Fused Deposition Modeling (FDM), Stereolithography (SLA), Direct Metal Laser Sintering (DMLS), and Multi Jet Fusion (MJF). This research focuses on FDM 3D printing, and the specifics of the printing process depend on the technique used. This section will cover the practical aspects of FDM 3D printing, and the specific attributes of the printers used in this work. The following chapters will then provide a comprehensive overview of the methodologies and parameters used for the FDM 3D printing of plastic scintillators.

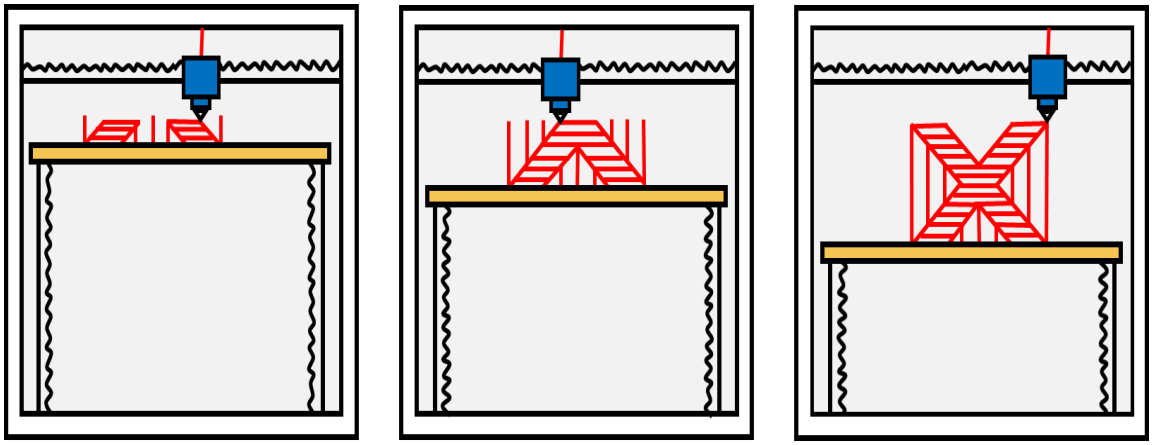

Figure 2.18: Illustration of the FDM 3D printing process creating a 3D structure layer by layer.

2.6.3.1 Printing Process

FDM 3D printing begins with creating a 3D model using computer-aided design (CAD) software. This model defines the size and shape of the final 3D-printed object. The digital model is then sliced into horizontal layers using slicing software and converted into 3D printer instructions (Geometric Code or G-code). G-code is a numerical control programming language for 3D printers that includes instructions for movements along the X, Y, and Z axes, filament retractions, and print speed. The printer then heats a thermoplastic filament to its melting point and extrudes it through a nozzle onto the print bed or previously printed layers, following the path determined by the G-code. As layers are deposited, the extruded material cools and solidifies, bonding to the previous layers and progressively fabricating the modeled object. Post-processing steps, including removal of support structures and surface treatments such as sanding or painting, may also be applied once printing is complete.

2.6.3.2 Extrusion Systems

The extrusion system of an FDM 3D printer is composed of a series of motors and drive gears that feed filament to the hotend. FDM 3D printers can be divided into two types based on their extrusion system: direct-drive or Bowden.. The choice between the two depends on the application and the compatibility of the material being printed.

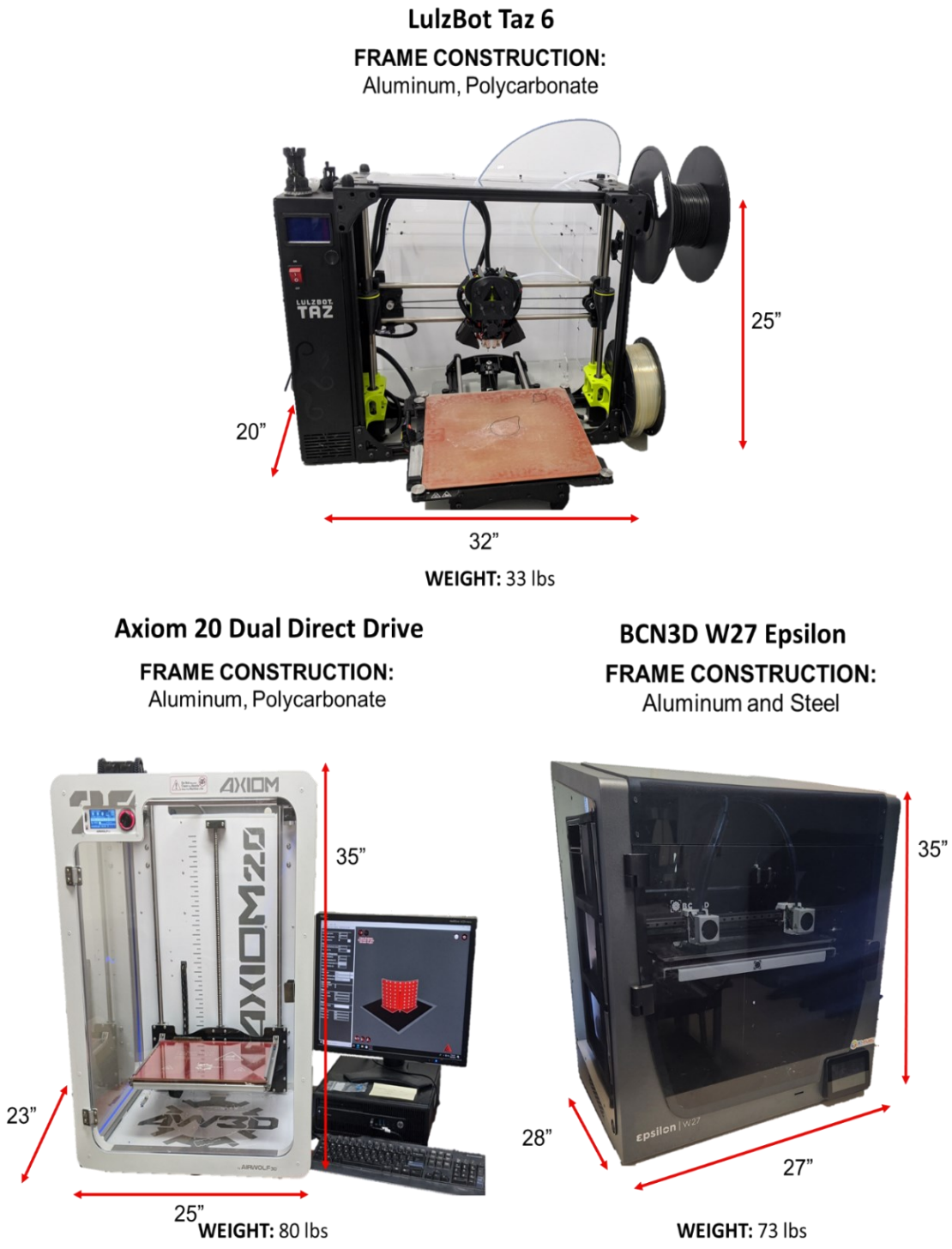

Figure 2.19: Images of 3D printers used throughout this study with dimensions.

In a direct-drive system, the filament is fed into the hotend by an extruder mounted on the printer head. This configuration allows for greater control over the filament, making it better suited for materials that require precise extrusion control (e.g. flexible filaments). However, this configuration can lead to slower print speeds due to the increased weight of the printer head. As shown in Fig 2.19, the Lulz Bot Taz 6 and the Axiom 20 used in this work are direct-drive FDM 3D printers.

On the other hand, in a Bowden extrusion system, the filament drive mechanism is located outside the hotend. The filament is fed from the extruder through a long polytetrafluoroethylene (PTFE) tube to the hotend. This configuration reduces the weight of the printer head, allowing for faster print speeds and better movement control compared to a direct drive extrusion system. However, Bowden systems can encounter challenges with filament retraction and oozing due to the distance between the extruder and the hotend. The BCN3D W27 Epsilon used in this work is a Bowden-style FDM 3D printer.

2.6.3.3 Hotend Design

An FDM 3D printer hotend is composed of several components, as illustrated in Fig 2.20. The precise dimensions and design of a hotend depend on the manufacturer and print application. In general, the extrusion system guides the filament into the hotend, where it traverses through various elements. First, it enters the heat sink, which dissipates the heat produced by the hotend using fans and lateral fins. Next, the filament progresses into the heater block, which connects the nozzle to the heat sink. The heater block contains a cylindrical resistive heating element (heater cartridge) and a thermistor. Then the heated filament reaches the nozzle and is extruded from the hotend. The nozzle's diameter dictates the print resolution in the XY plane.

Thermoplastic filaments used for FDM 3D printing consist of semicrystalline polymers whose viscosity depends on temperature. Examples of semicrystalline polymers commonly used in 3D printing include PLA (Polylactic Acid), ABS (Acrylonitrile Butadiene Styrene), PETG (Polyethylene Terephthalate Glycol), and Nylon. These materials possess two critical material properties: the Glass Transition Temperature (T_g) and the Melting Temperature (T_m). At temperature T_g the filament transitions to a rubbery state and expands. At temperature T_m, the material undergoes a phase change, transitioning from a solid to a liquid state to facilitate

its extrusion through the printer nozzle. Ideally, once the filament reaches the nozzle, its temperature is equal to T_m. Deviations above or below T_m result in either over-melted or un-melted filament, leading to issues such as a clogged hotend or under-extrusion.

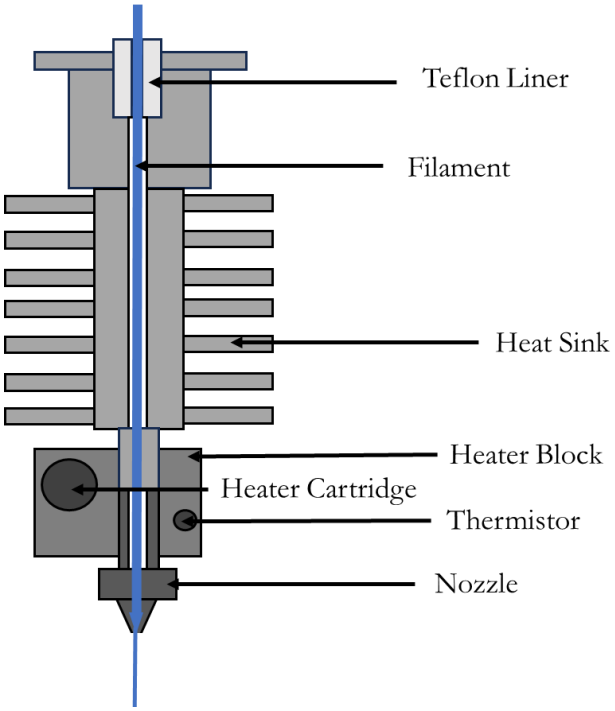

Figure 2.20: Simplified illustration of the internal structure of a 3D printer hotend.

2.5.3.4 Dual-Material 3D Printing

Dual-material 3D printing, also known as multi-material 3D printing, expands the capabilities of single-material 3D printing to create objects with varied mechanical or chemical properties. In the case of FDM, dual-material 3D printing permits the simultaneous deposition of two different materials, and each can vary widely in composition, color, hardness, and flexibility. The two materials are typically loaded into separate extruders mounted on a single printer head, such as with the LulzBot Taz 6 and Axiom 20 3D printers. In contrast, the BCN 3D W27 uses an Independent Dual Extrusion (IDEX) system where each material is isolated in its extruder and moves independently (Fig. 2.21).

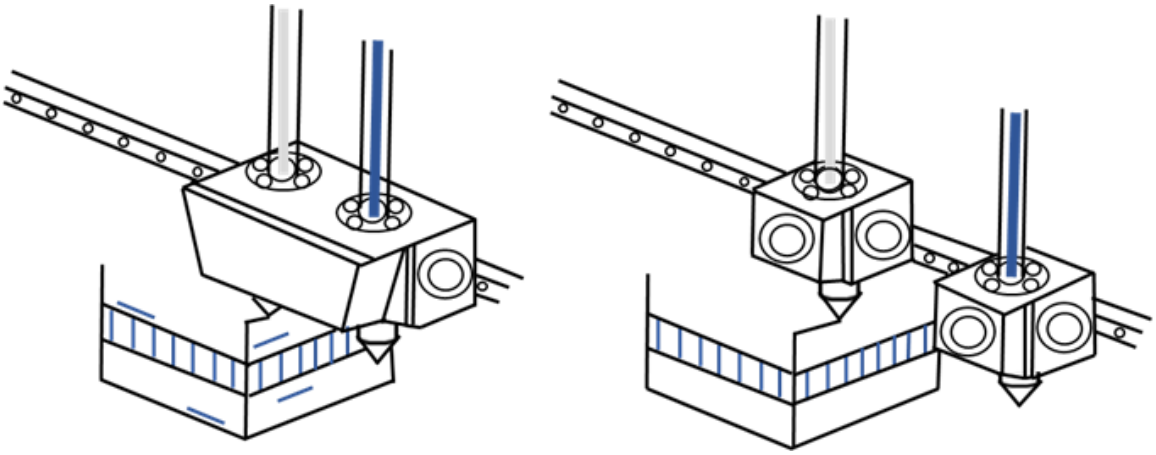

Figure 2.21: Diagram of a standard dual material extrusion system compared to IDEX illustrating material cross contamination caused by the unused nozzle oozing onto the printed part[20].

Dual-material 3D printing also requires adjustments to the 3D CAD model that represents the object to be printed. Material information must be explicitly included in the model to ensure the printer correctly assigns each material to its designated extruder during printing. This can involve assigning different colors or grouping objects in the CAD software. After model creation, it is exported to a slicer software as multiple files, each representing a different material, and assigned to its corresponding extruder. The digital model is then sliced into horizontal layers based on each material and converted into a G-code for each extruder. The object is subsequently printed layer by layer, alternating materials as specified by the original CAD model's material definitions.

2.5.4 sCMOS Cameras

Investigations into the use of complementary metal-oxide-semiconductor (CMOS), charge-coupled device (CCD), intensified charge-coupled device (ICCD), and electron multiplying-intensified charge-coupled device (EM-ICCD) cameras have been conducted for use in real-time *in-vivo* radiation treatment verification systems[147]. ICCD and EM-ICCD cameras are preferred due to their low light sensitivity, high frame rate and capacity for image gating[147]. This allows for sequential collection of background and signal images throughout the entire dose delivery, permitting precise background light removal and imaging under ambient treatment room lighting conditions[39,46]. Despite this, both ICCD and EM-ICCD cameras are prohibitively expensive, ranging from $55,000 to over $100,000[147].

In contrast, the 16-bit monochrome pco.panda 4.2 sCMOS cameras used in this work offer a highly sensitive and cost-effective option (~$ 10,000). Each camera used for this work has 2048 x 2048 active pixels with a pixel size of 6.5 μm x 6.5 μm and a full well capacity of 45,000 electrons. This section will outline the internal structure of the image sensors, discuss the parameters used to characterize their performance and provide the rationale for selecting the pco.panda 4.2 sCMOS model.

2.5.4.1 sCMOS Image Sensors

An sCMOS (scientific complementary metal-oxide-semiconductor) image sensor consists of an array of square pixels (arranged in rows and columns), each capable of capturing individual photons. Using integrated circuits in each pixel, the sensor combines the benefits of a CCD imaging substrate and CMOS readout.

A CCD imaging substrate is the photosensitive region of each pixel in the sCMOS sensor and is typically fabricated using semiconductor materials. The substrate consists of multiple layers whose precise design and doping profile varies depending on the camera manufacturer and imaging application. However, their fundamental properties remain consistent across different sensor architectures. As shown in Fig 2.22, the top layer of the substrate contains a light-sensitive region called a photodiode, which generates electron-hole pairs when exposed to incident photons[89]. Below the photodiode layer is a gate electrode. When a bias voltage is applied to the gate electrode it induces a depletion region between the photodiode and the substrate, creating a potential well. When light strikes the photodiode, electrons are generated and confined within this region. The trapped electrons accumulate, effectively storing the charge generated by incident photons[148].

Surrounding each photodiode are independent CMOS amplification and readout electronics which use on-chip storage capacitors and readout electronics to convert the accumulated charge into a voltage signal[149]. Channel stop implants are added to prevent the spread of charge between adjacent pixels[148]. Microlenses are also commonly employed to direct incident photons onto the light-sensitive region of the pixel to improve photon collection efficiency[148].

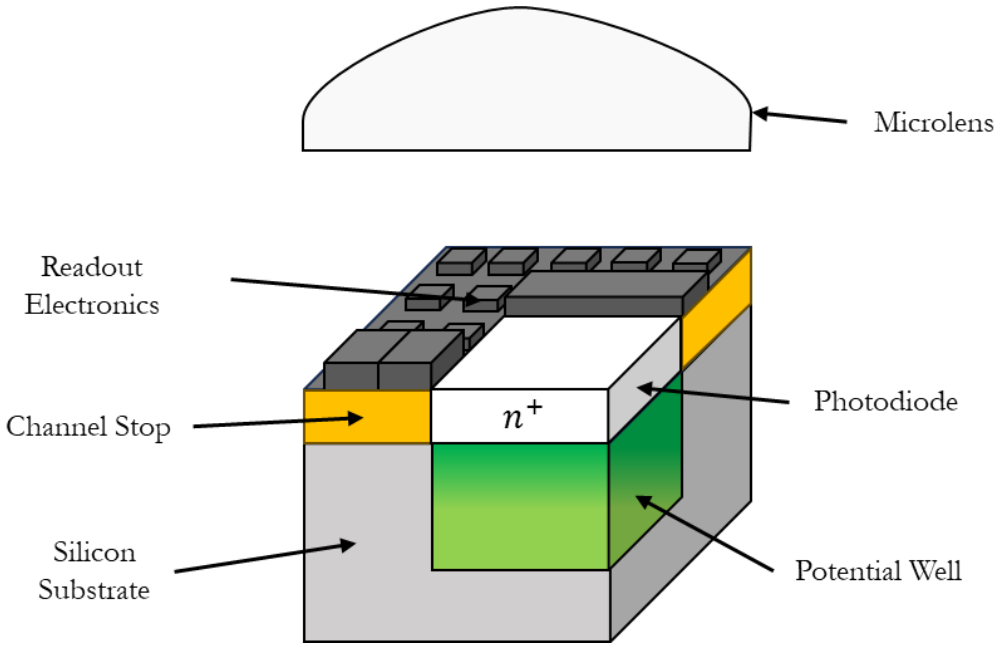

Figure 2.22: Simplified illustration of the internal structure of an sCMOS image sensor pixel.

An electronic shutter controls how long the sensor is exposed to light (exposure time) and, consequently, the signal intensity in the final image. sCMOS cameras employ a rolling shutter mechanism, where individual rows of pixels are read out sequentially from the top to the bottom of the sensor[148].

2.5.4.2 Dark Current and Dark Noise

The photodiodes in an sCMOS sensor generate free electrons in response to incident photons, with the number of free electrons produced being proportional to the number of photons that arrive at a given pixel[149]. However, inaccuracies arise from the collection of electrons that are not generated by the arrival of photons. Non-optical production of electrons can be caused by a combination of thermal noise, shot noise, and other electronic noise sources and can degrade image quality by introducing unwanted variations in pixel value[149]. This phenomenon is referred to as dark current and is related to the dark noise by the image integration time[148]. Dark noise is a form of shot noise, leading to variations in the measured signal that follow a Poisson distribution[148].

2.5.4.3 Pixel Size and Dynamic Range

Pixel size, measured in micrometers (μm), defines the dimensions of an individual pixel on the sensor and represents the area over which incident photons are collected[148]. The larger the pixel size, the greater the light collection area, but the lower the spatial resolution of the final image. Related to the pixel size, the dynamic range of an image sensor is the range of intensities that can be represented[150]. When the charge in a pixel exceeds the dynamic range, neighboring pixels may also become filled, resulting in a phenomenon known as Blooming, compromising the sensor's quantitative performance[150]. Previous studies in the volumetric scintillation dosimetry of photon, electron, and proton beams have used CCD cameras with pixel sizes of 7 μm x 7 μm to 10 μm x 10 μm and dynamic ranges of 14 to 16 bits, translating to 16,383 - 65,536 grayscale levels respectively[81,151,152].

2.5.4.4 Quantum Efficiency and Chroma

The spectral response of a given camera pixel is governed by the ability of photons to be absorbed in the depletion region of the substrate[148]. Spectral sensitivity can be expressed as the probability that a photon of a particular wavelength will be detected and converted into electrons[148]. This probability is expressed as a percentage and is often referred to as a Quantum Efficiency (QE) curve. For this application, the QE of the detector should ideally be maximized at the emission wavelength of the scintillator (425 nm). The QE curve for the pco.panda 4.2 sCMOS camera used in this work is shown in Fig 2.23.

sCMOS cameras are categorized into two main types: monochrome and color. Monochrome cameras output grayscale images, while color cameras use a pixel grid with red, green, and blue filters to capture color data directly. This is known as a Bayer mosaic color filter grid and typically consists of 25% red-filtered pixels, 50% green, and 25% blue[153]. However, compared to monochrome cameras, color cameras possess a lower signal-to-noise ratio as the Bayer filter matrix blocks a portion of the incoming photons[153]. As a result, color cameras require significantly more light than monochrome cameras. The presence of the Bayer filter matrix also requires interpolation between the color channels to produce the final image[153]. As they do not require interpolation, monochrome cameras are a better choice for quantitative imaging applications.

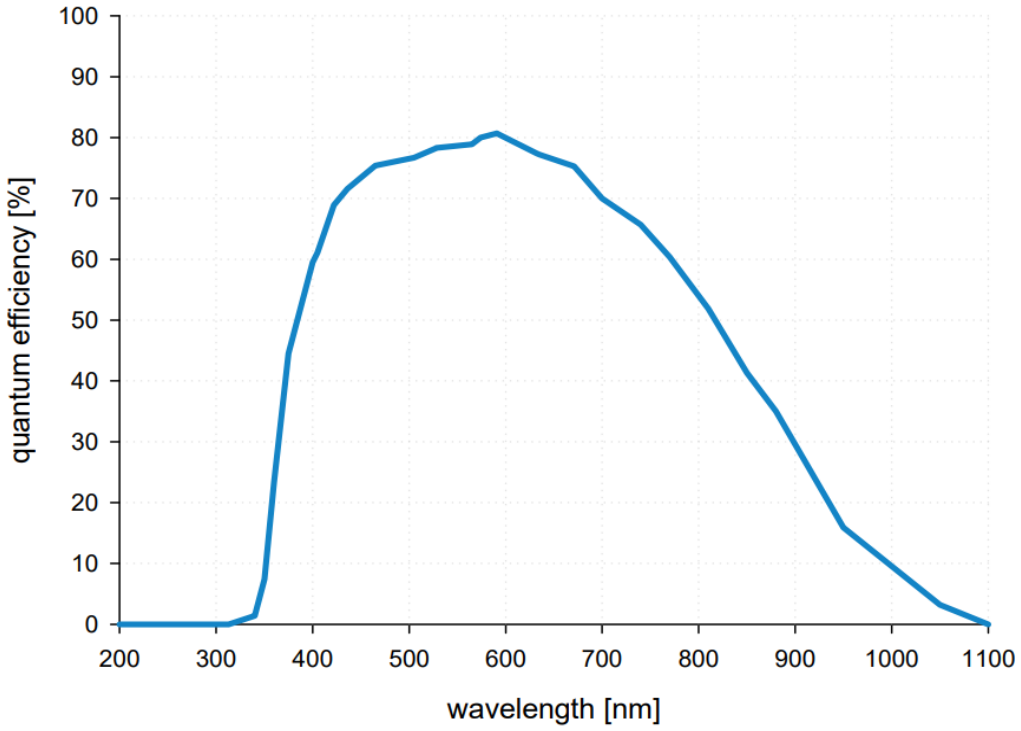

Figure 2.23: Quantum efficiency curve for the pco.panda 4.2 sCMOS camera. Reproduced with permission from technical data sheets provided by Excelitas Technologies Corp. (Appendix A.9).

2.5.4.5 Stray Radiation and Shielding

If the camera is positioned inside a medical LINAC vault, stray radiation induces transient noise on the surface of the sCMOS sensor and within the camera's electronics. Radiation-induced transient noise usually appears as sharp spikes or impulses affecting one or a small cluster of pixels[81]. Efforts to reduce stray radiation contamination have included mounting the camera at the furthest extent from the LINAC gantry, such as at the foot of the treatment couch, and enclosing cameras in lead shielding[79]. Using lead for shielding has been shown to mitigate the impact of stray radiation on CMOS cameras. However, complete shielding surrounding the camera would also be too cumbersome and limit the system's portability. As discussed in section 1.6, other scintillator systems, particularly volumetric approaches, rely on image filtration instead of shielding for dealing with transient noise from stray radiation. However, it is nearly impossible to completely remove all radiation-induced noise[81]

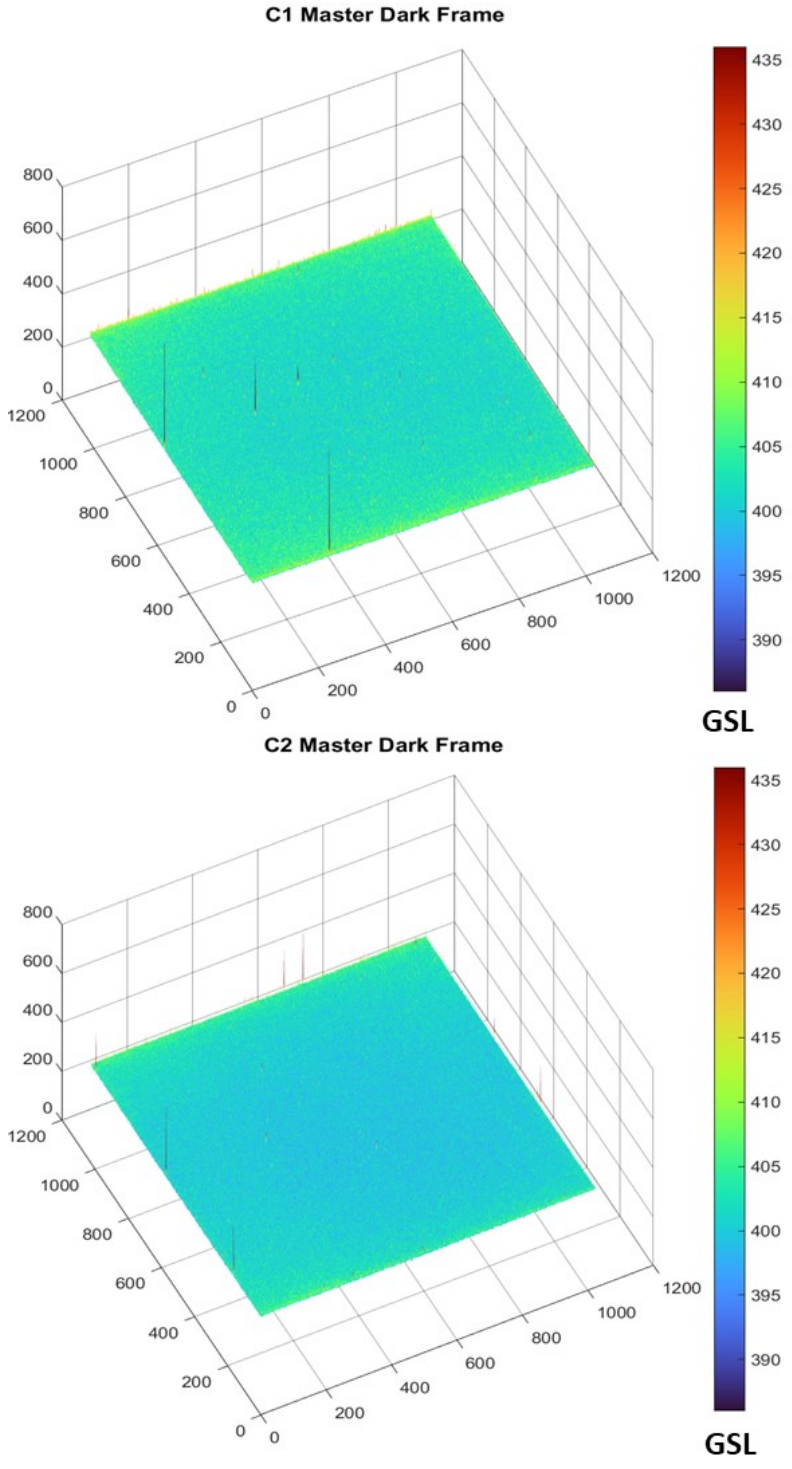

Figure 2.24: Dark noise images for the sCMOS cameras used in this work.

Consequently, the main effect of the ionizing energy transfer is an increase in the surface dark current of detectors over time[154]. The mean dark current increase is proportional to the ionizing dose received, however, the rate at which the mean dark current increases is detector dependent[154]. Non-uniformity in the dark current also increases over time due to displacement damage in the semiconductor material created by energetic particles[154]. This suggests that any rise in dark current will occur gradually over the camera's operational lifetime and that the system can be used inside the LINAC vault without the risk of immediate and permanent damage to the image sensor. Although the exact dose received by each camera over the course of this study was not recorded, the cameras have been present in the treatment room for the delivery of ~100-150 Gy. Thus far, neither of the sCMOS cameras employed in this study has shown any significant increase in mean dark current or number of hot pixels (Fig 2.24).

2.5.5 Computer Vision

Computer vision involves using 2D images for feature extraction and the determination of 3D spatial information. Most computer vision systems use visible-light cameras that passively capture scenes, however some computer vision systems employ active illumination methods to enhance the accuracy and detail of the captured data such as structured-light optical scanners[155–157], thermal cameras[158,159] and hyperspectral imagers[160]. Recent advancements in computer vision have expanded its applications into a variety of fields including medical imaging, robotic manufacturing, autonomous vehicles, security systems, remote sensing and virtual/augmented reality[161].

2.5.5.1 The Linear Camera Model

In computer vision applications, camera systems are represented by a simplified mathematical model known as the linear or pinhole camera model[162]. This model describes how 2D images are mapped to a corresponding 3D scene. In this model, the lens is treated as a pinhole located at a fixed distance from the image sensor, known as the focal length (f). As shown in Fig 2.25, all light rays from the 3D scene pass through the pinhole and project onto the 2D image sensor, forming an inverted image of the scene. The optical axis is then the imaginary line that passes through the center of the lens system and is perpendicular to the image sensor[162]. This axis represents the path along which light rays travel through the lens system without deviation[162]. The principal point (C), is then the intersection of the optical axis

with the image sensor. Additionally, to account for any imperfections in the sensor alignment such as a small angular deviation between the image sensor and the pinhole a skew coefficient is sometimes included in the model[162].

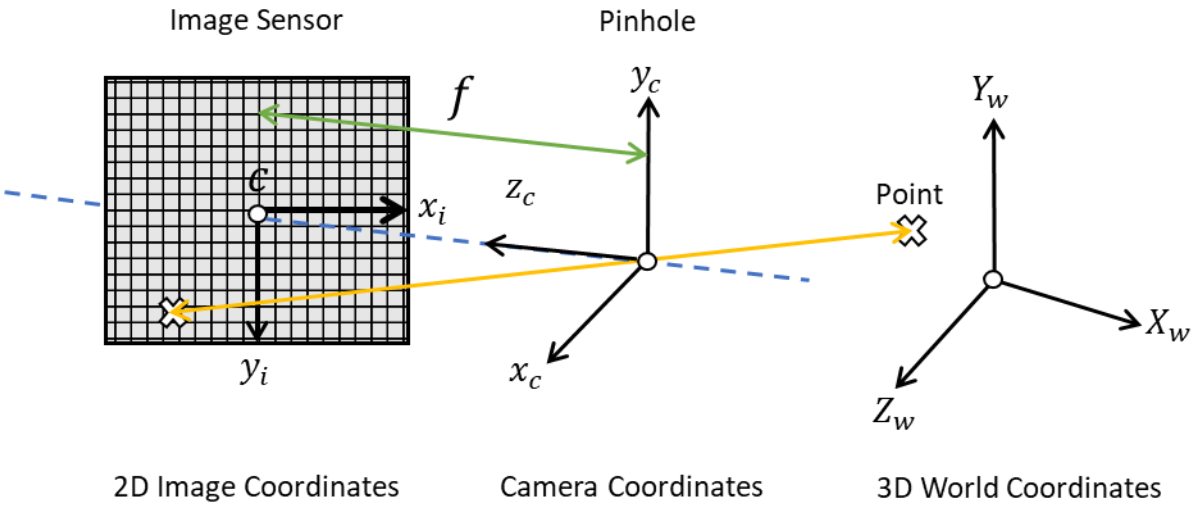

Figure 2.25: Illustration of the pinhole camera geometry demonstrating the relationship between the 3D world coordinates and 2D image coordinates.

The linear camera model assumes perfect projection and does not consider optical distortions such as radial or tangential distortion caused by the camera lens, nor does it account for blurring effects due to the camera aperture or motion[162].

2.5.5.2 Geometric Camera Calibration

The purpose of the camera calibration algorithm is to determine the mapping between the 3D world coordinate system (X, Y, Z) and the 2D image coordinate system (x, y). Doing so requires the determination of the camera matrix (P),

$$\begin{bmatrix} x \\ y \\ 1 \end{bmatrix} = P \begin{bmatrix} X \\ Y \\ Z \\ 1 \end{bmatrix} \tag{47}$$

The camera matrix can be decomposed into a series of two matrices, the camera intrinsic matrix K and the camera extrinsic matrix $[R_\theta \; M]$[163].

$$P = K[R_\theta \; M] \tag{48}$$

The camera intrinsic matrix describes the essential optical characteristics of the camera and is based on the linear camera model. The intrinsic parameters of the camera are those that remain constant and are independent of its position and orientation in space such as its focal length (f_x, f_y), optical center (or principal point) (C_x, C_y), and the skew coefficient (s). The camera intrinsic matrix, K, is defined as[163]:

$$K = \begin{bmatrix} f_x & s & C_x \\ 0 & f_y & C_y \\ 0 & 0 & 1 \end{bmatrix} \tag{49}$$

While in most cases the focal length and principal point along each axis are the same, the camera calibration algorithm separates the two to account for camera designs with a different number of pixels along the x and y axis or for cameras with rectangular pixels.

The intrinsic matrix represents a projective transformation that delineates the mapping from the 2D image coordinates to the 3D camera coordinates. The extrinsic parameters then encapsulate a rigid transformation from the 3D camera coordinate system to the 3D world coordinate system. This transformation is embodied by rotation (R_θ) and translation (M) parameters, defining the orientation and position of the camera.

To obtain the camera matrix, the calibration algorithm uses multiple images of a planar calibration pattern (checkerboard) with known dimensions to determine both the intrinsic and extrinsic properties of the camera (Fig 2.26)[163]. Initially, an estimate of the intrinsic and extrinsic parameters is made by the algorithm based on user-provided camera specifications and calibration pattern dimensions. Using these initial parameters, the algorithm projects a set of 3D points, derived from the estimated camera parameters, back onto the collected 2D images of the calibration pattern. The difference between the projected points and the actual observed points in the calibration images, known as the reprojection error, is calculated. The camera parameters are then refined using an optimization algorithm that iteratively minimizes the reprojection error. This method has been commercialized in the camera calibration function of the MATLAB Computer Vision Toolbox[164].

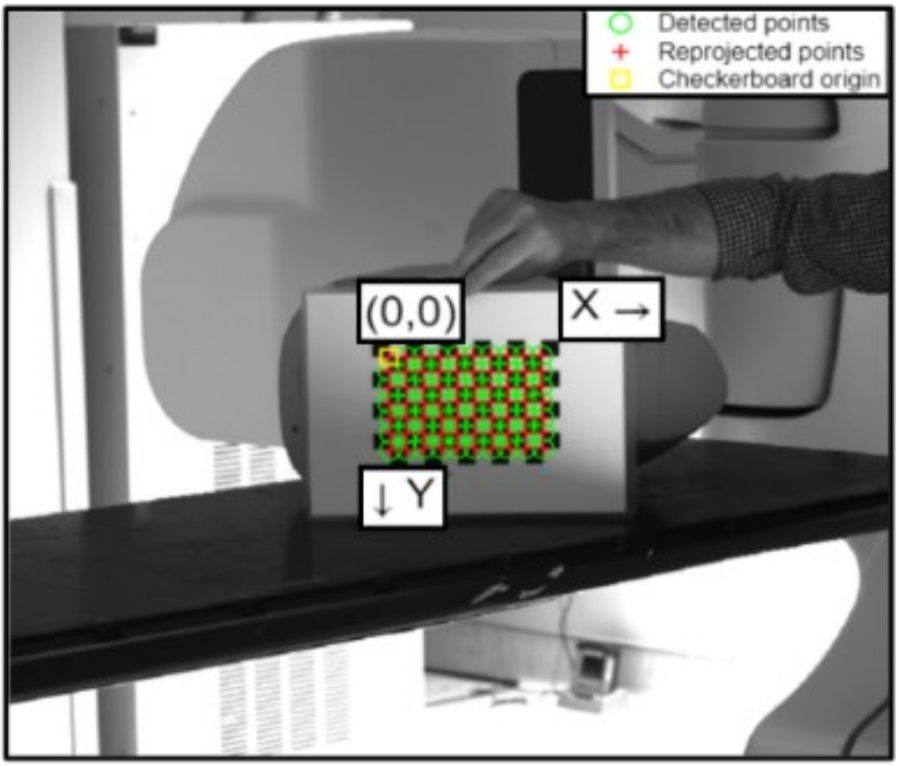

Figure 2.26: Image of checkerboard calibration pattern demonstrating the detected and reprojection positions of the calibration points.

It is worth noting that the camera matrix does not account for lens distortion, as it is based on an ideal pinhole camera geometry. To accurately represent a real camera, additional coefficients are required to address the slight deformation of straight lines near the periphery of the image. The camera calibration function accounts for lens distortion by incorporating distortion coefficients into the intrinsic parameters. These coefficients, which are iteratively determined during the calibration process, model the radial and tangential distortions caused by the lens. These distortion coefficients for a given pixel are a function of that pixel's radial distance (r) from the center of the image and are given as[163],

$$x_D = x(1 + d_1 \cdot r^2 + d_2 \cdot r^4 + d_3 \cdot r^6) \tag{50}$$

$$y_D = y(1 + d_1 \cdot r^2 + d_2 \cdot r^4 + d_3 \cdot r^6) \tag{51}$$

where x_D and y_D are the distorted pixel locations, x and y are the undistorted pixel locations and d_1, d_2, d_3 and the iteratively determined radial distortion coefficients.

2.5.5.3 Simple Stereo Systems and Depth Estimation

A simple stereo system consists of an arrangement of two calibrated cameras separated horizontally by a baseline (B). The two cameras capture images of the same scene from slightly different viewpoints and each point in the 3D scene projects to different locations in the two images. The goal is to find pairs of points in the left and right images that correspond to the same physical point in the 3D scene. This is achieved using a process known as image rectification. Rectification reduces the search area for matching points between two images by aligning identical objects in each image along the same horizontal epipolar lines[165]. Following rectification, any pair of corresponding points resides on the same pixel row.

Subsequently, the distance or horizontal shift between conjugate pixels in the left and right images can then be determined algorithmically using semi-global matching[166]. This computed disparity (Δ), known as the disparity map, is inversely proportional to the real-world distance of the corresponding point from the cameras. Larger disparities indicate objects which are closer, while smaller disparities indicate objects which are farther away. Using the disparities, the depth (Z) (distance from the camera) of each point in the scene can then be estimated using the triangulation equation[162].

$$Z = \frac{f \cdot B}{\Delta} \tag{52}$$

CHAPTER 3 MANUSCRIPT 1: CHARACTERIZATION OF NOVEL 3D PRINTED PLASTIC SCINTILLATION DOSIMETERS

3.1 PREAMBLE

This paper represents the first comprehensive analysis of 3D printed plastic scintillation dosimeters for radiotherapy applications and presents a novel methodology for the rapid fabrication of plastic scintillators with bespoke geometries. This work establishes the basic dosimetric properties of 3D printed scintillators and quantifies the dependence of the signal on 3D printing parameters. Both are fundamental requirements for the proposed development of a novel high-resolution skin surface dosimeter. Upon completion of the initial characterization of one exemplary scintillating material I wrote the above publication under the guidance of my graduate supervisors (coauthors). Biomedical Physics & Engineering Express (BPEX) was then selected for publication of this work as it is an international, peer-reviewed, multidisciplinary journal for papers relevant to biophysics, medical physics, and biomedical engineering with an emphasis on encouraging interdisciplinary work within these fields.

The following chapter has been reproduced with permissions (Appendix A.10) from: "Characterization of novel 3D printed plastic scintillation dosimeters" by Nicholas Lynch, James L Robar, Thalat Monajemi, 2020, *Biomedical Physics & Engineering Express,* 6(5):1-15 (https://doi.org/10.1088/2057-1976/aba880). Copyright 2020 by IOP Publishing. It differs only from the original text in the addition of revisions for additional clarity. This chapter also includes an addendum containing additional data not presented in the original manuscript.

3.2 ABSTRACT

We propose a new methodology for the fabrication and evaluation of scintillating detector elements using a consumer grade fusion deposition modeling (FDM) 3D printer. In this study we performed a comprehensive investigation into both the effects of the 3D printing process on the scintillation light output of 3D printed plastic scintillation dosimeters (PSDs) and their associated dosimetric properties. Fabrication properties including print variability, layer thickness, anisotropy and extrusion temperature were assessed for 1 cm^3 printed samples. We

then examined the stability, dose linearity, dose rate proportionality, energy dependence and reproducibility of the 3D printed PSDs compared to benchmarks set by commercially available products. Experimental results indicate that the shape of the emission spectrum of the 3D printed PSDs do not show significant spectral differences when compared to the emission spectrum of the commercial sample. However, the magnitude of scintillation light output was found to be strongly dependent on the parameters of the fabrication process. Dosimetric testing indicates that the 3D printed PSDs share many desirable properties with current commercially available PSDs such as dose linearity, dose rate independence, energy independence in the MV range, repeatability, and stability. These results demonstrate that not only does 3D printing offer a new avenue for the production and manufacturing of PSDs but also allows for further investigation into the application of 3D printing in dosimetry. Such investigations could include options for 3D printed, patient-specific scintillating dosimeters that may be used as standalone dosimeters or incorporated into existing 3D printed patient devices (e.g. bolus or immobilization) used during the delivery of radiation therapy.

3.3 INTRODUCTION

Plastic scintillation dosimeters (PSDs) have been studied extensively for dosimetry of photon and electron beams in the radiotherapy energy range. Water equivalence, high sensitivity, dose rate and energy independence, and stability make them ideal candidates[98(p199),117]. In this energy range, PSDs have been used both in routine beam characterization work, e.g., for quality assurance, determination of field output factors, small field dosimetry and *in-vivo* dosimetry[75–77].

Typically, plastic scintillators are fabricated by thermal polymerization at high temperatures above 100°C and the overall preparation process lasts several days[58]. When an initiator is added, the polymerization can be carried out at a lower temperature of 50°C to 60°C and the polymerization time can be shortened, but production within one day remains challenging[59–63]. In addition, the scintillators produced usually have regular geometric shapes, e.g. slabs, cylinders or fibers.

Recent advances in 3D printing technology have resulted in the production of a myriad of relatively low-cost consumer-grade printers. 3D printing is ideal for the rapid manufacturing of unique end products or small batches of products with bespoke or complex geometries. 3D

printing is classified as an additive manufacturing technique as the material is added in layers. In this way users can rapidly create complex shapes that would otherwise be difficult, costly and time consuming to produce by current forming and moulding techniques.

In 2014, there was a first study of a plastic scintillator produced by a 3D printer and photopolymerization with UV light. Its scintillation efficiency was 28.0% of that of the commercial scintillator EJ204[64]. Between 2017 and 2019 a team of researchers from the Department of Nuclear Engineering at Hanyang University in Seoul South Korea published a series of papers on 3D printing of plastic scintillators. These papers investigate various substitutions and additions in the classical fabrication of plastic scintillators to facilitate using Digital Light Processing (DLP) 3D printing techniques to manufacture high quality plastic scintillators[58,65–67]. DLP is a 3D printing technology which uses UV light to solidify a photopolymer resin layer by layer. The culmination of this work has been the development of a novel UV curable photopolymer, which contains a precise mixture of wavelength shifters and activators to allow for it to act as a scintillating material[65]. As a result, the fabricated plastic scintillator possessed a light output performance that was 67.0% that of the commercial plastic scintillator BC-408[65].

To date there has been a lack of studies concerning the application of Fusion Deposition Modelling (FDM) 3D printing to the fabrication of PSDs. Additionally, since the previous efforts in this area have focused on development of a scintillating material which can also be photopolymerized, no studies have been performed on 3D printed polystyrene PSDs. Since the FDM process is both commonly used for 3D printing and amenable to the use of polystyrene based scintillators it may be possible to further improve on the current performance benchmarks for 3D printed PSDs. FDM 3D printing of plastic scintillators would provide a simple, low-cost manufacturing option for the fabrication of PSDs. Additionally, 3D printing of plastic scintillators would allow for the rapid creation of scintillators with complex geometries and potentially patient-specific scintillating dosimeters that otherwise would be difficult to produce by current forming and moulding techniques. We believe this is the first reported study in which commercially available plastic scintillators are extruded through an FDM 3D printer to form new user specified scintillating elements.

3.4 METHODS AND MATERIALS

3.4.1 Scintillator Fabrication

The 3D printer used for fabrication was a LulzBot Taz 6, and the size of the fabricated PSDs was 1 x 1 x 1 cm^3. Fig. 3.1 shows a series of plastic scintillators fabricated by the FDM printing process. The printer filament used for the FDM process was a non-cladded BCF-10 plastic scintillating fiber (Saint Gobain Crystals, Ohio, USA) with a diameter of 3.0 mm.

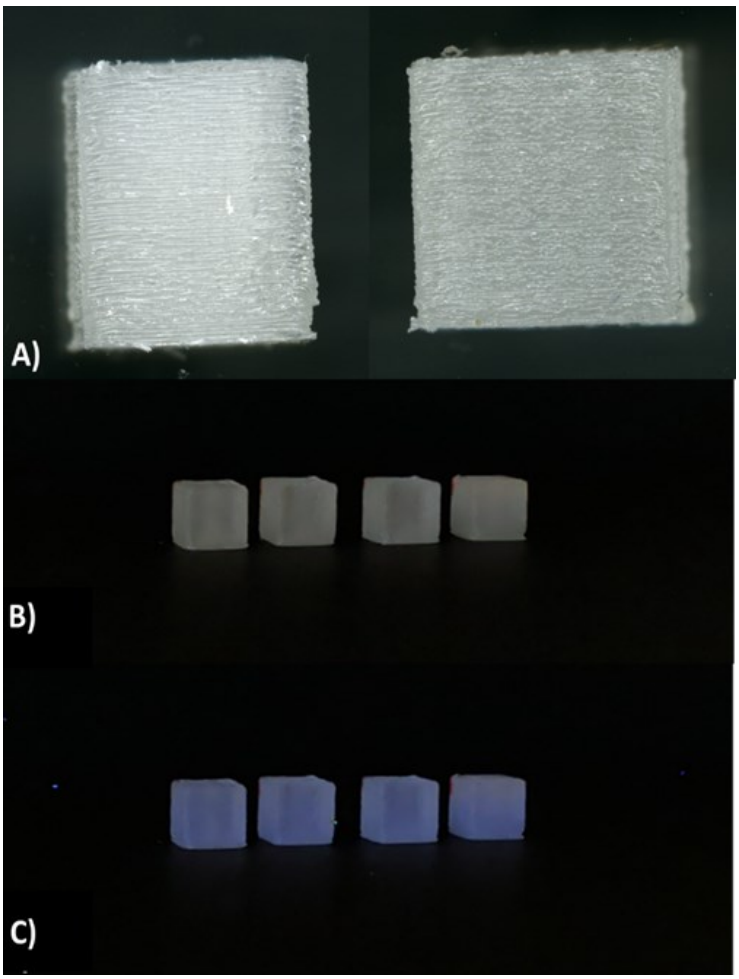

Figure 3.1: Images of novel 3D printed plastic scintillators, **A)** high-resolution optical scan taken with and Epson 10000 flatbed scanner, **B)** ordinary state and **C)** irradiated state, irradiated by 6 MV X-rays.

Several studies have examined the dimensional accuracy of the FDM 3D printing processes[167–169]. In general, the dimensional accuracy is found to be dependent on both the filament material used and the grade of the printer (hobbyist or industrial). The dimensional

accuracy of the 3D printed PSDs fabricated using this setup was determined from a series of 20 printed samples to be ± 5.0%. The average mass of a single 3D printed PSD was also determined using these 20 printed samples to be 1 ± 0.1 g.

The geometry of a standard FDM print can be described according to several aspects of its geometry as illustrated in Fig. 3.2, and the parameters of each aspect can be altered to optimise a given design. In 3D printing the height of each successive stacked addition of material is called the layer thickness. The walls of the print, not contacting the build plate, nor the top of the model, are referred to as the shell. The part of the print in contact with the heated build plate is referred to as the bottom layer. The part of the print facing upwards towards the extruding nozzle is called the top layer. Finally, the infill refers to the internal structure of the print which can vary in both direction and geometry. Unless specifically stated otherwise, the infill direction and geometry for all tests in this manuscript is 45° lines.

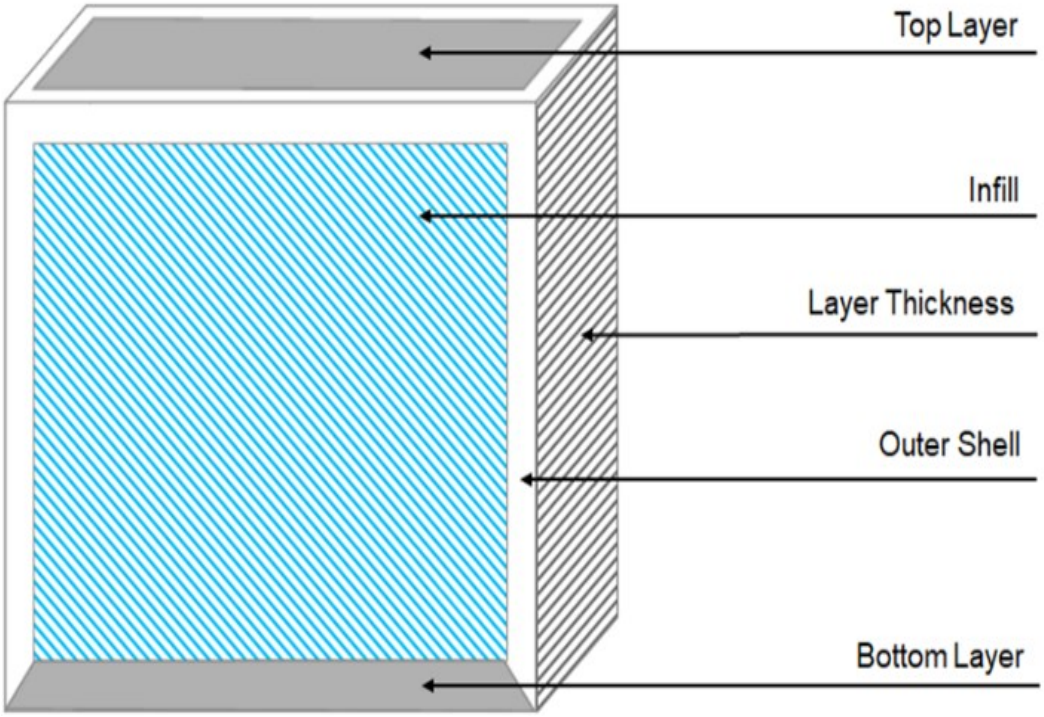

Figure 3.2: Sectioned diagram of the various components of an FDM 3D printed object.

Layer thickness is one of the principal characteristics of a 3D printed object as the layer height corresponds to the vertical resolution of the z-axis. Various studies have examined the effect of printing parameters on the surface quality of 3D printed materials[167,170]. Principally,

the surface roughness of the printed objects is proportional to and significantly increases with layer thickness.

The default settings for 3D printing parameters provided by the manufacturer do not guarantee the quality of a printed part. While this investigation does explore the impact and selection of optimized settings for working with a scintillating filament, initial testing identified a series of parameters which were critical to successful fabrication. These settings are filament retraction, print speed and fill density. In this study, to maximize the quality and consistency of printing with BCF-10 as a medium, we disabled retractions and reduced the print speed from the default of 40 mm/s to 10 mm/s. Through iterative trials, we found that these settings were required to prevent significant warping of the print due to poor adhesion and cooling. Since our goal was to produce solid PSD samples, we used an infill factor of 100% in all cases.

3.4.2 Data Acquisition

Optical signal measurements were performed with an Exemplar Plus spectrophotometer (Exemplar Plus, B&W Tek, Delaware, USA). As shown in Fig. 3.3 the scintillation signal was carried to the spectrophotometer outside the treatment room using an Eska Premier GH-4001 optical fiber with a core diameter of 1 mm. Printed scintillating elements were housed in a light-tight plastic box that facilitated reproducible sample positioning and coupling of the optical fiber. In addition, the dark spectrum was acquired immediately before and subtracted from each measurement.

3.4.3 Signal Processing

The signal acquisition and processing is identical to our previous work and is described briefly here[107]. The scintillation component of a PSD signal was determined using a full spectral method[125]. The signal from the PSD (T) was assumed to be a superposition of the Cherenkov (C), Fluorescence (F) and Scintillation (S) spectra as shown in equation 1:

$$T = aF + bC + dS \quad (1)$$

The scintillation-only spectra were acquired by exposing the PSDs to 100 kVp X-rays from an orthovoltage treatment unit (Xstrahl 300, Xtrahl LTD, Surrey, UK). This energy is below the 178keV threshold for Cherenkov production in PMMA optical fibers[171]. The fluorescence spectrum of the Eska fiber was obtained by exposing the optical fiber (without the scintillator)

to 100 kVp X-rays. The Cherenkov spectrum was obtained by exposing 10 cm of the ESKA fiber to 16 MeV electrons from a linear accelerator (Varian TrueBeam, Varian Medical Systems, Palo Alto, USA) while on the surface of a solid water phantom with the gantry rotated to 45 degrees[98]. In this geometry the contribution of fluorescence to the measured signal is negligible[127]. Fig. 3.4 illustrates the unit area normalized scintillation and Cherenkov spectrums for a sample 3D printed PSD.

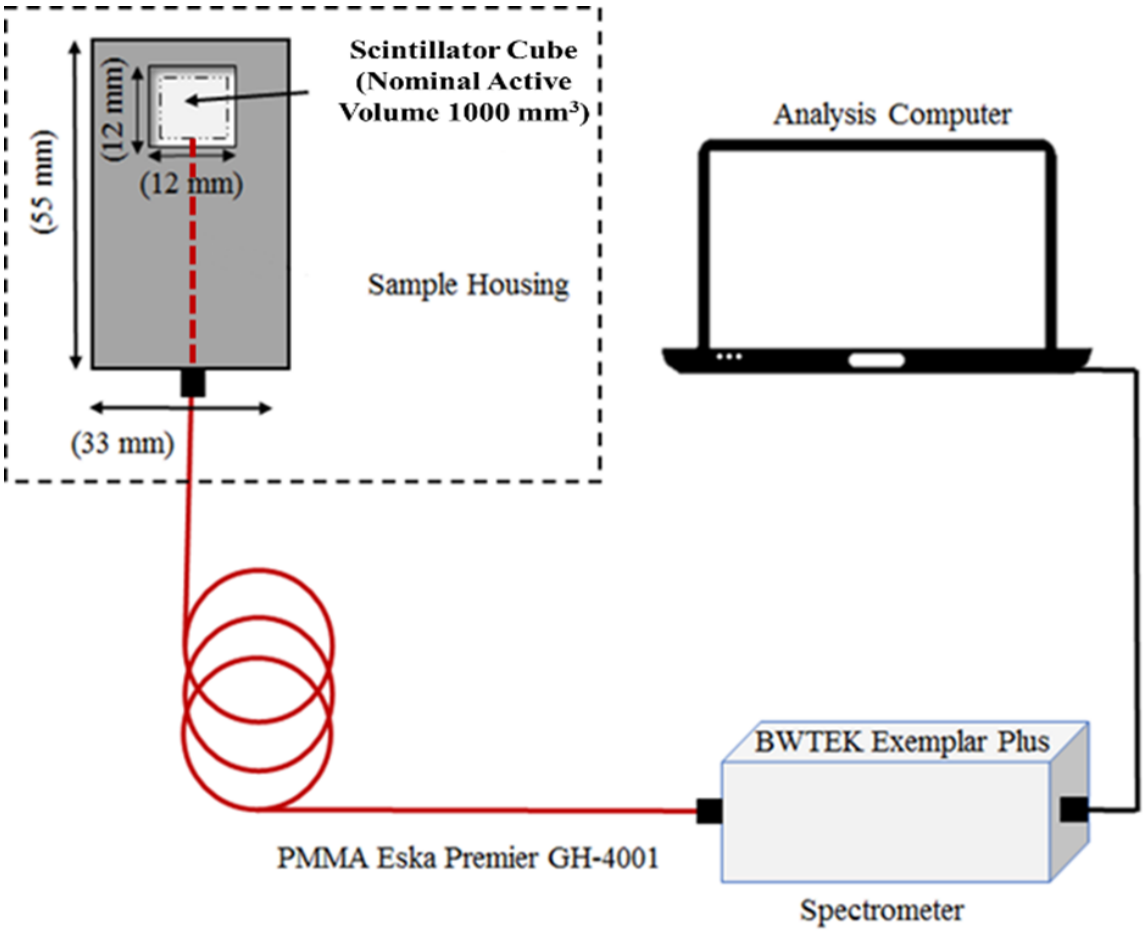

Figure 3.3: Experimental set-up for scintillation measurements. The dashed square shows an enlarged image of the fiber coupled scintillator arrangement.

A least squares fitting method was applied using the unit-area normalized C, F and S spectra to determine the coefficients a, b and d in equation 1 that best reproduce the total measured spectrum T. The area under the dS spectrum (total scintillation signal) was then assumed to be proportional to the absorbed dose.

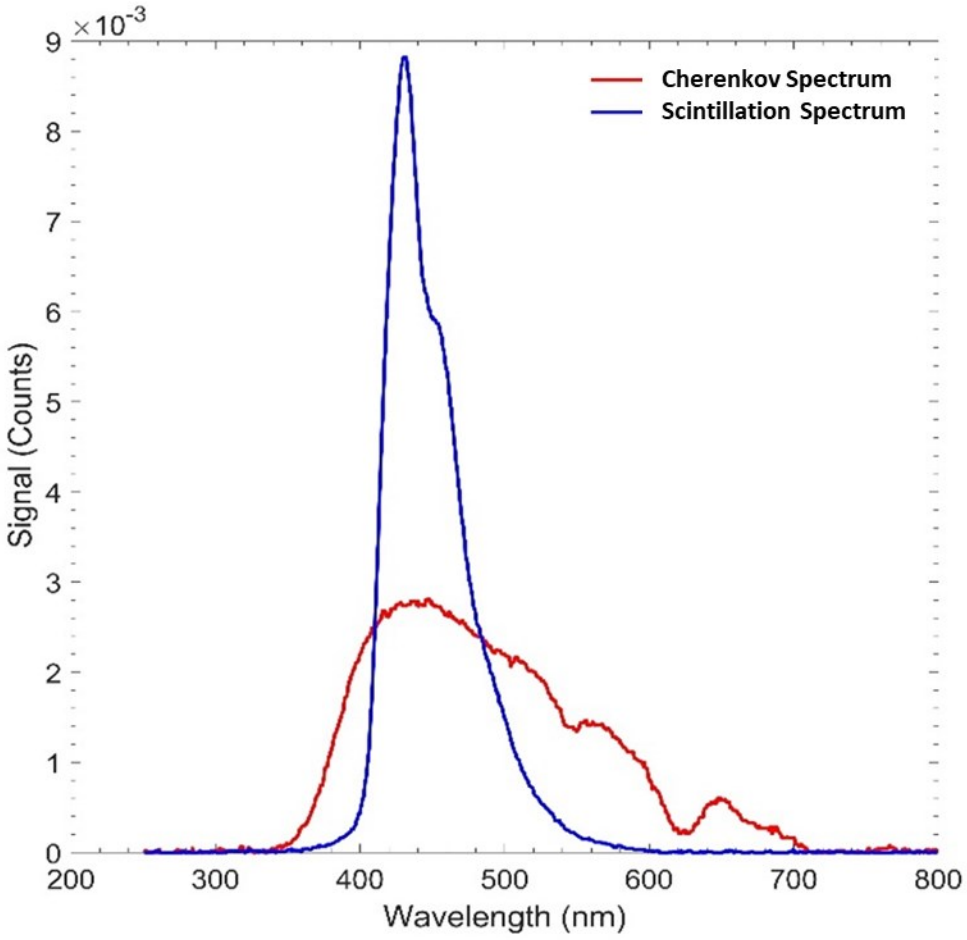

Figure 3.4: Unit area normalized scintillation and Cherenkov spectrums for a sample 3D printed PSD.

3.4.4 Fabrication Parameters

To establish the effects of various fabrication parameters on the scintillation spectrum, the samples were irradiated under identical conditions. 6 MV photon fields were delivered using gantry and collimator angles of 0 degrees, 200 Monitor Units (MU), field size of 5 x 5 cm^2 and a dose rate of 200 MU/min, and source-to-surface (SSD) distance of 100 cm. The light tight box which contained the scintillator sample was placed on 3 cm slab of solid water to provide some backscatter. Unless otherwise specified, the beam was incident on the top layer of the PSD and measured from the shell surface (-X side) as illustrated in Fig. 3.5.

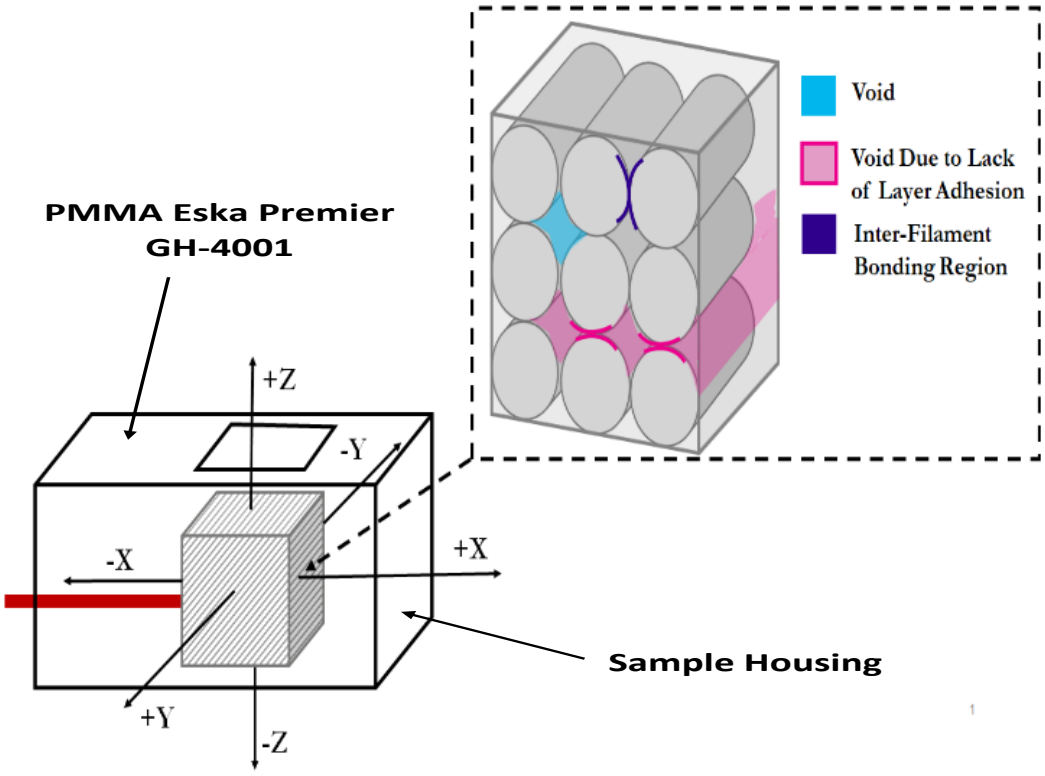

Figure 3.5: Illustration of sample orientation and infill geometry with demonstration of optical fiber coupling. When viewing the infill geometry at a molecular level, FDM 3D prints possess layers which are not bonded as strongly as the lines within each layer. As a result, there may be gaps due to the geometry of the rounded lines (voids) and layers may not fully adhere to one another (void due to lack of adhesion).

3.4.4.1 Print Variability

To investigate the degree of variability in the measured scintillation signal for the 3D printed PSDs, a series of ten cubes of scintillator material were printed at 210°C and a layer height of 0.2 mm.

3.4.4.2 Layer Thickness

In order to determine the effect of layer height on the measured scintillation signal of the 3D printed PSDs, cubes of scintillator material were printed at 210°C and layer thicknesses ranging from extra coarse (0.6 mm), coarse (0.5 mm), fast (0.4 mm), extra fast (0.3 mm), draft (0.2 mm), normal (0.15 mm), fine (0.1 mm), and extra fine (0.06 mm).

3.4.4.3 Anisotropy

FDM 3D printers assemble layers by depositing rounded linear segments of filament according to a pre-set direction. Due to this process, there exists a clear distinction between the bonding inside each layer and the bonds which hold the layers together[172]. The geometry of this relationship as well as the notation used to distinguish the orientations for a given sample are illustrated in Fig. 3.5. This difference in bonding effectiveness means that for a given infill direction, the two spatial axes orthogonal to the infill direction exhibit different mechanical properties[172]. Therefore, anisotropy in this context, refers to a given infill direction exhibiting differing scintillation signal when measured along the three orthogonal spatial axes X, Y, and Z.

To determine the degree of anisotropy present, four cubes of scintillator material were fabricated at 210°C, a layer height of 0.2 mm and four different infill rotation angles (0 °, 45 °, 90 °, 135 °). Where the infill rotation angle controls the directions of infill with respect to the exterior print surfaces. The samples were then irradiated 6 times with each sample rotated such that light was collected once from each surface of the cube, i.e. the bottom layer, top layer, all sides.

3.4.4.4 Extrusion Temperature

In order to assess the effect of fabrication temperature on the measured scintillation signal of 3D printed PSDs a series of scintillator cubes were printed with a layer thickness of 0.2 mm and extrusion temperatures ranging from 190°C to 225°C in 5°C increments. The lower and upper bound of 190°C and 225°C were selected as they represent the experimentally tested minimum and maximum extrusion temperatures at which it is was possible to print consistently using the BCF-10 scintillating material as a filament.

3.4.4.5 Volumetric Response

In order to characterize the signal due to sub-volumetric irradiation of 3D printed samples in our collection geometry, we used a lead collimator at 100 kVp. The beam was collimated using ~0.4 mm of lead. The collimated beam dimensions were 2 (X) x 10 (Y) mm. The collimator was placed directly on top of the light tight box (See Fig. 3.5). The slit was placed on five different locations on the top face (+Z) of the PSD such that the 2 mm opening slid

across the top surface in the X direction, from closest to the collecting fiber to farthest from the fiber. At each location 400 MUs were delivered, and the was collected. To determine the degree of anisotropy, these measurements were then repeated with the sample rotated such that light was collected once from each surface of the cube, i.e. the bottom layer, top layer, and all sides. Then for the purpose of comparison, these measurements were replicated with a commercial sample of BC-400 plastic scintillator (Saint Gobain Crystals, Ohio, USA) machined to dimensions of 1 x 1 x 1 cm^3.

In these measurements a cone of with 10 cm diameter and SSD of 30 cm was used. The light tight box which contained the scintillator sample was surrounded by vinyl gel sheets of uniform thickness to provide uniform scatter.

3.4.5 Dosimetric Properties

Each sample consisted of a solid cube of scintillator material fabricated at 210°C and a layer height of 0.2 mm. For the tests of stability and reproducibility the irradiation conditions were identical to those described in section 3.4.4. For the testing of dose linearity, dose rate proportionality and energy dependence the light tight box which contained the scintillator sample was placed on 10 cm of solid water with 4.5 cm of solid water placed on top. All remaining air gaps were then filled with vinyl gel sheets of uniform thickness (SuperFlab, Civco, Iowa, USA). The SSD was 95 cm and field size of 10 x 10 cm^2. This way, the center of the scintillator was placed at the linear accelerator isocenter under calibration conditions such that 1 MU delivers 1 cGy for a 6 MV beam.

3.4.5.1 Stability

In order to assess the total variation of the optical signal measurements collected using the spectrophotometer and optical fiber system a single 3D printed PSD was subjected to a series of twenty consecutive, 200 MU irradiations with 6 MV photons over a time period of 1 hour.

3.4.5.2 Dose Linearity

Measurements of scintillator linearity were performed using 6 MV photons. The 3D printed PSDs were assessed at a dose rate of 200 cGy/min for doses between 40 cGy to 440 cGy in increments of 40 cGy. The upper bound of 440 cGy was selected as it represents the experimentally tested saturation point of the spectrophotometer.

3.4.5.3 Dose Rate Proportionality

The dose-rate proportionality of the 3D printed PSDs was assessed using two different methods. First by varying the Linac pulse frequency and then by varying the dose deposition rate. Assessment of the pulse frequency dependence utilized a photon energy of 6 MV and dose-rates of 100 cGy/min to 600 cGy/min in increments of 100 cGy/min. For each exposure, a dose of 200 cGy was delivered. The dose deposition rate was investigated by delivering 200 MUs at a dose-rate of 600 MU/min and varying the SSD from 65.25 cm to 145.25 cm in 10 cm increments. The range of SSDs selected correspond to the experimentally determined minimum and maximum SSDs achievable. Complimentary measurements using an Exradin A12 ionization chamber and associated electrometer were then collected under identical irradiation conditions for comparison.

3.4.5.4 Energy Dependence

The energy dependence of the 3D printed PSDs was assessed by delivering 200 cGy at 6 MV beam quality from the linear accelerator. Additional exposures of the same dose were made for 100, 180 and 300 kVp beam qualities using a superficial/orthovoltage unit with a 5 cm diameter cone, SSD of 30 cm, no build up material and 3 cm of solid water for backscatter.

3.4.5.5 Reproducibility

To examine the short-term, daily reproducibility of the measured scintillation signal produced by the 3D printed PSDs, a sample was subjected to a series of once daily, 200 MU irradiations with 6 MV photons over a period of 14 days.

3.5 RESULTS

3.5.1 Fabrication Parameters

3.5.1.1 Print Variability

Fig. 3.6 illustrates the variability of the total scintillation signal measured for the ten 3D printed samples. The experimental data indicates that for a given set of PSDs printed using the same fabrication parameters the standard error is 0.0271 with a maximum deviation from 1 of 0.04.

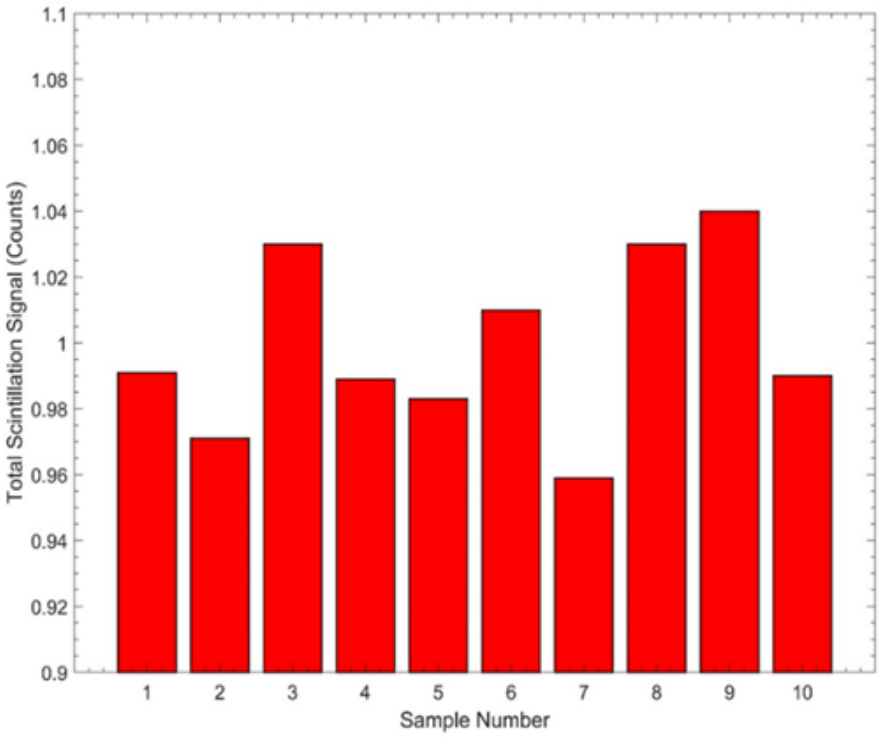

Figure 3.6: Variability of the total scintillation signal measured for the series of ten 3D printed PSDs. Measurements normalized to an average of 1.

3.5.1.2 Layer Thickness

Fig. 3.7 illustrates the relationship between the print layer thickness and the measured total scintillation signal. The lowest measured scintillation signal was observed at the extra fine layer thickness of 0.06 mm with the greatest scintillation signal being observed for the layer thickness of 0.4 mm. The percent difference between the maximum and minimum scintillation signal is ~10.0 %. This indicates that an increase in scintillation signal is observed with increasing layer thickness.

3.5.1.3 Anisotropy

The directional dependence of the 3D printed PSDs was assessed and is summarized for all four infill rotation angles in Fig. 3.8. The 3D printed PSDs demonstrated a strong directional dependence across all infill rotation angles tested. Samples with infill rotation angles parallel and perpendicular to the outer shell surfaces (0º and 90º) showed increased intensity when measured parallel to the direction of the infill and reduced intensity when measured

perpendicular to it. Conversely, the scintillation signals recorded along all four sides of the outer shell show good correlation when the infill angle is not directly perpendicular/parallel to the outer shell (45º and 135º).

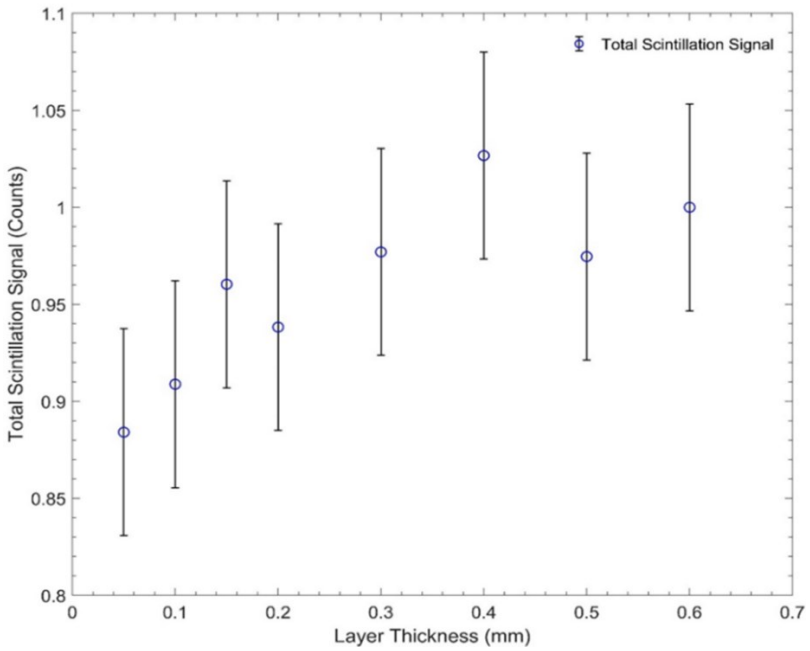

Figure 3.7: Effect of print layer thickness on the measured total scintillation signal for a 3D printed PSD, normalized to the scintillation signal measured at the maximum layer thickness of 0.6 mm.

Additionally, the bottom surfaces of all the tested samples displayed an approximate 15.0 % decrease in scintillation signal when compared to the outer shell surfaces. The top layers of all samples also displayed a reduction in scintillation signal of approximately 8.0 %. The reduction in signal of the top layers is not as prominent as the bottom layers despite them being geometrically equivalent surfaces with regards to the printing pattern. For samples with infill rotation angles parallel to an outer shell surface (0º and 90º), the reduction seen when measuring perpendicular to these rotation angles is comparable to the reduction exhibited by the top layers.

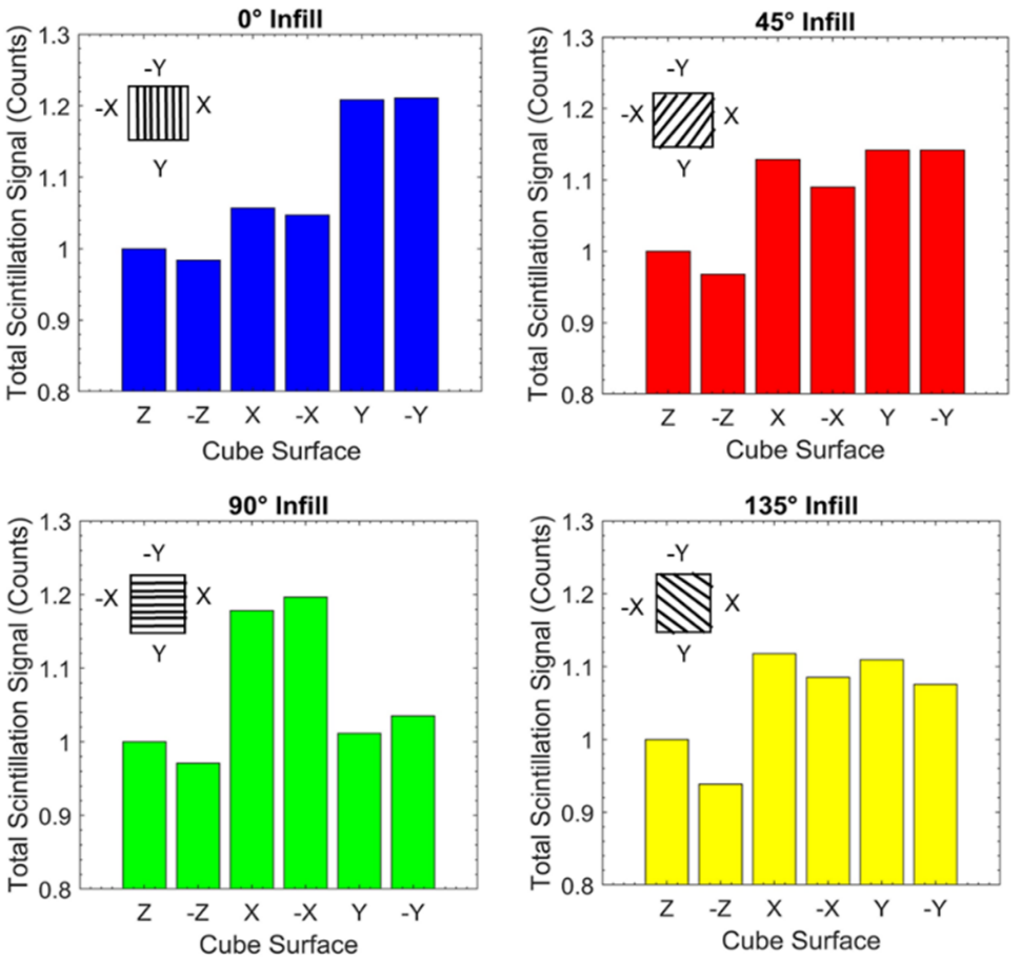

Figure 3.8: Anisotropy of total scintillation signal for 3D printed PSDs using four infill rotation angles. Measurements are normalized to the total scintillation signal measured on the Z surface of each cube.

3.5.1.4 Extrusion Temperature

Measurements indicate that PSDs 3D printed at higher extrusion temperatures exhibit reduced scintillation signal (Fig. 3.9) over the temperature range examined. The percent difference between the maximum and minimum scintillation signals is approximately 13.0 %.

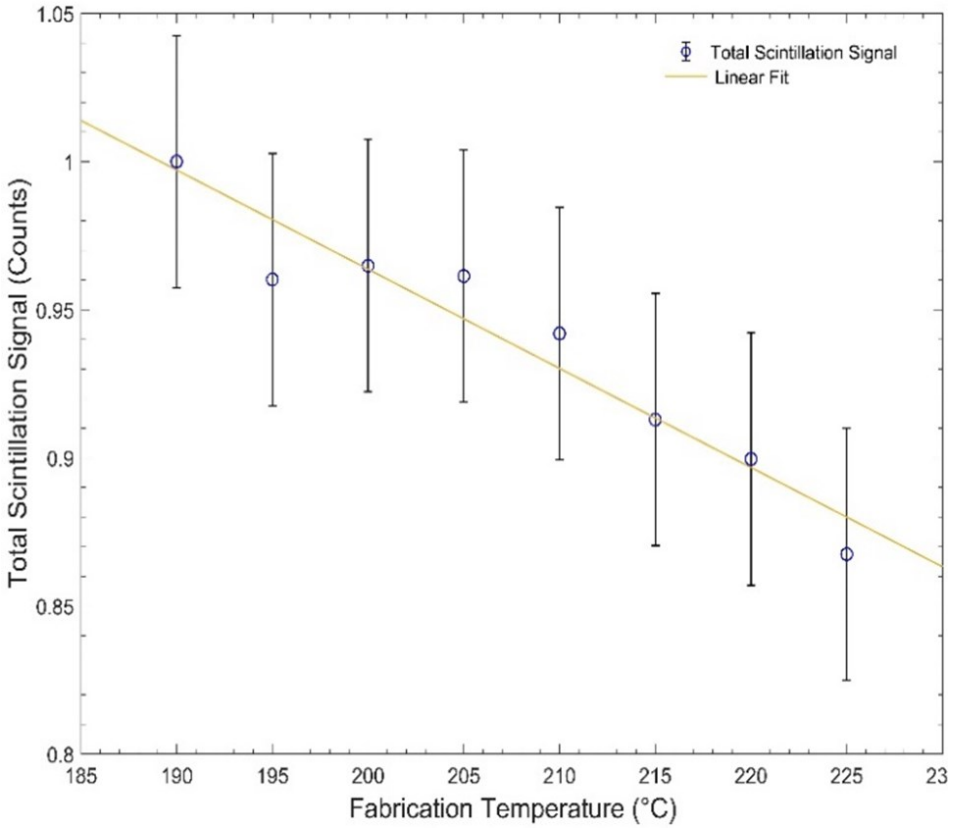

Figure 3.9: Effect of print extrusion temperature on the measured scintillation signal of 3D printed PSDs. Results are normalized to the total scintillation signal measurement at the minimum temperature of 190°C.

3.5.1.5 Volumetric Response

Fig. 3.10 illustrates the variation of total scintialltion signal as a function of the lead collimators postion relative to the coupling fiber. Data collected from each surface of the cube shows a decrease in the measured total scintillation signal as the irradiated subvolume moves farther away from the coupling fiber. Measurements collected from the X and Y surfaces of the PSD demonstrate an approximate 50% reduction in the total signal when comparing the closest and farthest subvolumes. The Z surfaces show a greater degree of variability and a larger decrease in the measured total scintillation signal when compared to the X and Y surfaces.

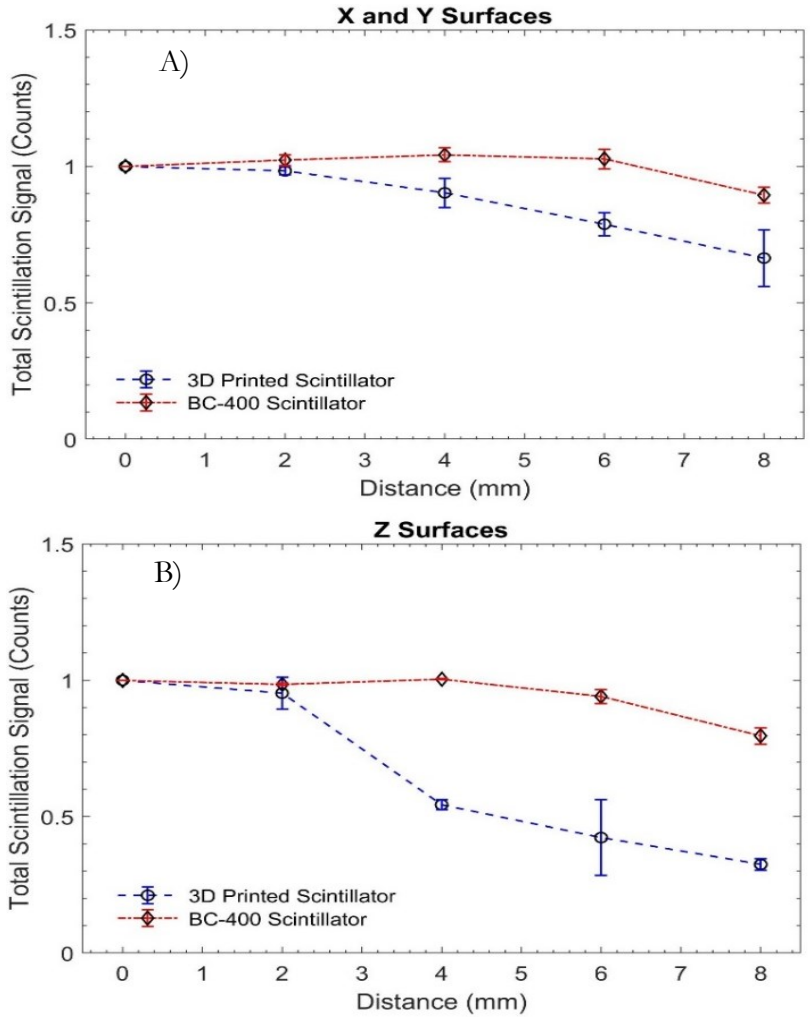

Figure. 3.10: Comparison of subvolume contributions to the measured total scintillation signal for a 3D printed and a commercial PSD, A) X and Y surfaces, B) Z surfaces. Measurements are normalized to the total scintillation signal measured at the initial collimator position.

3.5.2 Dosimetric Properties

3.5.2.1 Stability

Fig. 3.11 illustrates that the total scintillation signal measured over twenty consecutive readings resulted in a standard error of 0.0005.

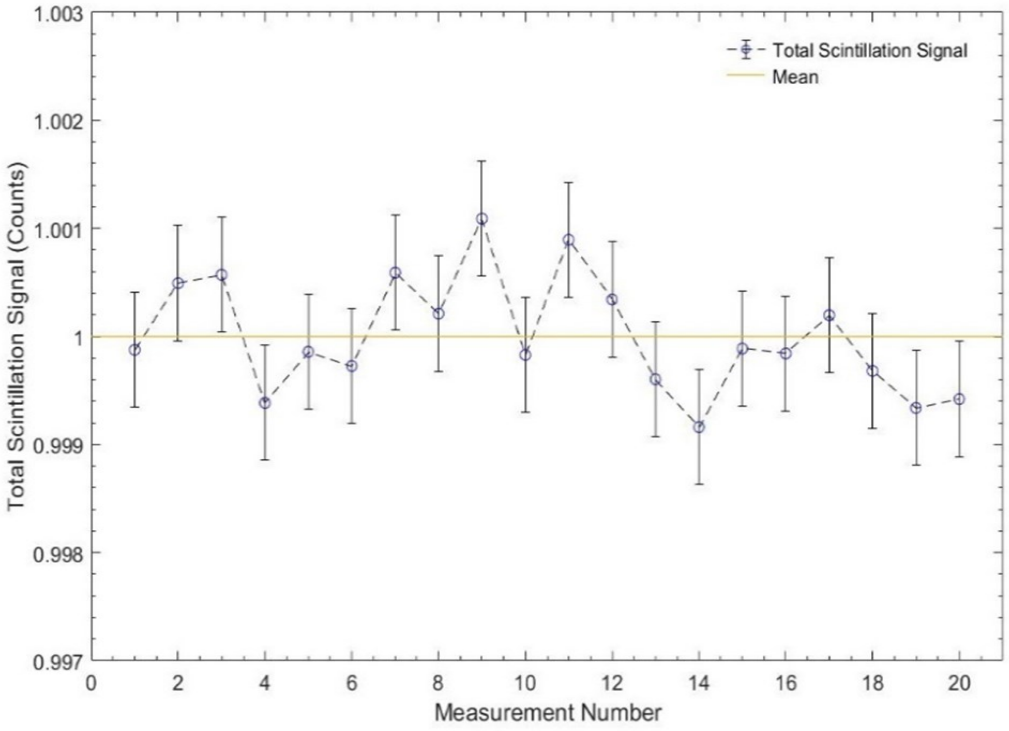

Figure 3.11: Stability of the total scintillation signal for a 3D printed PSD over twenty consecutive measurements under irradiation from a 6 MV photon beam. Measurements normalized to an average of 1.

3.5.2.2 Dose Linearity

Measurements showed no deviations from linearity greater than 0.38 % (Fig. 3.12). The root mean square deviation from linearity over the entire range of doses measured was determined to be 0.23 %.

3.5.2.3 Dose Rate Proportionality

Fig. 3.13 illustrates the total scintillation signal measured at each of the pulse rates examined. The collected data shows that the total scintillation signal did not vary more than 0.10 % from the mean for any pulse rate. The standard error of the measured total scintillation signals was determined to be 0.0008. Fig. 3.14 highlights the linear relationship between the dose rate measured by the ionization chamber and the total scintillation signal measurements across the SSDs of 62.25 cm to 145.25 cm. Measurements showed no deviations from linearity greater than 0.74 %. The root mean square deviation from linearity over the entire range was 0.38 %.

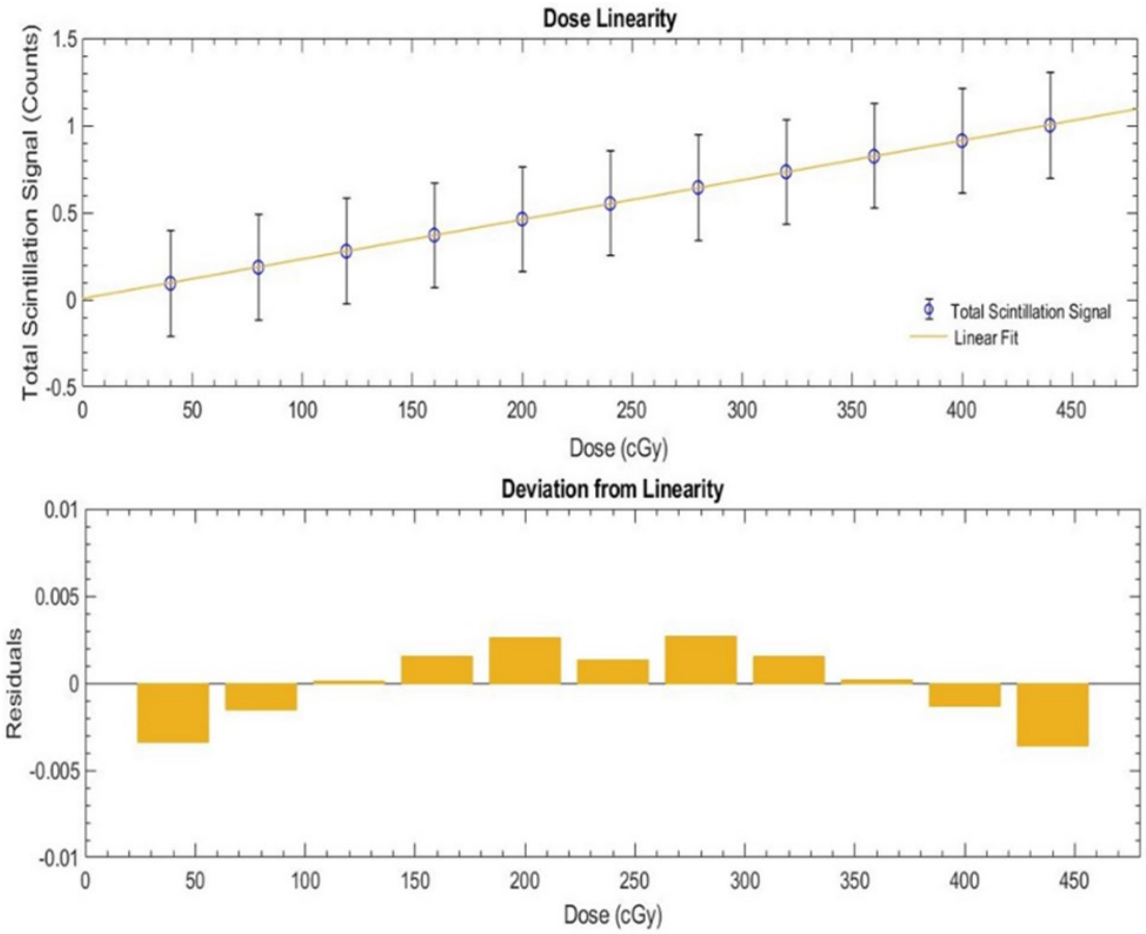

Figure 3.12: Scintillation signal linearity of a 3D printed PSD under irradiation from a 6 MV photon beam, measurements are normalized to the total scintillation signal measurement at the maximum dose of 440 cGy.

3.5.2.4 Energy Dependence

As shown in Fig. 3.15, the 3D printed PSD displays energy independence in the MV energy range. The signal drops to 32%, 46% and 66% at 100kVp, 180kVp and 300 kVp compared to its signal at 6 MV.

3.5.2.5 Reproducibility

As shown in Fig. 3.16, over the 14 days of daily irradiations, the standard error of the measured total scintillation signal was determined to be 0.0136. The collected data shows that the measured total scintillation signal did not vary more than 2.1 % from the mean for any daily irradiation.

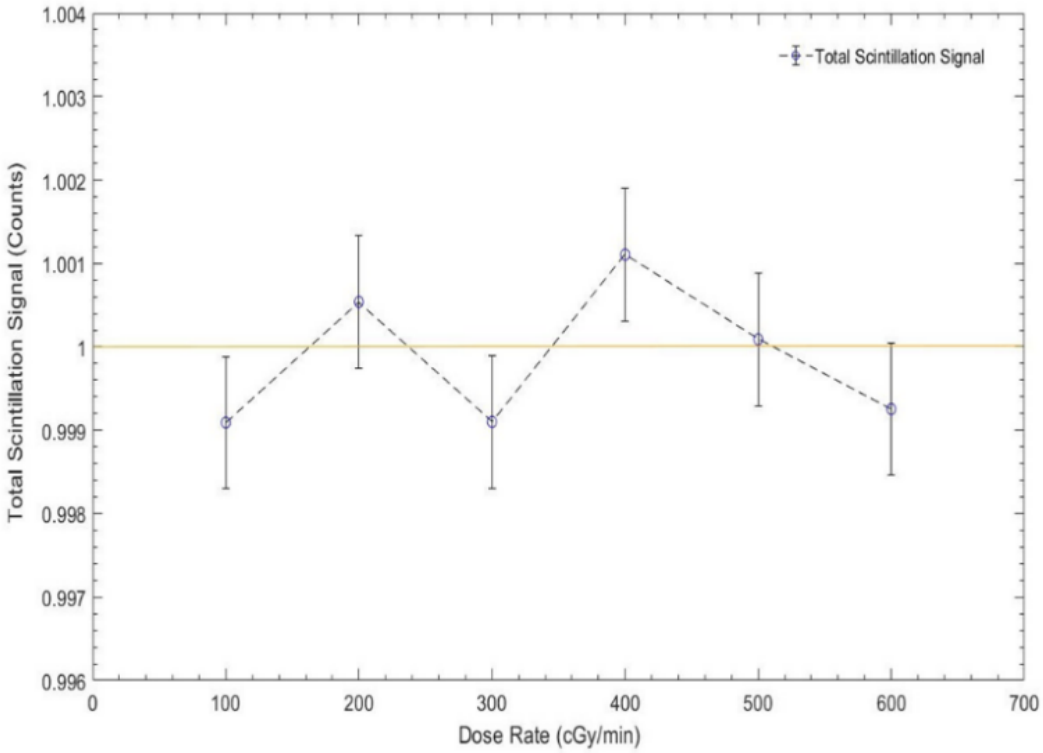

Figure 3.13: Pulse rate dependence of a 3D printed PSD for a 6 MV photon beam. Measurements have been normalized to an average of 1.

3.6 DISCUSSION

3.6.1 Layer Thickness

For any scintillation detector it is desirable to collect the largest possible fraction of emitted light with the uniformity of light collection dependent on the conditions which exist at interfaces within the scintillator itself. In the case of FDM 3D printing the quality and resolution of the interfaces is largely determined by the selected layer thickness[173]. The experimental data demonstrates an increase in the total relative intensity with increasing layer thickness. Increasing layer thickness results in a decrease of interfaces inside the 3D printed PSDs, thus improving the scintillation light transmission. We hypothesize that the bulk of the observed effect is the result of a decrease in light scattering due to a decrease in the number of layer interfaces inside the 3D printed PSD.

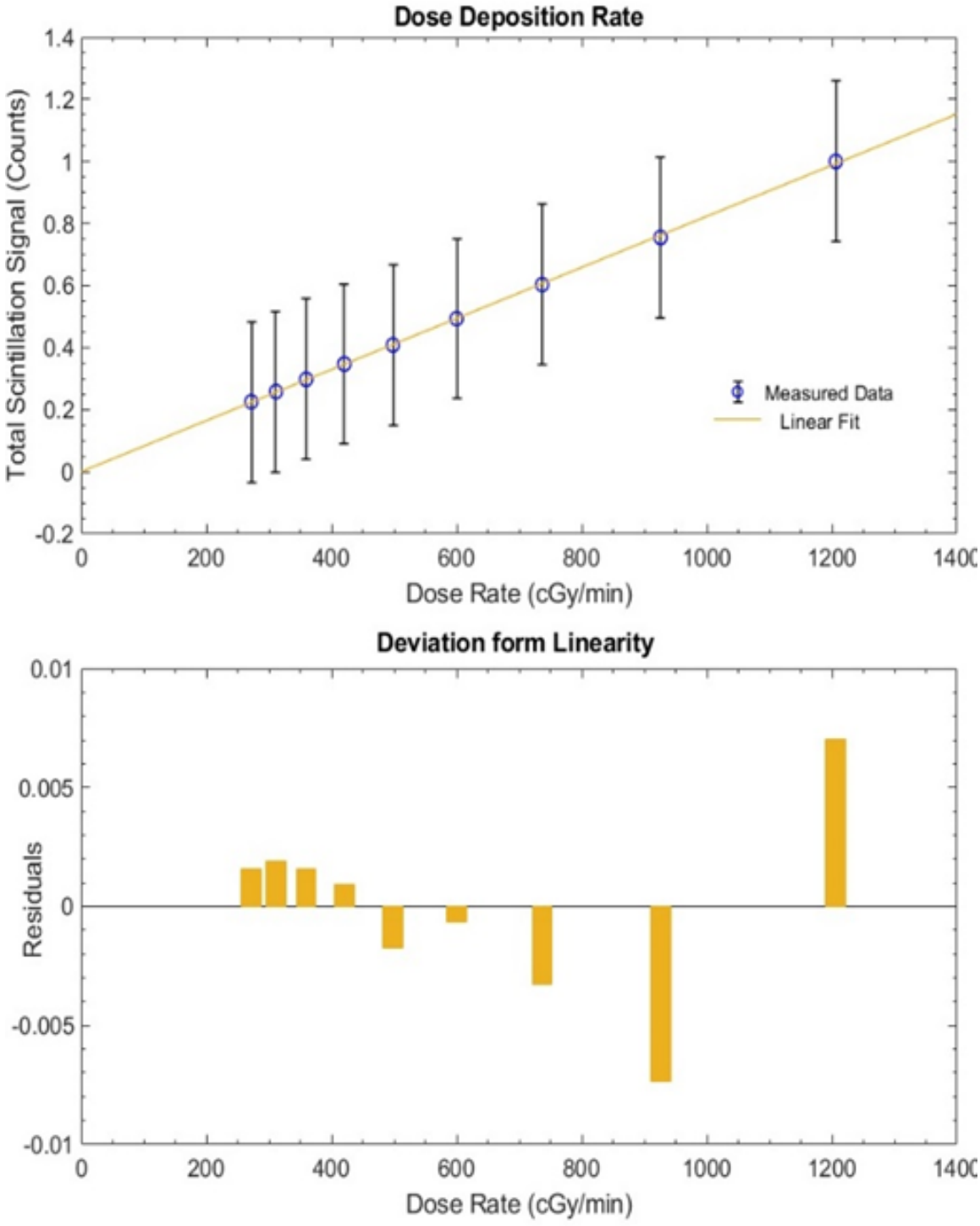

Figure 3.14: Plot of total scintillation signal as a function of ionization chamber (Exradin A12) charge for all SSDs. Measurements normalized to the total scintillation signal measurement at the smallest SSD of 65.25 cm.

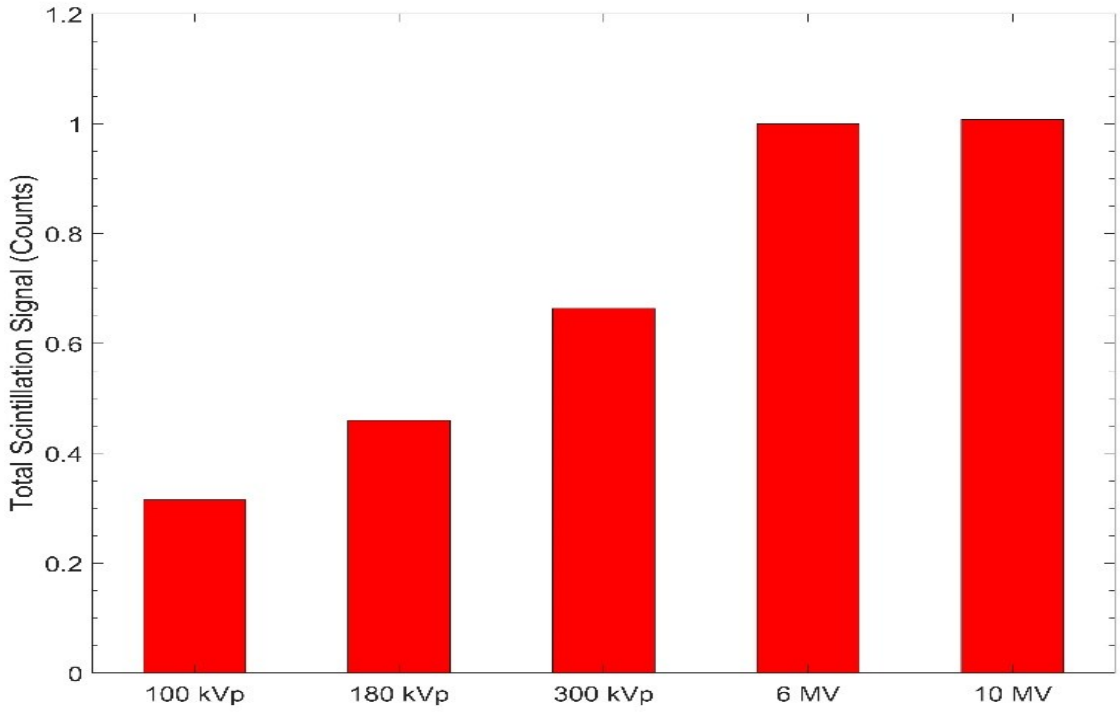

Figure 3.15: Energy dependence of a 3D printed PSD. Measurements are normalized to the scintillation signal measurement at 6 MV.

3.6.2 Extrusion Temperature

Preserving the function of active materials during printing is challenging as processing at high temperatures may modify the materials absorption and emission bands[173]. Here, the effect of heating the scintillating filament above the material's melting point during the extrusion process did not appear to affect the 3D printed PSDs maximum emission wavelength or spectral range. However, the data indicates that PSDs printed at increasing extrusion temperatures show reduced total relative intensity, with a 13% decrease observed over a 35°C range. Based on this, we hypothesize that heating of the filament during the printing process causes damage to the fluorescent dopants or results in polymer degradation. This observation is consistent with a process known as thermal degradation in which molecular deterioration of polymers occurs as a result of overheating[174]. At high temperatures the components of the long chain backbone of the polymer can begin to be broken and react with one another to change the properties of the polymer[174]. The elevated temperatures encountered during the printing process also makes the polymer matrix of the scintillating filament susceptible to attack by

atmospheric oxygen. This process is known as photo-oxidation and can occur simultaneously with thermal degradation[175].

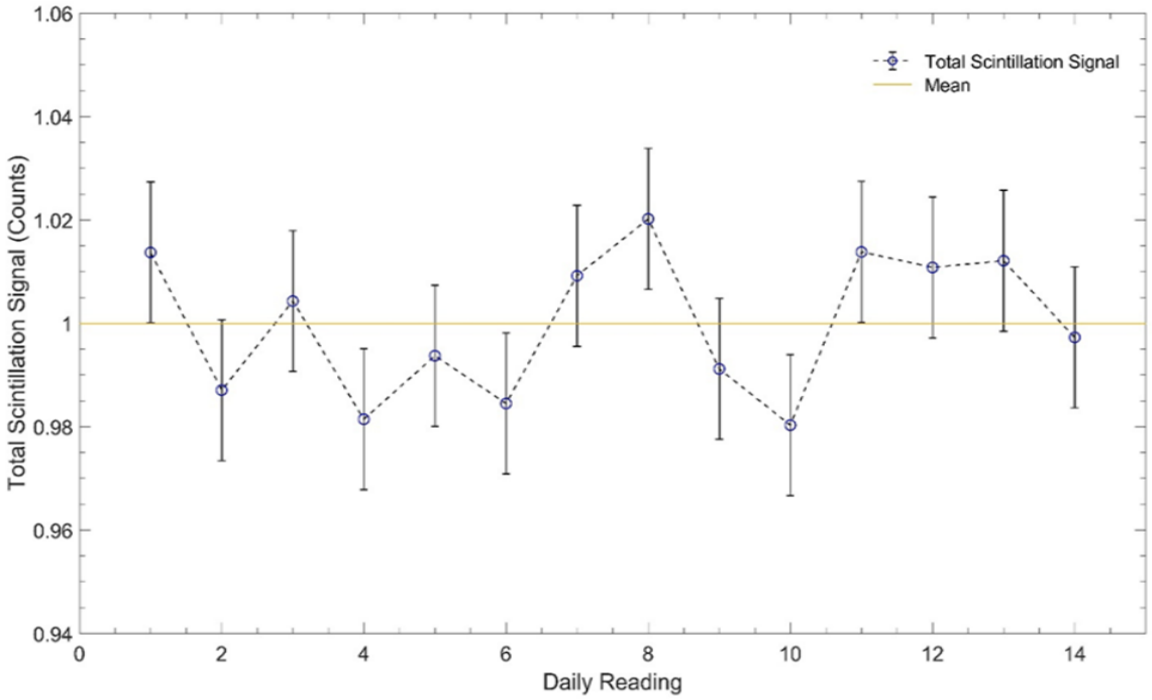

Figure 3.16: Daily reproducibility of a 3D printed PSD measured over a period of 14 consecutive days. Measurements normalized to average of 1.

3.6.3 Anisotropy

The 3D printed PSDs demonstrated a strong directional dependence. Compared to the outer shell the bottom surface exhibits a ~15.0 % decrease in total relative intensity while the top surface exhibits a reduction of ~8.0 %. Comparatively, the reduction in total relative intensity of the top layer is not as prominent as the bottom layer despite them being equivalent geometric surfaces. The disparity in total relative intensity may in part be attributed to the effects of thermal degradation discussed in section IV.B. The bottom surface is in contact with the build plate, which is maintained at 60°C during the printing process. This is done automatically to allow for proper adhesion between the printed PSD and the build plate. The extended exposure of this surface to the heated plate may result in increased thermal degradation. While the effects of thermal degradation may account for the disparity between the top and bottom surfaces, it may not account for the entirety of the reduction observed.

During the 3D printing process, material is added layer by layer in a regular stacking pattern. As a result, reflection, direct transmission, absorption, and refraction of light occurs at the interfaces between layers due to inhomogeneities introduced during the printing process. In this way the printed scintillator's layering acts as its own light pipe between the point of scintillation and the exit surface. In theory, the effectiveness of the transport of light would be affected by propagation losses resulting from several contributing factors: the absorption of the material at the frequency of the propagating light, the Rayleigh scattering by inhomogeneities (i.e., local variations of the refractive index, density, composition) and Rayleigh scattering by defects at the layer interface[176,177].

Furthermore, the shear forces exerted during extrusion may induce an anisotropic arrangement to the molecular constituents of the embedded fillers, favoring their alignment along the direction of print nozzle travel[178]. Recent experiments have highlighted a preferential alignment of elongated fillers (fibers, rods, and nanotubes) along the longitudinal axis of filaments, resulting in anisotropic behavior[173].

3.6.4 Volumetric Response

Finally, comparison of the subvolume contributions to the measured total scintillation signal for the 3D printed and commercial PSD shows significant differences. Unlike the commercial PSD, the 3D printed PSD shows a rapid decrease in signal contribution from subvolumes farther away from the measurement fiber. The subvolumes closest and farthest away from the coupling fiber when measured from the X and Y surfaces of the 3D printed PSD show an approximate 50% decrease signal not observed for the commercial PSD. This indicates that the 3D printed PSDs possess significant self-absorption. This is most likely the result of the tendency of FDM 3D printing to produce opaque objects. This lack of transparency results in the scintillation light produced at the extremities of the volume being reflected or absorbed reducing the amount transmitted to the measurement fiber. It is possible that a reflective coating or optical coupling agent could be employed to improve transparency and increase transmission. The increased variability and larger decrease in signal observed when measuring from the Z surfaces suggests that in addition to the lack of transparency there is also a contribution from the anisotropic behavior discussed in section 4.3. These results indicate that the FDM 3D printing of large volume PSDs may be subject to significant volumetric effects.

3.6.5 Stability, Dose Rate, Dose Linearity and Reproducibility

This investigation presented the experimentally derived dosimetric characteristics of the 3D printed PSDs. Their stability was assessed, and the results indicate that they are capable of highly stable sequential measurements with a standard error of 0.0005. The 3D printed PSDs also exhibit a linear response with dose, as no deviations from linearity greater than 0.38 % were observed. They are also independent of dose rate as the measured dose did not vary more than 0.10 from the mean for any dose rate. Finally, the results indicate that the readings are highly reproducible with the standard error over 14 days of daily irradiations determined to be 0.0136.

3.6.6 Energy Dependence

Consistent with their non-3D-printed counterparts, the 3D printed PSDs exhibit quenching in the kV range. There are many factors that can contribute to variation in signal quantity compared to a non-3D printed sample of the same shape and volume including surface finish and coupling efficacy. At this point, it is not certain if the magnitude of this quenching has been at all affected by 3D printing and will be subject of future work.

3.6 CONCLUSION

In this study, we performed the first comprehensive analysis on the fabrication parameters and dosimetric properties of FDM 3D printed PSDs. Our data show that it is possible to apply additive manufacturing techniques to the fabrication of PSDs. The experimental results indicate that the 3D printed PSDs also share many desirable properties with current commercially available products such as dose linearity, dose rate independence, energy independence in the MV range, repeatability, and stability. We have also demonstrated the presence of anisotropic and volumetric effects with 3D printed PSDs. These results indicate that not only does 3D printing offer a new avenue for the production and manufacturing of PSDs but also allows for further investigation into the application of 3D printing in dosimetry. Such investigations could include options for 3D printed, patient-specific scintillating dosimeters that may be used as standalone dosimeters or incorporated into existing patient devices (e.g. bolus or immobilization) used during the delivery of radiation therapy.

3.7 ADDENDUM

3.7.1 MicroCT Imaging

The optimal performance of any scintillation detector relies on capturing the maximum fraction of emitted light, with the uniformity of light collection usually dependent on interface conditions within the scintillator itself. The quality and resolution of interfaces within a 3D print are primarily influenced by the chosen layer thickness[173]. To assess layer adhesion and quantify any air pockets formed between layers during the printing process, MicroCT scans were conducted using a Bruker SkyScan 1276 MicroCT, with a slice thickness of 0.1 mm. Two samples, printed with identical print parameters to those described in section 3.4.4 except for the layer thickness, were scanned—one with a layer height of 0.6 mm and the other 0.2 mm.

MicroCT investigations suggest that despite the increased print speed associated with thicker layers, they may introduce undesired air gaps. As shown in Fig 3.17, at a layer thickness of 0.6 mm, sizeable air pockets are visible between the layers. Conversely, at 0.2 mm (Fig 3.18) the 3D-printed scintillators appear more uniform with no visible air gaps between layers.

Experimental investigations into the effect of layer thickness (section 3.5.1.2) demonstrated an increase in the measured total relative intensity of a 3D-printed scintillator with increasing layer thickness. We hypothesized that the bulk of the observed effect resulted from a decrease in light scattering due to a decrease in the number of layer interfaces inside the 3D-printed PSD. However, this effect appears to plateau at layer thicknesses of 0.4 mm and higher. The introduction of air gaps at larger layer thickness may contribute to the observed saturation by introducing unwanted scattering of scintillation light.

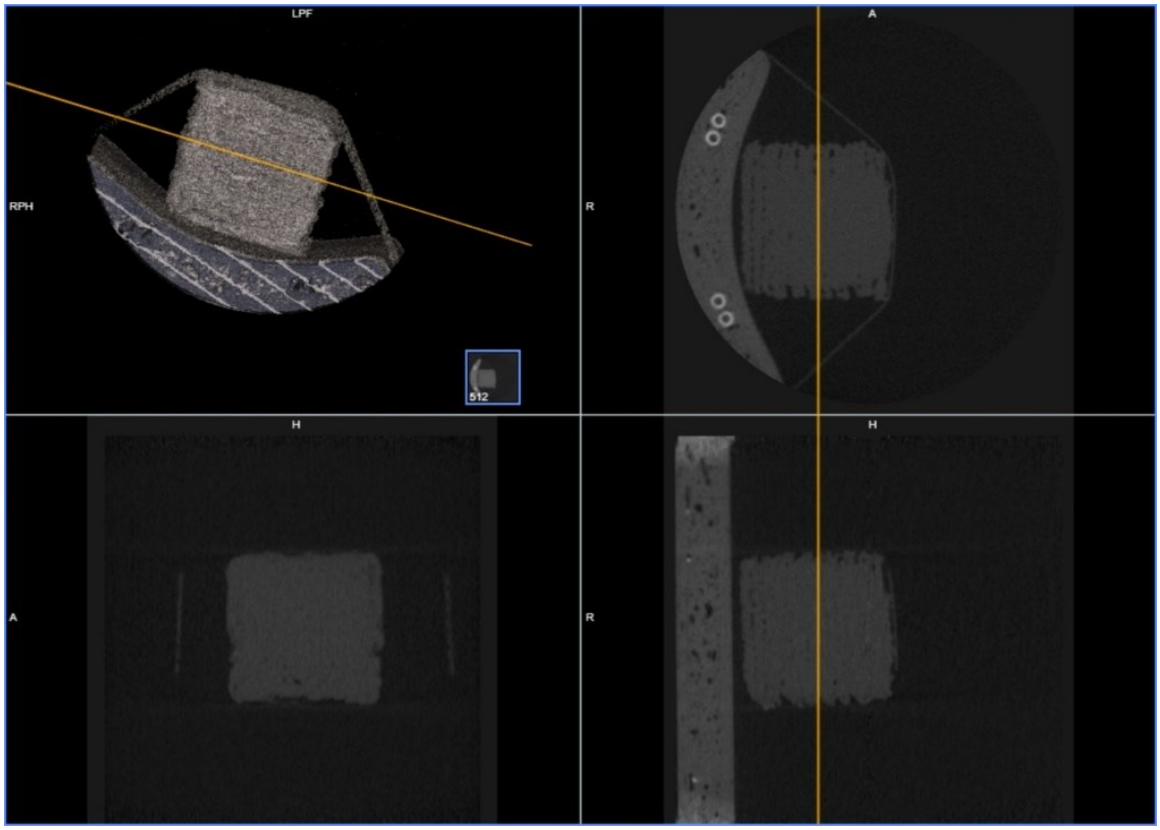

Figure 3.17: MicroCT scan of 1 x 1 x 1 cm^3 3D printed scintillator fabricated using a layer height of 0.6 mm.

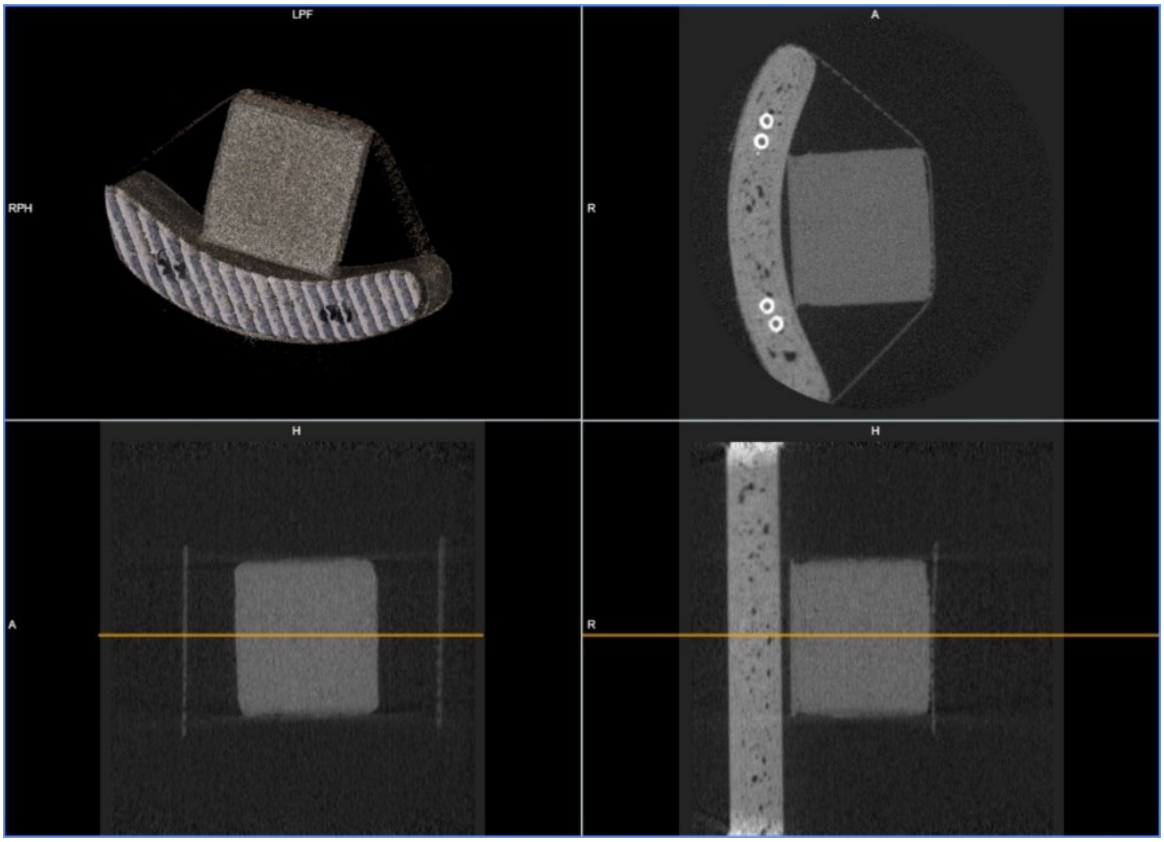

Figure 3.18: MicroCT scan of 1 x 1 x 1 cm^3 3D printed scintillator fabricated using a layer height of 0.2 mm.

CHAPTER 4 MANUSCRIPT 2: CAMERA BASED RADIOTHERAPY DOSIMETRY USING DUAL-MATERIAL 3D PRINTED SCINTILLATOR ARRAYS

4.1 PREAMBLE

This study presents a comprehensive exploration into the development of 3D printed scintillator arrays designed specifically for radiation therapy applications. It introduces a novel methodology for the fabrication of dual-material FDM 3D printed plastic scintillator arrays, marking a significant leap forward in 3D printed detector resolution and quality within the field. This foundational investigation also provides crucial dosimetric insights into the response of 3D printed scintillator arrays to irradiation, along with a rigorous quantification of their dosimetric accuracy against other detectors and simulations. This work constitutes the first distinct step towards the development of high-resolution, custom-designed scintillator arrays for surface dosimetry in radiation therapy. Following the fabrication and dosimetric characterization of various dual-material 3D printed scintillator arrays, I wrote the above publication under the guidance of my graduate supervisors (coauthors). Medical Physics was then selected for publication of this work as it is an international, peer-reviewed journal that publishes high impact, innovative physics and engineering research which possesses a significant potential for clinical translation.

The following chapter has been reproduced with permissions (Appendix A.11) from: "Camera-based radiotherapy dosimetry using dual-material 3D printed scintillator arrays" by Nicholas Lynch, James L Robar, Thalat Monajemi, 2023, *Medical Physics,* 50(3):1824-1842 (https://doi.org/10.1002/mp.16167). Copyright 2023 by John Wiley and Sons. It differs only from the original text in the addition of revisions for additional clarity. This chapter also includes an addendum containing additional data not presented in the original manuscript.

4.2 ABSTRACT

Purpose & Objective

To describe a methodology for the dual-material fused deposition modeling (FDM) 3D printing of plastic scintillator arrays, to characterize their light output under irradiation using

an sCMOS camera, and to establish a methodology for the dosimetric calibration of planar array geometries.

Materials & Methods

We have published an investigation into the fabrication and characterization of single element FDM printed scintillators intending to produce customizable dosimeters for radiation therapy applications[179]. This work builds on previous investigations by extending the concept to the production of a high-resolution (scintillating element size 3 x 3 x 3 mm^3) planar scintillator array. The array was fabricated using a BCN3D Epsilon W27 3D printer and composed of polylactic acid (PLA) filament and BCF-10 plastic scintillator. The array's response was initially characterized using a 20 x 20 cm^2 6 MV photon field with a source-to-surface (SSD) distance of 100 cm and the beam incident on the top of the array. The light signals emitted under irradiation were imaged using 200 ms exposures from a sCMOS camera positioned at the foot of the treatment couch (210 cm from the array). The collected images were then processed using purpose-built software to correct known optical artefacts and determine the light output for each scintillating element. The light output was then corrected for element sensitivity and calibrated to dose using Monte Carlo simulations of the array and irradiation geometry based on the array's digital 3D print model. To assess the accuracy of the array calibration both a 3D beam and a clinical VMAT plan were delivered. Dose measurements using the calibrated array were then compared to EBT3 GAFChromic film and OSLD measurements, as well as Monte Carlo simulations and TPS calculations.

Results

Our results establish the feasibility of dual-material 3D printing for the fabrication of custom plastic scintillator arrays. Assessment of the 3D printed scintillators response across each row of the array demonstrated a nonuniform response with an average percent deviation from the mean of 2.1% ± 2.8%. This remains consistent with our previous work on individual 3D printed scintillators which showed an average difference of 2.3% and a maximum of 4.0% between identically printed scintillators[179]. Array dose measurements performed following calibration indicate difficulty in differentiating the scintillator response from ambient background light contamination at low doses (< 20-25 cGy) and dose rates (≤ 100 MU/min). However, when analysis was restricted to exclude dose values less than 10% of the Monte

Carlo simulated max dose the average absolute percent dose difference between Monte Carlo simulation and array measurement was 5.3% ± 4.8% for the fixed beam delivery and 5.4% ± 5.2% for the VMAT delivery.

Conclusion

In this study, we developed and characterized a 3D printed array of plastic scintillators and demonstrated a methodology for the dosimetric calibration of a simple array geometry.

4.3 INTRODUCTION

3D printing is an additive manufacturing technique uniquely suited to the rapid manufacturing of bespoke or complex end products that would otherwise be difficult, costly, and time-consuming to produce. The lowest-cost and most common 3D printing method is Fused Deposition Modeling (FDM). FDM functions by heating, extruding, and then depositing thermoplastic filaments one horizontal layer at a time to additively produce 3D structures. Currently, it is possible to print using a range of filaments, including those that are carbon fiber-infused, conductive, magnetic, wood-filled, metal-filled, glass fiber reinforced and flexible. This broad range of available materials and the potential of combining their various mechanical/electrical properties into a single 3D printed design makes FDM an attractive option for fabricating patient-specific devices in radiation therapy (RT). 3D printing has already been used for the fabrication of phantoms, immobilization devices, boluses, brachytherapy applicators, and other patient-specific treatment accessories in RT[48]. The use of individualized patient-specific devices has been shown to improve treatment delivery, device conformity, patient comfort and cost-effectiveness while minimizing unnecessary treatment toxicity[48].

Despite numerous beneficial applications of 3D printing in RT and its continued development for the fabrication of miniaturized, low-cost sensors, there has been a sparsity of investigation into its potential to produce radiation detectors[49]. This has been partly due to the challenges encountered when attempting to print designs that incorporate multiple materials with distinctly different properties (insulating/conductive, rigid/flexible, etc.). Even when using commercially designed dual-material FDM 3D printers the quality and consistency of multi-material prints are not guaranteed. Problems with material-material adhesion, material mixing, and clogging of the print nozzles often result in poor print quality, low print success

rates, and reduced dimensional accuracy[50–53]. This is particularly the case when printing with thermoplastic filaments doped with additional materials such as metal, wood, glass, and carbon fiber.

The development of radiation detectors for RT-specific applications may benefit from FDM 3D printing, but this has only been pursued recently. The feasibility of using FDM 3D printing for the fabrication of radiation detectors was initially demonstrated in 2018[54]. A 3D printed drift tube composed of polylactic acid filament (PLA), P5 gas (95% Argon, 5% Methane) and a stainless-steel anode was used for the detection of cosmic ray muons. While the 3D printed detector was not fully composed of 3D printed parts it established FDM 3D printing as a potential avenue for radiation detector development.

In 2019, FDM 3D printing was used to produce a planar ionization chamber array using conductive polylactic acid (cPLA) and insulating components made of acrylonitrile butadiene styrene (ABS)[52]. The array possessed a spatial resolution of 5 x 7 mm^2 and had a detector volume of 96 mm^3. The rectangular array elements delivered comparable performance (within 2%) to a PTW diode detector under reference conditions. Continued development has improved array spatial resolution to 4 x 4 mm^2 and reduced detector volume to 28 mm^3 [55].

Finally, a CERN led international collaboration (CERN EP-Neutrino group) has also been working on developing FDM 3D-printed scintillators for use in neutrino detection at the T2K experiment. In 2020, the group demonstrated a novel FDM 3D printed polystyrene-based scintillator[70]. By doping polystyrene with 2% by weight of p-terphenyl, 0.05% by weight of POPOP and 5% by weight of the plasticizer biphenyl they produced a flexible plastic scintillating filament for use in FDM 3D printing. While not yet published at the time of writing, in March of 2022 the CERN EP-Neutrino group posted a preprint on arXiv demonstrating a 3 x 3 matrix of plastic scintillator cubes (1 cm^3) optically separated by a white reflector material that had been entirely FDM 3D printed[180].

Recently our group has published the first example of characterizing an FDM 3D printed scintillator produced using a commercially available scintillating fiber[179]. We demonstrated that these 3D printed scintillators shared many desirable properties with their commercial counterparts such as dose linearity, dose rate independence, energy independence in the MV range, repeatability, and stability. This work builds on the previous publication by integrating

techniques learned from 3D printing individual scintillating elements into the production of multi-element scintillating arrays and their wireless measurement using an sCMOS camera.

The long-term goal of this work is to develop a patient specific detector that will fulfill the unmet clinical need for accessible, routine, and real-time *in-vivo* dosimetry for patients undergoing radiotherapy[7,19]. The proposed detector system (Fig 4.1) consists of an array of plastic scintillators, produced using 3D printing, that conforms closely to the skin surface of the patient. During treatment, the array will emit light in response to receiving energy from the radiation beam. The emitted pattern of light will be read out by a stereoscopic pair of sCMOS cameras mounted at the foot of the treatment couch. With appropriate dosimetric calibration, the light output of the array can be related to the dose received by the patient and compared to the planned dose distribution.

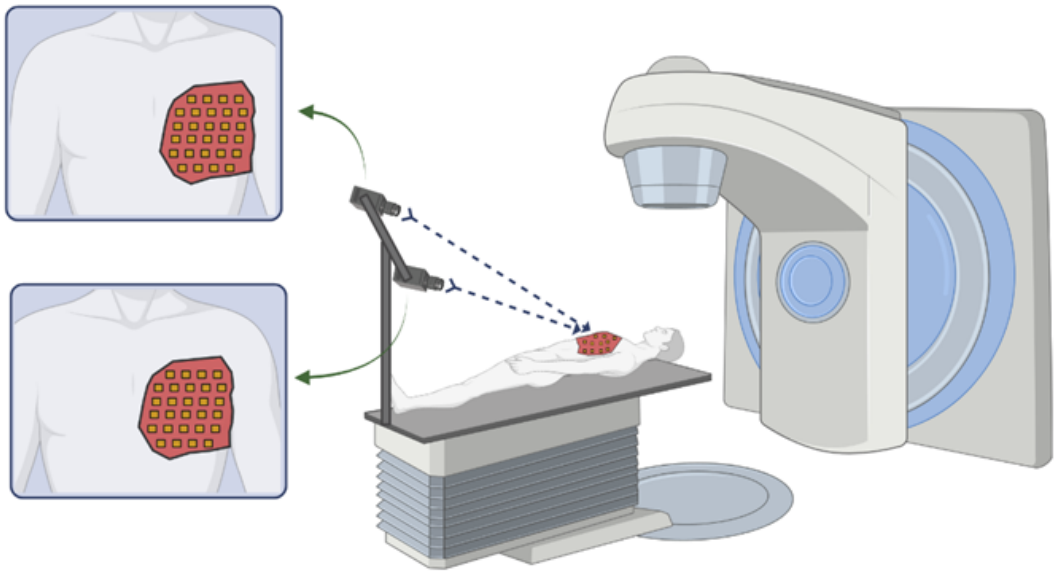

Figure 4.1: Schematic drawing of the skin-surface scintillator conforming to the patient surface with a stereoscopic camera system positioned at the foot of the treatment couch.

4.4 MATERIALS AND METHODS

4.4.1 Scintillator Array Fabrication

The scintillator arrays were fabricated using thermoplastic (PLA) and non-cladded BCF-10 scintillating fiber (Saint Gobain Crystals, Ohio, USA) both with a diameter of 3.0 mm. The 3D printer used for the manufacturing of the scintillator arrays was the Epsilon W27 (BCN3D

Technologies, Barcelona, Spain) which was specifically selected due to its Independent Dual Extruder (IDEX) design. In contrast to conventional dual extrusion printers which move both extruders together the IDEX design uses independently moving extruders (Fig. 4.2). While not strictly required, the IDEX design offers two distinct advantages over standard dual material 3D printers, that is, decreased material cross contamination and reduced printer head mass.

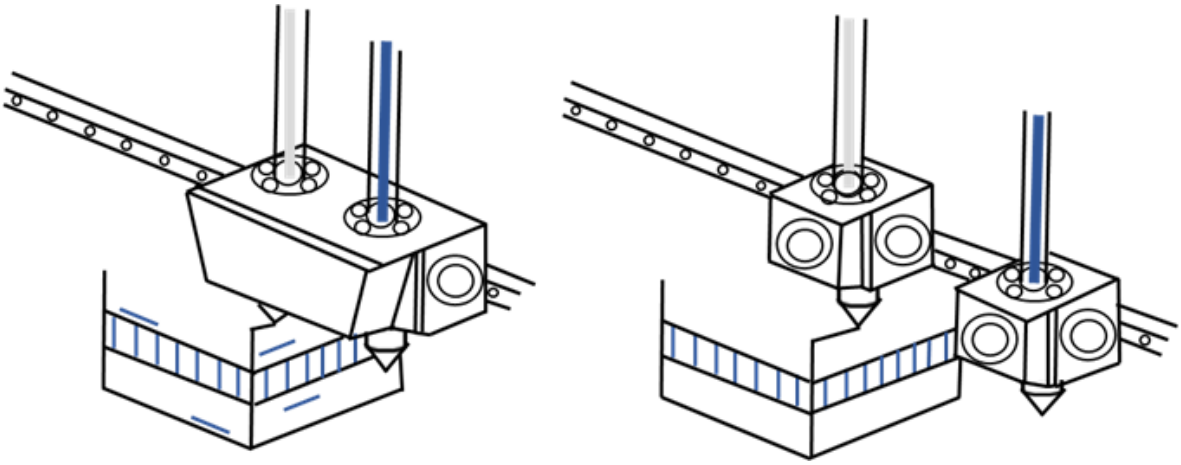

Figure 4.2: Diagram of a standard dual material extrusion system compared to IDEX illustrating material cross contamination caused by the unused nozzle oozing onto the printed part.

Material cross-contamination is of primary concern during scintillator array fabrication as it can result in occluded scintillators with poor light output and occurs as the unused nozzle oozes onto the printing array[180]. This can be mitigated at the expense of print time by using a combination of aggressive filament retractions and printing either a prime tower or adding a waiting period between material changes at a location far away from the print. However, it is challenging to eliminate and initial iterative investigations using the conventional dual extrusion printers available in our department (AirWolf Axiom 20 and the LulzBot Taz 6) were unsuccessful.

The second advantage of the IDEX design is the reduced printer head mass which improves the printer's dimensional accuracy. Standard dual extrusion systems use direct drive extrusion where the extruder is mounted on the printer head and pushes the filament directly into the heated nozzle. While offering greater control of the filament the high mass of the two print heads leads to reduced print accuracy when printing smaller objects with many quick changes in print head direction. Conversely, the Bowden extrusion system used by the BCN3D

W27s is situated at the back of the printer and pushes/pulls filament through a long polytetrafluoroethylene (PTFE) tube and into the heated print nozzle. This separates the extruder from the print nozzle allowing for faster prints and improves the print quality of small objects.

While the IDEX design is advantageous, the above does not preclude the use of other dual material 3D printers for the fabrication of scintillator arrays. Using a combination of precise printer calibration and the cross-contamination mitigation strategies previously outlined it may still be possible to fabricate scintillators arrays of sufficient quality using standard dual material 3D printers. However, in our experience only when using the IDEX design were arrays of sufficient quality and consistency able to be produced with relative ease.

In addition to the 3D printer used, the proper selection of material-specific print parameters is critical to achieving consistent scintillator array print quality. Material parameters for both the PLA and scintillating filaments were informed by our previous work and iterative testing[179]. Arrays were printed using a nozzle size of 0.4 mm, layer thickness of 0.1 mm, 100% infill density and a build plate temperature of 65°C. The PLA was printed using a print temperature of 195°C, line-based infill pattern and a print speed of 35 mm/s with retractions enabled.

Unlike PLA, we have found that additional scintillator-specific print settings are required to prevent jamming, significant warping, and poor adhesion of the scintillating filament during the printing process. Due to its elasticity, the heated scintillating filament tends to stretch inside the extruder mechanism when retracted from the print nozzle. Additionally, the scintillator exhibits poor adhesion to the PLA material until cooled. Therefore, if the scintillators are printed too quickly or if the infill pattern exhibits many changes in direction the print quality of the resulting scintillator is degraded due to lack of adhesion. As a result, the elimination of retractions, reduction of print speed, and a concentric infill pattern are recommended to mitigate issues with jamming and to ensure adhesion of the scintillator to the PLA. Due to the above considerations, the scintillator was printed at 210°C, a print speed of 10 mm/s with a concentric printing of infill and retractions disabled.

To demonstrate the feasibility of dual-material 3D printing for the fabrication of scintillator arrays, a planar scintillating array was designed. Using computer aided design (CAD)

software the array was modeled as two separate components, a body composed of PLA with gaps and a corresponding set of scintillating elements. Both components were then imported into the CURA slicer software and combined. CURA then slices the merged model according to the defined print parameters and produces a set of 3D printer instructions (g-code) used to print the planar array. As shown in Fig. 4.3, the 3D printed planar array has dimensions of 3 mm (thickness) x 125 mm x 125 mm with 133 scintillating elements. A single printed scintillating element has a volume of 27 $mm^{3,}$ (3 x 3 x 3 mm^3) and elements are separated by 6 mm of PLA (resulting in a 9 mm center-to-center spacing of scintillating element).

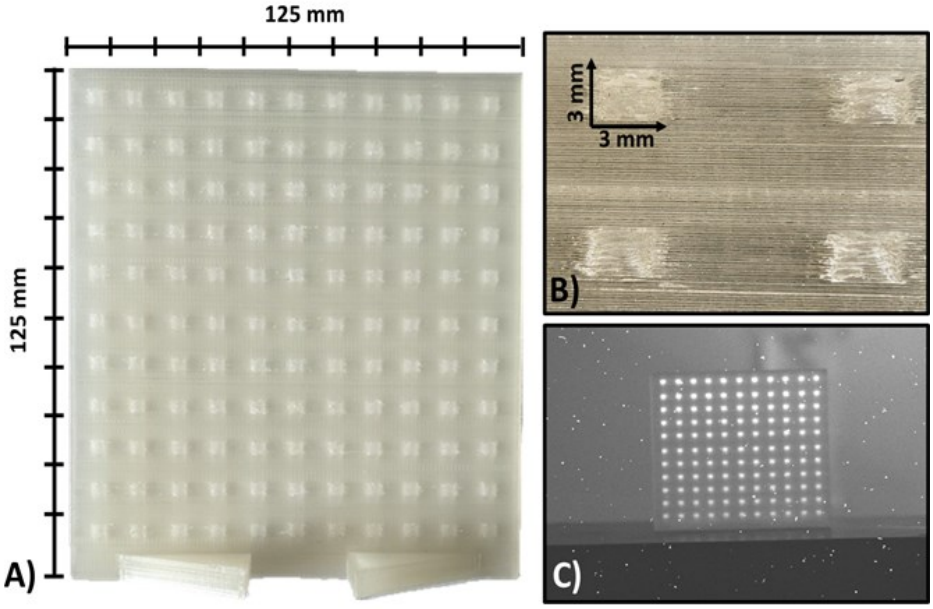

Figure 4.3: Images of dual-material 3D printed planar scintillator array, **A)** planar array, **B)** close-up of scintillating array elements and **C)** planar array irradiated by 6 MV X-rays.

In this case, due to its geometry, it was advantageous to print the array vertically on the build plate without the use of support structures. While not strictly required, in our previous work we found that changes in the print temperature of the scintillators demonstrated a marked effect on the resulting light output. We hypothesized that thermal degradation of the polymer was responsible[179]. Printing vertically prevents the scintillators from being in contact with the heated build plate for the duration of the printing process limiting prolonged heating of the scintillators and potential reduction in light output.

Following fabrication, initial testing showed that the color of the PLA used has a demonstrable effect on the total light output of the resulting scintillator array. Arrays fabricated using white and clear PLA produced greater signal compared to other darker colors, with clear PLA producing the greatest signal. As a result, for this investigation we have chosen to work with clear PLA despite it not being an optically isolating material. Arrays fabricated from clear PLA also have the potential future clinical benefit of allowing the array to be more easily positioned on the patient using tattoo markers, not unlike what is already done in the case of a radiotherapy bolus.

4.4.2 Planar Array Response

Prior to irradiation, the planar array was placed vertically on a 10 cm slab of solid water with additional solid water placed behind it to provide backscatter (Fig 4.4). The array's response was characterized using a 6 MV photon field (Truebeam, Varian Medical Systems, Alto, USA) delivered with gantry and collimator angles of 0 degrees, 200 Monitor Units (MU), field size of 20 x 20 cm^2, dose rate of 600 MU/min, and source-to-surface (SSD) distance of 100 cm with the beam incident on the top of the array.

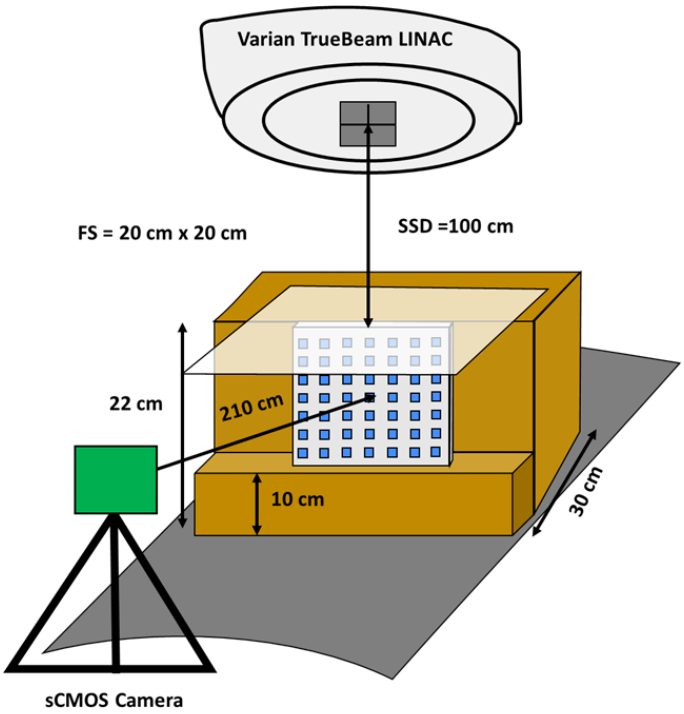

Figure 4.4: Diagram of array irradiation geometry illustrating the positioning of the sCMOS camera.

The response of the planar array under irradiation was imaged using an unshielded 16-bit pco.panda 4.2 monochrome sCMOS camera (PCO Photonics Ltd., Ontario, Canada) positioned at the foot of the treatment couch using a tripod (210 cm from the array). The camera was equipped with a 50 mm F/1.8 manual focus lens and aligned perpendicular to the array surface. The image sensor possesses a pixel size of 6.5 x 6.5 μm^2 and a total of 2048 x 2048 pixels.

Finally, a camera sampling rate of 5 frames per second (FPS) was selected for imaging as it represents the highest practical acquisition rate given the current limitations of the acquisition system. While the maximum sampling rate of the sCMOS camera is 40 FPS, the USB-C data transfer interface allows a data bandwidth of ~450 MB/s and depending on the chosen sampling rate, the camera can record several GBs of image data in only a few seconds. Therefore, for the purposes of this investigation the images were collected, downloaded, and then stored as 16-bit TIFF files for later processing following image acquisition. While the long-term goal of this work is real-time *in-vivo* measurement of dose for patients undergoing radiotherapy additional modifications to the current camera-computer interface will be required to overcome these challenges and will be the subject of a future investigation. In particular, we anticipate the need of an external high-speed serial computer expansion bus (PCI-E), USB range extension system and external triggering of the camera using coaxial cables to enable efficient implementation of real-time data acquisition.

4.4.3 Image Processing

To accurately relate the measured light output of the individual scintillating elements to dose the raw images must first be corrected for various optical artefacts. Optical artefacts result from a combination of sensor and lens-based artefacts. These include sensor noise, background light contamination, stray radiation, vignetting, and lens distortion (Fig.4.5). These artefacts and their subsequent correction methods have been discussed in detail by other groups and are summarized briefly here[79,81,82].

Initially, dark images (no light, no radiation) and background images (light with no radiation) are collected prior to irradiation. The median dark and background images are then subtracted from each of the raw images.

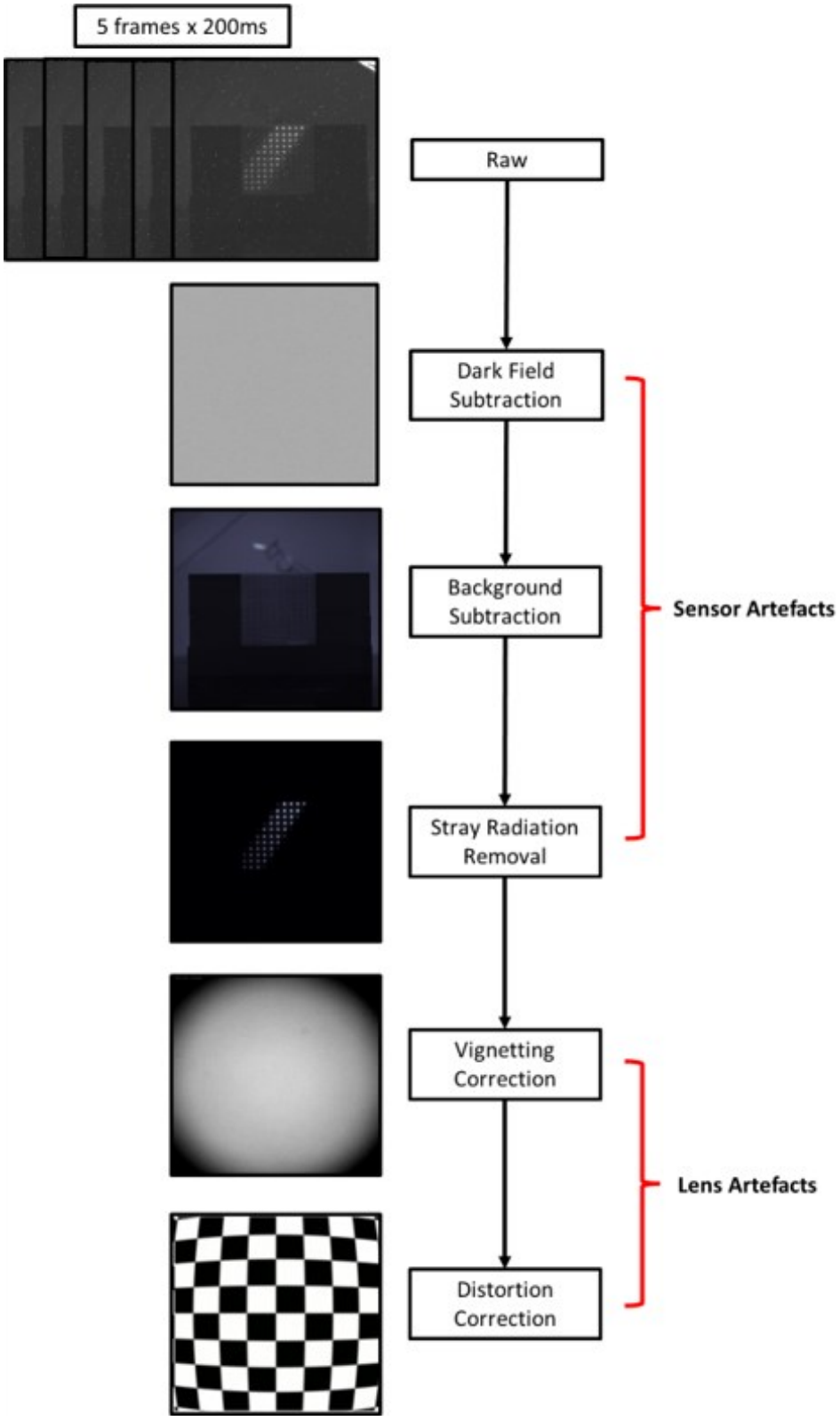

Figure 4.5: Image processing stream illustrating the removal of the various optical artefacts from the raw camera images.

A vignetting correction is then applied by dividing the processed images by a flat-field image. This correction accounts for variation in pixel-to-pixel sensitivity and the brightness reduction which occurs near the image's periphery due to occlusion by the camera aperture. The flat-field image is acquired by imaging a uniformly illuminated surface. In this case, we used the light from a flat-screen LCD computer monitor diffused by a white sheet of paper[181].

Following vignetting correction, lens distortion effects resulting from the optical design of the 50 mm camera lens were corrected for using the Camera Calibration function of the MATLAB Computer Vision Toolbox[164]. This correction accounts for the slight deformation of straight lines that occurs near the periphery of the image. The calibration is performed using multiple images of a planar calibration pattern (checkerboard) with known dimensions[163]. By acquiring images at different distances, angles, and positions relative to the optical axis of the camera the resulting distortions can be modeled by comparing the calibration pattern dimensions in each image to its known dimensions[182].

Finally, to remove stray radiation, a rolling temporal median filter is then applied. Temporal median filtering is the preferred method for stray radiation removal as it guarantees that pixel values falling far outside the norm (in this case, transient noise from stray radiation) will be removed from the final processed images[81]. Beginning with the first image, the temporal filter takes five consecutive images (1 s of data) and computes a median image. It then increments to the second image, performs this operation again, and continues iteratively until all the collected images are filtered.

Perspective-based artefacts resulting from differences in the radial distance of each scintillating element to the camera were not examined. There is less than a 0.1% difference between the minimum and maximum radial distances when imaging the planar array in the irradiation geometry. However, such perspective-based artefacts are not negligible in the case of nonplanar array geometries or when acquiring images at angles that are not perpendicular to the array surface. Mitigating these geometric and perspective-based artefacts as they concern the measurement of non-planar array geometries will be the subject of future investigation and is discussed further in section **IV.B**.

4.4.4 Data Processing

Following the correction of optical artefacts, the processed images (~100–600 images depending on the type of dose delivery) are added together to produce a final image representing the entire dose delivery as shown in Fig 4.6. A). As the signal produced by the scintillating array elements is substantially higher than the remaining background following processing, a binary image mask can be produced using a grayscale level (GSL) threshold. The binary image mask is analyzed using MATLAB Blob Analysis to identify the center of each scintillating element in the mask and image (Fig 4.6. B)). The light output for each element is then determined by calculating the total light output in GSL of a 25 x 25-pixel window (known pixel dimensions of the printed scintillators) positioned at the center of each element.

4.4.5 Dosimetric Methods

Independent measurements using EBT3 GAFChromic film in addition to Monte Carlo simulations and Eclipse Treatment Planning System (TPS) calculations were performed at all stages. Supplementary point dose measurements were also performed using optically stimulated luminescence dosimeters (OSLDs).

4.4.5.1 GAFChromic Film

To account for the dose variation across the 3 mm thickness of the array, GAFchromic film measurements were performed by placing pieces of film on both the front and back surfaces of the planar array. Following irradiation, the films were scanned using an Epson 10000XL optical scanner. The measured optical density was then converted to dose using a calibration curve generated by exposing strips of film (~3 cm x 20 cm) to doses ranging from 0 cGy to 500 cGy in intervals of 50 cGy at a dose rate of 600 MU/min. The film strips were positioned at the center of a 10 x 10 cm^2 6 MV photon field at 95 cm SSD and 5 cm depth. Following the generation of the calibration curve, triple-channel radiochromic film dosimetry was performed using the FilmQApro (Ashland, New Jersey, United States) software[183].

4.4.5.2 Optically Stimulated Luminescence Dosimetry

As a means of verifying dose at discrete locations, point dose measurements were performed using nanoDot OSLDs (Landauer, Illinois, United States) adhered to the front of the planar array. After irradiation the stored charge was read out for each OSLD using a

microStar OSLD slide reader (Landauer, Illinois, United States). The stored charge was then converted to dose using a calibration curve generated by exposing OSLDs from the same vendor shipment to doses of 0 cGy, 50 cGy, 150 cGy and 300 cGy at a dose rate of 600 MU/min. For these calibration exposures, OSLDs were positioned at the center of a 10 x 10 cm^2 6 MV photon field at 95 cm SSD and 5 cm depth.

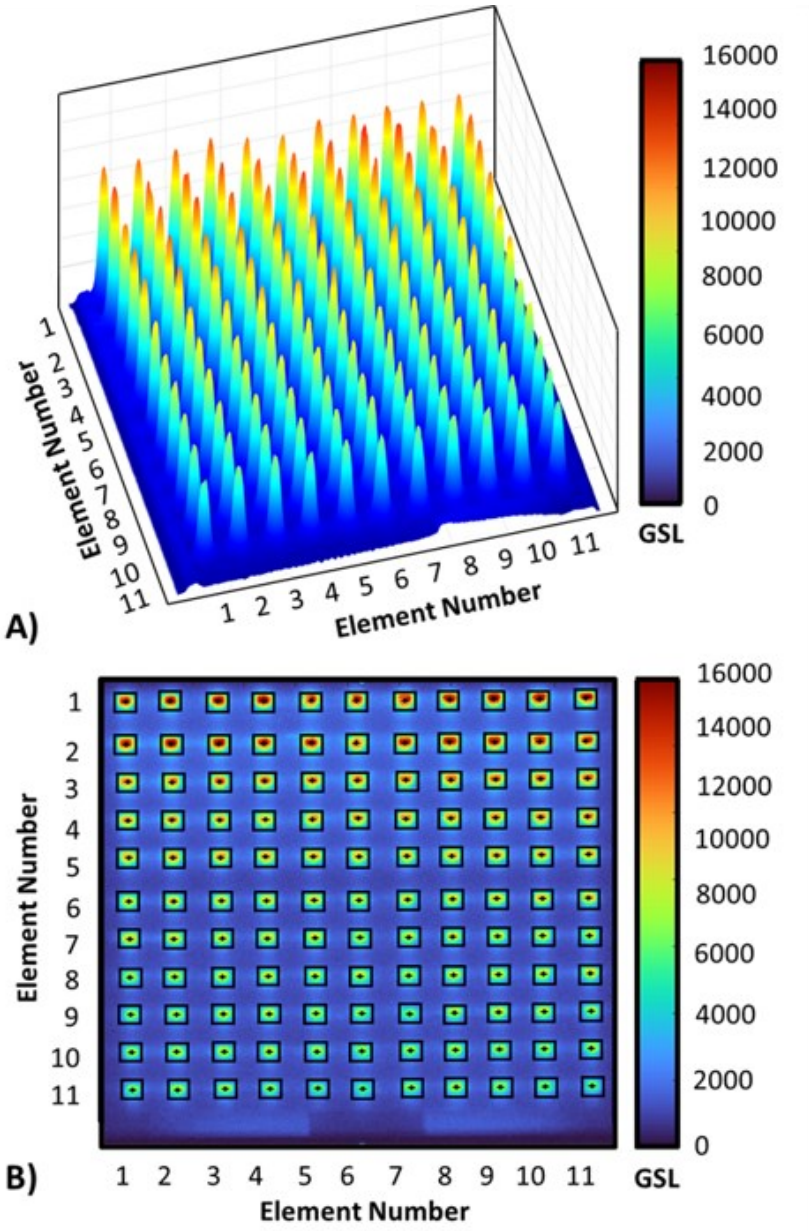

Figure 4.6: A) Final image of planar array following irradiation (geometry illustrated in Fig. 4.4) corrected for all optical artefacts, **B)** identical image of planar array illustrating the detected locations of all scintillating elements.

4.4.5.3 Eclipse Treatment Planning

While the dose calculation algorithms used by modern TPS are considered accurate, it is well known that modern RT treatment planning systems do not accurately predict dose in the superficial layers of skin or in the presence of large inhomogeneities[13]. In comparison, Monte Carlo simulations, which determine the dose stochastically from first principles, should be accurate under these conditions. However, the TPS is the principle means by which patient treatment plans are generated and the standard by which most traditional *in-vivo* detectors are compared to when employed clinically for dosimetric verification. Therefore, for completeness, both TPS calculations and Monte Carlo simulations were employed in the process of characterizing the planar array's response.

To leverage existing *a priori* information, the CAD model of the array used by the 3D printer was also used to generate a synthetic geometry for both TPS calculations and Monte Carlo simulations. This was accomplished by first reconstructing the calibration geometry (array and solid water) in the CAD modeling software. The resulting model of the calibration geometry was then segmented into a series of 121 slices with voxels sizes of 1 mm x 1 mm x 3 mm using the automated segmentation tools provided by the open-source image processing software 3DSlicer[184]. The Hounsfield units of each voxel in the model were then assigned using the 3DSlicer masking tool. A value of -1000 HU (0.001 g/cm^3) was used for air, 0 HU (1.00 g/cm^3) for water, 50 HU (1.05 g/cm^3) for the BCF-10 scintillator (polystyrene) and 400 HU (1.25 g/cm^3) for PLA. Following masking, the segmented model was exported from 3DSlicer as an RT-DICOM file for use in simulations.

Calculations were performed using the Eclipse TPS (Varian Medical Systems, Palo Alto, USA), Acuros AXB algorithm version 15.6.06, with a dose calculation grid of 2 mm. The volume of each scintillator was manually contoured, and the mean dose was extracted from the corresponding dose-volume histograms following dose calculation.

4.4.5.4 Monte Carlo Simulations

Monte Carlo simulations were performed using a Varian Truebeam 6 MV phase space file scored above the accelerator jaws and the PRIMO Monte Carlo software[133] . The Monte Carlo simulations were performed using $1.4 * 10^{11}$ histories, yielding an average dose uncertainty of ± 2%. Simulations were calibrated from eV/g to dose in cGy by simulating a set of reference

conditions (6 MV, 95 SSD, 10 x 10 cm^2, 5 cm depth, large water phantom) in both the TPS and PRIMO. Following dose calibration, PRIMO simulations were benchmarked using PDD and dose profile distributions of 10 x 10 cm^2 and 40 x 40 cm^2 reference fields. PRIMO simulations showed gamma analysis (2%/1 mm) pass rates of 99.8% and 96.8%, respectively, compared to TPS.

Plan specific parameters, including the planning geometry, dose delivery method, field arrangement and multileaf collimator (MLC) positions were all directly exported from the TPS and imported into PRIMO. In all cases, following completion of the simulation, the dose plane corresponding to the array was then exported from PRIMO for analyses. Using MATLAB, the ROIs corresponding to each scintillator were localized in the dose plane using a scintillator only image mask. The mask was derived from thresholding the corresponding slice of the RT-DICOM used for simulation for the scintillator's known HU value of 50. The mean dose for each scintillator was then calculated from each ROI.

4.4.6 Planar Array Dose Calibration

Array calibration was performed under identical conditions to those described in section **4.4.2.** Manual image registration was performed prior to array measurements using cone beam computed tomography (CBCT) to ensure array alignment with TPS and Monte Carlo simulation geometry.

Each scintillating element of the array was then calibrated to dose for future measurements using a unique calibration coefficient C_{cal} determined from the following relationship:

$$S_M \times C_{cal} = S_M \times \left(\frac{D_{Cal}}{S_{Cal}}\right) = D_M$$

Where S_M is the corrected total light output of a given scintillator in GSL, S_{Cal} is the corrected total light output of the same scintillator in the calibration geometry in GSL, D_{Cal} is the corresponding dose in cGy determine by Monte Carlo simulation in the calibration geometry and D_M is the final dose measurement in cGy.

4.4.7 Dose Rate Dependence

While our previous work focused on the characterization of the fundamental dosimetric properties of 3D printed scintillators, in that work the primary acquisition system consisted of

an optical fiber coupled to a spectrometer[179]. As our long-term goal is the wireless real-time measurement of dose using sCMOS cameras, unlike with the spectrometer the dose distribution must be sampled incrementally during dose delivery. To assess the effect of the chosen camera sampling rate of 5 FPS, a known dose of 40 MU was delivered at low dose rates of 10, 20, 40, 60, 80 MU/min and high dose rates of 100 to 600 MU/min (intervals of 100 MU/min).

4.4.8 Repeatability

To determine the total variation present in repeat measurements of the planar array and to examine the short-term, daily reproducibility of the measurement set-up two calibration irradiations were performed consecutively each day for a period of 3 days.

4.4.9 Multiple Static Field Delivery

To assess the accuracy of the array calibration 200 cGy was delivered to a common field isocenter using four 6 MV photon fields with arbitrarily chosen MLC apertures. The isocenter was positioned at the top center of the array (Fig. 4.7 A) with field-specific parameters summarized in Table 1. The camera and array were set up and positioned relative to each other as described in **4.4.2.**

Field	**MLC**	**Gantry Rotation**	**Collimator Rotation**	**Field X (cm)**	**Field Y (cm)**	**SSD (cm)**	**MU**
1	Static	0°	0°	9.8	6.6	100	102
2	Static	315°	0°	13.6	6	100	99
3	Static	45°	0°	10.3	5.7	100	100
4	Static	270°	0°	14.2	5.9	94.2	83

Table 4.1: Summary of field-specific beam parameters used for multiple static field dose delivery.

4.4.10 VMAT Delivery

To assess the ability of the calibrated array to measure a clinical dose distribution a three-arc VMAT plan was delivered using 6 MV photon fields to a common field isocenter. The isocenter was positioned at the center of the array (Fig. 4.7 B) with field-specific

parameters summarized in Table 2. The camera and array were set up and positioned relative to each other as described in **II.B**.

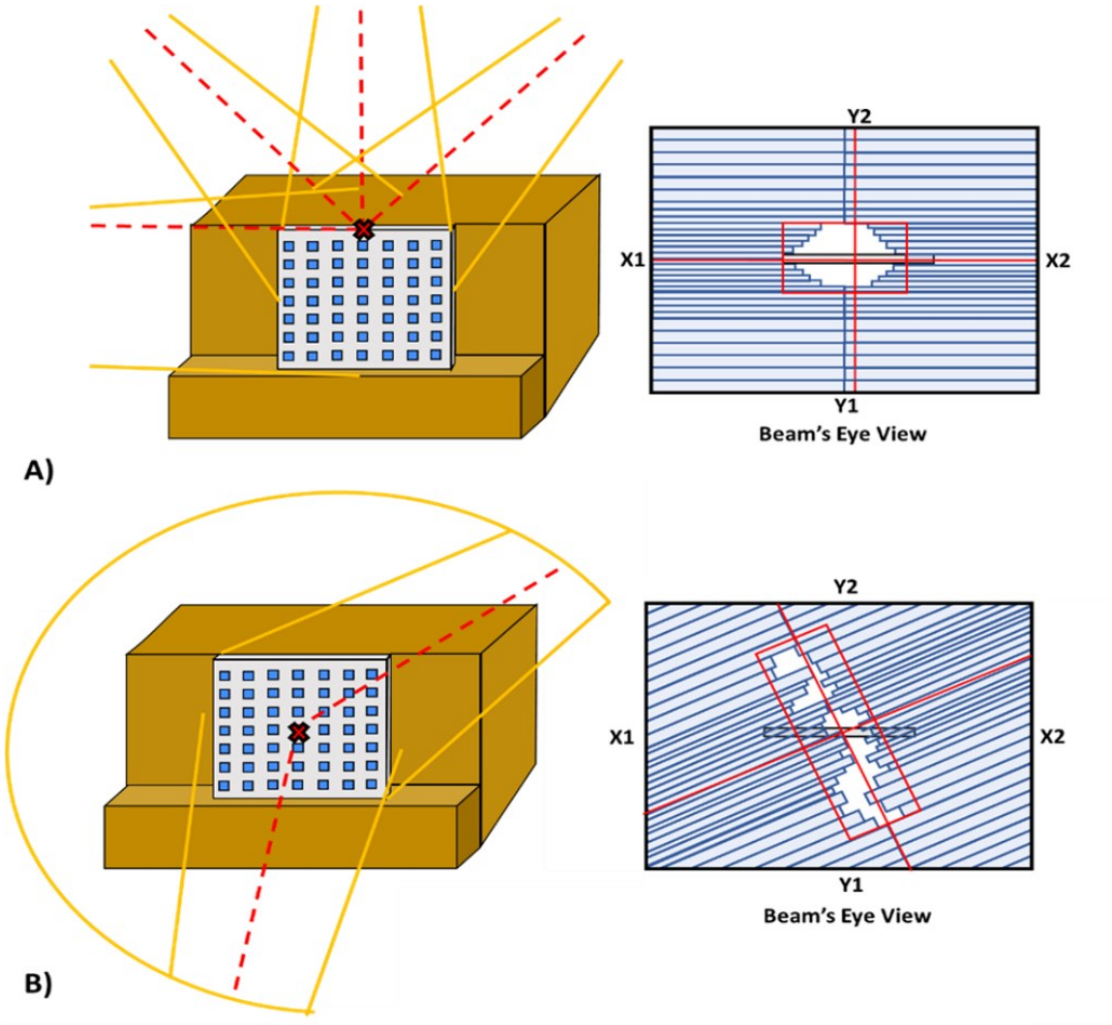

Figure 4.7: Illustration of array geometry, field arrangement, and MLC apertures for **A)** multiple static field delivery and **B)** VMAT. Location of field isocenter marked with red X.

The chosen MLC pattern corresponds to that used in treatment of a patient at the right post-mastectomy chest wall. The planned dose was recalculated on the array calibration geometry using Acuros version 15.6.06. The original prescription dose was 4000 cGy in 15 fractions. Once recalculated on the array geometry the dose in the high-dose region correlated to ~50% - 90% of the original prescription dose.

Field	MLC	Gantry Rotation	Collimator Rotation	Field X (cm)	Field Y (cm)	SSD (cm)	MU
CW	VMAT	195° CW 50°	15°	18.8	26	88.3	258
CCW	VMAT	50° CCW 195°	345°	18.7	26	91.9	245
CW1	VMAT	195° CW 50°	85°	18.8	23	88.3	262

Table 4.2: Summary of field-specific beam parameters used for VMAT dose delivery.

4.5 RESULTS

4.5.1. Array Simulations

The Monte Carlo simulated dose distribution based on the CAD model is shown in Fig. 4.8 and compared with AXB and film. Dosimetric measurements performed using GAFChromic film depict dose variation across the 3 mm thickness of the array. These measurements provide a broad dose envelope, and the average value of the two films (front/back) compares favorably with both Monte Carlo simulation and TPS calculation.

4.5.2 Planar Array Dose Calibration

Analysis of the measured light output of the scintillating array elements indicates that they exhibit a non-uniform sensitivity prior to dose calibration as shown in Fig 4.9 B. Assessment of the 3D printed scintillators response across each row of the array resulted in an average percent deviation from the mean of 2.1% ± 2.8%. Following calibration, the resulting element specific calibration coefficients (Fig 4.9 D) showed an average value of $1.848*10^{-5}$ cGy/GSL ± $9.222*10^{-7}$ cGy/GSL. The minimum value of a calibration coefficient was $1.675*10^{-5}$ cGy/GSL, with a maximum value of $2.143*10^{-5}$ cGy/GSL.

4.5.3. Dose Rate Dependence

The relationship between dose rate and the total light output was consistent across all 133 scintillating elements. The array elements were determined to be dose rate independent from 200 MU/min to 600 MU/min with an average percent deviation from the mean response of 1.65% ± 0.9%. However, at dose rates at or below 100 MU/min, an increasing under response was observed (Fig 4.10). Below 10 MU/min, the scintillator response becomes indistinguishable from the background and results in recorded values of 0 cGy.

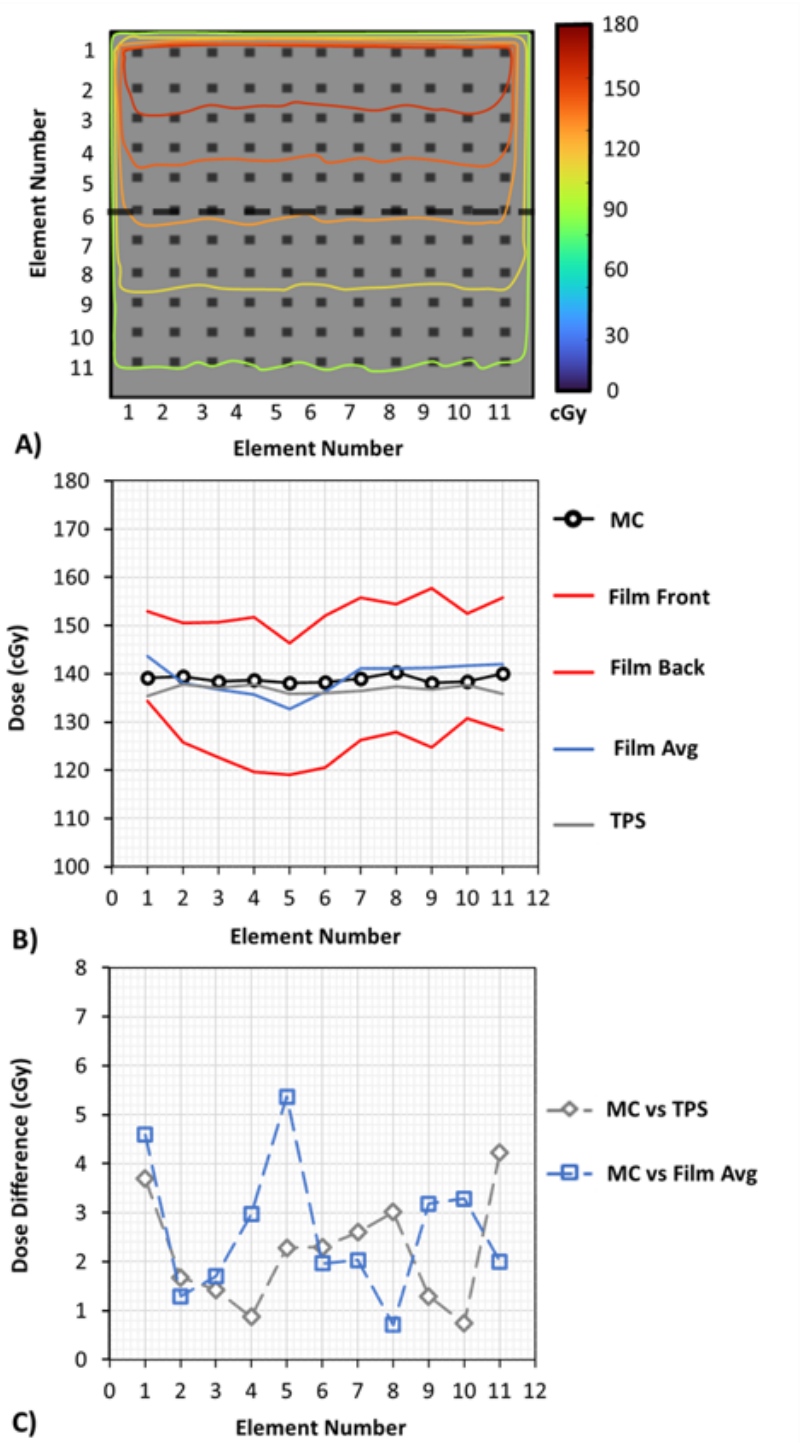

Figure 4.8: A) PRIMO simulated dose distribution with simulation geometry based on the 3D printer CAD model. **B)** Comparison of profiles (dashed line) for TPS calculations, film measurements and PRIMO-based simulations. **C)** Difference plot of each method and Monte Carlo simulation. Profile error bars not visible for Monte Carlo (± 2%).

4.5.4 Repeatability

As shown in Fig 4.11, the response of the central axis 11 array elements compared to their corresponding mean response over the 6 irradiations shows an average absolute percent difference of 0.8% ± 0.6% with no individual deviation greater than 3.00%. When this metric is calculated for the entire planar array the average absolute percent difference between an element's response and its mean response is 1.4% ± 0.5%. Therefore, provided care is taken to reproduce the camera placement and irradiation geometry the camera acquisition system and image processing stream are capable of yielding highly repeatable measurements.

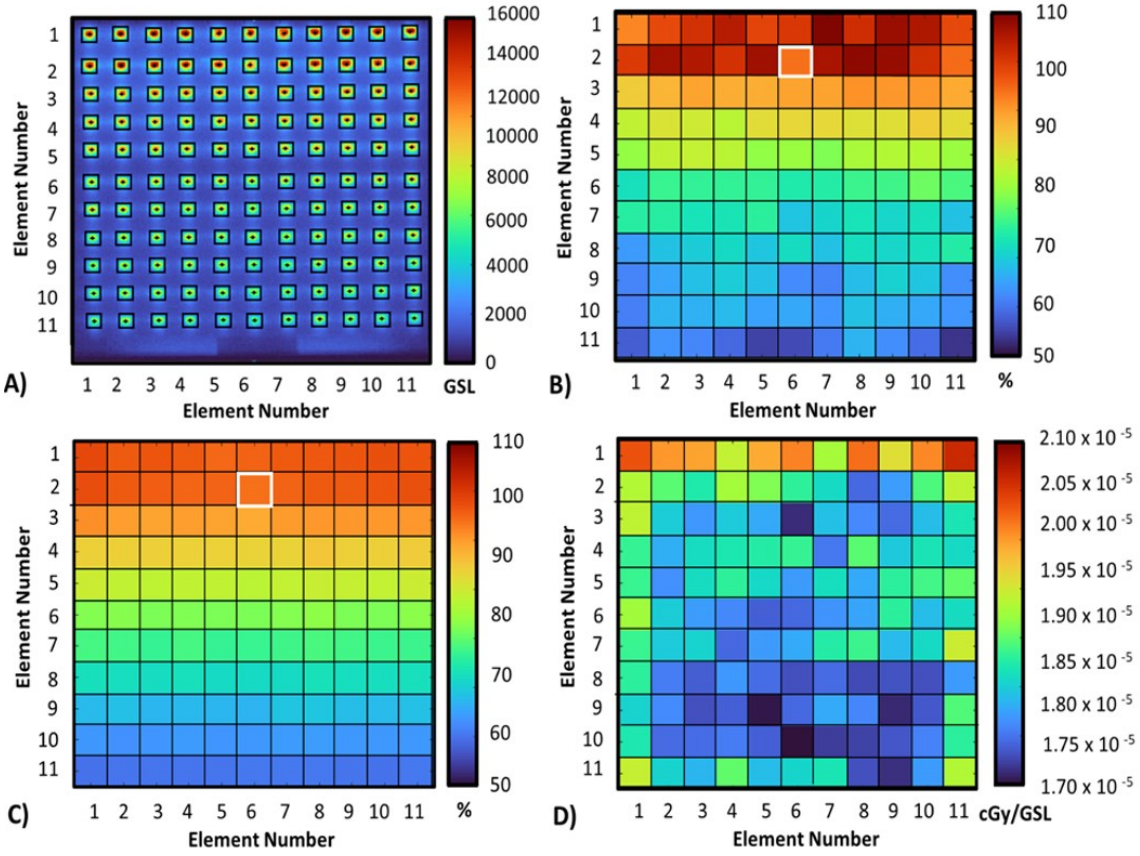

Figure 4.9: A) Corrected image of the planar array calibration illustrating the detected locations of all scintillating elements, **B)** extracted total light output for each array element normalized to the response at element 2 x 6 (outlined in white), **C)** normalized Monte Carlo simulated dose and **D)** calculated calibration coefficients for each array element.

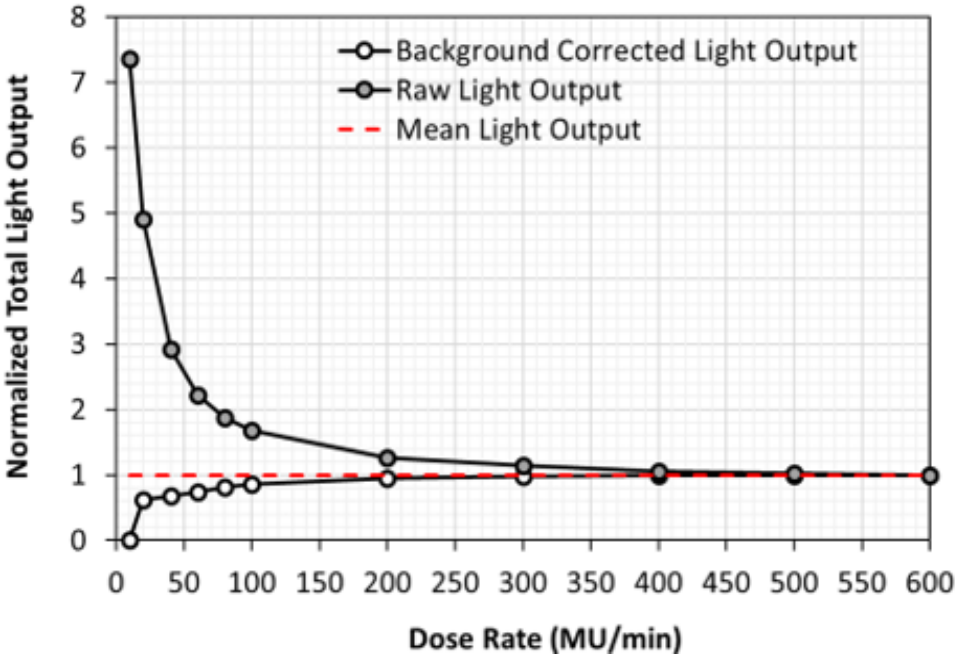

Figure 4.10: Average total light output of all 133 array elements as a function of dose rate normalized to the response at 600 MU/min. The total light output with and without background correction are provided to illustrate the exponentially increasing discrepancy with decreasing dose rate. Profile error bars not (± 0.9%).

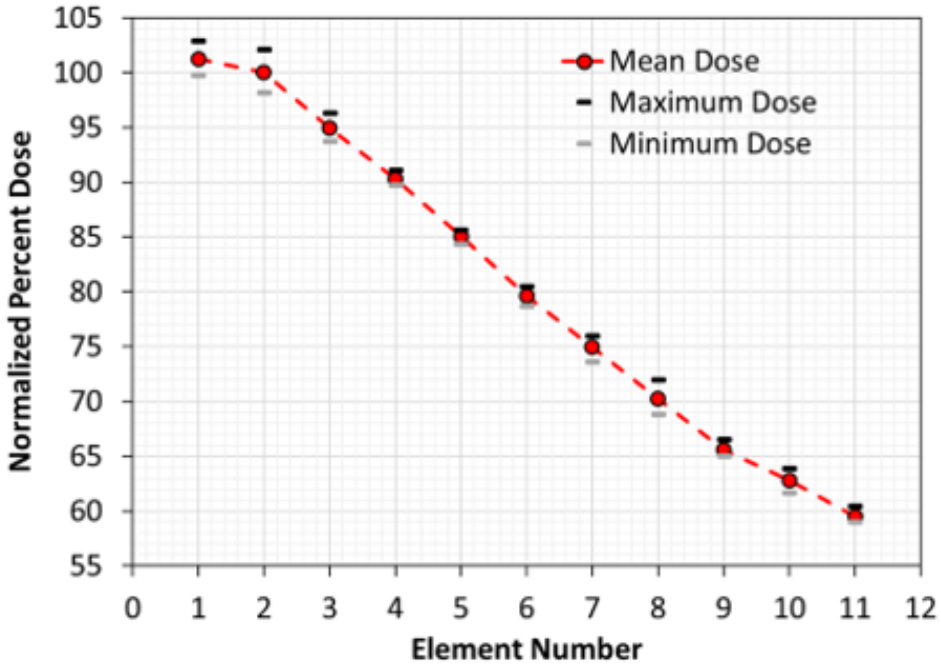

Figure 4.11: Average dose measured along the central axis 11 array elements over 6 consecutive irradiations. Normalized to the response at element 2 x 6.

4.5.5 Multiple Static Field Delivery

The expected variation in dose to the scintillators determined from the treatment plan ranges from a minimum of 91.2 cGy at element 11 x 11 to a maximum of 317.4 cGy at element 2 x 2. The corresponding array measurements demonstrated a range of doses from a minimum of 85.3 cGy to a maximum of 334.9 cGy with their element locations corresponding to that of the treatment plan. The average absolute dose difference between the TPS calculated dose and the dose measured by the array elements was 12.4 cGy ± 11.9 cGy with a minimum difference of 0.2 cGy and maximum difference 47.5 cGy. The average absolute percent dose difference between the TPS calculated dose and array was 6.1% ± 5.6% with the maximum absolute percent dose difference of 36.7% occurring at element 5 x 11.

Correspondingly, the variation in dose to the scintillators determined by Monte Carlo simulation ranges from a minimum of 77.7 cGy to a maximum of 326.4 cGy with their respective element locations corresponding to that of the treatment plan and array measurement. The average absolute dose difference between the Monte Carlo simulated dose and the dose measured by the array elements was 9.1 cGy ± 7.8 cGy with a minimum difference of 0.2 cGy and maximum difference 42.8 cGy. The average absolute percent dose difference between the Monte Carlo simulated dose and measurements was 5.3% ± 4.8%. The spatial distribution of these differences is illustrated in Fig. 4.13 with the maximum absolute percent dose difference of 41.2% occurring at element 5 x 11.

Measurements performed using GAFChromic film depict a variation in dose ranging from a minimum of 100.9 cGy to a maximum of 331.6 cGy with their respective element locations corresponding to that of the treatment plan and array measurement. The average absolute dose difference between the film and array measurements was 12.7 cGy ± 11.4 cGy with a minimum difference of 0.9 cGy and maximum difference 49.9 cGy. The average absolute percent dose difference between the averaged film and array measurements was 7.6% ± 6.6% with the maximum absolute percent dose difference of 45.6% occurring at element 11 x 11.

Finally, qualitative comparison between the calibrated array and OSLD point dose measurements shows good agreement between both methods. While OSLDs measurements were on average 25.0 cGy larger than those of the calibrated array, they were within the range of the film measurements. Calibrated array measurements show greater correspondence with

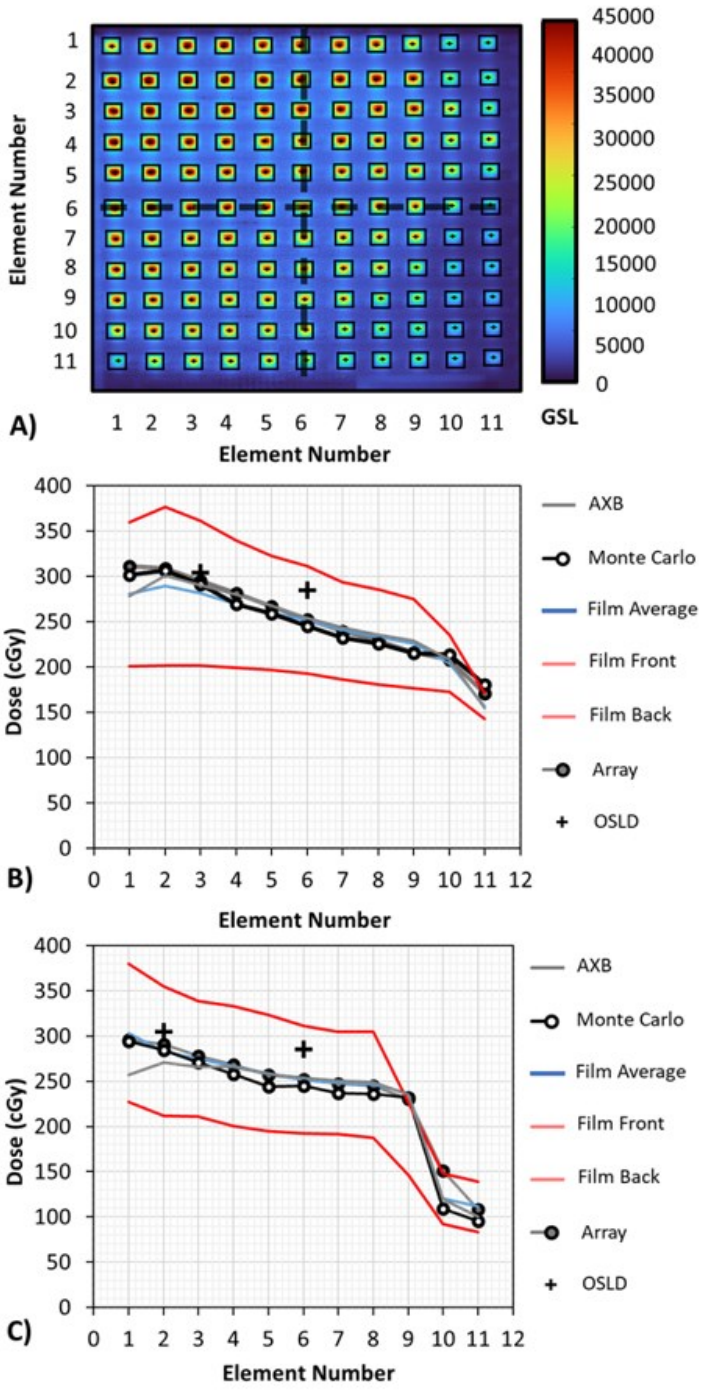

Figure 4.12: A) Image of planar array under irradiation by multiple static fields showing the detected locations of all scintillating elements, **B)** vertical dose profile (dashed line) of calibrated array compared to other dosimetric methods and **C)** horizontal dose profile (dashed line) of calibrated array compared to other dosimetric methods. Profile error bars are not visible for both Monte Carlo (± 2%) and planar array measurements (± 2.5%).

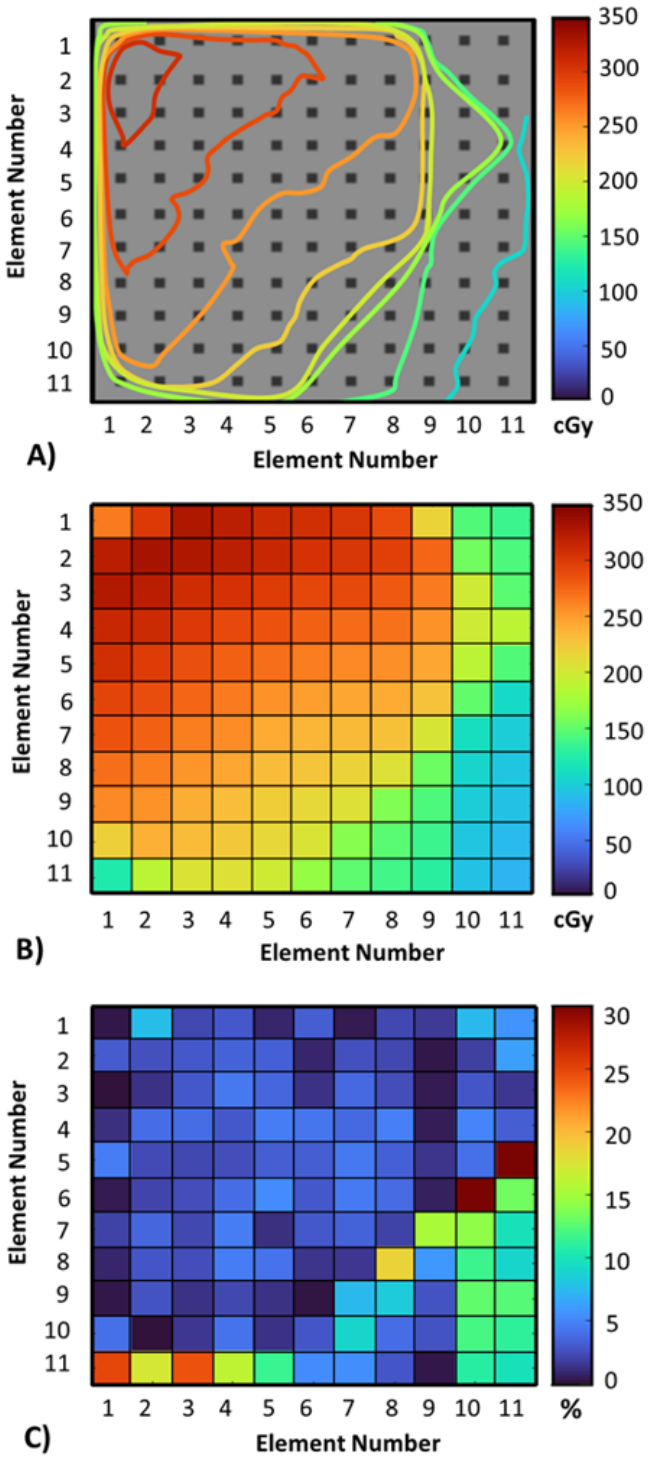

Figure 4.13: A) PRIMO simulated dose distribution of multiple static fields illustrating isodose lines, **B)** corresponding calibrated array dose measurement, **C)** the absolute percent dose difference between the simulated dose and the dose measured using the calibrated planar array.

the average of the two films (front/back) and OSLDs with the front piece film due to their relative positions within the field and the high dose gradient present near the surface.

4.5.6 VMAT Delivery

The expected variation in dose to the scintillators determined by the treatment plan ranges from a minimum of 22.7 cGy at element 6 x 11 to a maximum of 231.0 cGy at element 7 x 2. The corresponding array measurements demonstrated a range of doses from a minimum of 0 cGy at element 11 x 8 to a maximum of 208.7 cGy at element 3 x 5. The average absolute dose difference between the TPS calculated dose and the dose measured by the array elements was 18.6 cGy ± 7.5 cGy with a minimum difference of 1.2 cGy at element 2 x 11 and a maximum difference 41.5 cGy at element 11 x 3. The average absolute percent dose difference between the TPS calculated dose and all 133 planar array elements was 24.6% ± 23.8% with the maximum absolute percent dose difference of 87.6% occurring at element 10 x 9.

This represents an increase in the average absolute percent dose difference between the array measurements and the treatment plan of 18.5% when compared to the static field delivery. This is primarily the result of increasing uncertainty in scintillator measurements performed in low dose regions. At cumulative doses below ~ 20 - 25 cGy given at dose rates below 100 MU/min it becomes increasingly difficult to distinguish the scintillator response from ambient background light contamination. These regions are reported as 0 cGy post background correction (as 16-bit integers do not permit negative values) leading to an increasing underestimate of dose in these regions. If analysis is restricted to dose values greater than 10% of the Monte Carlo simulated max dose (20.9 cGy) the average absolute percent dose difference between the treatment plan and array measurements improves to 9.8% ± 7.5%.

Correspondingly, the variation in dose to the scintillators determined by Monte Carlo simulation ranges from a minimum 18.3 cGy at element 11 x 8 to a maximum of 209.8 cGy at element 3 x 5. The average absolute dose difference between the Monte Carlo simulated dose and the dose measured by the array elements was 10.1 cGy ± 6.3 cGy with a minimum difference of 0.2 cGy and a maximum difference of 42.8 cGy. Applying the same minimum dose criteria of 20.9 cGy, the average absolute percent dose difference between the Monte Carlo simulated dose and measurements was 5.4% ± 5.2%. The spatial distribution of these differences is illustrated in Fig. 4.15.

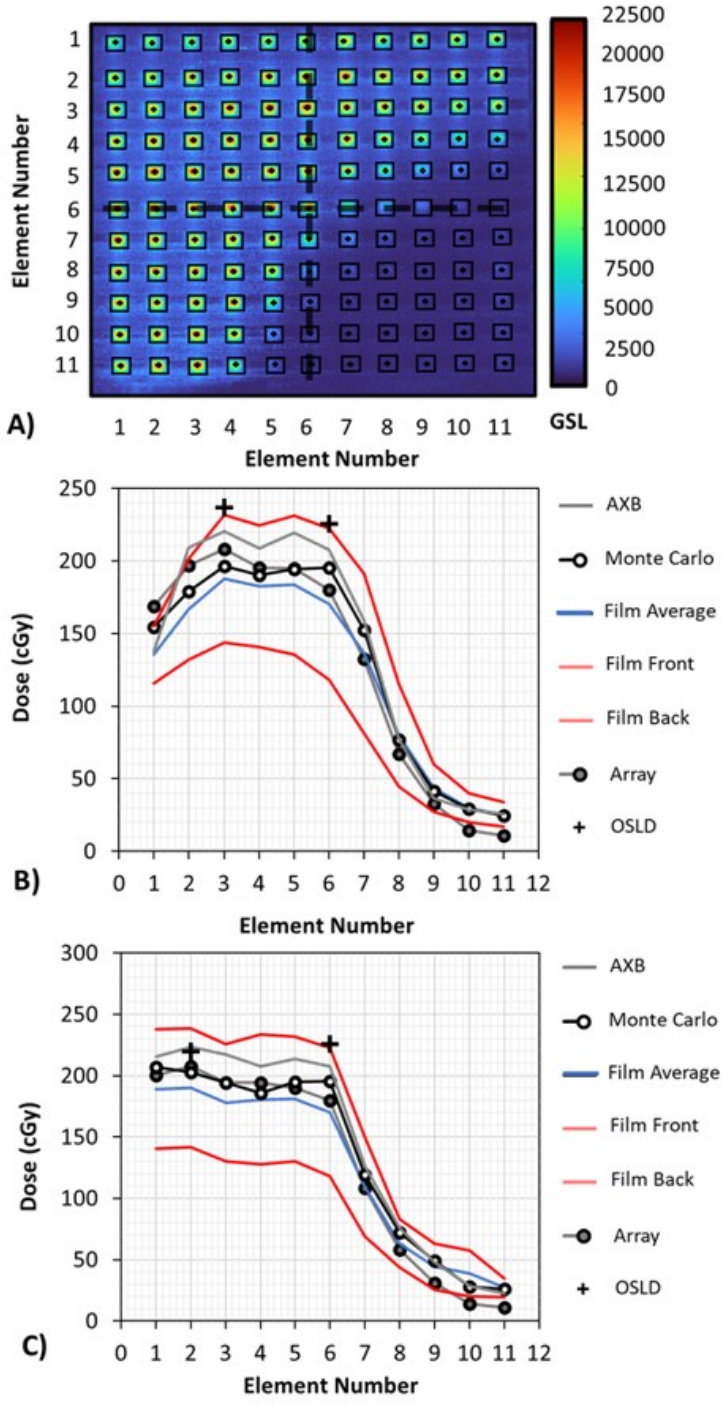

Figure 4.14: A) Image of planar array under irradiation by VMAT plan showing the detected locations of all scintillating elements, **B)** vertical dose profile (dashed line) of calibrated array compared to the other dosimetric methods **C)** horizontal dose profile (dashed line) of calibrated array compared to the other dosimetric methods. Profile error bars not visible for both Monte Carlo (± 2%) and planar array measurements (± 2.5%).

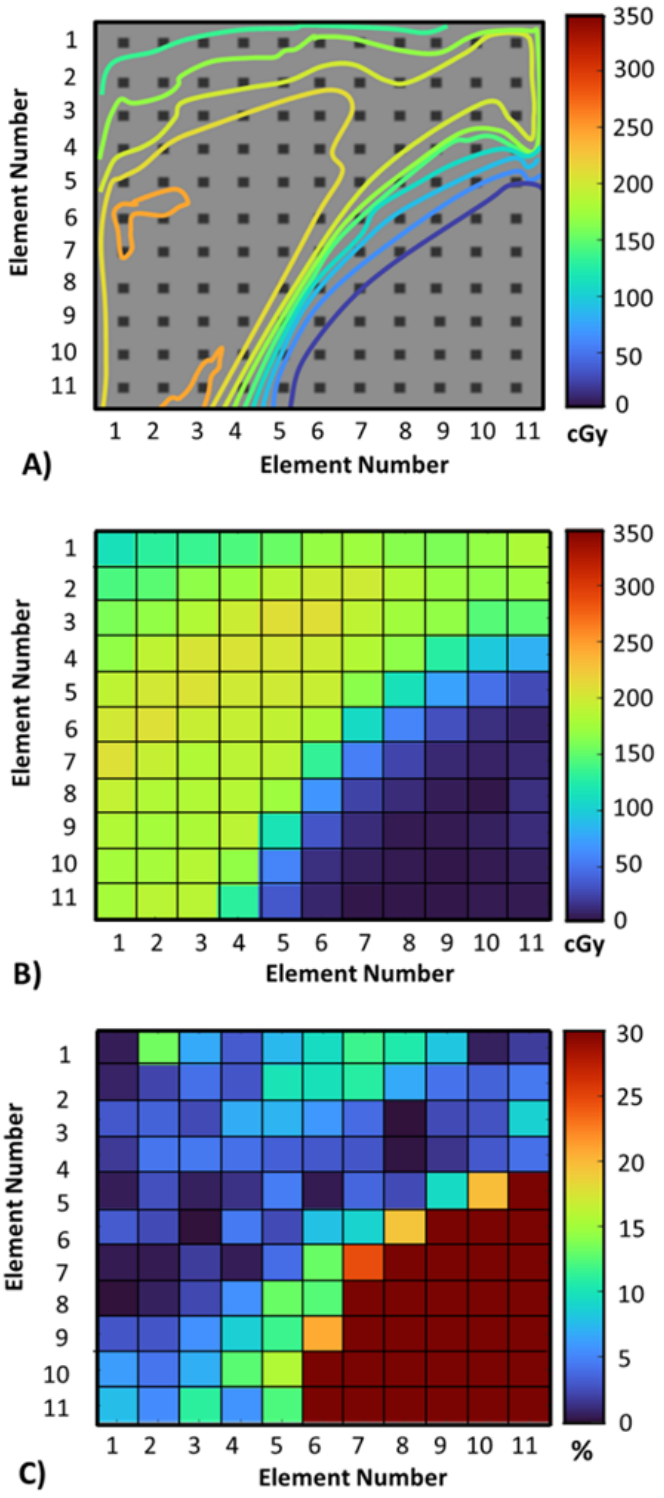

Figure 4.15: A) PRIMO simulated VMAT dose distribution illustrating isodose lines**, B)** corresponding calibrated array dose measurement, **C)** the absolute percent dose difference between the simulated dose and the dose measured using the calibrated planar array.

Measurements performed using GAFChromic film depict a variation in dose ranging from a minimum 14.0 cGy at element 11 x 10 to a maximum of 192.7 cGy at element 7 x 1. The average absolute dose difference between the film and array measurements was 13.7 cGy ± 7.4 cGy with a minimum difference of 0.1 cGy and maximum difference 33.5 cGy. The average absolute percent dose difference between the averaged film and array measurements using all 133 planar array elements was 8.1% ± 8.0%.

Finally, qualitative comparison between the calibrated array and OSLD point dose measurements performed along the central axis are in good agreement. OSLDs measurements were on average 35.8 cGy larger than those of the calibrated array. Calibrated array measurements show greater correspondence with the average of the two films (front/back) and OSLDs with the front piece film.

4.6 DISCUSSION

This study demonstrates the first application of multi-material FDM 3D printing for the fabrication of novel scintillator arrays. In this study, we established both a methodology for the 3D printing of multi-element scintillating arrays and a procedure for the wireless dosimetric calibration of simple array geometries. This has been completed with a view to developing a patient specific dosimeter that will be able to fulfill the unmet clinical need for accessible real-time *in-vivo* dosimetry.

4.6.1 Dual-Material 3D Printing of Scintillator Arrays

Multi-material FDM 3D printing is complicated by the material-specific properties of the chosen filaments. Differences in print temperature, speed, retraction settings, purging, and cooling between the materials make multi-material prints of sufficient quality and consistency challenging to produce. The IDEX design of the W27 3D printer allowed for the consistent printing of high-quality multi-material scintillator arrays and eliminated the need for time-consuming assembly/post-processing of prints.

Assessment of the uniformity of the 3D printed scintillators' response demonstrated that they possessed a nonuniform sensitivity. The average percent deviation from the mean response was 2.1% ± 2.8% necessitating calibration. We hypothesize that the bulk of this effect results from optical nonuniformities and inhomogeneities introduced by the additive

manufacturing process. For comparison, our previous work also showed an average difference of 2.3% and a maximum of 4.0% between scintillators printed with identical print parameters[179]. However, identically designed arrays printed using the same print parameters demonstrate a similar distribution of element sensitivities. This suggests that there is potential for improvements to the printing process. As previously discussed, visibly greater uniformity in 3D printed scintillators is achieved when printing slowly and using an infill pattern which contains minimal changes in printer head direction. Therefore, while printer specific, changes in printing temperature, print speed, material print order and infill pattern could potentially be used to further mitigate the observed non-uniform sensitivity.

The goal of this investigation was to determine the feasibility of dual material 3D printing for the fabrication of planar scintillating arrays and to present a methodology for their dosimetric calibration. However, for future patient-specific applications a greater degree of geometric complexity will be required to ensure proper conformity of the array to the skin surface of the patient. Our initial investigation into the fabrication of a curved array approximating the abdominal curvature of a patient phantom is shown in Fig. 4.16 A). The curved array has dimensions of 3 mm (thickness) x 210 mm x 126 mm with 264 scintillating elements. The array was printed using the same print parameters as the planar array and without the use of support structures. Nonetheless, there may be situations where patient specific array geometries have large unsupported overhangs, or their design is such that they cannot be oriented on the heated build plate in a stable manner without the use of supports. While this is undesirable as it requires additional post processing of the print to properly remove the PLA supports it is not an uncommon practice.

Dosimetric measurements performed using GAFChromic film depict dose variation across the 3 mm thickness of the planar array indicating its relative thickness is large compared to the dose gradient. This indicates that there is the potential for the array to introduce an unwanted bolusing effect. A significant bolus effect is observed for thermoplastic immobilizers with comparable thickness to the array (1–5 mm)[185,186]. It would therefore be desirable to produce scintillating arrays with minimal thickness to reduce any potential increase in skin dose and to ensure a thickness correction is not required to determine the surface dose at the patient/array interface. However, reduction in array thickness will cause a decrease of scintillator volume which may exacerbate existing low dose insensitivity. While the production

of thinner planar arrays (~ 1 mm) is possible, it can only be accomplished when printing flat on the print bed. This technique is not amenable to geometrically complex (i.e., patient-specific) arrays. Despite the use of support structures, significant deformation occurs during the printing process due to an insufficient amount of material supporting the weight of additional layers.

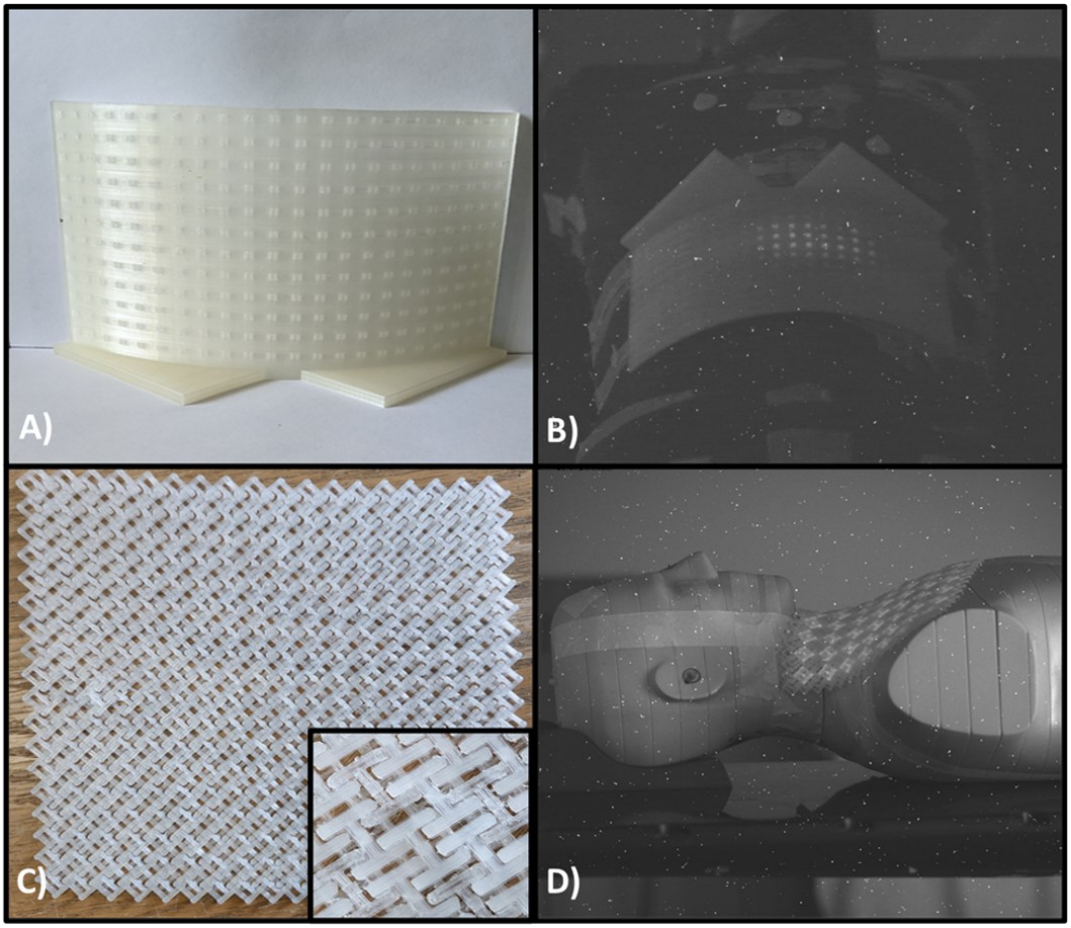

Figure 4.16: Images of more complex prototype dual-material 3D printed array geometries **A)** curved array, **B)** curved array in irradiated state demonstrating approximation of abdominal curvature, **C)** interlocking mesh scintillator array and **D)** its corresponding irradiated state illustrating conformable array geometry.

This limitation could be overcome if the rigid PLA intermediary material used in this investigation was replaced with a flexible alternative such as thermoplastic polyurethane (TPU) or polyethylene terephthalate glycol (PETG). An array composed of scintillating elements and flexible intermediary material could be printed directly on the build plate, allowing the array to

be made thinner and a single array to assume several arbitrary geometries. This would potentially enable the use of a single array for multiple patients or applications. Additionally, sensitivity calibration would only need to be performed once, and it would decrease both plastic waste and manufacturing costs.

Similarly, fabricating scintillating arrays with modular or interlocking geometries would allow for arrays composed of rigid materials to remain flexible. One such example is shown in Fig. 4.16 C). The mesh array has dimensions of 5 mm x 170 mm x 170 mm with 49 scintillating elements. In the current design, the mesh array has elements sizes of ~5 mm (thickness) x 15 mm x 15 mm due to its interlocking geometry. This fabrication limitation would need to be addressed in the future if the mesh array is to be used for point dosimetry. However, it demonstrates the potential for using dual-material 3D printing to fabricate flexible array designs which incorporate overhangs and bridged gaps using modular elements composed of either PLA or scintillator material.

4.6.2 Model-Based Array Simulations and Dosimetric Calibration

The results demonstrate that the geometry used for dosimetric simulations of 3D printed scintillator arrays can be based on the CAD model of the array produced during the design process. Subsequent simulations of both static and VMAT fields using a CAD model-based geometry remained in good agreement with dose measurements performed using the calibrated array and GAFChromic film. This indicates that by leveraging existing *a priori* information contained in the CAD model, the Monte Carlo simulation used for array sensitivity correction and dose calibration can be performed in tandem with array fabrication. In a clinical setting, this workflow would drastically reduce the overall preparation time required prior to performing patient-specific *in-vivo* dosimetry with 3D printed scintillator arrays, as the array does not need to have completed printing before beginning calibration.

However, the key limitation of the current calibration process is that the sCMOS camera always remained orthogonal relative to the surface of the array. While this was advantageous to isolate the effects of optical artefacts from geometric artefacts, in practice the array will have a much more complex geometry and need to be oriented on the patient at an oblique angle relative to the camera. As previously discussed, this requires additional consideration for geometric (perspective based) artefacts. For example, the response of the curved array under

irradiation is shown in Fig 4.17. Following correction for optical artefacts, the central array elements still appear brighter while the periphery elements appear dimmer due to their different relative distances from the camera or their "depth" within the image.

If the depth of each element was known, an inverse square correction could be applied to account for this effect. While it is not possible to estimate the depth of a point object within an image using a single camera, recent work with deformable arrays of scintillating fibers and stereoscopic camera arrangements have shown that such real-time position tracking is possible[83,84]. Another potential method of correcting geometric artefacts would be to subsume such corrections into the calibration process. If it is possible to perform the calibration in an identical geometry and orientation to the final measurements, the depth (inverse square correction) would be accounted for by the calibration. In the case of a patient-specific array geometry, one potential option is to perform optical surface imaging of the array on the patient to generate a CAD geometry for simulation which incorporates both print specific material information and the patient specific geometric information.

There are two potential sources of error for this calibration. The first is the orientation of the array parallel to the beam axis that results in each row of scintillators being exposed to a different calibration dose and dose rate. Consequently, any existing dependence on the relationship between dose rate and camera acquisition speed may be present in the derived calibration coefficients. This would be mitigated by using a stereoscopic camera arrangement placed at an oblique angle and a calibration geometry which positions the array perpendicular to the beam axis.

Secondly, error may be introduced due to differences in the cameras Cherenkov light collection efficiency in the calibration versus the measurement conditions. Since the direction of secondary electrons in a 6 MV beam is somewhat diffuse[127], we expect that most of the Cherenkov light emitted by the plastics to scale with dose and be collected by the camera. However, due to the direction and energy dependence of Cherenkov light, future work on its amount and collection efficiency by the camera is warranted. In addition to Cherenkov light production, the indigenous fluorescence of the plastics has not been quantified and our calibration process assumes that this light is emitted isotropically and scales linearly with dose.

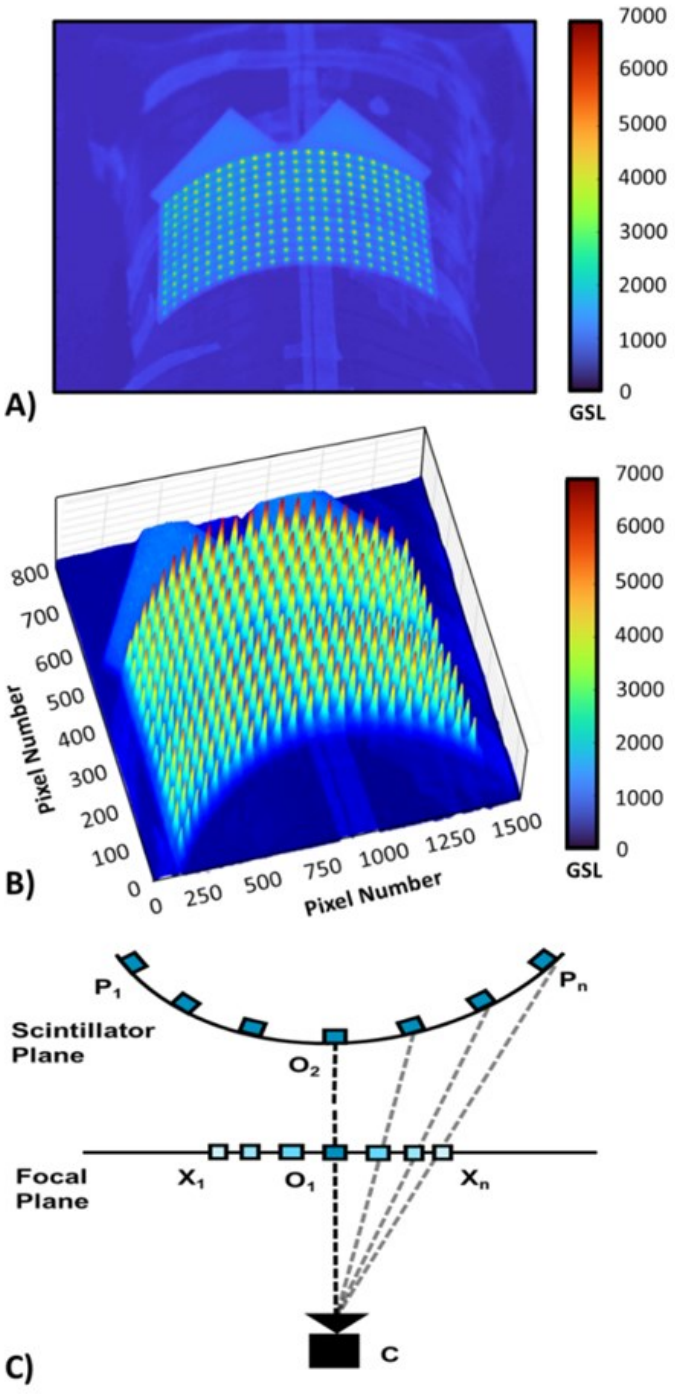

Figure 4.17: A) Single image frame of the curved array under irradiation by 6MV X-rays corrected for all-optical artefacts, **B)** final composite curved array image illustrating the need for perspective-based corrections of non-planar array geometries. **C)** Central array elements are recorded as brighter, while periphery array elements are recorded as dimmer due to differences in their radial distances from the camera.

Finally, it is also worth noting that traditionally, scintillators have been read out using an optical fiber coupled to a photodetector. This has the advantage of acting as a means for readout that would forgo the camera specific calibration issues discussed previously and permit measurement of custom 3D printed scintillator arrays regardless of the array's orientation or geometry. However, the use of optical fibers for readout would be undesirable as placing hundreds of optical fibers on the patient during treatment delivery would make their routine use as an *in-vivo* dosimeter in clinics prohibitively cumbersome.

4.6.3 Multiple Static Field Delivery

Following calibration, comparison of planar array dose measurements with Monte Carlo simulations, TPS calculations and GAFChromic film measurements produced similar minimum/maximum doses, absolute dose variations and absolute percent dose differences. The greatest degree of agreement was found to be between Monte Carlo simulation and calibrated array measurement with an average absolute percent dose difference of 5.3% ± 4.8%. This result indicates that for the fixed beam arrangement dose measurements performed using the calibrated planar array are comparable to the clinically acceptable range of 5% - 10% used for *in-vivo* measurements performed with other point detectors such as MOSFETs, OSLDs, TLDs and diodes[26].

Qualitative inspection of the spatial distribution of these differences indicates increasing discrepancy in lower dose regions and in areas of high dose gradient. The maximum absolute percent dose difference between the calibrated array measurements and Monte Carlo simulation was 41.2%. Studies on surface dosimetry using commercially available point dosimeters such as OSLDs and TLDs have demonstrated similar discrepancies of between 10% – 40% between measurements and simulations[187]. A combination of factors impacts the expected-to-measured dose agreement of point detectors. This includes the dose gradient compared to the size of the detector (volume averaging) and the substantial impact of even small offsets between detector placement and simulation geometry[19,188]. While the minimum volume of each element is currently limited to 27 mm^3, the spatial resolution of array elements need not be fixed as in this study. The location of scintillating elements is entirely customizable and array designs can be informed by prior Monte Carlo simulation or TPS calculation of the patient's specific treatment plan.

4.6.4 VMAT Delivery

Array dose measurements performed following calibration for a three-arc clinical VMAT plan indicate difficulty in differentiating the scintillator response from ambient background light contamination at low doses (< 20-25 cGy) and dose rates (≤ 100 MU/min). These regions are reported as 0 cGy post background correction and strongly bias a global comparison of all 133 array elements to Monte Carlo simulation.

We hypothesize that this discrepancy at low doses is the result of multiple factors. In the case of VMAT delivery, to avoid under sampling the rapidly varying dose distribution and offer the potential for future real-time feedback a rapid acquisition speed is desirable. However, increasing the acquisition speed will also decrease exposure time. As the exposure time is reduced, it becomes increasingly challenging to reconstruct low dose regions as the scintillation signal contained in each frame is also reduced. This indicates that the relationship between camera acquisition speed, dose rate and the arrays low dose insensitivity requires further investigation to better quantify this dependence and determine the optimal acquisition speed for use in clinical dosimetry. A real-time *in vivo* dosimetry system capable of more accurately reproducing VMAT dose distributions may require triggering and gating of image acquisition based on the accelerator pulse rate[147,189].

In addition to the relationship between dose rate and camera acquisition speed, there is no guarantee that the measured light output represents the entire active volume of the scintillator. Prior work with individual 3D printed scintillators demonstrates a directional dependence of light output[179]. The amount of light produced in each region of the active volume is uncertain, as it may be scattered or absorbed prior to exiting the surface aligned with the direction of the camera. As the array has no backing, this effect may be further complicated in the case of *in-vivo* measurements on patients. Natural differences in skin color between patients or changes in a given patient's skin pigmentation over the course of treatment (such as in the case of erythema) may result in different optical reflections into the scintillator. This effect could be controlled by printing an additional thin wall of PLA covering the entire side touching the patient to ensure an identical background for the calibration and measurement. Conversely, if it is possible to find a skin safe product, the arrays could also be coated with a thin layer of optically reflective material to increase their total light output. This reflective

material could even potentially be optimized for the specific emission wavelength of the scintillators (~425 nm).

When analysis is restricted to exclude these low dose regions (dose values less than 10% of the Monte Carlo simulated max dose of 20.9 cGy) the average absolute percent dose difference between Monte Carlo simulation and array measurement is 5.4% ± 5.2% with an average absolute dose difference of 10.1 cGy ± 6.3 cGy. This result is comparable to the fixed beam arrangement where the average absolute percent dose difference between the Monte Carlo simulated dose and array measurements was 5.3% ± 4.8% with an average absolute dose difference of 9.1 cGy ± 7.8 cGy.

On the other hand, VMAT delivery shows increased discrepancy between TPS calculations and calibrated array measurements. For the fixed beam arrangement, the average absolute percent dose difference between TPS calculation and array measurement is 6.1% ± 5.6% with an average absolute dose difference of 12.4 cGy ± 11.9 cGy. For VMAT delivery both the average absolute percent dose difference and the average absolute dose difference increased to 9.8% ± 7.5% and 18.6 cGy ± 7.5 cGy respectively. As previously discussed, one of the primary motivations for *in-vivo* measurement of surface dose is that most RT treatment planning systems do not accurately predict dose in the superficial layers of skin[13]. Therefore, the greater degree of agreement between array measurement and Monte Carlo simulation is expected as the array is calibrated using Monte Carlo simulations not TPS calculations.

4.7 CONCLUSION

In this study, we presented a novel methodology for the fabrication of dual-material FDM 3D printed plastic scintillator arrays with both high spatial resolution and arbitrary geometry. We subsequently demonstrated a dosimetric calibration for planar array geometries, which leverages the unique aspects of the 3D printing process. Surface dose measurements of a fixed beam arrangement and clinical VMAT plan performed using the calibrated planar array were on average within 5% - 10% of the Monte Carlo simulated dose. These results indicate that dose measurements performed using the calibrated planar array are comparable to the clinically acceptable range used for *in-vivo* surface dose measurements performed with MOSFETs, OSLDs, TLDs and Diodes. Despite this, array dose measurements of the clinical VMAT plan clearly demonstrate an increasing insensitivity to low doses and dose rates. GAFChromic film

measurements also illustrate the potential of an array generated bolusing effect which may require mitigation by reduction of the array thickness. Future investigations include the extension of this work to 3D printed patient-specific real-time scintillating dosimeters that will be able to fulfill the unmet clinical need for accessible, routine, and real-time *in vivo* dosimetry for patients undergoing radiotherapy.

4.8 ADDENDUM

4.8.1 Element Size and Thickness

The element size does not need to be fixed, as it was in this study. Our method offers versatility in customizing the size and shape of scintillating elements, with the option to adapt designs to specific requirements. However, altering the scintillator element size should be carefully considered due to its potential impact on the SNR and low dose sensitivity. As a result, it is worth investigating the effect of scintillator thickness and volume on the observed total light output.

An array of scintillators was fabricated using identical print parameters to those described in section 4.4.1. As shown in Fig 4.18 A, it consisted of volume elements ranging from (1 mm x 1 mm x 1 mm) to (10 mm x 10 mm x 10 mm) in increments of 1 mm^3. It also contained thickness elements ranging from (5 mm x 5 mm x 1 mm) to (5 mm x 5 mm x 10 mm) in increments of 1 mm. These elements were then individually placed at the center of a 30 x 30 cm^2, 6 MV photon field and irradiated with 200 MU delivered at a gantry angle of 0^{o} and SSD of 100 cm. The response of each scintillator under irradiation was then imaged three times using a pco.panada 4.2 sCMOS camera positioned at the foot of the treatment couch.

As shown in Fig 4.18 B, the total light output of 3D printed scintillators increased linearly with thickness from 1 mm to 6 mm, but further thickness increases did not enhance the signal. This suggests a maximum recommended scintillator thickness of 6 mm as light produced at greater depths ultimately fails to exit the exterior surface of the scintillator facing the camera. As shown in Fig 4.18 C, 3D printed scintillators also exhibit an increase in measured signal with increasing volume. However, our findings indicate that this increase is attributable to the expansion of surface area rather than volume. The greater the surface area the more pixels are occupied by the scintillator in the measurement image resulting in a higher total light output.

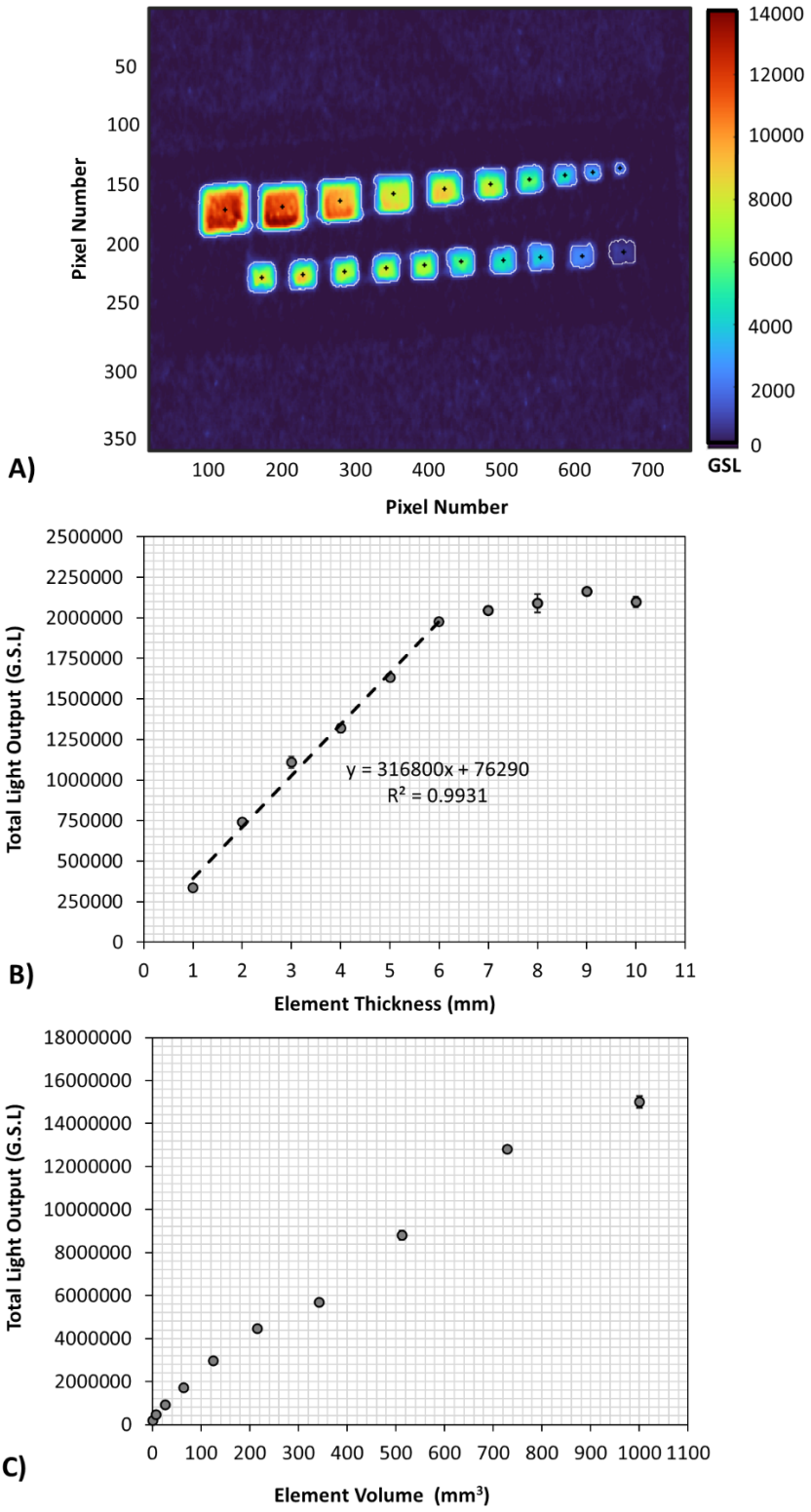

Figure 4.18: A) Single image frame of scintillating elements of various sizes under irradiation, **B)** total scintillator light output as a function of thickness and **C)** total scintillator light output as a function of element volume.

CHAPTER 5 MANUSCRIPT 3: CAMERA BASE MULTIPOINT IN-VIVO DOSIMETRY USING 3D PRINTED PATIENT SPECIFIC SCINTILLATOR ARRAYS

5.1 PREAMBLE

This manuscript presents the first prototype of the proposed novel *in-vivo* dosimetry system. Building on the experience gained from the 3D printing of simple array geometries this manuscript provides a methodology for fabricating patient-specific plastic scintillator arrays based on treatment planning data. Notably, it demonstrates a unique dosimetric calibration method that leverages both 3D printing and stereoscopic imaging. The dosimetric accuracy of the calibrated patient specific scintillator array is shown to be similar to other *in-vivo* surface detectors, with average absolute percent dose differences of 5% - 10%. This research not only facilitates the fabrication of customized, high-resolution plastic scintillator arrays with user-defined geometries but also paves the way for expanding the application of 3D printing in radiotherapy to detector fabrication. At the time of writing, this manuscript, developed under the guidance of my graduate supervisors (coauthors) has been submitted for publication in Medical Physics and is currently under review.

Publication: Nicholas Lynch, James L Robar, Thalat Monajemi. "Camera-based multipoint in-vivo dosimetry using 3D printed patient specific scintillator arrays". Submitted: May 6th, 2024 to Medical Physics and, at the time of writing, is currently under peer review. The included chapter differs only from the submitted manuscript in the addition of revisions for additional clarity.

5.2 ABSTRACT

Background

Measurement of radiation is an essential component of a radiotherapy program, yet many detectors are designed to measure radiation in a quality control and assurance setting. This makes them too impractical or cumbersome for direct use on patients, limiting the widespread clinical use of *in-vivo* dosimetry.

Purpose

This study aims to develop a novel wireless radiation dosimeter consisting of a 3D-printed patient-specific plastic scintillator array capable of addressing the clinical need for accessible routine *in-vivo* dosimetry of patients undergoing radiotherapy.

Methods

Based on a CT scan of an anthropomorphic phantom, a custom scintillator array was designed by delineating a 3.0 mm chestwall bolus in the treatment planning system. Following export to bolus design software, 27 mm^3 square dosimeter pockets, representing the scintillators, were positioned within the bolus using user-defined reference points. The resulting 3D model was then employed to generate printer instructions for a BCN3D Epsilon W27 dual extrusion 3D printer. The array was composed of white polylactic acid (PLA) filament and non-cladded BCF-10 plastic scintillating fiber. Under irradiation, the array's response was imaged using a pair of stereo-calibrated sCMOS cameras. The collected images were processed using purpose-built software applications to correct for optical artifacts and determine the light output of each scintillator. Calibration was performed by placing the array on a 3D printed calibration block which replicated the exterior surface of the phantom and irradiating with a 6 MV 30 x 30 cm^2 open photon field delivered as an arc. Stereoscopic surface imaging was used to ensure camera perspective alignment between calibration and measurement. Array response was calibrated to dose using Monte Carlo simulations, and the calibration accuracy assessed using subsequent measurement of two clinical chest wall plans (tangential photon fields and a VMAT arc plan). Dose measurements with the calibrated array were then compared to Monte Carlo simulations and TPS calculations.

Results

Our results confirm the viability of dual-material 3D printing for creating plastic scintillator arrays with patient-specific geometries. They demonstrate that the number and location of scintillating elements is entirely customizable and can be based on prior TPS calculation or Monte Carlo simulation of a patient's specific treatment plan. Following dosimetric calibration, surface dose measurements for clinical chest wall plans agreed with Monte Carlo simulated doses. For tangential fields, the average dose difference was 8.0 cGy ± 11.5 cGy, with a range of -17.9 cGy to 27.3 cGy, and an average percent dose difference of

2.4% ± 4.6%. For VMAT, the average dose difference was -0.5 cGy ± 9.4 cGy, with a range of -19.2 cGy to 21.6 cGy, and an average percent dose difference of 0.2% ± 5.8%. Comparison with TPS-calculated doses revealed average percent dose differences of 15.1% ± 9.6% for tangential fields and 11.1% ± 9.2% for VMAT.

Conclusion

In this study, we developed a novel patient specific radiation detector and demonstrated its ability to wirelessly measure clinical surface dose distributions.

5.3 INTRODUCTION

Patient-specific quality assurance is a key issue in radiation therapy, as such treatments are carefully planned, checked, and verified prior to treatment. Despite this, the radiation dose received by a patient is still susceptible to errors in the overall radiotherapy process (setup, calculation and/or transcription)[1–4]. Consequently, direct measurement of the radiation dose received by the patient during treatment (*in-vivo* dosimetry) is recommended for all patients undergoing radiation treatments by the International Atomic Energy Agency (IAEA)[1], the World Health Organization (WHO)[4] and the International Commission on Radiological Protection (ICRP)[5]. It is also well known that modern radiotherapy treatment planning systems do not accurately predict dose in the superficial layers of skin[13], leading to discrepancies of 10% - 30% between simulated and measured surface doses[14–16]. Routine *in-vivo* measurement of dose would provide dosimetric data that could be linked directly to clinical outcomes for patients (e.g., local control and side effects/morbidity).

While the measurement of radiation is an essential component of a radiotherapy program, most detectors are best suited to measuring radiation in a quality control and assurance setting (i.e., in the absence of a patient)[6]. As a result, the design of most detectors is such that they are either too rigid, fragile, bulky, or cumbersome to use directly on patients, limiting the routine clinical use of *in-vivo* dosimetry[7]. Some detectors are still capable of performing *in-vivo* dose measurements, examples include Radiochromic film[8], OSLDs[9], and MOSFETs[10]. While the existence of these detectors means *in-vivo* monitoring of patients is possible, their widespread adoption in clinical settings remains hindered by practical challenges[7].

One potential avenue for routine *in-vivo* dosimetry is Cherenkov imaging as it offers high spatial and temporal resolution imaging of the dose distribution in real-time. Cherenkov

imaging has already been shown capable of determining coincidence between measured and planned field dimensions and Multileaf Collimator (MLC) positions[46,47]. Color Cherenkov imaging has also demonstrated the potential for providing information about tissue properties such as blood volume, oxygen saturation and vasculature[190]. Despite these promising attributes, dose quantification is impacted by the non-uniform optical properties of tissue which introduce complexities in the conversion from Cherenkov light intensity to absolute dose[38,39]. Overcoming these challenges is essential for harnessing the full potential of Cherenkov imaging for providing quantitative dosimetric data, constituting a dynamic and ongoing area of research[39,191–194].

An alternative technological avenue that holds promise is Fused Deposition Modeling 3D printing. FDM 3D printing involves the heating and extrusion of thermoplastic filaments, layer by layer, to build 3D structures. This additive manufacturing method, characterized by its ability to rapidly create intricate designs, could provide a complementary or alternative means for achieving routine *in-vivo* measurement of dose during radiation therapy. FDM 3D printing has already been shown to be suitable for the generation of patient specific treatment accessories in radiation therapy[48]. Development of novel radiation detectors has also been shown to benefit from 3D printing as it allows for the rapid prototyping of highly customizable and intricate detector designs[20,52,56,70].

Our group has previously established the basic dosimetric properties of a 3D printed plastic scintillator and quantified its light signal dependence on printing parameters[179]. We subsequently demonstrated the ability to print simple array geometries (planes, curves, etc.) consisting of tens to several hundreds of 3x3x3 mm^3 scintillators and developed techniques for their wireless readout and dose calibration[20]. This study extends the techniques advanced in these publications to the wireless measurement of a 3D-printed patient-specific array of plastic scintillators using a stereoscopic arrangement of sCMOS cameras.

The overarching objective of our research is the creation of a patient-specific radiation detector capable of meeting the current clinical demand for routine real-time *in-vivo* dosimetry in radiation therapy[7,19]. As illustrated in Fig. 5.1, the detector system consists of a 3D-printed array of plastic scintillators designed to adapt to the exterior surface of the patient. The light emitted by the array during treatment is then measured using a stereoscopic arrangement of cameras positioned within the treatment room. The arrays light output is correlated to dose

through pretreatment dosimetric calibration, facilitating real-time comparison between the patient's received dose and the planned dose distribution during treatment.

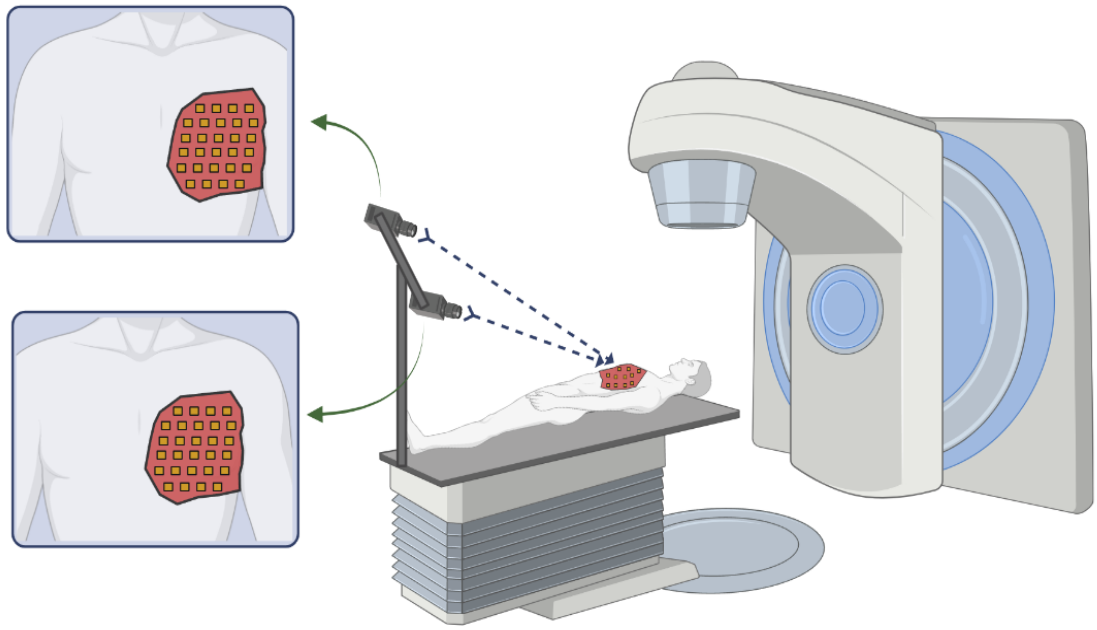

Figure 5.1: Illustration of a patient specific 3D-printed scintillator array contouring to the surface a the patient and measured using a stereoscopic pair of cameras[20].

5.4 MATERIALS AND METHODS

5.4.1 Patient-Specific Array Fabrication and Design

The array was fabricated using an Epsilon W27 dual-material 3D printer (BCN3D Technologies, Barcelona, Spain) and is composed of polylactic acid (PLA) and non-cladded BCF-10 scintillating fiber (Saint Gobain Crystals, Ohio, USA). The 3D printing parameters and techniques used for the manufacturing of the patient specific scintillator array were consistent with our preceding work[20,179].

The design process of the patient specific scintillator array began with a computed tomography (CT) scan of an anthropomorphic patient phantom. To establish the array's geometry, a 3.0 mm thickness bolus was defined within the Eclipse treatment planning system (Varian Medical Systems, Palo Alto, CA). To delineate the locations of the scintillating elements, reference points were placed within the planning system. The location of scintillating elements is entirely customizable and can be informed by prior TPS calculation or Monte Carlo

simulation of a given treatment plan[20]. In this case, elements were positioned along the perimeter of a manually defined Planning Target Volume (PTV). Along the PTV perimeter elements were horizontally spaced at 45mm (center-to-center) and vertically spaced at 25 mm. Regions of higher spatial resolution were concentrated at the array's center and along its vertical and horizontal profiles with a spacing of 20 mm. For further details regarding the treatment planning process refer to section 5.4.5.1.

The bolus and reference points were exported to Adaptiiv's 3D Bolus software (Adaptiiv Medical Technologies Inc, Halifax, Canada). In this software, a smoothing technique was applied, and the structure was cropped along the bottom edge to ensure adhesion to the 3D printer's build plate. The reference points placed within the planning system were used to define 3 x 3 x 3 mm^3 dosimeter pockets within the bolus. This corresponds to the current minimum recommended scintillating element volume of 27 mm^3 [20]. However, the spatial dimensions of any one array element need not be fixed as in this study.

Following export to computer aided design (CAD) software, the TPS generated bolus was used to model the patient specific array as two separate components, a body composed of PLA containing the pockets and a corresponding set of scintillating elements. The model was then imported into the CURA slicer software (UltiMaker B.V., New York, USA) as two files, each assigned to its corresponding print material and independent extruder. Cura then merged and sliced the model into horizontal layers based on each materials specific print parameters and converted it into print instructions (G-Code) for each extruder. The object was subsequently printed layer by layer, with materials alternating as specified by the original CAD model's material definitions. As shown in Fig. 5.2, the patient specific array has dimensions of 3 mm (thickness) x 115 mm x 215 mm with 29 scintillating elements. Each scintillating element has dimensions of 3 x 3 x 3 mm^3 and each is optically separated by PLA. The array was printed vertically on the build plate without any additional support structures. The cumulative print duration for the patient specific array was 18 hours and 36 minutes.

Our prior research also identified the potential of patients skin color and changes in skin pigmentation over the course of treatment to modify optical reflections into the scintillators[20]. To address this, the array should be optically isolated from the patient surface. In this study, the back of the array was coated with a thin layer of white acrylic paint, effectively optically isolating the scintillators from the phantom surface, and augmenting their total light output by

providing a reflective background. In practice, this effect could also be achieved by printing a thin layer of PLA to cover the surface in contact with the patient.

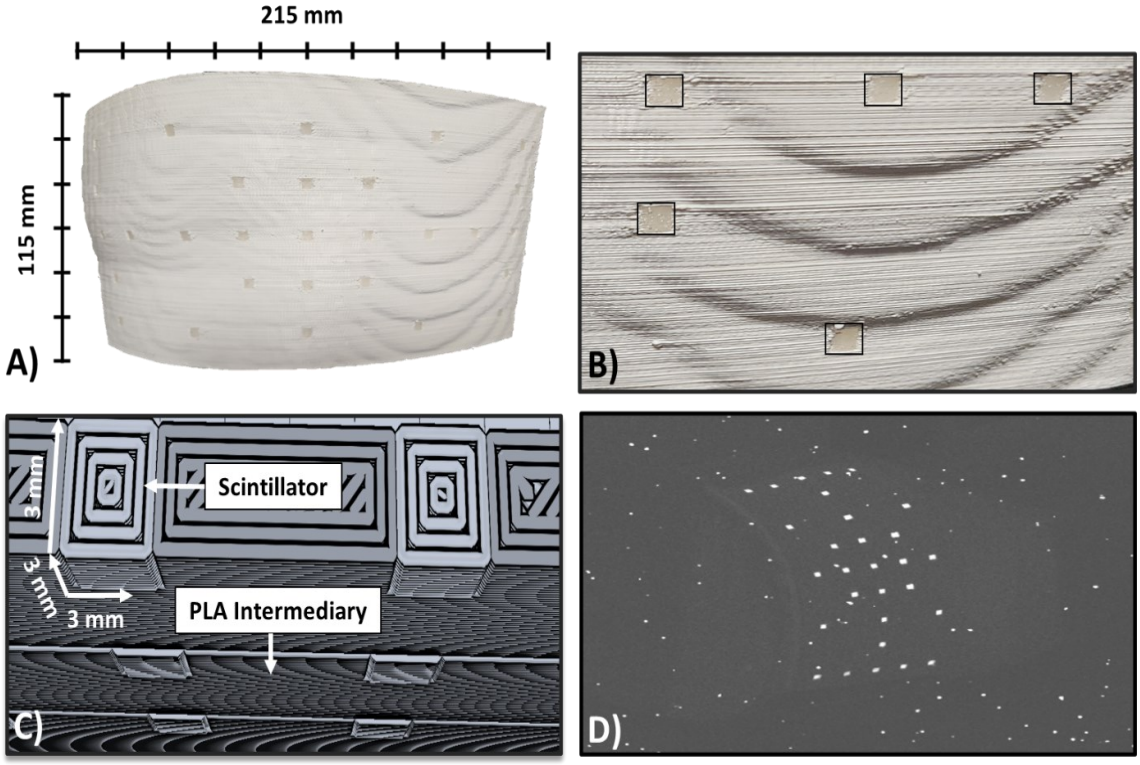

Figure 5.2: A) Images of 3D-printed patient-specific scintillator array, **B)** close-up of scintillating array with outlined elements, **C)** illustration of the array's internal layering geometry and **D)** array under irradiated by 6 MV X-rays.

5.4.2 Image Acquisition

The arrays light output during irradiation was measured using two unshielded 16-bit pco.panda 4.2 monochrome sCMOS cameras (PCO Photonics Ltd., Ontario, Canada). Each camera has a total image resolution of 2048 x 2048 pixels, pixel size of 6.5 x 6.5 μm^2 and was fitted with a 50 mm F/1.8 manual focus lens. The images were further enhanced using a 2 x 2 sensor binning, resulting in a final image resolution of 1024 x 1024 pixels. Binning is beneficial in low-light conditions where signal strength is comparable to background noise, a circumstance encountered at low doses and dose rates[20]. The cameras were positioned approximately 270 cm from the array using a tripod and aligned obliquely to the array surface.

Each camera is connected through its USB-C interface to its own Icron USB 3.1 Raven multimode fiber extension system (Analog Devices Inc, Massachusetts, United States). This system consists of a transmitter in the treatment room and a receiver located outside near the console, connected via a lightweight optical fiber. This approach mitigated signal attenuation issues encountered when using traditional copper cables for long-distance signal transmission. Subsequently, each receiver is connected to an individual external high-speed serial computer expansion bus (PCI-E) housed within an acquisition computer. This configuration enables system control and manual triggering from outside the treatment room.

While the long-term goal for this work includes real-time measurement, despite implementing the suggested upgrades from our earlier publication (PCI-E, range extension and external triggering)[20], hardware-related constraints persist. At the current sampling rate of 5 frames per second (FPS) (exposure time of 200 ms) a typical chestwall VMAT arc delivery comprises approximately 200 images per camera (400 total images) and can now be fully processed (see section 5.4.4) within 5 minutes post-irradiation. However, this processing delay hinders real-time acquisition, escalating with higher sampling rates. To overcome this challenge, it is imperative to integrate camera acquisition triggering and readout directly into the processing software and necessitates the use of a robust GPU for accelerated image processing. Therefore, following our previously established methodology, images were collected, downloaded, and stored as 16-bit TIFF files for subsequent processing[20].

Currently, image acquisition requires a light-free environment in the treatment room. This involves conducting imaging sessions with the room lights turned off and the removal or covering of any additional diffuse light sources. While imaging with ambient light is possible with the gated intensifier-coupled cameras (ICCDs) used for Cherenkov imaging[195], the sCMOS cameras used in this work are not capable of achieving sufficient signal at such low exposure times (~ 8 - 50 ms). Consequently, it is imperative that the ambient light background within the treatment room remains constant throughout the entire treatment duration. This measure ensures the integrity of the imaging process, acknowledging the specific capabilities and constraints of the sCMOS cameras employed in this study[147]. While investigations into controlling the spectral content of treatment room lighting using LEDs of specific wavelength and corresponding spectral filtering have been performed[196], such mitigation strategies were not pursued in this study.

5.4.3 Cherenkov Background Mitigation

Cherenkov radiation, despite producing a coherent signal that can be correlated with dose in superficial layers[192], is a source of noise in scintillation dosimetry. The reduction, and preferably complete removal, of the Cherenkov background is desirable to enhance dosimetric accuracy. Separating scintillation and Cherenkov light is challenging due to their overlapping spectral and temporal properties, necessitating knowledge of their spectral characteristics for effective discrimination[179]. This task is particularly complex when using sCMOS cameras for measurements, as opposed to spectrometers, where detailed spectral information is unavailable.

Spectral investigations into the radioluminescence of immobilizer plastics in Cherenkov imaging of head and neck radiotherapy have identified a combination of Cherenkov emission and material fluorescence[195]. Lighter material colors have the potential to enhance the visibility of Cherenkov through increased reflectivity, and clear materials, by permitting less absorption, may enable a greater collection of emitted Cherenkov light. Additionally, material fluorescence is closely tied to the optical properties of the plastic and the color may alter its overall fluorescence characteristics. This underscores the significance of the choice of PLA color, as it could impact the dose accuracy of 3D printed scintillator arrays by introducing unwanted background noise.

Preliminary testing demonstrated a correlation between the color of the PLA intermediary material and the observed radioluminescence of the resulting scintillator array (Fig. 5.3). Although black PLA initially appeared advantageous due to its light-absorbing properties, it also led to a significant reduction in scintillation signal. This exacerbated the known low dose insensitivity of our system and contributed to an increase in element-to-element variability. As a result, a white reflective material was selected as the best compromise. This choice aims to minimize array radioluminescence while maximizing scintillation light output at low doses and dose rates. Radioluminescence only calibrations using arrays composed solely of PLA also led to significant overcorrection (~15-20%) of the observed scintillator light output, indicating the non-representative nature of the plastics radioluminescence compared to the scintillators.

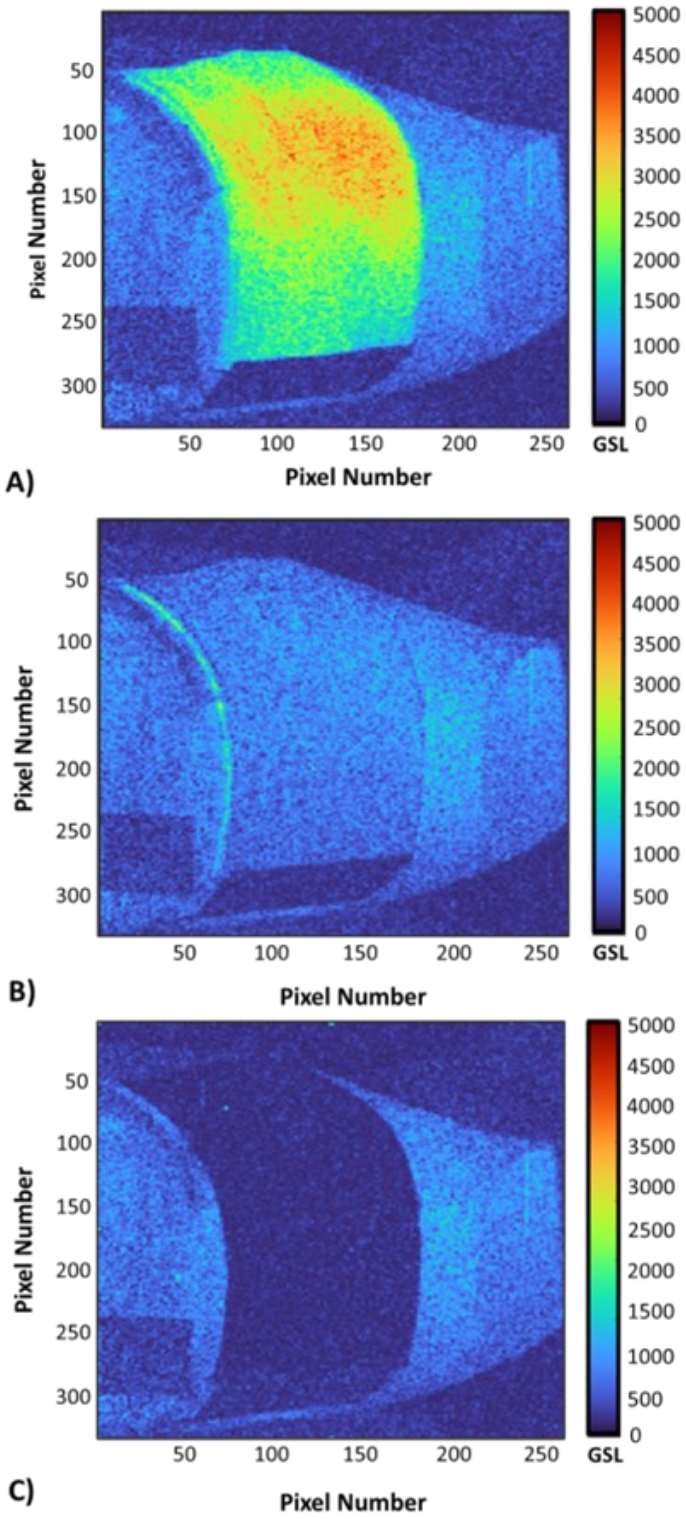

Figure 5.3: Arrays composed solely of PLA intermediary material irradiated by 6MV X-rays **A)** clear, **B)** white and **C)** black.

Studies have demonstrated that the Cherenkov contribution can be modified using wavelength and polarizing lens filters (Fig. 5.4)[195–198]. Therefore, to further mitigate the Cherenkov contribution to the observed signal each camera was equipped with a 40.5 mm circular polarizer and light pollution (IR cut) filter (URTH, Ontario, Canada). While the reduction is influenced by the beam angle, qualitative evaluation of images captured at different polarizer angles found that a 90^{o} polarizer orientation yielded the greatest average reduction of the PLA radioluminescence background. This dual-filter approach also brings additional advantages, working synergistically they diminish reflections from surfaces within the treatment room and reduce any residual ambient light contamination by specifically removing red and orange wavelengths.

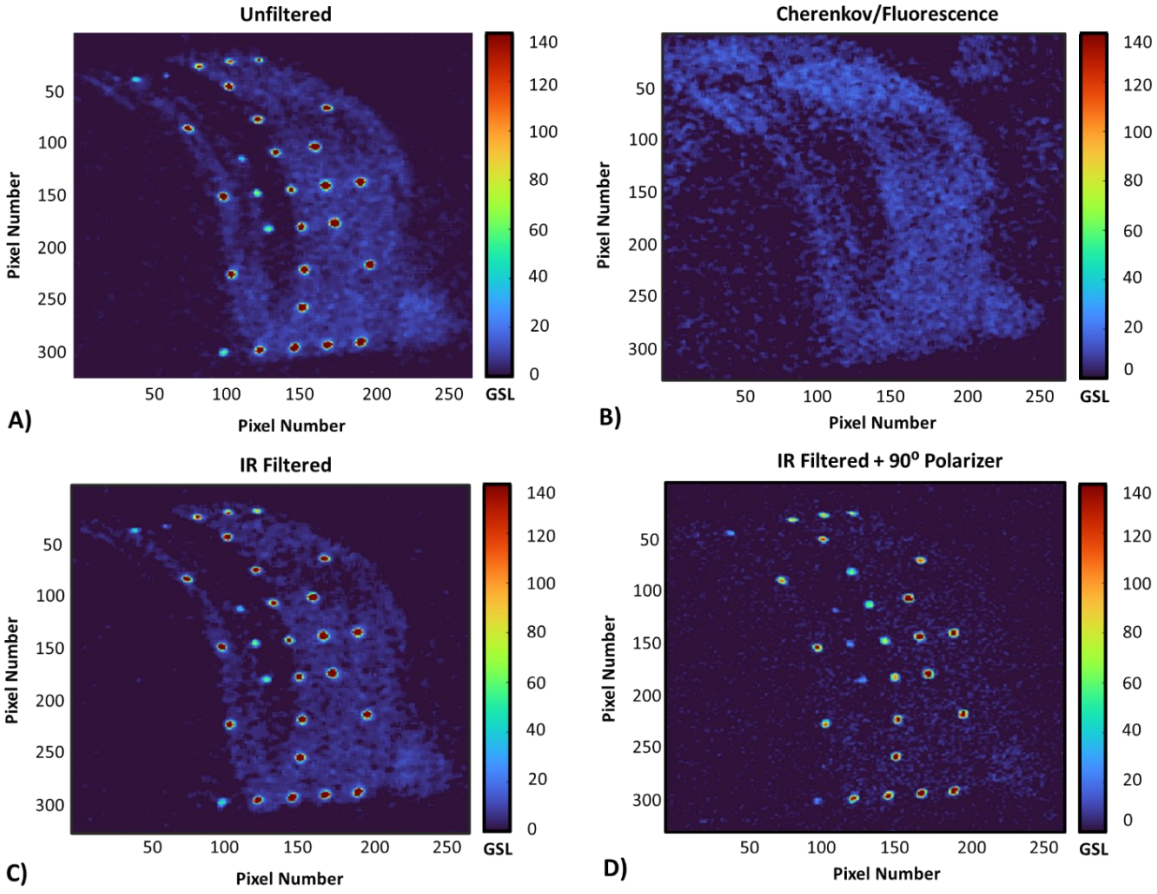

Figure 5.4: A) Unfiltered single frame captured during VMAT delivery showing the patient-specific array under irradiation, **B)** the corresponding frame for the PLA-only array, illustrating the Cherenkov/fluorescence signal in the absence of scintillation, **C)** the same frame with an optical IR filter, and **D)** the frame with both optical IR and polarizing filters.

However, despite efforts to mitigate Cherenkov contribution through the application of polarizing/optical filters and array material optimization, its complete removal proved infeasible. Consequently, a rotational calibration (section 5.4.6) becomes necessary to account for the variability of the radioluminescence background as a function of the incident beam angle. With the current methods the scintillation signal is approximately ~5-6 times greater than the observed radioluminescence signal of the PLA intermediary.

5.4.4 Data Processing

All data processing was executed using purpose built and standalone MATLAB (MathWorks, Massachusetts, United States) application, with each section employing its own dedicated code. As previously discussed, image processing occurred retrospectively following irradiation. Stereoscopic camera calibration was conducted during the initial setup prior to data collection.

5.4.4.1 Image Processing

The image processing code used in this study corrects optical artefacts arising from the camera image sensor and optics. As shown in Fig. 5.5, these artefacts include dark noise, background light contamination, stray radiation, vignetting, and lens distortion. The methods used for correcting these artifacts are based upon established techniques developed by other research groups[79,81,82] and the codes functionality is consistent with that of our earlier publication[20]. In summary, the code initially subtracts a median dark and background image from the raw images. The images are then filtered using a 1s rolling median filter and a 2 x 2 spatial median filter to mitigate noise induced by stray radiation. Finally, lens-related artifacts are then corrected with a geometric camera calibration process performed using multiple images of a checkerboard pattern and the camera calibration function of the MATLAB Computer Vision Toolbox[164].

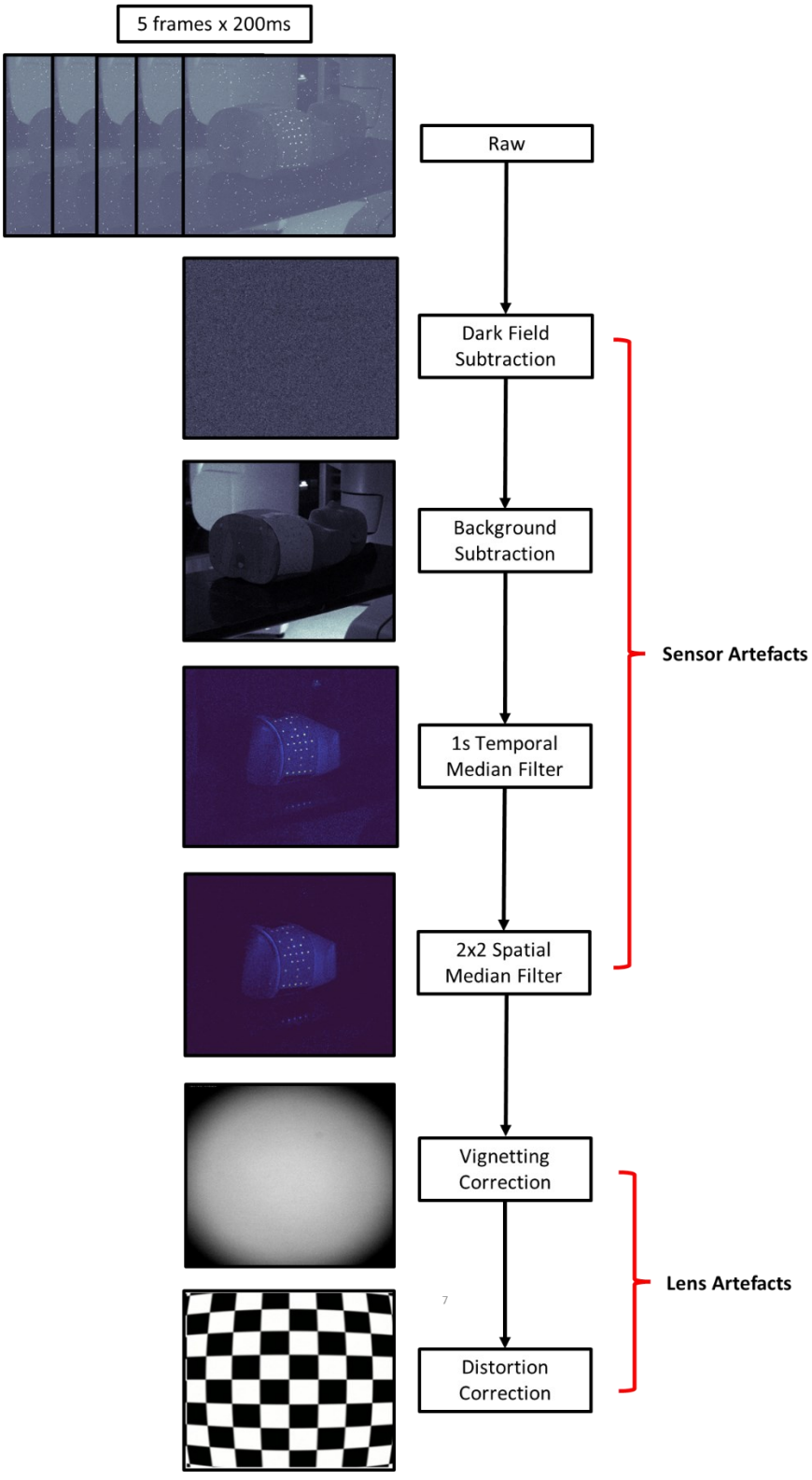

Figure 5.5: Illustration of the processing steps used to remove optical artifacts from the raw camera images.

5.4.4.2 Stereoscopic Camera Calibration and Depth Estimation

Perspective-based artifacts, arising from variations in the radial distance of each scintillating element to the camera, become non-negligible in scenarios involving non-planar array geometries or non-perpendicular imaging angles. Addressing these artifacts necessitates knowledge of each scintillator position and orientation relative to the camera. Fortunately, in addition to correcting the lens distortion of a single camera, when the camera calibration is performed for a pair of cameras it can provide additional information regarding the cameras' position and orientation relative to a global coordinate system. The process of extracting 3D spatial information from a pair of stereoscopic cameras is outlined in Fig. 5.6.

Doing so first requires the determination of the camera matrix (P), which maps the 3-D world coordinates (X, Y, Z) to the 2D image points (x, y).

$$W\begin{bmatrix} x \\ y \\ 1 \end{bmatrix} = P\begin{bmatrix} X \\ Y \\ Z \\ 1 \end{bmatrix}$$

The calibration algorithm calculates the camera matrix by using complimentary images of a planar calibration pattern from a pair of stereo-aligned cameras as shown in Fig. 5.7. The mathematical formulation detailing the algorithm's computation of the camera matrix is already presented in existing literature[163,164,199], and only a concise summary of its function is presented here.

To obtain the camera matrix, the algorithm uses the calibration images to determine both the intrinsic and extrinsic properties of each camera. The intrinsic properties are the essential optical characteristics of the camera that remain constant and are independent of its position and orientation in space such as its focal length (f_x, f_y), optical center (or principal point) (C_x, C_y), and the lens skew coefficient (s). The camera intrinsic matrix, K, is defined as:

$$K = \begin{bmatrix} f_x & s & C_x \\ 0 & f_y & C_y \\ 0 & 0 & 1 \end{bmatrix}$$

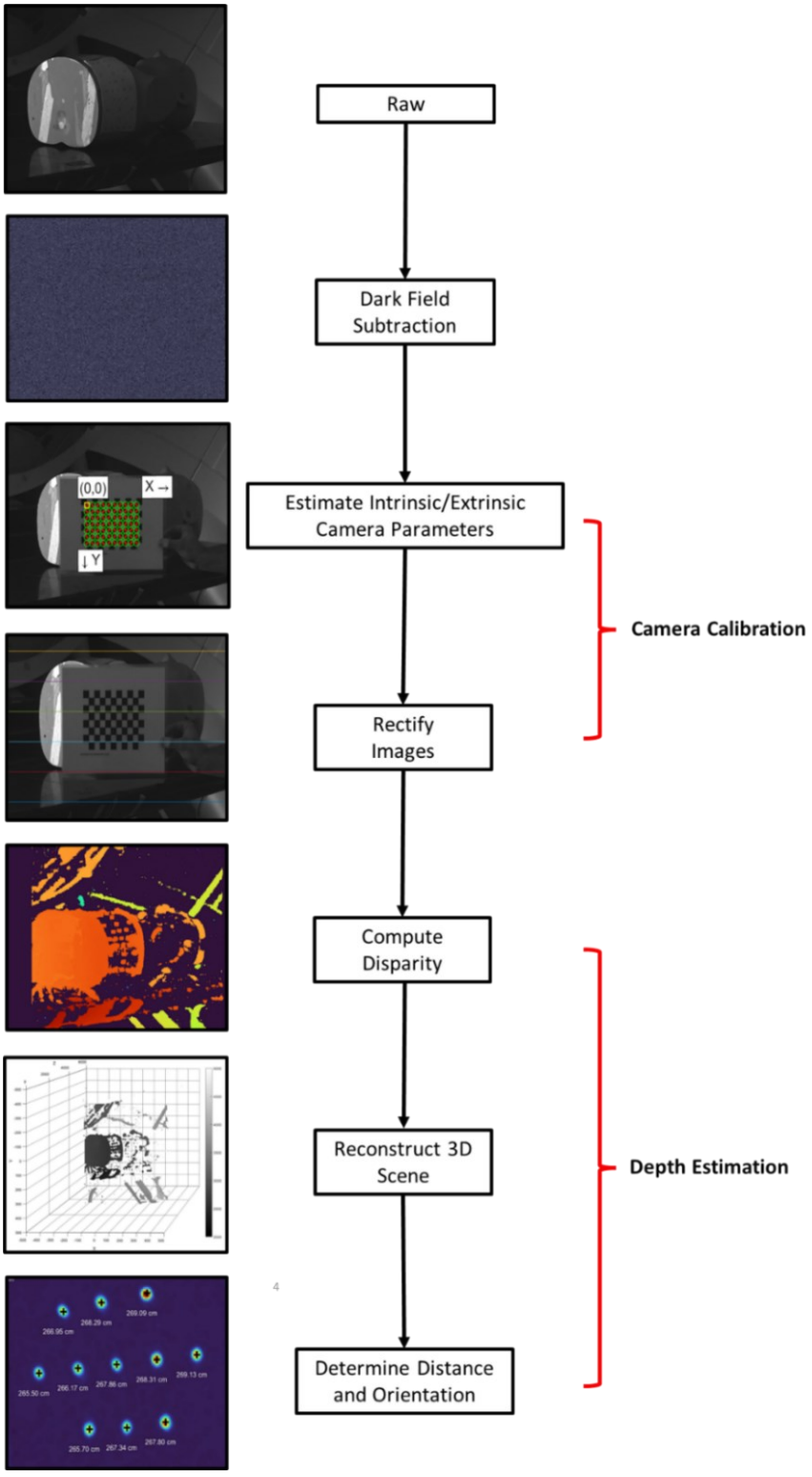

Figure 5.6: Illustration of the processing used for extracting 3D spatial information from a pair of stereoscopic cameras.

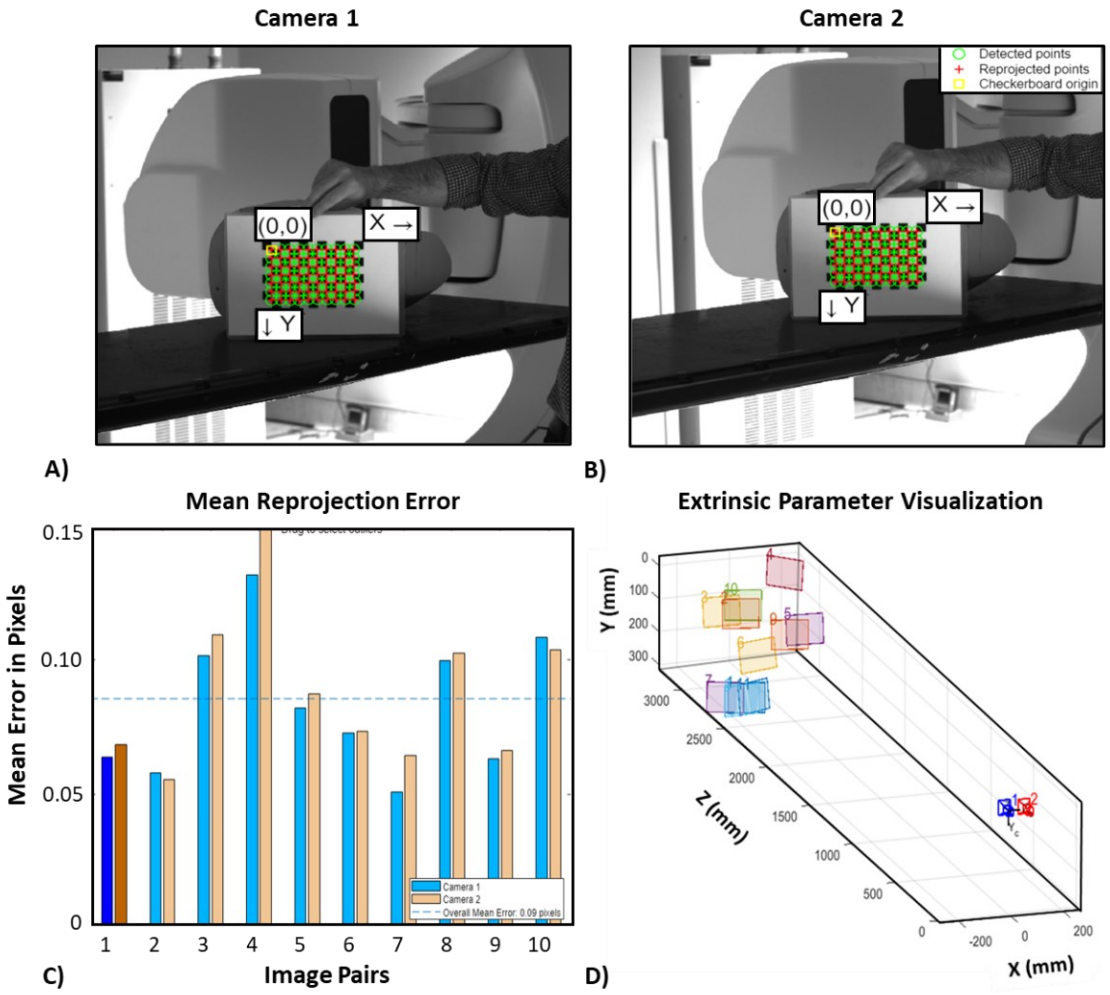

Figure 5.7: Labeled depiction of the stereoscopic camera calibration process. **A)** and **B)** demonstrate the identification of the checkerboard calibration pattern by each camera, **C)** showcases the reprojection error of the calibration, and **D)** presents the resulting 3D visualization of the various calibration checkerboard positions relative to the camera cameras with baseline X_c = 70.62 mm, Y_c = 12.17 mm and Z_c = 0.42 mm.

This represents a projective transformation that delineates the mapping from the 2D image coordinates to 3D camera coordinates. The extrinsic parameters then encapsulate a rigid transformation from the 3D camera coordinate system to the 3D world coordinate system. This transformation is embodied by rotation (R_θ) and translation (M) parameters, defining the orientation and position of the camera. The camera matrix is then,

$$P = K[R_\theta \; M]$$

After performing stereo calibration, the camera matrix enables image rectification[165]. This process aligns identical objects in each image along horizontal epipolar lines. Following rectification, any pair of corresponding points resides on the same pixel row. The distance or horizontal shift between conjugate pixels in the left and right images can then be determined algorithmically using semi-global matching[166]. This is referred to as the disparity map and it is proportional to the real-world distance of the corresponding point from the camera.

The 3D world coordinates of points corresponding to each pixel of the disparity map can then be reconstructed to produce a 3D surface map. These 3D world coordinates can also be used to compute the pitch, roll and yaw of each scintillator relative to the optical axis of camera 1 using the four-quadrant inverse tangent.

$$Pitch\ (\theta) = atan2(-x, y)$$

$$Roll\ (\phi) = atan2(x, z)$$

$$Yaw\ (\psi) = atan2(-z, y)$$

5.4.4.3 Element Contouring and Light Output Determination

Following optical artifact correction, the processed images are added together to produce a composite image of the full dose delivery. The image is then cropped using user defined coordinates to better visualize the array. Previously, a straightforward automated approach, leveraging the substantial signal disparity between the scintillators and the background, utilized their known pixel dimensions to position 25 x 25-pixel Regions of Interest (ROIs) to monitor each scintillator[20]. While effective for planar geometries, the influence of perspective in patient-specific geometries, encompassing both image depth and the obliquity of the measurement angle, results in each scintillator being represented by a varying number of pixels. Although not required in concept, for the purposes of this study manual contouring of scintillators was performed in MATLAB on pre-irradiation images. This manual approach allows for precise adaptation to the array's shape and accommodates perspective variations, ensuring accurate alignment of the contours with the curved geometry. Subsequently, the light output for each element is determined by calculating the total light output in Grey Scale Levels (GSL) within the user-defined boundary and is positioned at the center of each element.

5.4.5 Dosimetric Methods

The Varian Acurous XB (AXB) treatment planning algorithm is one of the most accurate dose calculation algorithms clinically available[200]. Since its release there have been many planning studies investigating the efficiency and accuracy of the AXB algorithm[142,144–146]. These studies have found AXBs dose prediction ability is comparable to Monte Carlo (~1-2%) and superior to other clinical dose calculation methods such as the Anisotropic Analytical Algorithm (AAA) particularly in heterogenous media. However, AXBs solutions are approximate resulting in a potential loss of accuracy compared to fully stochastic Monte Carlo solutions in certain clinical scenarios[200]. Despite this, the TPS remains the primary clinical tool for patient treatment planning and dosimetric verification. Therefore, for the purposes of this study, both Monte Carlo simulations and TPS calculations using the AXB algorithm were performed to provide a comprehensive and comparative assessment of surface dose.

The geometry used for both TPS calculations and Monte Carlo simulations was based on an axial CT scan (slice thickness 1.25 mm) of the array and patient phantom. To ensure array alignment between measurement and the TPS/Monte Carlo simulation geometry manual image registration was performed prior to all array measurements using cone beam computed tomography (CBCT).

5.4.5.1 Treatment Planning

Dose calculations were performed using the Eclipse TPS (Varian Medical Systems, Palo Alto, USA) AXB algorithm version 15.6.06. The volume of each scintillator was delineated using manual contouring performed within the TPS. Given that the BCF-10 scintillator is primarily composed of polystyrene, a density of 50 HU (1.05 g/cm^3) was assigned uniformly to each volume. The mean dose for each scintillator was then determined from its corresponding dose-volume histogram.

5.4.5.2 Monte Carlo Simulations

Monte Carlo simulations were conducted using the PRIMO Monte Carlo software[133] and Varian Truebeam 6 MV phase space files, scored above the accelerator jaws. In order to achieve and average dose uncertainty of ± 2% Monte Carlo simulations were performed with $2.1 * 10^{11}$ histories. Simulations were then calibrated from eV/g to dose in cGy following the procedure outlined in our previous publication[20]. Plan-specific parameters were then directly

exported from the TPS and imported into PRIMO. This included the planning CT, structure set, field arrangement and MLC patterns. Similarly to the TPS, the mean dose for each scintillator was determined using the associated contoured structure.

5.4.6. Array Dose Calibration

The dosimetric calibration of a patient-specific array introduces several factors not encountered when using planar arrays[20]. Patient-specific arrays have conformal geometries and require the cameras to be positioned at an oblique angle relative to the patient to ensure visibility of all scintillators and prevent occlusion by the gantry at specific beam angles. The scintillators are also placed on the surface of a phantom rather than at some depth relative to the beam axis. Therefore, even after correcting for optical artifacts, elements which receive the same dose may still exhibit different brightness attributable to differences in their distances from the camera and observation angles. One potential approach to mitigate perspective-based artifacts involves incorporating their correction into the calibration process. Despite being time-intensive, by performing the calibration in an identical geometry and orientation to the final measurements, the perspective correction would be accounted for by the calibration. This can be achieved using stereoscopic imaging of the array during both calibration and measurement to ensure consistent alignment of the camera's perspective.

To ensure the calibration is performed under similar dosimetric conditions we can leverage 3D printing to fabricate a piece of conformal backscatter (calibration block) for the array using the exterior contour of the patient. Using Adaptiiv's 3D Bolus software and the pre-established 3.0 mm bolus, a gel bolus mold was created and subsequently divided into two halves. The anterior segment of the mold was then exported as a CAD file and imported into CURA. The calibration block is composed entirely of white PLA and was printed using the same print parameters described in section **5.4.1**. The cumulative print duration for the calibration block was 23 hours and 16 minutes.

For calibration the array was placed on the 3D-printed calibration block with additional solid water placed behind it to provide backscatter as shown in Fig. 5.8. Stereoscopic surface imaging, facilitated by the calibrated cameras, was performed iteratively to align the cameras using the depth, pitch, roll, and yaw data of each scintillator obtained from the surface imaging of the array on the patient phantom.

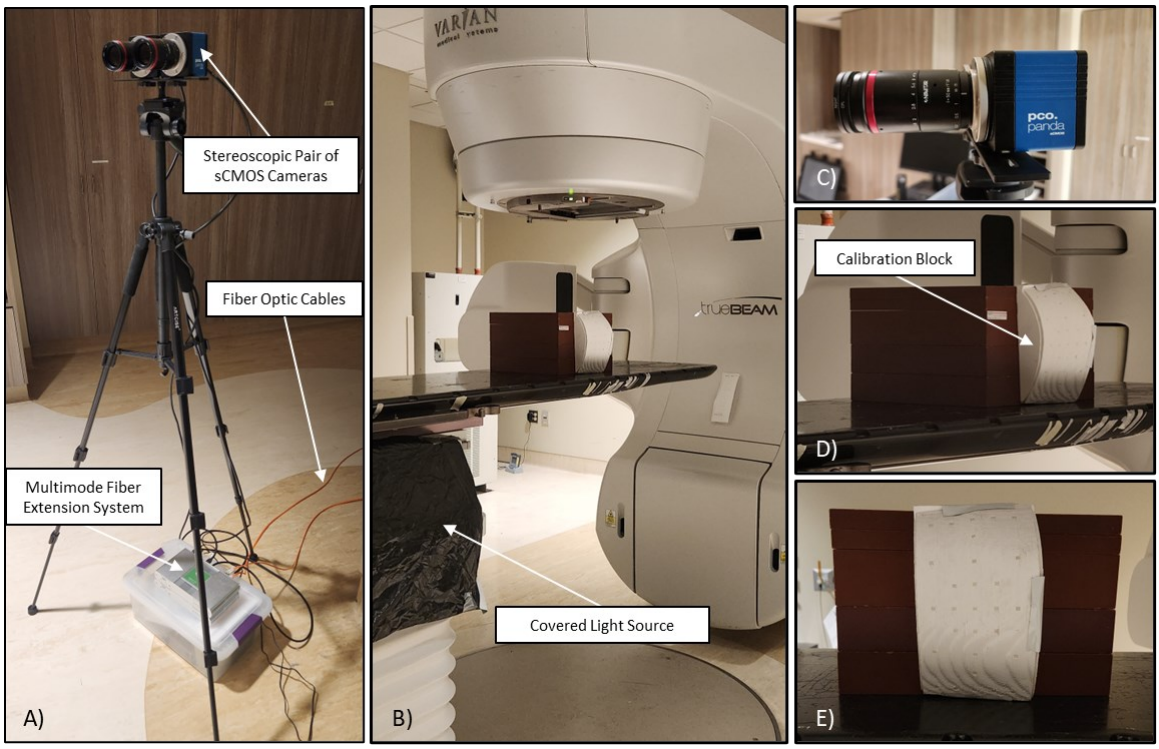

Figure 5.8: Images of array calibration (lighting remains on for visualization). **A)** Camera and tripod setup, including fiber extension system and optical fibers responsible for transmitting signals to the acquisition computer. **B)** Array calibration irradiation geometry, **C)** camera lens aperture and focal length settings as well as arrangement of optical filters. **D)** and **E)** close-ups of the array and calibration block, highlighting fit and orientation.

In practice, without a precise mechanical gantry, achieving exact alignment is infeasible. Analytical corrections are desirable to account for variations in observation angle and depth between calibration and measurement geometries. Investigation into the signal variations caused by the displacement of scintillating fibers observed by optical cameras have demonstrated that the distance to signal relationship of commercial scintillators obeys the inverse square law[199]. Additionally, rotation relative to the camera's optical axis was shown to decrease the collected signal according to a gaussian distribution[199]. To investigate the potential for such corrections, the distance to signal relationship for the patient specific array was assessed by displacing the tripod in 10 cm increments form its initial starting position (~270 cm from the array) for 100 cm. However, attempts to model the scintillator pitch and yaw angular dependence using a Gaussian function proved unsuccessful and is further discussed in section **5.6.2**.

Following alignment, each scintillating element in the array was calibrated to dose using the same methodology detailed in our previous work[20]. Each scintillator is assigned a unique calibration coefficient (C_{cal}) given by,

$$S_M \times C_{cal} = S_M \times \left(\frac{D_{Cal}}{S_{Cal}}\right) = D_M$$

Where S_M is the corrected total light output of a given scintillator in GSL, S_{Cal} is the corrected total light output of the same scintillator in the calibration geometry in GSL, D_{Cal} is the corresponding dose in cGy determine by Monte Carlo simulation of the calibration geometry and D_M is the final dose measurement in cGy.

For calibration the array was irradiated using a 6 MV photon field (Truebeam, Varian Medical Systems, Alto, USA) with collimator angle of 0°, 300 Monitor Units (MU), field size of 30 x 30 cm^2, dose rate of 600 MU/min and the isocenter positioned at the center of the calibration block. To assess the robustness and accuracy of the calibration process as well as identify any potentially angle-dependent discrepancies, the calibration irradiation was performed at gantry angles ranging from 310° to 150° in increments of ~ 25°. The start and end points of 310° to 150° were chosen as they coincide with the beam angles to be measured during treatment delivery (section **5.4.7**). The resulting calibration coefficients were then used to determine the measured dose for the clockwise arc of the VMAT delivery and assessed based on the average percent dose agreement between calibrated array measurement and Monte Carlo simulated dose. Additionally, the angular dependence of the calibration was examined for three identically printed patient-specific arrays to gauge the consistency and reproducibility of array manufacturing. The angular dependence of the calibration is further discussed in sections **5.5.1** and **5.6.2**. For the final dose calibration, a rotational calibration that spanned the beam angles to be measured was performed as it has been shown to enhance the robustness of the resulting calibration coefficients by averaging out the residual Cherenkov contribution to the measured signal at each angle.

5.4.7. Tangent Field Delivery

To evaluate the accuracy of the patient specific calibration two clinical chest wall treatment plans were delivered, both with an original prescription dose of 4000 cGy in 15 fractions. For the first case, two tangential 6 MV photon fields, oriented approximately 180 degrees apart

were created with planning considerations to avoid the contoured heart and lung structures while including the chest wall. Each angle consists of an open tangent field and one MLC blocked subfield as shown in Fig. 5.9 A with field-specific parameters summarized in Table 1.

Field	**MLC**	**Gantry Rotation**	**Collimator Rotation**	**Aperture X (cm)**	**Aperture Y (cm)**	**SSD (cm)**	**MU**
1	IMRT	325°	0°	13.2	7.2	90.0	163
2	IMRT	150°	0°	13.2	7.2	81.7	143

Table 5.1: Summary of field-specific beam parameters used for the tangent field dose delivery.

5.4.8. VMAT Delivery

The second case consisted of an arc plan representative of a VMAT chest wall treatment (Fig. 5.9 B). The MLC patterns were algorithmically determined by the optimizer, with arc angles tailored to the contoured PTV. The field-specific parameters are summarized in Table 2. Despite the common practice in VMAT chest wall plans to incorporate skin flash accommodating breathing and setup uncertainties, this practice is not included in this specific treatment plan.

Field	MLC	Gantry Rotation	Collimator Rotation	Aperture X (cm)	Aperture Y (cm)	MU
CW	VMAT	310° CW 150°	20°	13.3	15.0	244
CCW	VMAT	150° CCW 310°	340°	11.3	14.1	186
CCW2	VMAT	150° CW 310°	355°	11.6	14.5	160

Table 5.2: Summary of field-specific beam parameters used for VMAT dose delivery.

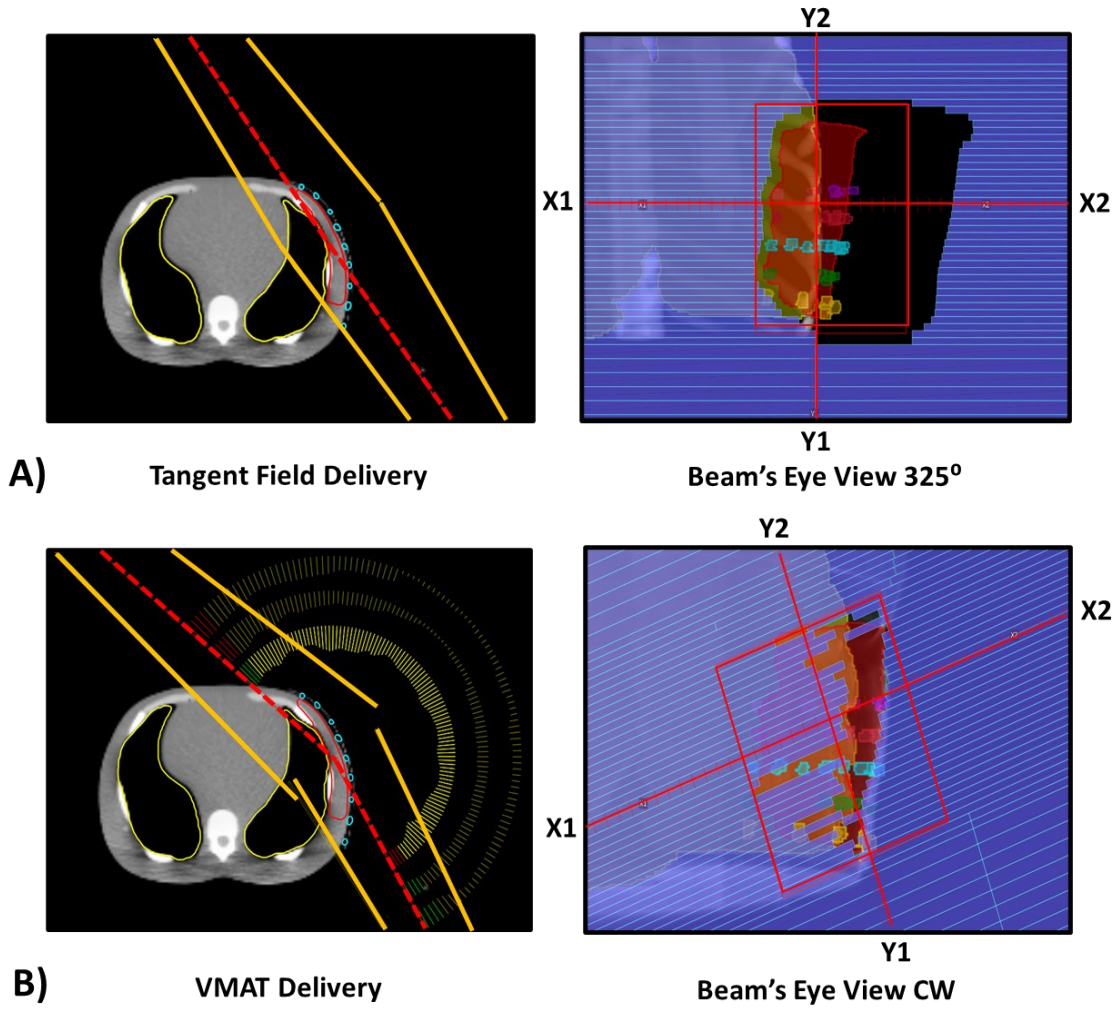

Figure 5.9: Illustration of the field arrangement and MLC apertures for **A)** tangential filed delivery and **B)** VMAT delivery.

5.5 RESULTS

5.5.1 Array Dose Calibration

Fig. 5.10 illustrates the depth pitch, roll, and yaw for the central nine array elements, derived from the average results of three repeated setups, with error bars indicating the range of minimum to maximum values. This data highlights the possible alignment agreement achievable between the camera in the calibration and measurement geometries. The average difference in scintillator depth between calibration and measurement phases was found to be 0.95 cm with a min/max range of 0.53 cm to 1.47 cm. Furthermore, the assessment of perspective alignment, determined through pitch, roll, and yaw measurements at the center of

each scintillator, revealed average differences of 0.19^{o} (0.17^{o} - 0.22^{o}), 0.20^{o} (0.17^{o} - 0.23^{o}) and 0.30^{o} (-0.18^{o} - 0.72^{o}), respectively.

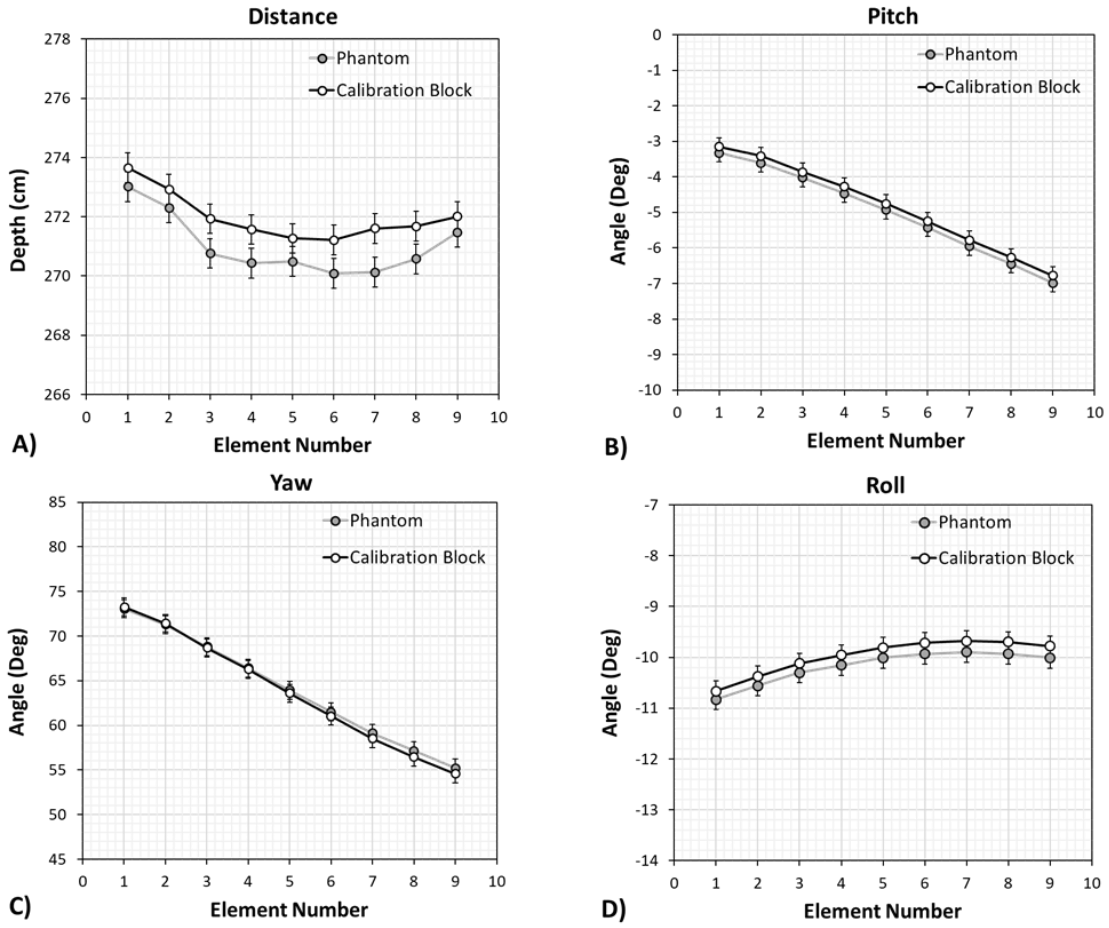

Figure 5.10: Comparison of the measured depth, pitch, roll, and yaw for the central nine array elements for the phantom measurement and array calibration.

Fig. 5.11 depicts the average normalized total light intensity for all 29 scintillators as a function of distance from the array. Evaluation of the arrays distance-to-signal relationship revealed an average percent deviation from the ideal inverse square dependence of 1.0% ± 1.2% for camera 1 and 1.2% ± 1.4% for camera 2.

The data presented in Fig. 5.12 illustrates the angular dependence of the calibration process for the three identically printed patient-specific arrays. It delineates the average percent dose difference between Monte Carlo simulation and dose measurements performed using all 29 scintillators at each of the gantry angles tested. The error bars delineate the range of

minimum to maximum single-element percent deviation, while the dashed line represents the average percent dose dependence for the array across all angles.

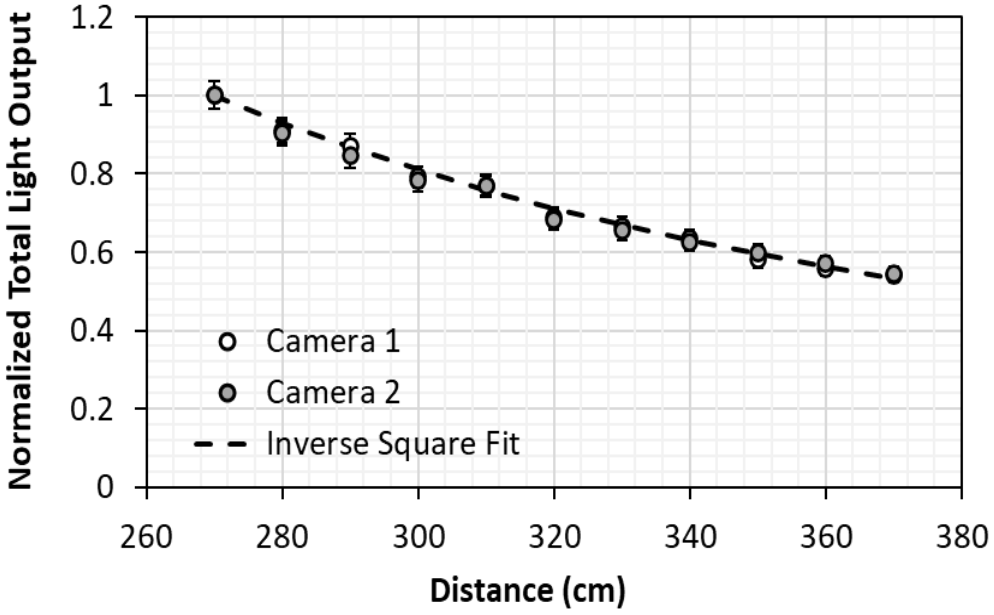

Figure 5.11: Distance-to-signal relationship of the patient-specific array.

Notably, a consistent pattern is observed across arrays manufactured with identical print parameters. For Array 1, the average angular percent dose dependence was 0.5% ± 4.8%, with a minimum single-element deviation of -18.6% occurring at gantry angle 104° and a maximum of 15.7% at gantry angle 335°. Array 2 exhibited an average angular percent dose dependence of -0.4% ± 4.5%, with a minimum single-element deviation of -17.2% at gantry angle 104° and a maximum of 15.7% at gantry angle 310°. Array 3 demonstrated an average angular percent dose dependence of 0.8% ± 5.2%, with a minimum single-element deviation of -18.7% at gantry angle 104° and a maximum of 15.8% at gantry angle 310°.

Following rotational calibration, the resulting element specific calibration coefficients for camera 1 (Fig. 5.13 D) showed an average value of $3.19*10^{-4}$ cGy/GSL ± $1.22*10^{-4}$ cGy/GSL. The minimum value of a calibration coefficient was $1.75*10^{-4}$ cGy/GSL, with a maximum value of $6.99*10^{-4}$ cGy/GSL.

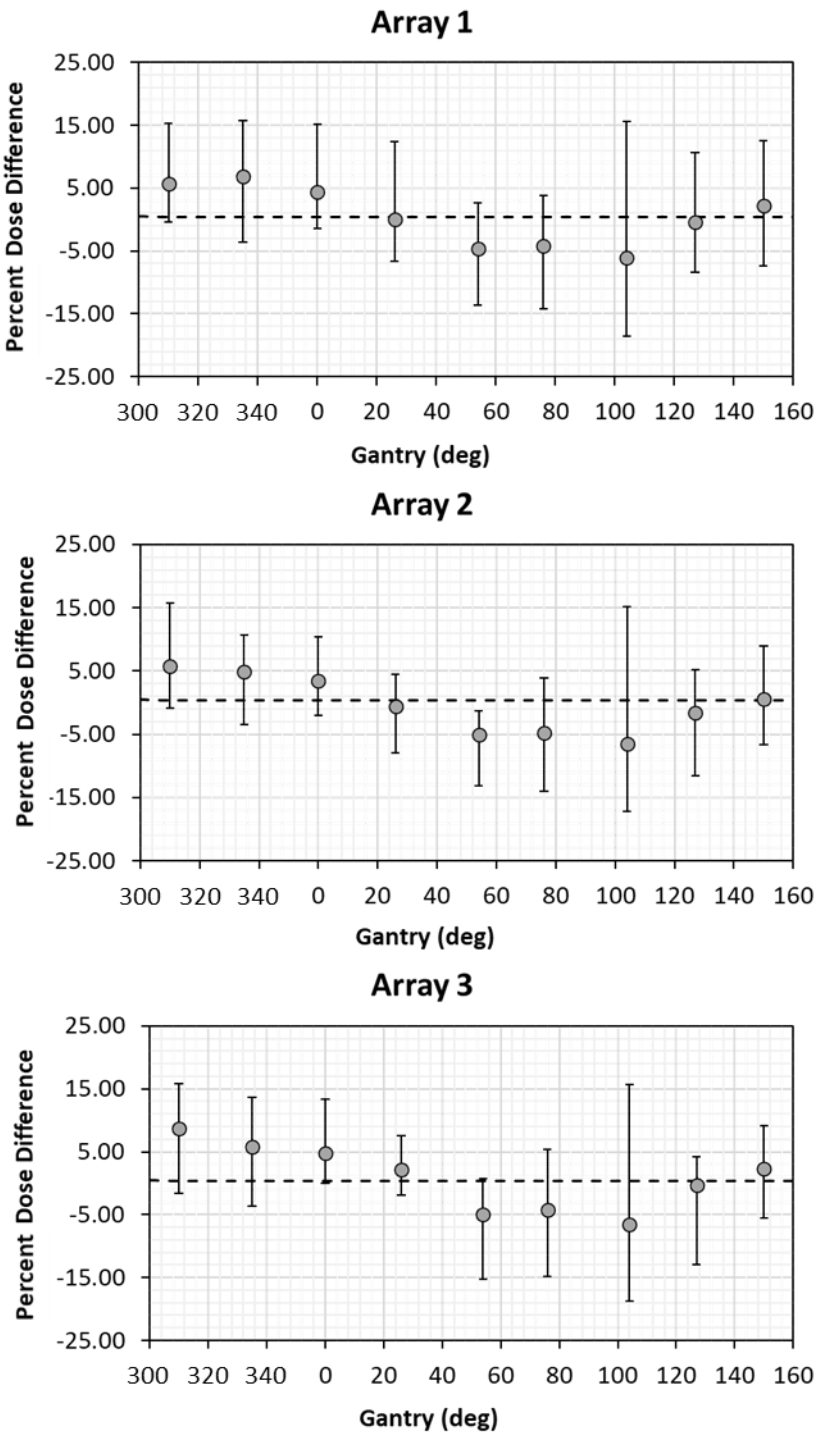

Figure 5.12: Angular dependence of array calibration for three identically printed patient-specific arrays, showing the average percent dose difference between Monte Carlo simulation and array measurement at tested gantry angles. Error bars indicate the range of single-element percent deviation, with the dashed line representing the average percent dose dependence across all angles.

5.5.2 Tangent Field Delivery

Fig 5.14 B) and C) show the horizontal and vertical dose profiles respectively for the cumulative tangential dose delivery. The expected variation in dose to the scintillators determined from the treatment plan ranges from a minimum of 47.5 cGy to a maximum of 256.8 cGy. The corresponding array measurements demonstrated a range of doses from a minimum of 58 cGy to a maximum of 288.9 cGy. The average dose difference between the TPS calculated dose and the dose measured by the array elements was 29.6 cGy ± 23.1 cGy with a minimum difference of -12.8 cGy and maximum difference 72.1 cGy. The average percent dose difference between the TPS calculated dose and array was 15.1% ± 9.6% with a minimum percent difference of 0.5% and maximum percent difference 33.2%. The average percent dose difference between MC simulations and TPS calculations was 10.7% ± 7.1%.

Correspondingly, the variation in dose to the scintillators determined by Monte Carlo simulation ranges from a minimum of 53.80 cGy to a maximum of 272.8 cGy. The average dose difference between the Monte Carlo simulated dose and the dose measured by the array elements was 8.0 cGy ± 11.5 cGy with a minimum difference of -17.9 cGy and maximum difference 27.3 cGy. The average percent dose difference between the Monte Carlo simulated dose and measurements was 2.4% ± 4.6%. with a minimum percent difference of -7.1% and maximum percent difference 11.4%. The average absolute percent dose difference between the Monte Carlo simulated dose and measurements was 4.6% ± 3.4%. The distribution of these differences is illustrated in Fig 5.15 C) with a maximum absolute percent dose difference of 11.3%.

5.5.3 VMAT Delivery

Fig 5.14 E) and F) show the horizontal and vertical dose profiles respectively for the cumulative VMAT dose delivery. The expected variation in dose to the scintillators determined from the treatment plan ranges from a minimum of 44.8 cGy to a maximum of 195.8 cGy. The corresponding array measurements demonstrated a range of doses from a minimum of 51.8 cGy to a maximum of 214.0 cGy. The average dose difference between the TPS calculated dose and the dose measured by the array elements was 15.6 cGy ± 13.5 cGy with a minimum difference of -13.4 cGy and maximum difference 38.8 cGy. The average percent dose difference between the TPS calculated dose and array was 11.1% ± 9.3%. with a minimum

percent difference of -3.4% and maximum percent difference 33.2%. The average percent dose difference between MC simulations and TPS calculations was 11.0% ± 8.2%.

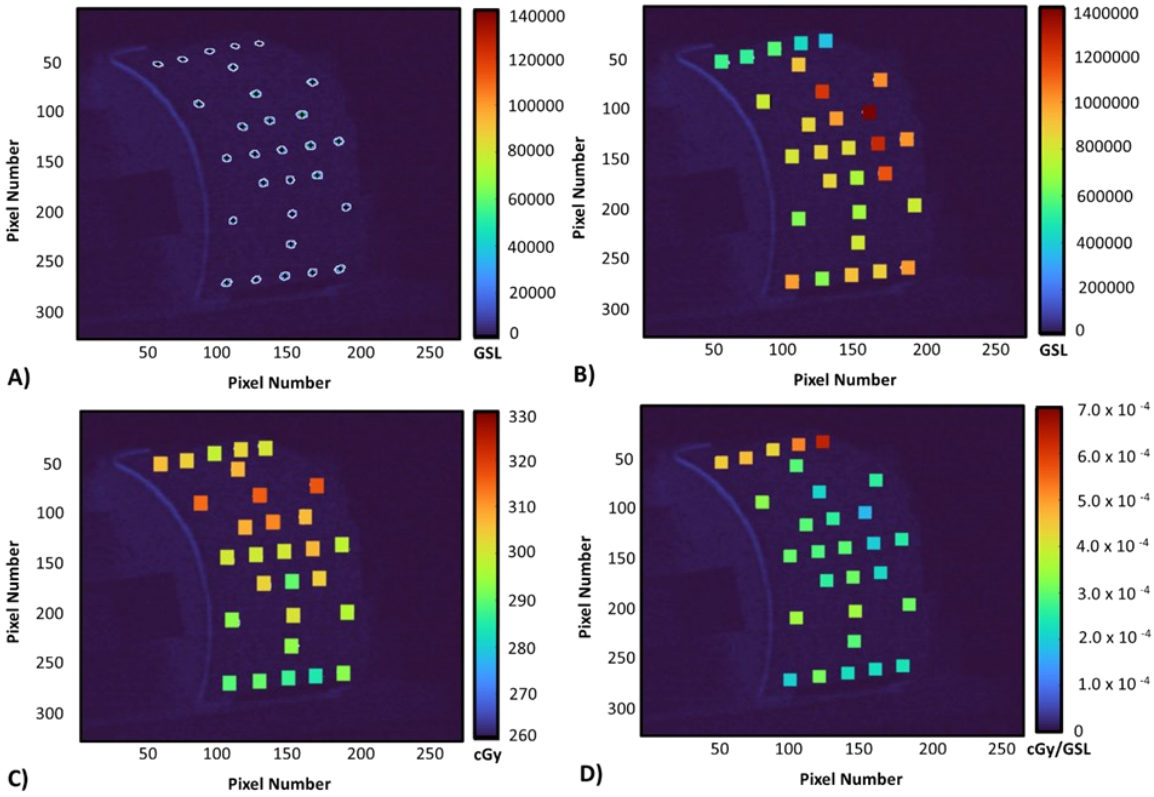

Figure 5.13: **A)** Final corrected image of the patient specific array calibration illustrating the contoured locations of all scintillating elements, **B)** extracted total light output for each array element, **C)** Monte Carlo simulated dose and **D)** calculated calibration coefficients for each array element.

Correspondingly, the variation in dose to the scintillators determined by Monte Carlo simulation ranges from a minimum of 51.3 cGy to a maximum of 217.8 cGy. The average dose difference between the Monte Carlo simulated dose and the dose measured by the array elements was -0.5 cGy ± 9.4 cGy with a minimum difference of -19.2 cGy and maximum difference 21.6 cGy. The average percent dose difference between the Monte Carlo simulated dose and measurements was 0.2% ± 5.8% with a minimum percent difference of -11.5% and maximum percent difference 11.7%. The average absolute percent dose difference between the Monte Carlo simulated dose and measurements was 4.4% ± 3.8%. The distribution of

these differences is illustrated in Fig 5.15 F) with a maximum absolute percent dose difference of 11.8%.

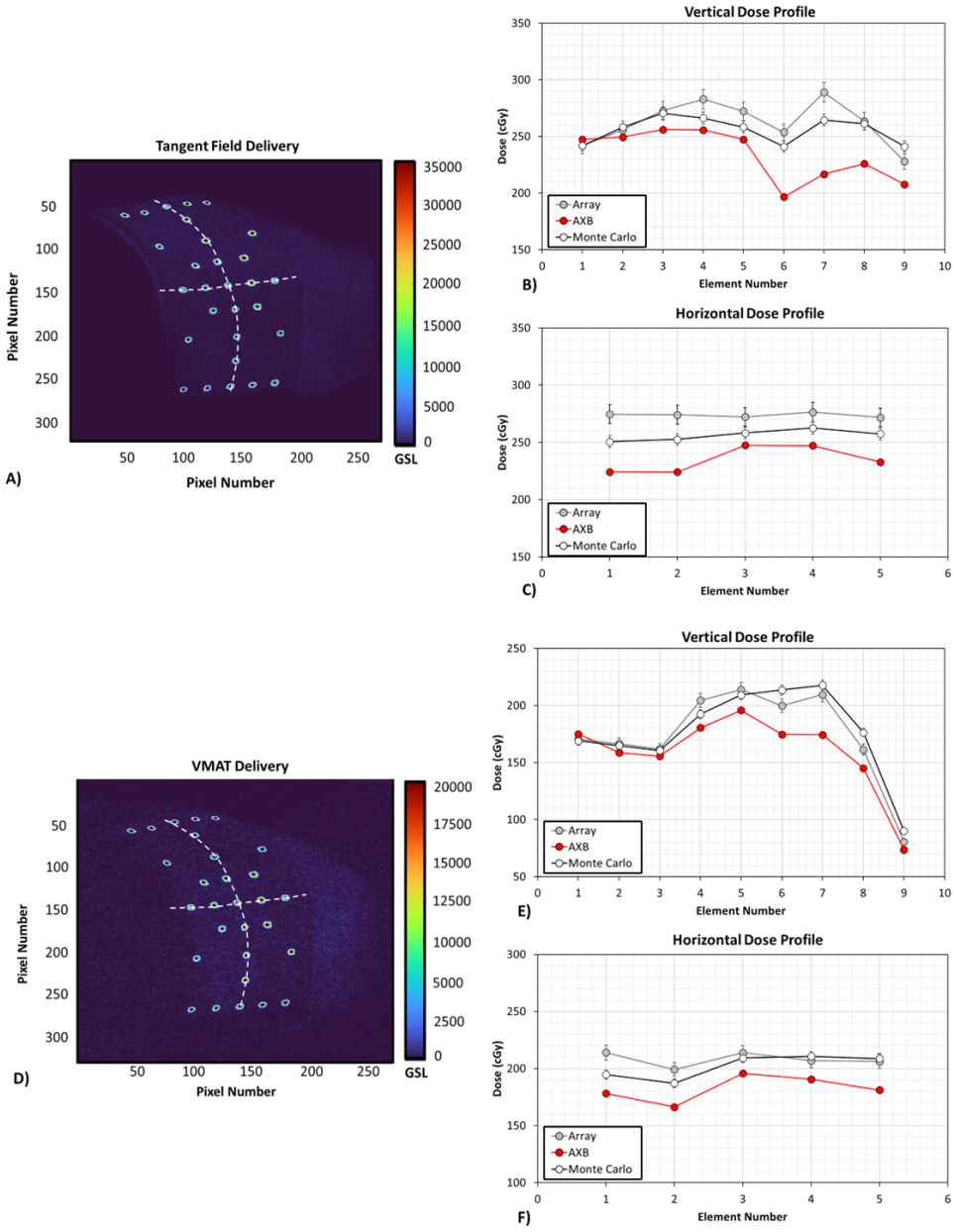

Figure 5.14: A) Image of array under irradiation by 325° tangential field showing the contoured locations of all scintillating elements, **B)** vertical dose profile (dashed line) of calibrated array compared to other dosimetric methods and **C)** corresponding horizontal dose profile (dashed line). **D)** Image of array under irradiation by CW VMAT field showing the contoured locations of all scintillating elements, **E)** vertical dose profile (dashed line) and **F)** corresponding horizontal dose profile (dashed line).

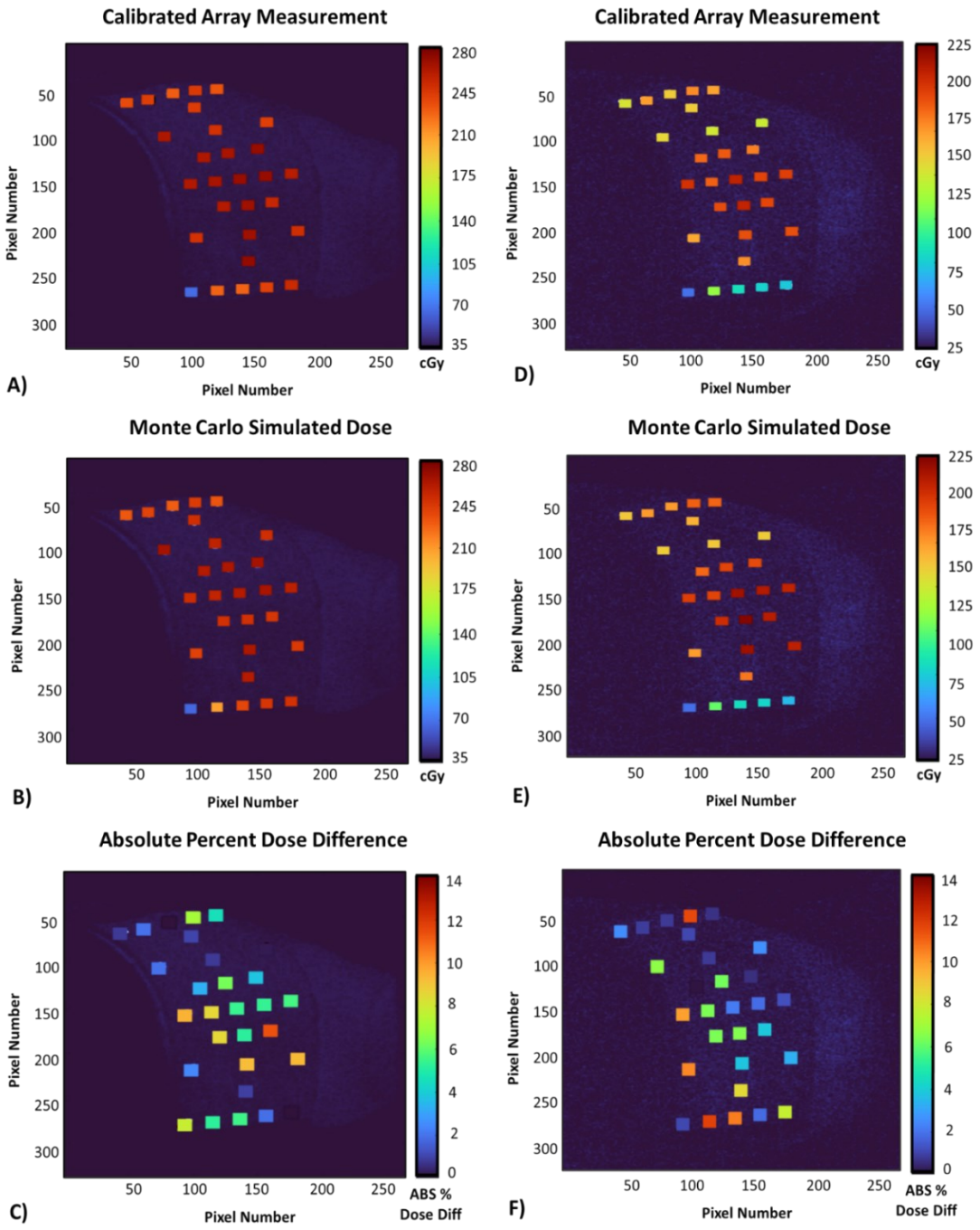

Figure 5.15: A) Calibrated array dose measurement of tangential field plan, **B)** corresponding Monte Carlo simulated dose distribution and **C)** the absolute percent dose difference between the simulated dose and the dose measured using the calibrated array. **D)** Calibrated array dose measurement of the VMAT delivery, **E)** corresponding Monte Carlo simulated dose distribution and **F)** the absolute percent dose difference between the simulated dose and the dose measured.

5.6. DISCUSSION

This study presents the first application of dual-material FDM 3D printing for the fabrication of a patient-specific radiation detector. This research establishes a methodology for 3D printing scintillating arrays tailored to individual patients and outlines a procedure for wireless dosimetric calibration. Its overarching goal is to contribute to the development of a patient-specific dosimeter, capable of addressing the practical challenges involved in achieving accessible real-time and multi-point *in-vivo* dosimetry within a clinical setting.

5.6.1 3D Printing of Patient Specific Scintillator Arrays

This investigation highlights the feasibility of employing dual-material 3D printing to fabricate patient-specific scintillator arrays. These arrays are based on medical imaging data and could also be derived from optical surface imaging of the patient, eliminating the need for dedicated medical imaging procedures for design purposes. The customizable placement of scintillating elements, guided by the patient's radiotherapy treatment plan, allows for adaptive sampling in regions of varying dose, high dose gradients, or proximity to critical structures. Our method also offers versatility in customizing the size and shape of scintillating elements, with the option to adapt designs to specific requirements. However, altering scintillator element size should be carefully considered due to its potential impact on the SNR and low dose sensitivity. The choice of PLA color is also crucial, as it effects the observed radioluminescence and therefore the dose accuracy of the resulting scintillator array by introducing unwanted background noise.

Ensuring conformity to the patient's external surface is essential for accurate surface dose measurement. CT scans of the 3D printed array on the patient phantom underscore the conformal nature of the array, revealing no significant air gaps (> 3 mm). This precision of fit aligns with that of existing 3D printed chest wall boluses[201], ensuring accuracy in array application. The printed array's dimensional accuracy, assessed through three repeat prints, displayed deviations of ± 1 mm along the layering direction and ± 0.5 mm perpendicular to it, affirming the reliability and consistency of the printing process. The array also demonstrates excellent layer adhesion ensuring structural integrity and durability despite its 3 mm thickness. This characteristic enhances impact resistance, safeguarding the array against potential damage from accidental drops or impacts.

Despite prolonged exposure to radiation over the course of this study the scintillators exhibited no signs of yellowing or degradation. Although the study did not involve delivering high ablative doses, this underscores the robustness of the scintillator material. This indicates that for a standard fractionated course of radiotherapy, scintillator degradation leading to drift or invalidation of the calibration over the treatment duration is unlikely.

Finally, manual contouring poses challenges due to the limited Hounsfield Unit (HU) contrast between scintillators and PLA, both materials approximating water equivalence. A preferable calibration method would involve using Monte Carlo simulation with a synthetic CAD model[20]. While the array possesses a 3D CAD model, the calibration geometry lacks a comparable representation. In the past, the array's simple planar calibration geometry was easily replicated using basic geometric shapes[20]. However, this method proves unsuitable for complex patient-specific arrays. An alternative solution lies in optical surface imaging of the array on the patient, facilitated by the existing camera system. This approach could offer a means to generate a simulation geometry representative of the patient's surface, overcoming the challenges associated with complex array irradiation geometries.

5.6.2 Array Dose Calibration

Practical dosimetric calibration of patient-specific arrays presents unique challenges, particularly with respect to the arrays' conformal geometry and the need for cameras to be positioned at oblique angles relative to the patient. Even after correcting for optical artifacts, a notable challenge arises elements receiving the same dose may still exhibit different brightness levels due to variations in their distances from the camera and observation angles. To address this issue, our study explores integrating the correction of perspective-based artifacts into the calibration process. In this study, it was achieved by ensuring a precise match between the calibration setup and the phantom geometry. This involved the 3D printing of a calibration block and integrating stereoscopic imaging during both calibration and measurement, to ensure consistent alignment of the camera's perspective.

For patient-specific array geometries, incorporating stereoscopic imaging during the initial fit assessment could provide the required spatial information needed for calibration, meaning it could be integrated into existing clinical workflows. This approach also holds promise for enabling real-time motion tracking by leveraging stereoscopic imaging data acquired during *in-*

vivo dose measurement. It is important to note that while stereo camera calibration using the checkerboard pattern was performed prior to measurements in this study, this does not necessitate conducting the camera calibration before every patient session. For a system fixed within the treatment room, calibration would be required as a commissioning task, supplemented by a monthly quality assurance check. This periodic assessment designed to detect and address any potential drift or geometric alterations in the camera alignment.

Despite this, the current array calibration, though not reliant on the patient, faces challenges in routine implementation due to the time-intensive nature of 3D printing the calibration block. The calibration process also requires significant patient-specific geometric information, potentially leading to inefficiencies in clinical workflows and delays in the case of print failure. Ideally, one would want a patient-specific detector with a patient agnostic standardized calibration. Doing so may require moving away from rigid bolus array designs entirely and opting for deformable arrays. These arrays, utilizing either a flexible intermediary material or a rigid material with an interlocking design, could conform to any desired surface. Some examples are shown in Fig. 5.16, the interlocking array has dimensions of 5 mm x 170 mm x 170 mm with 49 scintillating elements (size ~5 mm (thickness) x 15 mm x 15 mm). The mesh array has dimensions of 1 mm x 130 mm x 200 mm with 154 scintillating elements (size 0.5 mm 5 mm x 5mm). Preliminary investigations have also confirmed the feasibility of 3D printing arrays composed of flexible intermediary materials using thermoplastic polyurethane (TPU), thermoplastic polyamide (TPA) and polyethylene terephthalate glycol (PETG) of varying shore hardness. With this method, a single calibration would suffice, and the arrays could potentially be applied to multiple patients. However, doing so requires an understanding of the effect of changes in camera perspective, primarily translation and rotation, on the observed scintillator light output.

In this study we demonstrated the distance-to-signal relationship for 3D-printed scintillators adheres to the inverse square law. This result is consistent with that observed for commercial scintillators[199]. These findings indicate a correction of the form,

$$D_M = S_M \times \left(\frac{CDD_M}{CDD_{Cal}}\right)^2 \times \left(\frac{D_{Cal}}{S_{Cal}}\right)$$

could be applied to account for variations in scintillator light output resulting from depth changes between calibration (CDD_{Cal}) and measurement (CDD_M). However, the perspective-to-signal relationship remains uncharacterized. Initial investigations into camera rotations demonstrated appropriate calibration when perspectives align, but large deviations (~15%-20%) arise with distinctly different camera perspectives. While measuring the pitch, roll, and yaw of a scintillator proved feasible for alignment, isolating, and moving the camera incrementally along each rotational axes at a precise sampling interval proved challenging with the current camera tripod. A more reliable approach would involve using a motorized tripod to provide translations and rotations for the camera system. Comparable investigations using a small robot arm have been performed for scintillating fibers observed by optical cameras[199]. Assumed to behave like a Lambertian surface, rotation relative to the camera's optical axis was shown to decrease the collected signal according to a gaussian distribution. Given the known anisotropy of 3D-printed scintillators[179], dependent on their measurement surface, it is probable that the perspective-to-signal relationship as a function of pitch, roll and yaw is complex and not well modeled by a gaussian distribution. The layered construction of 3D printed scintillators suggests that rotation along the layering direction (yaw) verses across (pitch) may result in distinctly different responses. Monte Carlo simulations of layered scintillators, followed by optical photon transport simulations, could also assist in determining whether artifact correction is solely dependent on print parameters and can be applied to multiple arrays or if it is influenced by patient-specific geometric factors.

Finally, the selection of the calibration irradiation angle was shown to have a discernible impact on the average percent dose agreement with Monte Carlo in subsequent measurements. The observed discrepancies prompted consideration of various potential contributing sources such as non-diffuse light within the treatment room that is partially obstructed by the gantry at specific angles, or an anisotropic scintillator response associated with the 3D printing process. However, this discrepancy persists despite exhaustive removal of all treatment room lighting and remains consistent across various 3D-printed arrays. In our previous work we hypothesized that errors may be introduced into the scintillation light to dose conversion process, due to differences in the cameras' Cherenkov light collection efficiency in the calibration versus the measurement conditions[20]. In our previous work[20], such angular

dependence was not observed, this is attributable to the scintillators now being placed on the surface of a phantom rather than at some depth parallel to the beam axis.

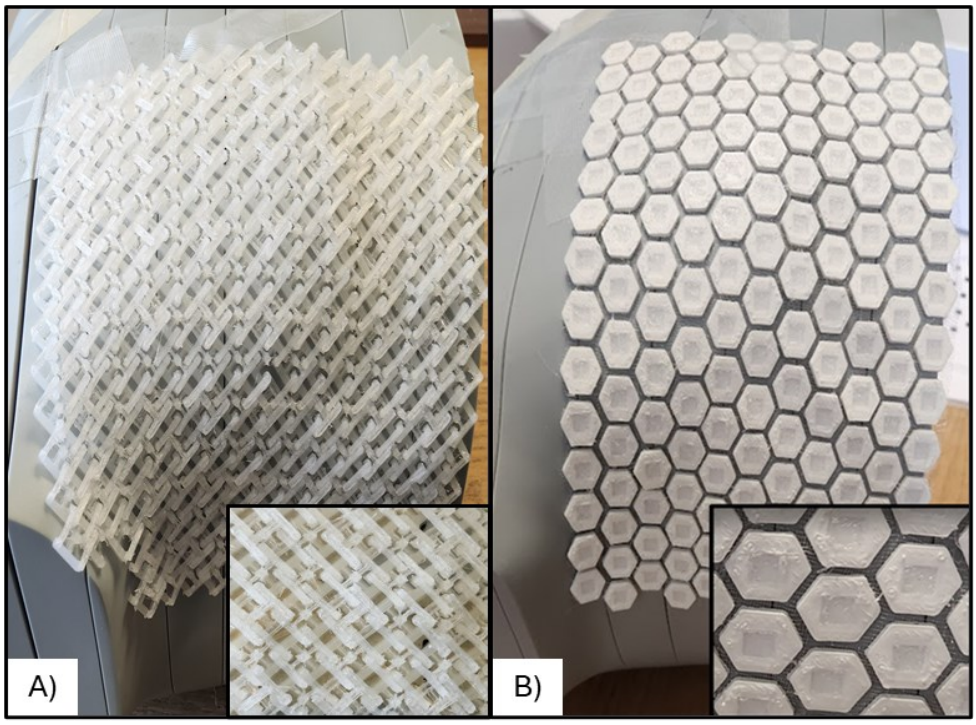

Figure 5.16: Images of flexible 3D printed array prototypes conforming to the exterior of a patient phantom **A)** interlocking scintillator array, **B)** scintillator array created using embedded lightweight nylon mesh.

5.6.3 Tangent Field Delivery

Following dosimetric calibration, surface dose measurements of tangential photon fields performed using the calibrated array exhibited close agreement with Monte Carlo simulated doses, with an average percent dose difference of 2.4% ± 4.6%. The rotational calibration process plays a crucial role in enhancing the accuracy of the resulting array measurements. Due to the variability of the Cherenkov background in the case of static tangential fields a field-to-field approach may be preferable for calibration. While this could offer increased dose accuracy, it is at odds with the objective of achieving a calibration method that is universally applicable across various patients.

Comparison with TPS-calculated doses revealed an average percent dose difference of 15.1% ± 9.6%. This disparity emphasizes the greater degree of agreement between array measurements and Monte Carlo simulations. This result is expected as the calibration method

relies on Monte Carlo simulations rather than TPS calculations. It is also worth noting the average percent dose difference between MC simulations and TPS calculations was 10.7% ± 7.1%. This suggests that the difference observed between array measurements and TPS calculations is indicative of both the arrays inherent measurement uncertainty (~5%) and the average discrepancy between Monte Carlo simulations and TPS calculations (~10%).

Recent investigations comparing PRIMO Monte Carlo simulations using Varian 6MV phase space files and AXB calculations for clinical IMRT and VMAT plans have demonstrated good agreement across various treatment sites. With 3D gamma pass rates (3%/2mm) on average greater than 99% for both whole body and PTV[137]. However, these high pass rates may not fully reflect differences observed within boundary regions. Discrepancies between AXB and Monte Carlo have been noted in regions of high heterogeneity, with reported differences ranging from 1% - 10% for lung/bone interfaces[142,200,202] and 1% - 40% for surface/buildup regions[142,203]. The reported level of agreement between AXB and Monte Carlo within the build up region may also be influenced by a given studies definition of surface thickness, dose calculation grid size[204] and potential differences in the modeling of electron contamination, flatting-filter, and head scatter[140,142].

5.6.4 VMAT Delivery

Following calibration, dose measurements for a three-arc clinical VMAT plan exhibited an average percent dose difference of 0.2% ± 5.8%. Despite gantry rotation and the dynamic use of MLCs inherent to VMAT deliveries, this result is comparable to the fixed tangential beam arrangement. In the fixed beam scenario, the average percent dose difference between Monte Carlo simulated doses and array measurements was 2.4% ± 4.6%. Comparison between VMAT data to TPS calculations reveals discrepancies of similar magnitude to those observed in the tangential delivery. The average percent dose difference between TPS-calculated doses and array measurements for VMAT was 11.1% ± 9.3%. This indicates that, despite the dynamic nature and inherent complexities of VMAT deliveries, the dose measurement discrepancies are comparable to those observed in fixed beam arrangements 15.1% ± 9.6%.

5.7 CONCLUSION

In this study, we demonstrated the capability of FDM 3D printing to produce patient-specific plastic scintillator arrays. The method's flexibility and precision permit the creation of

a variety of user specified designs and position it as a promising avenue for detector development in radiation dosimetry. Subsequently, we demonstrated a wireless dosimetric calibration method for patient specific array geometries that employs both 3D printing and stereoscopic imaging. Following array calibration, surface dose measurements of two clinical chest wall treatment plans (tangential field and VMAT) were on average within 5% - 10% of the Monte Carlo simulated doses. However, barriers to routine clinical implementation remain and addressing these challenges is crucial for maximizing the utility of this detector technology for routine clinical *in-vivo* dosimetry.

CHAPTER 6 CONCLUSIONS

6.1 SUMMARY

This work aims to develop a detector capable of fulfilling the unmet clinical need for accessible, routine, and real-time *in-vivo* dosimetry. The detector system consists of a 3D-printed patient-specific array of plastic scintillators, which can be measured wirelessly, enabling comparison between patients measured and planned surface doses. Chapter 3 of this study focuses on the feasibility of using FDM 3D printing to fabricate individual scintillators and provides a characterization of the detector material, both crucial initial steps. Chapter 4 demonstrates the ability of dual-material FDM 3D printing to create arrays containing tens to several hundreds of scintillators and presents a means of wirelessly calibrating and measuring simple array geometries. Finally, Chapter 5 facilitates the production of customized, high-resolution plastic scintillator arrays with patient-specific geometries. It also demonstrates that integrated stereoscopic surface imaging can enable wireless surface dose measurements.

The first manuscript leverages FDM 3D printing to produce 3D-printed plastic scintillators with the required dimensional accuracy, clarity, and light yield to function as effective radiation dosimeters. This work represents the first comprehensive analysis of 3D-printed plastic scintillators for radiotherapy applications. Using optical signal measurements performed with a spectrophotometer, fabrication properties, including print variability, layer thickness, anisotropy, and extrusion temperature, were assessed for 1 cm^3 printed samples[179]. The magnitude of scintillation light output was shown to be strongly dependent on the parameters used in the fabrication process[179]. Dosimetric testing demonstrated that 3D-printed scintillators exhibit several favorable properties, including dose linearity, dose rate independence, energy independence in the MV range, repeatability, and stability[179].

The second manuscript introduces methods for overcoming known issues with dual-material FDM 3D printing and presents the first 3D-printed high-resolution plastic scintillator array designed for radiotherapy applications. It also provides an image processing algorithm capable of correcting various optical artifacts, facilitating wireless array readout using a single sCMOS camera. This investigation provides crucial dosimetric insights into the response of 3D-printed scintillator arrays to irradiation with comparisons to EBT3 GAFChromic film and OSLD measurements, as well as Monte Carlo simulations and TPS calculations. Array dose

measurements of the 3D beam and clinical VMAT treatment plans illustrate the difficulty in differentiating the scintillator response from ambient background light contamination at low doses (< 20-25 cGy) and dose rates (≤ 100 MU/min)[20]. Despite this, when the analysis is restricted to exclude dose values less than 10% of the Monte Carlo simulated max dose, the average absolute percent dose difference between the Monte Carlo simulation and array measurement was 5.3% ± 4.8% for the fixed beam delivery and 5.4% ± 5.2% for the VMAT delivery[20].

The third manuscript presents the first prototype of the proposed novel *in-vivo* dosimetry system. Using knowledge gained from 3D printing simple array geometries, this manuscript provides a methodology for creating patient-specific plastic scintillator arrays using CT scan data. It also demonstrates that the number and location of scintillating elements can be determined using TPS calculation of a patient's treatment plan. Integrated stereoscopic surface imaging using a pair of sCMOS cameras enabled wireless surface dose measurements with calibrated patient-specific scintillator arrays to achieve comparable dosimetric accuracy to planar array geometries. Dose measurements of two clinical chest wall plans (tangential photon fields and VMAT) performed using the patient-specific array showed an absolute percent dose difference between the Monte Carlo simulated dose and array measurement of 4.6% ± 3.4% for the tangential delivery and 4.4% ± 3.8% for the VMAT delivery.

This work confirms that dose measurements performed with calibrated scintillator arrays can possess comparable dosimetric accuracy (within 5% - 10% of simulated doses) to other point detectors used for *in-vivo* surface dose measurements such as MOSFETs, OSLDs, TLDs, and Diodes[20]. This research also permits the production of personalized, high-resolution plastic scintillator arrays and demonstrates the ability of 3D printing to create patient-specific radiation detectors. Despite this, several barriers still hinder the routine application of the proposed detector. Practical limitations, including the time-consuming nature of the dose calibration process, the inability to perform measurements in ambient treatment room lighting, and the current lack of real-time feedback, render the detector still too impractical for regular clinical use.

6.2 FUTURE WORK

The overarching goal of this work is to contribute to developing a patient-specific *in-vivo* detector. Moving forward, research should focus on overcoming the detector's remaining practical limitations to enable accessible real-time and multi-point *in-vivo* dosimetry in clinical environments.

6.2.1 Real-Time *In-Vivo* Dosimetry

While this work aims to achieve real-time measurements, processing delays still hinder real-time acquisition. To address this, future work should focus on integrating camera acquisition triggering and readout directly into the MATLAB-based processing software. This is feasible as the manufacturer of the sCMOS cameras used in this study (Pioneering in Cameras and Optoelectronics (PCO)) provides free developer tools and drivers for MATLAB, including functions for querying camera properties, software-based triggering, and viewing live recordings. Future work should integrate a robust GPU into the acquisition computer to permit accelerated parallel image processing. Fortunately, MATLAB also provides a Parallel Computing Toolbox designed for high-performance image processing applications. This toolbox integrates directly with the image processing functions already employed in the software and is supported by detailed documentation and example code.

Finally, image acquisition currently necessitates a light-free environment, which involves conducting imaging sessions with the treatment room lights off and any additional diffuse light sources removed or covered. This approach is clinically impractical, as some ambient lighting is necessary for setup accuracy and patient comfort. Imaging in ambient room light poses challenges due to variations in the background light distribution, particularly when the gantry partially occludes a light source during rotation. One potential method of enabling imaging using the current sCMOS camera system would be to control the spectral content of treatment room lighting using LEDs of specific wavelengths and optical filtering. While cost may be a limiting factor, employing ICCD cameras, like those used in Cherenkov imaging, could also enable imaging of scintillator arrays under ambient treatment room lighting conditions[39,46]. These cameras are capable of image gating, allowing for sequential collection of background and signal images throughout the entire dose delivery, permitting precise background light removal. This feature also promises to improve the detector's low dose insensitivity and

dosimetric accuracy due to the camera's improved SNR and background removal, further discussed in section 6.2.3.

6.2.2 Dosimetric Calibration

Dosimetric calibration of patient-specific arrays poses unique challenges. Ideally, the calibration process should be patient-independent and standardized. However, arrays could be applied to diverse treatment sites with varying geometric configurations in a clinical setting, making a uniform calibration process difficult. In particular, the absence of patient anatomy for backscatter during the calibration requires a conformal substitute. In this work, 3D printing provides the required backscatter material at the expense of increased calibration complexity/time and substantial plastic consumption.

Achieving a clinically practical dose calibration process may require moving away from rigid bolus-like array designs and opting for deformable arrays[20]. Using a block of solid water for backscatter, a flexible array could be placed flat and calibrated at a fixed SSD perpendicular to the axis of the beam. This would enable standardized calibration and ensure each array element is exposed uniformly to the same dose. Flexible arrays also possess several key advantages, including the ability to adapt to patient anatomical changes during treatment and could be applied to multiple patients. However, transitioning to such designs necessitates understanding how changes in camera perspective, including translation and rotation, impact the observed scintillator light output. This work demonstrated that the distance-to-signal relationship for 3D-printed scintillators adheres to the inverse square law. Future work should employ a mechanical tripod to investigate rotations along the layering direction and across it to characterize the light output dependence and derive potential correction factors. It is important to note that these correction factors may not solely depend on print parameters and could be influenced by patient-specific geometric considerations.

The detection process for scintillators includes both ionizing radiation and optical photons. This work has thus far taken an ionizing radiation-only approach and has yet to account for light transport. Therefore, computational studies using Monte Carlo simulations of layered scintillators followed by optical photon transport simulations should be performed to further understanding of calibration angular dependencies. This includes transport simulations of light absorption, scattering, and the angular distribution of the light exiting the

scintillator. Monte Carlo simulation on this level of detail would require transitioning from PRIMO, which is designed to simulate treatment plans, to a more sophisticated Monte Carlo code.

Modeling optical photon transport in scintillators poses several challenges, primarily due to the high number of ionizing radiation and optical events required to achieve acceptable simulation uncertainty. This can range anywhere from 10^{10}-10^{21} events and requires detailed tracking of primaries and all secondaries[205,206]. For comparison, simulating clinical treatment plans for this work required a 300GB source phase space file and around ~10^{11} histories. Additionally, accurate modeling is hindered by limited information on the surface properties between 3D-printed layers. However, a simplified treatment of optical photon transport could still provide insights into the 3D-printed scintillator's optical behavior. In particular, the ratio of Cherenkov to scintillation light at different incident irradiation angles. Simplifications could be made, such as assigning uniform or regional values to layer surface roughness, limiting the possible angular distribution of reflected photons, and minimizing the probability of crosstalk. While Monte Carlo codes like GEANT4 and PENELOPE can determine the required photon absorption probabilities, few codes are available for subsequent optical photon transport. Some packages do still exist, such as ScintSim2[207], GATE[206,208], and MANTIS[205,209], but many researchers rely on in-house codes tailored to their specific application[206].

6.2.3 Dosimetric Accuracy and Low Dose Insensitivity

The dosimetric accuracy of calibrated scintillator arrays is similar to other *in-vivo* surface detectors, with average absolute percent dose differences of 5% - 10% and maximum point variations of 15% - 20%[20]. If doses are administered at low doses/dose rates or if the individual scintillating element volume is large compared to the measured dose gradient, discrepancies may be greater than 40%[20]. While dose gradient and low dose effects can be mitigated by using TPS calculations or Monte Carlo simulations to guide element placement, achieving dosimetric precision of ideally around 2% - 3% from Monte Carlo simulated doses necessitates further removal of Cherenkov noise.

One potential avenue for improvement is the exploration of alternative intermediary plastics. Future work should investigate the radioluminescence of various thermoplastic intermediary materials to identify those with reduced radioluminescence to mitigate unwanted

background signal. However, it was also observed that the radioluminescence of the plastic intermediary did not accurately represent that of the scintillators, so the potential degree of improvement is challenging to quantify. Another possible direction for future research is experimenting with a different plastic scintillator that emits scintillation light in the green portion of the visible spectrum. This would significantly improve the spectral separation between the emitted Cherenkov and scintillation light, enabling more effective optical filtering, particularly of blue wavelengths where Cherenkov emission is more intense.

Finally, array dose measurements of clinical treatment plans illustrate the challenge of differentiating the scintillator response from ambient background at low doses (< 20-25 cGy) and dose rates (≤ 100 MU/min). One promising approach to mitigate this issue for low-dose applications is using inorganic scintillators. Due to their simplified light production and emission process, inorganic scintillators offer significantly higher light output per incident photon than organic scintillators[176]. Flexible 3D printable inorganic scintillating filaments, a recent development as part of the CERN 3D printed Detector (3DET) R&D collaboration, have shown promise[210]. These filaments, composed of granules of either ZnSe:Al, GOS:Pr, GAGG:Ce, or CsI:Tl and suspended in a thermoplastic polymer matrix, exhibit a substantial response to 20–90 keV X-ray irradiation, even with thin scintillator layers (0.15 mm to 0.3 mm)[210]. However, it is important to note that due to the high atomic number of inorganic scintillators, they are not water equivalent and may perturb the beam fluence. The dose absorbed in the detector material will also not directly correspond to the dose absorbed in tissue.

6.3 CONCLUSION

This dissertation presents the development of a novel patient-specific radiation detector with the goal of fulfilling an unmet need in radiotherapy for routine clinical *in-vivo* dosimetry. The three manuscripts which compose this thesis present the development of the detector from a single 3D-printed scintillator to the wireless measurement of complex 3D-printed scintillator arrays containing anywhere from tens to several hundred scintillators. Using measurements performed with other detectors and simulations, it confirms that calibrated 3D-printed scintillator arrays can possess comparable dosimetric accuracy to other point detectors used for *in-vivo* dosimetry. Although this work focuses on applications in medicine, the

research and development presented are also applicable to the broader physics community, where experiments may require accessible, complex, and custom-designed plastic scintillators.

REFERENCES

1. International Atomic Energy Agency. *Investigation of an Accidental Exposure of Radiotherapy Patients in Panama*. IAEA Expert Report; 2001.

2. Boadu M, Rehani MM. Unintended exposure in radiotherapy: Identification of prominent causes. *Radiotherapy and Oncology*. 2009;93(3):609-617. doi:10.1016/j.radonc.2009.08.044

3. Tsegmed U, Fahim N, Batcha AK, Nakashima T, Nagata Y, Abdel-Wahab M. Accidental overexposure related to new radiation therapy technologies. *J Radiat Oncol*. 2017;6(2):117-132. doi:10.1007/s13566-017-0309-4

4. World Health Organization. Radiotherapy Risk Profile. Published online 2008.

5. International Commission on Radiological Protections. *Prevention of Accidental Exposures to Patients Undergoing Radiation Therapy*. ICRP Publications; 2001.

6. Seco J, Clasie B, Partridge M. Review on the characteristics of radiation detectors for dosimetry and imaging. *Phys Med Biol*. 2014;59(20):R303-347. doi:10.1088/0031-9155/59/20/R303

7. Mijnheer B, Beddar S, Izewska J, Reft C. In vivo dosimetry in external beam radiotherapy. *Med Phys*. 2013;40(7):070903. doi:10.1118/1.4811216

8. Casolaro P, Campajola L, Breglio G, et al. Real-time dosimetry with radiochromic films. *Scientific Reports*. 2019;9(1):5307. doi:10.1038/s41598-019-41705-0

9. Jursinic PA. Characterization of optically stimulated luminescent dosimeters, OSLDs, for clinical dosimetric measurements. *Med Phys*. 2007;34(12):4594-4604. doi:10.1118/1.2804555

10. Kumar AS, Sharma SD, Ravindran BP. Characteristics of mobile MOSFET dosimetry system for megavoltage photon beams. *J Med Phys*. 2014;39(3):142-149. doi:10.4103/0971-6203.139002

11. MacDougall ND, Graveling M, Hansen VN, Brownsword K, Morgan A. In vivo dosimetry in UK external beam radiotherapy: current and future usage. *Br J Radiol*. 2017;90(1072):20160915. doi:10.1259/bjr.20160915

12. Woulfe P, Sullivan FJ, O'Keeffe S. Optical fibre sensors: their role in in vivo dosimetry for prostate cancer radiotherapy. *Cancer Nanotechnology*. 2016;7(1). doi:10.1186/s12645-016-0020-y

13. Akino Y, Das IJ, Bartlett GK, Zhang H, Thompson E, Zook JE. Evaluation of superficial dosimetry between treatment planning system and measurement for several breast cancer treatment techniques. *Med Phys*. 2013;40(1):011714. doi:10.1118/1.4770285

14. Reynolds TA, Higgins P. Surface dose measurements with commonly used detectors: a consistent thickness correction method. *Journal of Applied Clinical Medical Physics*. 2015;16(5):358-366. doi:10.1120/jacmp.v16i5.5572

15. Apipunyasopon L, Srisatit S, Phaisangittisakul N. An investigation of the depth dose in the build-up region, and surface dose for a 6-MV therapeutic photon beam: Monte Carlo simulation and measurements. *Journal of Radiation Research*. 2013;54(2):374-382. doi:10.1093/jrr/rrs097

16. Fraass B, Doppke K, Hunt M, et al. American Association of Physicists in Medicine Radiation Therapy Committee Task Group 53: Quality assurance for clinical radiotherapy treatment planning. *Medical Physics*. 1998;25(10):1773-1829. doi:10.1118/1.598373

17. Wang L, Cmelak AJ, Ding GX. A simple technique to improve calculated skin dose accuracy in a commercial treatment planning system. *J Appl Clin Med Phys*. 2018;19(2):191-197. doi:10.1002/acm2.12275

18. Di Franco R, Sammarco E, Calvanese MG, et al. Preventing the acute skin side effects in patients treated with radiotherapy for breast cancer: the use of corneometry in order to evaluate the protective effect of moisturizing creams. *Radiat Oncol*. 2013;8:57. doi:10.1186/1748-717X-8-57

19. Olaciregui-Ruiz I, Beddar S, Greer P, et al. In vivo dosimetry in external beam photon radiotherapy: Requirements and future directions for research, development, and clinical practice. *Physics and Imaging in Radiation Oncology*. 2020;15:108-116. doi:10.1016/j.phro.2020.08.003

20. Lynch N, Robar JL, Monajemi T. Camera-based radiotherapy dosimetry using dual-material 3D printed scintillator arrays. *Med Phys*. 2023;50(3):1824-1842. doi:10.1002/mp.16167

21. Khan FM, Sperduto PW, Gibbons JP. *Khan's Treatment Planning in Radiation Oncology:* . Lippincott Williams & Wilkins; 2021.

22. Yu CX. Intensity-modulated arc therapy with dynamic multileaf collimation: an alternative to tomotherapy. *Phys Med Biol*. 1995;40(9):1435. doi:10.1088/0031-9155/40/9/004

23. Otto K. Volumetric modulated arc therapy: IMRT in a single gantry arc. *Medical Physics*. 2008;35(1):310-317. doi:10.1118/1.2818738

24. Hunte SO, Clark CH, Zyuzikov N, Nisbet A. Volumetric modulated arc therapy (VMAT): a review of clinical outcomes—what is the clinical evidence for the most effective implementation? *Br J Radiol*. 2022;95(1136):20201289. doi:10.1259/bjr.20201289

25. Bojechko C, Phillps M, Kalet A, Ford EC. A quantification of the effectiveness of EPID dosimetry and software-based plan verification systems in detecting incidents in radiotherapy. *Medical Physics*. 2015;42(9):5363-5369. doi:10.1118/1.4928601

26. Agency IAE. *Development of Procedures for in Vivo Dosimetry in Radiotherapy*. International Atomic Energy Agency; 2013.

27. Klein EE, Drzymala RE, Purdy JA, Michalski J. Errors in radiation oncology: A study in pathways and dosimetric impact. *Journal of Applied Clinical Medical Physics*. 2005;6(3):81. doi:10.1120/jacmp.v6i3.2105

28. Fiorino C, Corletto D, Mangili P, et al. Quality assurance by systematic in vivo dosimetry: results on a large cohort of patients. *Radiother Oncol*. 2000;56(1):85-95. doi:10.1016/s0167-8140(00)00195-x

29. Tariq M, Gomez C, Riegel AC. Dosimetric impact of placement errors in optically stimulated luminescent in vivo dosimetry in radiotherapy. *Phys Imaging Radiat Oncol*. 2019;11:63-68. doi:10.1016/j.phro.2019.08.004

30. Jursinic PA, Yahnke CJ. In vivo dosimetry with optically stimulated luminescent dosimeters, OSLDs, compared to diodes; the effects of buildup cap thickness and fabrication material. *Med Phys*. 2011;38(10):5432-5440. doi:10.1118/1.3633939

31. Jornet N, Carrasco P, Jurado D, Ruiz A, Eudaldo T, Ribas M. Comparison study of MOSFET detectors and diodes for entrance in vivo dosimetry in 18 MV x-ray beams. *Med Phys*. 2004;31(9):2534-2542. doi:10.1118/1.1785452

32. Kadesjö N, Nyholm T, Olofsson J. A practical approach to diode based in vivo dosimetry for intensity modulated radiotherapy. *Radiother Oncol*. 2011;98(3):378-381. doi:10.1016/j.radonc.2010.12.018

33. Chuang CF, Verhey LJ, Xia P. Investigation of the use of MOSFET for clinical IMRT dosimetric verification. *Med Phys*. 2002;29(6):1109-1115. doi:10.1118/1.1481520

34. Duch MA, Ginjaume M, Chakkor H, Ortega X, Jornet N, Ribas M. Thermoluminescence dosimetry applied to in vivo dose measurements for total body irradiation techniques. *Radiother Oncol*. 1998;47(3):319-324. doi:10.1016/s0167-8140(98)00013-9

35. Ribas M, Jornet N, Eudaldo T, et al. Midplane dose determination during total body irradiation using in vivo dosimetry. *Radiother Oncol*. 1998;49(1):91-98. doi:10.1016/s0167-8140(98)00094-2

36. Bloemen-van Gurp EJ, Mijnheer BJ, Verschueren TAM, Lambin P. Total body irradiation, toward optimal individual delivery: dose evaluation with metal oxide field effect transistors, thermoluminescence detectors, and a treatment planning system. *Int J Radiat Oncol Biol Phys*. 2007;69(4):1297-1304. doi:10.1016/j.ijrobp.2007.07.2334

37. Le Deroff C, Pérès EA, Ledoux X, Toutain J, Frelin-Labalme AM. In vivo surface dosimetry with a scintillating fiber dosimeter in preclinical image-guided radiotherapy. *Med Phys*. 2020;47(1):234-241. doi:10.1002/mp.13903

38. Ong YH, Li AQ, Zhu TC. Monte Carlo investigation of the effect of skin tissue optical properties on detected Cherenkov emission. *Proc SPIE Int Soc Opt Eng*. 2019;10862:108621D. doi:10.1117/12.2509854

39. Xie Y, Petroccia H, Maity A, et al. Cherenkov imaging for total skin electron therapy (TSET). *Med Phys*. 2020;47(1):201-212. doi:10.1002/mp.13881

40. Fuangrod T, Greer PB, Woodruff HC, et al. Investigation of a real-time EPID-based patient dose monitoring safety system using site-specific control limits. *Radiation Oncology*. 2016;11(1):106. doi:10.1186/s13014-016-0682-y

41. Mijnheer B, Olaciregui-Ruiz I, Rozendaal R, et al. 3D EPID-based in vivo dosimetry for IMRT and VMAT. *J Phys: Conf Ser*. 2013;444(1):012011. doi:10.1088/1742-6596/444/1/012011

42. Esposito M, Piermattei A, Bresciani S, et al. Improving dose delivery accuracy with EPID in vivo dosimetry: results from a multicenter study. *Strahlenther Onkol*. 2021;197(7):633-643. doi:10.1007/s00066-021-01749-6

43. Martins JC, Maier J, Gianoli C, et al. Towards real-time EPID-based 3D in vivo dosimetry for IMRT with Deep Neural Networks: A feasibility study. *Phys Med*. 2023;114:103148. doi:10.1016/j.ejmp.2023.103148

44. Spreeuw H, Rozendaal R, Olaciregui-Ruiz I, et al. Online 3D EPID-based dose verification: Proof of concept. *Medical Physics*. 2016;43(7):3969-3974. doi:10.1118/1.4952729

45. Dogan N, Mijnheer BJ, Padgett K, et al. AAPM Task Group Report 307: Use of EPIDs for Patient-Specific IMRT and VMAT QA. *Medical Physics*. 2023;50(8):e865-e903. doi:10.1002/mp.16536

46. Jarvis LA, Hachadorian RL, Jermyn M, et al. Initial Clinical Experience of Cherenkov Imaging in External Beam Radiation Therapy Identifies Opportunities to Improve Treatment Delivery. *Int J Radiat Oncol Biol Phys*. 2021;109(5):1627-1637. doi:10.1016/j.ijrobp.2020.11.013

47. Jarvis LA, Zhang R, Gladstone DJ, et al. Cherenkov Video Imaging Allows for the First Visualization of Radiation Therapy in Real Time. *International Journal of Radiation Oncology*Biology*Physics*. 2014;89(3):615-622. doi:10.1016/j.ijrobp.2014.01.046

48. Rooney MK, Rosenberg DM, Braunstein S, et al. Three-dimensional printing in radiation oncology: A systematic review of the literature. *J Appl Clin Med Phys*. 2020;21(8):15-26. doi:10.1002/acm2.12907

49. Khosravani MR, Reinicke T. 3D-printed sensors: Current progress and future challenges. *Sensors and Actuators A: Physical*. 2020;305:111916. doi:10.1016/j.sna.2020.111916

50. Ngo TD, Kashani A, Imbalzano G, Nguyen KTQ, Hui D. Additive manufacturing (3D printing): A review of materials, methods, applications and challenges. *Composites Part B: Engineering*. 2018;143:172-196. doi:10.1016/j.compositesb.2018.02.012

51. Tamburrino F, Graziosi S, Bordegoni M. The influence of slicing parameters on the multi-material adhesion mechanisms of FDM printed parts: an exploratory study. *Virtual and Physical Prototyping*. 2019;14(4):316-332. doi:10.1080/17452759.2019.1607758

52. Brivio D, Naumann L, Albert S, Sajo E, Zygmanski P. 3D printing for rapid prototyping of low-Z/density ionization chamber arrays. *Medical physics*. Published online 2019. doi:10.1002/mp.13841

53. Rafiee M, Farahani RD, Therriault D. Multi-Material 3D and 4D Printing: A Survey. *Advanced Science*. 2020;7(12):1902307. doi:10.1002/advs.201902307

54. Fargher S, Steer C, Thompson L. The Use of 3D Printing in the Development of Gaseous Radiation Detectors. *EPJ Web Conf*. 2018;170:01016. doi:10.1051/epjconf/201817001016

55. Albert S, Brivio D, Aldelaijan S, Sajo E, Hesser J, Zygmanski P. Towards customizable thin-panel low-Z detector arrays: electrode design for increased spatial resolution ion chamber arrays. *Physics in medicine & biology*. 2020;65(8):08NT02-08NT02. doi:10.1088/1361-6560/ab8109

56. Berns S, Boillat E, Boyarintsev A, et al. Additive manufacturing of fine-granularity optically-isolated plastic scintillator elements. *J Inst*. 2022;17(10):P10045. doi:10.1088/1748-0221/17/10/P10045

57. Beddar S, Beaulieu L. *Scintillation Dosimetry*. CRC Press; 2016.

58. Lee S, Son J, Kim DG, Choi J, Kim YK. Characterization of plastic scintillator fabricated by UV LED curing machine. *Nuclear Instruments and Methods in Physics Research Section A: Accelerators, Spectrometers, Detectors and Associated Equipment*. 2019;929:23-28. doi:10.1016/j.nima.2019.03.048

59. Birks JB. *The Theory and Practice of Scintillation Counting: International Series of Monographs in Electronics and Instrumentation*. Elsevier; 2013.

60. Liu C, Li Z, Hajagos TJ, Kishpaugh D, Chen DY, Pei Q. Transparent Ultra-High-Loading Quantum Dot/Polymer Nanocomposite Monolith for Gamma Scintillation. *ACS Nano*. 2017;11(6):6422-6430. doi:10.1021/acsnano.7b02923

61. Rozman IM, Kilin SF. LUMINESCENCE OF PLASTIC SCINTILLATORS. *Sov Phys Usp*. 1960;2(6):856. doi:10.1070/PU1960v002n06ABEH003184

62. Lee CH, Son J, Kim TH, Kim YK. Characteristics of Plastic Scintillators Fabricated by a Polymerization Reaction. *Nuclear Engineering and Technology*. 2017;49(3):592-597. doi:10.1016/j.net.2016.10.001

63. Kapłon Ł, Kochanowski A, Molenda M, et al. Plastic scintillators for positron emission tomography obtained by the bulk polymerization method. *Bio-Algorithms and Med-Systems*. 2014;10(1):27-31. doi:10.1515/bams-2013-0108

64. Mishnayot Y, Layani M, Cooperstein I, Magdassi S, Ron G. Three-dimensional printing of scintillating materials. *Review of Scientific Instruments*. 2014;85(8):1-4. doi:10.1063/1.4891703

65. Son J, Kim DG, Lee S, et al. Improved 3D Printing Plastic Scintillator Fabrication. *J Korean Phys Soc*. 2018;73(7):887-892. doi:10.3938/jkps.73.887

66. Kim DG, Lee S, Kim YK, Seon SJ, Kim YK. Performance of 3D Printing Plastic Scintillator by Applying OLED Wavelength Shifter. *Transactions of the Korean Nuclear Society Autumn Meeting*. Published online August 27, 2019:1-2.

67. Kim DG, Lee S, Kim YK, et al. Scintillation Light Output of 3D Printed Plastic Scintillators. *Transactions of the Korean Nuclear Society Spring Meeting*. Published online May 18, 2018:1-2.

68. Kim TH, Lee S, Kim DG, et al. A feasibility study of using a 3D-printed tumor model scintillator to verify the energy absorbed to a tumor. *Nuclear Engineering and Technology*. 2021;53(9):3018-3025. doi:10.1016/j.net.2021.03.033

69. Kim TH, Yang HJ, Jeong JY, Schaarschmidt T, Kim YK, Chung HT. Feasibility of isodose-shaped scintillation detectors for the measurement of gamma knife output factors. *Medical Physics*. 2022;49(3):1944-1954. doi:10.1002/mp.15469

70. Berns S, Boyarintsev A, Hugon S, et al. A novel polystyrene-based scintillator production process involving additive manufacturing. *J Inst*. 2020;15(10):P10019-P10019. doi:10.1088/1748-0221/15/10/P10019

71. Whittaker CA, Santos AMC, Kalnins CAG, Ebendorff-Heidepriem H, Ottaway D, Spooner NA. Evaluating the energy dependence of various polystyrene based plastic scintillators. *Radiation Measurements*. 2019;122:57-62. doi:10.1016/j.radmeas.2019.01.007

72. Létourneau D, Pouliot J, Roy R. Miniature scintillating detector for small field radiation therapy. *Med Phys*. 1999;26(12):2555-2561. doi:10.1118/1.598793

73. Beddar AS, Kinsella KJ, Ikhlef A, Sibata CH. A miniature "scintillator-fiberoptic-PMT" detector system for the dosimetry of small fields in stereotactic radiosurgery. *IEEE Transactions on Nuclear Science*. 2001;48(3):924-928. doi:10.1109/23.940133

74. Morin J, Béliveau-Nadeau D, Chung E, et al. A comparative study of small field total scatter factors and dose profiles using plastic scintillation detectors and other stereotactic dosimeters: The case of the CyberKnife. *Medical Physics*. 2013;40(1):011719. doi:10.1118/1.4772190

75. Archambault L, Briere TM, Pönisch F, et al. Toward a real-time in vivo dosimetry system using plastic scintillation detectors. *Int J Radiat Oncol Biol Phys*. 2010;78(1):280-287. doi:10.1016/j.ijrobp.2009.11.025

76. Therriault-Proulx F, Briere TM, Mourtada F, Aubin S, Beddar S, Beaulieu L. A phantom study of an in vivo dosimetry system using plastic scintillation detectors for real-time verification of 192Ir HDR brachytherapy. *Medical Physics*. 2011;38(5):2542-2551. doi:10.1118/1.3572229

77. Wootton L, Kudchadker R, Lee A, Beddar S. Real-timein vivorectal wall dosimetry using plastic scintillation detectors for patients with prostate cancer. *Phys Med Biol*. 2014;59(3):647-660. doi:10.1088/0031-9155/59/3/647

78. Goulet M, Rilling M, Gingras L, Beddar S, Beaulieu L, Archambault L. Novel, full 3D scintillation dosimetry using a static plenoptic camera. *Medical Physics*. 2014;41(8Part1):082101. doi:10.1118/1.4884036

79. Jennings MW, Rutten TP, Ottaway DJ. Evaluation of the signal quality of an inexpensive CMOS camera towards imaging a high-resolution plastic scintillation detector array. *Radiation Measurements*. 2017;104:22-31. doi:10.1016/j.radmeas.2017.07.004

80. Cloutier E, Beaulieu L, Archambault L. On the use of polychromatic cameras for high spatial resolution spectral dose measurements. *Phys Med Biol*. 2022;67(11):11NT01. doi:10.1088/1361-6560/ac6b0e

81. Archambault L, Briere TM, Beddar S. Transient noise characterization and filtration in CCD cameras exposed to stray radiation from a medical linear accelerator. *Med Phys*. 2008;35(10):4342-4351. doi:10.1118/1.2975147

82. Robertson D, Hui C, Archambault L, Mohan R, Beddar S. Optical artefact characterization and correction in volumetric scintillation dosimetry. *Phys Med Biol*. 2014;59(1):23-42. doi:10.1088/0031-9155/59/1/23

83. Cloutier E, Archambault L, Beaulieu L. Deformable scintillation dosimeter I: challenges and implementation using computer vision techniques. *Phys Med Biol*. 2021;66(17). doi:10.1088/1361-6560/ac1ca1

84. Cloutier É, Beaulieu L, Archambault L. Deformable scintillation dosimeter: II. Real-time simultaneous measurements of dose and tracking of deformation vector fields. *Physics in medicine and biology*. Published online 2021. doi:10.1088/1361-6560/ac1ca2

85. Karzmark CJ, Morton RJ. *A Primer on Theory and Operation of Linear Accelerators in Radiation Therapy*. Medical Physics Publishing; 2018.

86. Whelan B, Holloway L, Constantin D, et al. Performance of a clinical gridded electron gun in magnetic fields: Implications for MRI-linac therapy. *Med Phys*. 2016;43(11):5903-5914. doi:10.1118/1.4963216

87. Tan C, Leach AS, Heenan TMM, Jervis R, Brett DJL, Shearing PR. 3D X-Ray Characterization of Energy Storage and Conversion Devices. In: Gao Y jun, Song W, Liu JL, Bashir S, eds. *Advances in Sustainable Energy: Policy, Materials and Devices*. Springer International Publishing; 2021:513-544. doi:10.1007/978-3-030-74406-9_18

88. Podgorsak EB. *Radiation Physics for Medical Physicists*. Springer International Publishing; 2016. doi:10.1007/978-3-319-25382-4

89. Andreo P, Burns DT, Nahum AE, Seuntjens J. *Fundamentals of Ionizing Radiation Dosimetry*. John Wiley & Sons; 2017.

90. Fornalski KW. Simple empirical correction functions to cross sections of the photoelectric effect, Compton scattering, pair and triplet production for carbon radiation shields for intermediate and high photon energies. *J Phys Commun*. 2018;2(3):035038. doi:10.1088/2399-6528/aab408

91. Griffiths DJ. *Introduction to Electrodynamics*. Cambridge University Press; 2023.

92. Berger MJ, Inokuti M, Anderson HH, et al. ICRU 37: Formulae for the Collision Stopping Power. *Journal of the International Commission on Radiation Units and Measurements*. 1984;os19(2):4-6. doi:10.1093/jicru/os19.2.4

93. Kawrakow I, Bielajew AF. On the condensed history technique for electron transport. *Nuclear Instruments and Methods in Physics Research Section B: Beam Interactions with Materials and Atoms*. 1998;142(3):253-280. doi:10.1016/S0168-583X(98)00274-2

94. Kumar S, Deshpande DD, Nahum AE. Monte-Carlo-derived insights into dose–kerma–collision kerma inter-relationships for 50 keV–25 MeV photon beams in water, aluminum and copper. *Phys Med Biol*. 2014;60(2):501. doi:10.1088/0031-9155/60/2/501

95. Ma CM, Coffey CW, DeWerd LA, et al. AAPM protocol for 40–300 kV x-ray beam dosimetry in radiotherapy and radiobiology. *Medical Physics*. 2001;28(6):868-893. doi:10.1118/1.1374247

96. Klevenhagen SC, Aukett RJ, Harrison RM, Moretti C, Nahum AE, Rosser KE. The IPEMB code of practice for the determination of absorbed dose for x-rays below 300 kV generating potential (0.035 mm Al - 4 mm Cu HVL; 10 - 300 kV generating potential). *Phys Med Biol*. 1996;41(12):2605. doi:10.1088/0031-9155/41/12/002

97. Almond PR, Biggs PJ, Coursey BM, et al. AAPM's TG-51 protocol for clinical reference dosimetry of high-energy photon and electron beams. *Medical Physics*. 1999;26(9):1847-1870. doi:10.1118/1.598691

98. Beddar AS, Mackie TR, Attix FH. Water-equivalent plastic scintillation detectors for high-energy beam dosimetry: I. Physical characteristics and theoretical considerations. *Phys Med Biol*. 1992;37(10):1883-1900. doi:10.1088/0031-9155/37/10/006

99. Ogunleye OT, Attix FH, Paliwal BR. Comparison of Burlin cavity theory with LiF TLD measurements for cobalt-60 gamma rays. *Phys Med Biol.* 1980;25(2):203. doi:10.1088/0031-9155/25/2/001

100. Ogunleye OT. A comparison of the Burlin and Kearsley general cavity theories with LiF TLD measurements for 10 MV X-rays. *Phys Med Biol.* 1987;32(7):901. doi:10.1088/0031-9155/32/7/009

101. Haider JA, Skarsgard LD, Lam GK. A general cavity theory. *Phys Med Biol.* 1997;42(3):491-500. doi:10.1088/0031-9155/42/3/004

102. Horowitz YS, Moscovitch M, Dubi A. Modified general cavity theory applied to the calculation of gamma dose in 60Co thermoluminescence dosimetry. *Phys Med Biol.* 1983;28(7):829. doi:10.1088/0031-9155/28/7/005

103. Kearsley E. A new general cavity theory. *Phys Med Biol.* 1984;29(10):1179. doi:10.1088/0031-9155/29/10/001

104. Mobit PN, Nahum AE, Mayles P. An EGS4 Monte Carlo examination of general cavity theory. *Phys Med Biol.* 1997;42(7):1319-1334. doi:10.1088/0031-9155/42/7/007

105. Mobit PN, Sandison GA. A Monte Carlo comparison of the response of the PTW-diamond and the TL-diamond detectors in megavoltage photon beams. *Med Phys.* 1999;26(11):2503-2507. doi:10.1118/1.598771

106. Rogers DWO. Fifty years of Monte Carlo simulations for medical physics. *Phys Med Biol.* 2006;51(13):R287-301. doi:10.1088/0031-9155/51/13/R17

107. Monajemi TT, Ruiz EA. Application of plastic scintillating fibres to surface dosimetry in megavoltage photon and electron beams: considerations for Cerenkov correction. *Phys Med Biol.* 2018;63(18):185003. doi:10.1088/1361-6560/aad9b6

108. Therriault-Proulx F, Beddar S, Beaulieu L. On the use of a single-fiber multipoint plastic scintillation detector for 192Ir high-dose-rate brachytherapy. *Medical Physics.* 2013;40(6). doi:10.1118/1.4803510

109. Linares Rosales HM, Archambault L, Beddar S, Beaulieu L. Dosimetric performance of a multipoint plastic scintillator dosimeter as a tool for real-time source tracking in high dose rate 192 Ir brachytherapy. *Med Phys.* 2020;47(9):4477-4490. doi:10.1002/mp.14246

110. Lambert J, McKenzie DR, Law S, Elsey J, Suchowerska N. A plastic scintillation dosimeter for high dose rate brachytherapy. *Phys Med Biol.* 2006;51(21):5505-5516. doi:10.1088/0031-9155/51/21/008

111. Linares Rosales HM, Duguay-Drouin P, Archambault L, Beddar S, Beaulieu L. Optimization of a multipoint plastic scintillator dosimeter for high dose rate brachytherapy. *Medical Physics.* 2019;46(5):2412-2421. doi:10.1002/mp.13498

112. Gagnon JC, Thériault D, Guillot M, et al. Dosimetric performance and array assessment of plastic scintillation detectors for stereotactic radiosurgery quality assurance. *Med Phys*. 2012;39(1):429-436. doi:10.1118/1.3666765

113. Birks JB. Scintillations from Organic Crystals: Specific Fluorescence and Relative Response to Different Radiations. *Proc Phys Soc A*. 1951;64(10):874. doi:10.1088/0370-1298/64/10/303

114. Peralta L. Temperature dependence of plastic scintillators. *Nuclear Instruments and Methods in Physics Research Section A: Accelerators, Spectrometers, Detectors and Associated Equipment*. 2018;883:20-23. doi:10.1016/j.nima.2017.11.041

115. Nusrat H, Pang G, Ahmad SB, Keller B, Sarfehnia A. Quantifying the impact of lead doping on plastic scintillator response to radiation. *Medical Physics*. 2019;46(9):4215-4223. doi:10.1002/mp.13691

116. Wang LLW, Klein D, Beddar AS. Monte Carlo study of the energy and angular dependence of the response of plastic scintillation detectors in photon beams. *Medical Physics*. 2010;37(10):5279. doi:10.1118/1.3488904

117. Beddar AS, Mackie TR, Attix FH. Water-equivalent plastic scintillation detectors for high-energy beam dosimetry: II. Properties and measurements. *Phys Med Biol*. 1992;37(10):1901-1913. doi:10.1088/0031-9155/37/10/007

118. Archambault L, Beddar AS, Gingras L, Roy R, Beaulieu L. Measurement accuracy and cerenkov removal for high performance, high spatial resolution scintillation dosimetry. *Med Phys*. 2006;33(1):128-135. doi:10.1118/1.2138010

119. Clift MA, Johnston PN, Webb DV. A temporal method of avoiding the Cerenkov radiation generated in organic scintillator dosimeters by pulsed mega-voltage electron and photon beams. *Phys Med Biol*. 2002;47(8):1421-1433. doi:10.1088/0031-9155/47/8/313

120. Naseri P, Suchowerska N, McKenzie DR. Scintillation dosimeter arrays using air core light guides: simulation and experiment. *Phys Med Biol*. 2010;55(12):3401-3415. doi:10.1088/0031-9155/55/12/009

121. Justus BL, Falkenstein P, Huston AL, Plazas MC, Ning H, Miller RW. Gated fiber-optic-coupled detector for in vivo real-time radiation dosimetry. *Appl Opt*. 2004;43(8):1663-1668. doi:10.1364/ao.43.001663

122. Madden L. Separation of scintillation and Cerenkov radiation in fiber optic dosimeters. *University of Wollongong Thesis Collection 2017*. Published online January 1, 2018. https://ro.uow.edu.au/theses1/217

123. Fontbonne JM, Iltis G, Ban G, et al. Scintillating fiber dosimeter for radiation therapy accelerator. *IEEE Transactions on Nuclear Science*. 2002;49(5):2223-2227. doi:10.1109/TNS.2002.803680

124. Frelin AM, Fontbonne JM, Ban G, et al. Spectral discrimination of Cerenkov radiation in scintillating dosimeters. *Med Phys*. 2005;32(9):3000-3006. doi:10.1118/1.2008487

125. Archambault L, Therriault-Proulx F, Beddar S, Beaulieu L. A mathematical formalism for hyperspectral, multipoint plastic scintillation detectors. *Phys Med Biol*. 2012;57(21):7133-7145. doi:10.1088/0031-9155/57/21/7133

126. Therriault-Proulx F, Archambault L, Beaulieu L, Beddar S. Development of a novel multi-point plastic scintillation detector with a single optical transmission line for radiation dose measurement. *Phys Med Biol*. 2012;57(21):10.1088/0031-9155/57/21/7147. doi:10.1088/0031-9155/57/21/7147

127. Therriault-Proulx F, Beaulieu L, Archambault L, Beddar S. On the nature of the light produced within PMMA optical light guides in scintillation fiber-optic dosimetry. *Phys Med Biol*. 2013;58(7):2073-2084. doi:10.1088/0031-9155/58/7/2073

128. Bielajew AF, Rogers DWO. Variance-Reduction Techniques. In: Jenkins TM, Nelson WR, Rindi A, eds. *Monte Carlo Transport of Electrons and Photons*. Ettore Majorana International Science Series. Springer US; 1988:407-419. doi:10.1007/978-1-4613-1059-4_18

129. OECD. *PENELOPE 2018: A Code System for Monte Carlo Simulation of Electron and Photon Transport: Workshop Proceedings, Barcelona, Spain, 28 January – 1 February 2019*. Organisation for Economic Co-operation and Development; 2019. Accessed March 12, 2024. https://www.oecd-ilibrary.org/nuclear-energy/penelope-2018-a-code-system-for-monte-carlo-simulation-of-electron-and-photon-transport_32da5043-en

130. Baró J, Sempau J, Fernández-Varea JM, Salvat F. PENELOPE: An algorithm for Monte Carlo simulation of the penetration and energy loss of electrons and positrons in matter. *Nuclear Instruments and Methods in Physics Research Section B: Beam Interactions with Materials and Atoms*. 1995;100(1):31-46. doi:10.1016/0168-583X(95)00349-5

131. Kueng R, Frei D, Volken W, et al. Adaptive step size algorithm to increase efficiency of proton macro Monte Carlo dose calculation. *Radiation Oncology*. 2019;14(1):165. doi:10.1186/s13014-019-1362-5

132. Brualla L, Rodriguez M, Sempau J, Andreo P. PENELOPE/PRIMO-calculated photon and electron spectra from clinical accelerators. *Radiation Oncology*. 2019;14(1):6. doi:10.1186/s13014-018-1186-8

133. Rodriguez M, Sempau J, Brualla L. PRIMO: a graphical environment for the Monte Carlo simulation of Varian and Elekta linacs. *Strahlenther Onkol*. 2013;189(10):881-886. doi:10.1007/s00066-013-0415-1

134. Hermida–López M, Sánchez–Artuñedo D, Calvo–Ortega JF. PRIMO Monte Carlo software benchmarked against a reference dosimetry dataset for 6 MV photon beams from Varian linacs. *Radiat Oncol*. 2018;13(1):144. doi:10.1186/s13014-018-1076-0

135. Esposito A, Silva S, Oliveira J, Lencart J, Santos J. Primo software as a tool for Monte Carlo simulations of intensity modulated radiotherapy: a feasibility study. *Radiat Oncol*. 2018;13(1):91. doi:10.1186/s13014-018-1021-2

136. Paganini L, Reggiori G, Stravato A, et al. MLC parameters from static fields to VMAT plans: an evaluation in a RT-dedicated MC environment (PRIMO). *Radiat Oncol*. 2019;14(1):216. doi:10.1186/s13014-019-1421-y

137. Calvo-Ortega JF, Hermida-López M. PRIMO Monte Carlo software as a tool for commissioning of an external beam radiotherapy treatment planning system. *Rep Pract Oncol Radiother*. 2023;28(4):529-540. doi:10.5603/RPOR.a2023.0060

138. Efendi MA, Funsian A, Chittrakarn T, Bhongsuwan T. Monte Carlo simulation using PRIMO code as a tool for checking the credibility of commissioning and quality assurance of 6 MV TrueBeam STx varian LINAC. *Reports of Practical Oncology & Radiotherapy*. 2020;25(1):125-132. doi:10.1016/j.rpor.2019.12.021

139. Bedford JL. Calculation of absorbed dose in radiotherapy by solution of the linear Boltzmann transport equations. *Phys Med Biol*. 2019;64(2):02TR01. doi:10.1088/1361-6560/aaf0e2

140. Vassiliev ON, Wareing TA, McGhee J, Failla G, Salehpour MR, Mourtada F. Validation of a new grid-based Boltzmann equation solver for dose calculation in radiotherapy with photon beams. *Phys Med Biol*. 2010;55(3):581-598. doi:10.1088/0031-9155/55/3/002

141. Vassiliev ON, Wareing TA, Davis IM, et al. Feasibility of a Multigroup Deterministic Solution Method for 3D Radiotherapy Dose Calculations. *Int J Radiat Oncol Biol Phys*. 2008;72(1):220-227. doi:10.1016/j.ijrobp.2008.04.057

142. Han T, Mikell JK, Salehpour M, Mourtada F. Dosimetric comparison of Acuros XB deterministic radiation transport method with Monte Carlo and model-based convolution methods in heterogeneous media. *Med Phys*. 2011;38(5):2651-2664. doi:10.1118/1.3582690

143. Kan MWK, Yu PKN, Leung LHT. A Review on the Use of Grid-Based Boltzmann Equation Solvers for Dose Calculation in External Photon Beam Treatment Planning. *Biomed Res Int*. 2013;2013:692874. doi:10.1155/2013/692874

144. Bush K, Gagne IM, Zavgorodni S, Ansbacher W, Beckham W. Dosimetric validation of Acuros XB with Monte Carlo methods for photon dose calculations. *Med Phys*. 2011;38(4):2208-2221. doi:10.1118/1.3567146

145. Fogliata A, Nicolini G, Clivio A, Vanetti E, Cozzi L. On the dosimetric impact of inhomogeneity management in the Acuros XB algorithm for breast treatment. *Radiation Oncology*. 2011;6(1):103. doi:10.1186/1748-717X-6-103

146. Fogliata A, Nicolini G, Vanetti E, Clivio A, Cozzi L. Dosimetric validation of the anisotropic analytical algorithm for photon dose calculation: fundamental characterization in water. *Phys Med Biol*. 2006;51(6):1421-1438. doi:10.1088/0031-9155/51/6/004

147. Andreozzi JM, Zhang R, Glaser AK, Jarvis LA, Pogue BW, Gladstone DJ. Camera selection for real-time in vivo radiation treatment verification systems using Cherenkov imaging. *Med Phys*. 2015;42(2):994-1004. doi:10.1118/1.4906249

148. Holst GC, Lomheim TS. *CMOS/CCD Sensors and Camera Systems*. JCD Publishing; 2011.

149. Bushberg J, Seibert JA, Leidholdt E, Boone J. *The Essential Physics of Medical Imaging*. 3rd ed. Lippincott Williams & Wilkins; 2011.

150. International Atomic Energy Agency. *Diagnostic Radiology Physics*. International Atomic Energy Agency; 2014:1-682. Accessed April 25, 2024. https://www.iaea.org/publications/8841/diagnostic-radiology-physics

151. Beddar S. Real-time volumetric scintillation dosimetry. *J Phys: Conf Ser*. 2015;573(1):012005. doi:10.1088/1742-6596/573/1/012005

152. Beddar S, Archambault L, Sahoo N, et al. Exploration of the potential of liquid scintillators for real-time 3D dosimetry of intensity modulated proton beams. *Med Phys*. 2009;36(5):1736-1743. doi:10.1118/1.3117583

153. Hijazi A, Al-Masri A, Rawashdeh N. On the use of Bayer Sensor Color Cameras in Digital Image Correlation. In: *2022 11th International Symposium on Signal, Image, Video and Communications (ISIVC)*. ; 2022:1-7. doi:10.1109/ISIVC54825.2022.9800739

154. Bardoux A, Penquer A, Gilard O, Ecoffet R, Auvergne M. Radiation effects on image sensors. In: *International Conference on Space Optics — ICSO 2012*. Vol 10564. SPIE; 2017:186-194. doi:10.1117/12.2309026

155. DePiero FW, Trivedi MM. 3-D Computer Vision Using Structured Light: Design, Calibration, and Implementation Issues. In: Zelkowitz MV, ed. *Advances in Computers*. Vol 43. Elsevier; 1996:243-278. doi:10.1016/S0065-2458(08)60646-4

156. Li L, Ke Y, Jiang K. Surface Reconstruction Based on Computer Stereo Vision Using Structured Light Projection. In: *2009 International Conference on Intelligent Human-Machine Systems and Cybernetics*. Vol 2. ; 2009:451-454. doi:10.1109/IHMSC.2009.235

157. Zhang Y, Luo Z, Hou J, Tan L, Guo X. Computer Vision Techniques for Improving Structured Light Vision Systems. In: *2020 IEEE International Conference on Electro Information Technology (EIT)*. ; 2020:437-442. doi:10.1109/EIT48999.2020.9208332

158. He Y, Zhang H, Arens E, et al. Smart detection of indoor occupant thermal state via infrared thermography, computer vision, and machine learning. *Building and Environment*. 2023;228:109811. doi:10.1016/j.buildenv.2022.109811

159. Ward S, Hensler J, Alsalam B, Gonzalez LF. Autonomous UAVs wildlife detection using thermal imaging, predictive navigation and computer vision. In: *2016 IEEE Aerospace Conference*. ; 2016:1-8. doi:10.1109/AERO.2016.7500671

160. Nguyen HV, Banerjee A, Chellappa R. Tracking via object reflectance using a hyperspectral video camera. In: *2010 IEEE Computer Society Conference on Computer Vision and Pattern Recognition - Workshops*. ; 2010:44-51. doi:10.1109/CVPRW.2010.5543780

161. Singh G, Pidadi P, Malwad DS. A Review on Applications of Computer Vision. In: Abraham A, Hong TP, Kotecha K, Ma K, Manghirmalani Mishra P, Gandhi N, eds. *Hybrid Intelligent Systems*. Springer Nature Switzerland; 2023:464-479. doi:10.1007/978-3-031-27409-1_42

162. Hartley R, Zisserman A. *Multiple View Geometry in Computer Vision*. Cambridge University Press; 2003.

163. Zhang Z. A flexible new technique for camera calibration. *IEEE Transactions on Pattern Analysis and Machine Intelligence*. 2000;22(11):1330-1334. doi:10.1109/34.888718

164. Bouguet J. Camera calibration toolbox for matlab. *Computational Vision at the California Institute of Technology*. Published online 2001. Accessed March 7, 2022. http://www.vision.caltech.edu/bouguetj/calib_doc/

165. Pollefeys M, Koch R, Van Gool L. A simple and efficient rectification method for general motion. In: *Proceedings of the Seventh IEEE International Conference on Computer Vision*. IEEE; 1999:496-501 vol.1. doi:10.1109/ICCV.1999.791262

166. Hirschmuller H. Accurate and Efficient Stereo Processing by Semi-Global Matching and Mutual Information. In: *2005 IEEE Computer Society Conference on Computer Vision and Pattern Recognition (CVPR'05)*. Vol 2. IEEE; 2005:807-814. doi:10.1109/CVPR.2005.56

167. Cheng PY, Khan SF. Dimensional accuracy and surface finish of investment casting parts by indirect additive manufacturing from fused filament fabrication. *IOP Conf Ser: Mater Sci Eng*. 2018;429:1-6. doi:10.1088/1757-899X/429/1/012100

168. Baturynska I. Statistical analysis of dimensional accuracy in additive manufacturing considering STL model properties. *Int J Adv Manuf Technol*. 2018;97(5):2835-2849. doi:10.1007/s00170-018-2117-4

169.Kitsakis K, Alabey P, Kechagias J, Vaxevanidis N. A Study of the dimensional accuracy obtained by low cost 3D printing for possible application in medicine. *IOP Conf Ser: Mater Sci Eng*. 2016;161:1-6. doi:10.1088/1757-899X/161/1/012025

170. Ayrilmis N. Effect of layer thickness on surface properties of 3D printed materials produced from wood flour/PLA filament. *Polymer Testing*. Published online September 1, 2018. doi:10.1016/j.polymertesting.2018.09.009

171. Jang KW, Shin SH, Kim SG, et al. Measurement of Cerenkov radiation induced by the gamma-rays of Co-60 therapy units using wavelength shifting fiber. *Sensors (Basel)*. 2014;14(4):7013-7025. doi:10.3390/s140407013

172. Zekavat AR, Jansson A, Larsson J, Pejryd L. Investigating the effect of fabrication temperature on mechanical properties of fused deposition modeling parts using X-ray computed tomography. *Int J Adv Manuf Technol*. 2019;100(1):287-296. doi:10.1007/s00170-018-2664-8

173. Camposeo A, Persano L, Farsari M, Pisignano D. Additive Manufacturing: Applications and Directions in Photonics and Optoelectronics. *Advanced Optical Materials*. 2019;7(1):1800419. doi:10.1002/adom.201800419

174. Novakovic K, Katsikas L, Popovic I. The thermal degradation of poly(iso-butyl methacrylate) and poly(sec-butyl methacrylate). *J Serb Chem Soc*. 2000;65(12):867-875. doi:10.2298/JSC0012867N

175. Geuskens G, David C. Photooxidation of polymers a comparison with low molecular Wight compounds. *Pure and Applied Chemistry - PURE APPL CHEM*. 1979;51:233-240. doi:10.1351/pac197951020233

176. Knoll GF. *Radiation Detection and Measurement*. Wiley; 1989.

177. Imperatore P, Iodice A, Pastorino M, Pinel N. Modelling Scattering of Electromagnetic Waves in Layered Media: An Up-to-Date Perspective. *International Journal of Antennas and Propagation*. 2017;2017:1-14. doi:10.1155/2017/7513239

178. Raney JR, Compton BG, Mueller J, Ober TJ, Shea K, Lewis JA. Rotational 3D printing of damage-tolerant composites with programmable mechanics. *PNAS*. 2018;115(6):1198-1203. doi:10.1073/pnas.1715157115

179. Lynch N, Monajemi T, Robar JL. Characterization of novel 3D printed plastic scintillation dosimeters. *Biomed Phys Eng Express*. 2020;6(5):055014. doi:10.1088/2057-1976/aba880

180. Berns S, Boillat E, Boyarintsev A, et al. *Additive Manufacturing of Fine-Granularity Optically-Isolated Plastic Scintillator Elements*. arXiv; 2022. doi:10.48550/arXiv.2202.10961

181. Schoonees JA, Palmer GT. Camera shading calibration using a spatially modulated field. In: *2009 24th International Conference Image and Vision Computing New Zealand*. ; 2009:191-196. doi:10.1109/IVCNZ.2009.5378412

182. Heikkila J, Silven O. A four-step camera calibration procedure with implicit image correction. In: *Proceedings of IEEE Computer Society Conference on Computer Vision and Pattern Recognition*. ; 1997:1106-1112. doi:10.1109/CVPR.1997.609468

183. Howard ME, Herman MG, Grams MP. Methodology for radiochromic film analysis using FilmQA Pro and ImageJ. *PLOS ONE*. 2020;15(5):e0233562. doi:10.1371/journal.pone.0233562

184. Fedorov A, Beichel R, Kalpathy-Cramer J, et al. 3D Slicer as an Image Computing Platform for the Quantitative Imaging Network. *Magn Reson Imaging*. 2012;30(9):1323-1341. doi:10.1016/j.mri.2012.05.001

185. Hsu SH, Roberson PL, Chen Y, Marsh RB, Pierce LJ, Moran JM. Assessment of skin dose for breast chest wall radiotherapy as a function of bolus material. *Phys Med Biol*. 2008;53(10):2593-2606. doi:10.1088/0031-9155/53/10/010

186. Lee N, Chuang C, Quivey JM, et al. Skin toxicity due to intensity-modulated radiotherapy for head-and-neck carcinoma. *Int J Radiat Oncol Biol Phys*. 2002;53(3):630-637. doi:10.1016/s0360-3016(02)02756-6

187. Kry SF, Alvarez P, Cygler JE, et al. AAPM TG 191: Clinical use of luminescent dosimeters: TLDs and OSLDs. *Medical Physics*. 2020;47(2):e19-e51. doi:10.1002/mp.13839

188. Barnett E, Mackenzie M, Fallone B. IMRT point dose measurements with a diamond detector. *Radiology and Oncology*. 2005;39.

189. Ashraf MR, Bruza P, Krishnaswamy V, Gladstone DJ, Pogue BW. Technical Note: Time-gating to medical linear accelerator pulses: Stray radiation detector. *Med Phys*. 2019;46(2):1044-1048. doi:10.1002/mp.13311

190. Wickramasinghe VA, Decker SM, Streeter SS, et al. Color-resolved Cherenkov imaging allows for differential signal detection in blood and melanin content. *J Biomed Opt*. 2023;28(3):036005. doi:10.1117/1.JBO.28.3.036005

191. Li Y, Liu H, Huang N, Wang Z, Zhang C. The Measurement of the Surface Dose in Regular and Small Radiation Therapy Fields Using Cherenkov Imaging. *Technol Cancer Res Treat*. 2022;21:15330338211073432. doi:10.1177/15330338211073432

192. Zhang R, Glaser AK, Gladstone DJ, Fox CJ, Pogue BW. Superficial dosimetry imaging based on Čerenkov emission for external beam radiotherapy with megavoltage x-ray beam. *Med Phys*. 2013;40(10):101914. doi:10.1118/1.4821543

193. Hachadorian R, Bruza P, Jermyn M, et al. Correcting Cherenkov light attenuation in tissue using spatial frequency domain imaging for quantitative surface dosimetry during whole breast radiation therapy. *J Biomed Opt*. 2019;24(7):071609. doi:10.1117/1.JBO.24.7.071609

194. Hachadorian RL, Bruza P, Jermyn M, et al. Remote dose imaging from Cherenkov light using spatially resolved CT calibration in breast radiotherapy. *Med Phys*. 2022;49(6):4018-4025. doi:10.1002/mp.15614

195. Alexander DA, Tendler II, Brůža P, et al. Assessment of Imaging Cherenkov and Scintillation Signals in Head and Neck Radiotherapy. *Physics in medicine and biology*. 2019;64(14):145021. doi:10.1088/1361-6560/ab25a3

196. Rahman M, Bruza P, Hachadorian R, et al. Optimization of in vivo Cherenkov imaging dosimetry via spectral choices for ambient background lights and filtering. *J Biomed Opt*. 2021;26(10):106003. doi:10.1117/1.JBO.26.10.106003

197. Cloutier É, Beaulieu L, Archambault L. Direct in-water radiation dose measurements using Cherenkov emission corrected signals from polarization imaging for a clinical radiotherapy application. *Sci Rep*. 2022;12(1):9608. doi:10.1038/s41598-022-12672-w

198. Cloutier É, Archambault L, Beaulieu L. Accurate dose measurements using Cherenkov emission polarization imaging. *Med Phys*. 2022;49(8):5417-5422. doi:10.1002/mp.15693

199. Cloutier E, Archambault L, Beaulieu L. Deformable scintillation dosimeter I: challenges and implementation using computer vision techniques. *Phys Med Biol*. 2021;66(17). doi:10.1088/1361-6560/ac1ca1

200. Ojala J, Kapanen M. Quantification of dose differences between two versions of Acuros XB algorithm compared to Monte Carlo simulations — the effect on clinical patient treatment planning. *J Appl Clin Med Phys*. 2015;16(6):213-225. doi:10.1120/jacmp.v16i6.5642

201. Robar JL, Moran K, Allan J, et al. Intrapatient study comparing 3D printed bolus versus standard vinyl gel sheet bolus for postmastectomy chest wall radiation therapy. *Pract Radiat Oncol*. 2018;8(4):221-229. doi:10.1016/j.prro.2017.12.008

202. Zaman A, Kakakhel MB, Hussain A. A comparison of Monte Carlo, anisotropic analytical algorithm (AAA) and Acuros XB algorithms in assessing dosimetric perturbations during enhanced dynamic wedged radiotherapy deliveries in heterogeneous media. *Journal of Radiotherapy in Practice*. 2019;18(1):75-81. doi:10.1017/S1460396918000262

203. Soh RCX, Tay GH, Lew WS, Lee JCL. A depth dose study between AAA and AXB algorithm against Monte Carlo simulation using AIP CT of a 4D dataset from a moving phantom. *Reports of Practical Oncology & Radiotherapy*. 2018;23(5):413-424. doi:10.1016/j.rpor.2018.08.003

204. Huang B, Wu L, Lin P, Chen C. Dose calculation of Acuros XB and Anisotropic Analytical Algorithm in lung stereotactic body radiotherapy treatment with flattening filter free beams and the potential role of calculation grid size. *Radiation Oncology*. 2015;10(1):53. doi:10.1186/s13014-015-0357-0

205. Sharma D, Badano A. Validation of columnar CsI x-ray detector responses obtained with hybridMANTIS, a CPU-GPU Monte Carlo code for coupled x-ray, electron, and optical transport. *Med Phys*. 2013;40(3):031907. doi:10.1118/1.4791642

206. Roncali E, Mosleh-Shirazi MA, Badano A. Modelling the transport of optical photons in scintillation detectors for diagnostic and radiotherapy imaging. *Phys Med Biol*. 2017;62(20):R207-R235. doi:10.1088/1361-6560/aa8b31

207. Mosleh-Shirazi MA, Zarrini-Monfared Z, Karbasi S, Zamani A. A new optical photon transport Monte Carlo code for modelling parallel- and focused-element scintillation detector arrays and its use for examination of the full MTF responses of thick segmented CsI(Tl) scintillators. *Physica Medica: European Journal of Medical Physics*. 2014;30:e28. doi:10.1016/j.ejmp.2014.07.092

208. Roncali E, Stockhoff M, Cherry SR. An integrated model of scintillator-reflector properties for advanced simulations of optical transport. *Phys Med Biol*. 2017;62(12):4811. doi:10.1088/1361-6560/aa6ca5

209. Sharma D, Badal A, Badano A. hybridMANTIS: a CPU–GPU Monte Carlo method for modeling indirect x-ray detectors with columnar scintillators. *Phys Med Biol.* 2012;57(8):2357. doi:10.1088/0031-9155/57/8/2357

210. Sibilieva T, Alekseev V, Barsuk S, et al. 3D printing of inorganic scintillator-based particle detectors. *J Inst.* 2023;18(03):P03007. doi:10.1088/1748-0221/18/03/P03007

APPENDIX A COPYRIGHT PERMISSIONS

A.1 PERMISSON FOR: EXCERPTS FROM "CAMERA-BASED RADIOTHERAPY DOSIMETERY USING DUAL-MATERIAL 3D PRINTED SCINTILLATOR ARRAYS"

CCC Marketplace

This is a License Agreement between Nicholas Lynch ("User") and Copyright Clearance Center, Inc. ("CCC") on behalf of the Rightsholder identified in the order details below. The license consists of the order details, the Marketplace Permissions General Terms and Conditions below, and any Rightsholder Terms and Conditions which are included below.

All payments must be made in full to CCC in accordance with the Marketplace Permissions General Terms and Conditions below.

Order Date	23-Apr-2024	Type of Use	Republish in a thesis/dissertation
Order License ID	1476337-1		
ISSN	2473-4209	Publisher	American Association of Physicists in Medicine [by the American Institute of Physics]
		Portion	Excerpt (up to 400 words)

LICENSED CONTENT

Publication Title	Medical physics	Publication Type	Journal
Article Title	Camera-based radiotherapy dosimetry using dual-material 3D printed scintillator arrays	Start Page	1824
		End Page	1842
		Issue	3
Author/Editor	American Institute of Physics., American Association of Physicists in Medicine.	Volume	50
		URL	http://scitation.aip.org/content/aapm/journal/medphys
Date	01/01/1974		
Language	English		
Country	United States of America		
Rightsholder	John Wiley & Sons - Books		

REQUEST DETAILS

Portion Type	Excerpt (up to 400 words)	Distribution	United States and Canada
Number of Excerpts	2	Translation	Original language of publication
Format (select all that apply)	Print, Electronic	Copies for the Disabled?	No
Who Will Republish the Content?	Academic institution	Minor Editing Privileges?	Yes
Duration of Use	Life of current edition	Incidental Promotional Use?	No
Lifetime Unit Quantity	Up to 499	Currency	CAD
Rights Requested	Main product		

NEW WORK DETAILS

Title	A 3D PRINTED PATIENT SPECIFIC IN-VIVO DOSIMETRY SYSTEM	Institution Name	Dalhousie Univeristy

Instructor Name	Dr. James Robar	**Expected Presentation Date**	2024-05-20

ADDITIONAL DETAILS

The Requesting Person / Organization to Appear on the License	Nicholas Lynch

REQUESTED CONTENT DETAILS

Title, Description or Numeric Reference of the Portion(s)	Introduction: Lines 1- 26 and Lines 26 - 49	**Title of the Article / Chapter the Portion Is From**	Camera-based radiotherapy dosimetry using dual-material 3D printed scintillator arrays
Editor of Portion(s)	Lynch, Nicholas; Robar, James L.; Monajemi, Thalat	**Author of Portion(s)**	Lynch, Nicholas; Robar, James L.; Monajemi, Thalat
Volume / Edition	50		
Page or Page Range of Portion	1824-1842	**Publication Date of Portion**	2023-03-17

RIGHTSHOLDER TERMS AND CONDITIONS

No right, license or interest to any trademark, trade name, service mark or other branding ("Marks") of WILEY or its licensors is granted hereunder, and you agree that you shall not assert any such right, license or interest with respect thereto. You may not alter, remove or suppress in any manner any copyright, trademark or other notices displayed by the Wiley material. This Agreement will be void if the Type of Use, Format, Circulation, or Requestor Type was misrepresented during the licensing process. In no instance may the total amount of Wiley Materials used in any Main Product, Compilation or Collective work comprise more than 5% (if figures/tables) or 15% (if full articles/chapters) of the (entirety of the) Main Product, Compilation or Collective Work. Some titles may be available under an Open Access license. It is the Licensors' responsibility to identify the type of Open Access license on which the requested material was published, and comply fully with the terms of that license for the type of use specified Further details can be found on Wiley Online Library http://olabout.wiley.com/WileyCDA/Section/id-410895.html.

Marketplace Permissions General Terms and Conditions

The following terms and conditions ("General Terms"), together with any applicable Publisher Terms and Conditions, govern User's use of Works pursuant to the Licenses granted by Copyright Clearance Center, Inc. ("CCC") on behalf of the applicable Rightsholders of such Works through CCC's applicable Marketplace transactional licensing services (each, a "Service").

1) **Definitions.** For purposes of these General Terms, the following definitions apply:

"License" is the licensed use the User obtains via the Marketplace platform in a particular licensing transaction, as set forth in the Order Confirmation.

"Order Confirmation" is the confirmation CCC provides to the User at the conclusion of each Marketplace transaction. "Order Confirmation Terms" are additional terms set forth on specific Order Confirmations not set forth in the General Terms that can include terms applicable to a particular CCC transactional licensing service and/or any Rightsholder-specific terms.

"Rightsholder(s)" are the holders of copyright rights in the Works for which a User obtains licenses via the Marketplace platform, which are displayed on specific Order Confirmations.

"Terms" means the terms and conditions set forth in these General Terms and any additional Order Confirmation Terms collectively.

A.2 PERMISSION FOR: REPRODUCTION AND MODIFICATION OF FIGURE 2.1

May 20th, 2024

Medical Physics Publishing
4555 Helgesen Dr
Madison, WI 53718

I am preparing my PhD thesis for submission to the Faculty of Graduate Studies at Dalhousie University, Halifax, Nova Scotia, Canada. I am seeking your permission to include a figure from the following publication in the thesis:

Figure 38 from "A Primer on the Theory and Operation of Linear Accelerators in Radiation Therapy," third edition, page 28 by C.J Karzmark and Robert J. Morton, Medical Physics Publishing, 2017.

Dalhousie graduate theses are collected and stored online by Dalhousie University and Library and Archives of Canada. I am seeking your permission for the material described above to be stored online in Dalhousie University's institutional repository and in Library and Archives of Canada (LAC)'s Theses Canada Collection.

Full publication details and a copy of this permission letter will be included in the thesis.

Yours sincerely,

Nicholas Lynch

Permission is granted for:

a) the inclusion of the material described above in your thesis.

b) for the material described above to be included in the copy of your thesis that is sent to the Library and Archives of Canada inclusion in Theses Canada.

c) For the material described above to be included in the copy of your thesis that is sent to Dalhousie University's institutional repository.

Name: Jeff Shaub Title: Customer Service

Signature: Date: 6/10/2024

A.3 PERMISSION FOR: REPRODUCTION AND MODIFICATION OF FIGURE 2.2

JOHN WILEY AND SONS LICENSE
TERMS AND CONDITIONS

Apr 25, 2024

This Agreement between Dalhousie University -- Nicholas Lynch ("You") and John Wiley and Sons ("John Wiley and Sons") consists of your license details and the terms and conditions provided by John Wiley and Sons and Copyright Clearance Center.

License Number	5775990899079
License date	Apr 25, 2024
Licensed Content Publisher	John Wiley and Sons
Licensed Content Publication	Wiley Books
Licensed Content Title	Introduction to Elementary Particles, 2nd, Revised Edition
Licensed Content Author	David Griffiths
Licensed Content Date	Oct 1, 2008
Licensed Content Pages	1
Type of use	Dissertation/Thesis
Requestor type	University/Academic
Format	Print and electronic
Portion	Figure/table

Number of figures/tables	1
Will you be translating?	No
Title of new work	A 3D Printed Patient Specific In-Vivo Dosimetry System
Institution name	Dalhousie Univeristy
Expected presentation date	May 2024
Portions	Chapter 6 The Feynman Calculus, Section 6.1.2 Cross-Sections, Figure 6.3, Page 201
Requestor Location	Dalhousie University 5511 Bloomfield St. Unit 505 Halifax, NS B3K 0H3 Canada Attn: Dalhousie University
Publisher Tax ID	EU826007151
Total	0.00 CAD

A.4 PERMISSION FOR: REPRODUCTION OF FIGURE 2.3

SPRINGER NATURE LICENSE
TERMS AND CONDITIONS

Mar 11, 2024

This Agreement between Dalhousie University -- Nicholas Lynch ("You") and Springer Nature ("Springer Nature") consists of your license details and the terms and conditions provided by Springer Nature and Copyright Clearance Center.

License Number	5745850563015
License date	Mar 11, 2024
Licensed Content Publisher	Springer Nature
Licensed Content Publication	Springer eBook
Licensed Content Title	3D X-Ray Characterization of Energy Storage and Conversion Devices
Licensed Content Author	Chun Tan, Andrew S. Leach, Thomas M. M. Heenan et al
Licensed Content Date	Jan 1, 2021
Type of Use	Thesis/Dissertation
Requestor type	academic/university or research institute
Format	print and electronic
Portion	figures/tables/illustrations
Number of figures/tables/illustrations	1

Will you be translating?	no
Circulation/distribution	1 - 29
Author of this Springer Nature content	no
Title of new work	A 3D Printed Patient Specific In-Vivo Dosimetry System
Institution name	Dalhousie Univeristy
Expected presentation date	May 2024
Order reference number	3446
Portions	Figure 18.2 Relative importance of principal photon interaction mechanisms
Requestor Location	Dalhousie University 5511 Bloomfield St. Unit 505 Halifax, NS B3K 0H3 Canada Attn: Dalhousie University
Total	0.00 CAD

A.5 PERMISSION FOR: REPRODUCTION AND MODIFICATION OF FIGURE 2.11

SPRINGER NATURE LICENSE
TERMS AND CONDITIONS

Apr 24, 2024

This Agreement between Dalhousie University -- Nicholas Lynch ("You") and Springer Nature ("Springer Nature") consists of your license details and the terms and conditions provided by Springer Nature and Copyright Clearance Center.

License Number	5775500694032
License date	Apr 24, 2024
Licensed Content Publisher	Springer Nature
Licensed Content Publication	Springer eBook
Licensed Content Title	Interactions of Charged Particles with Matter
Licensed Content Author	Ervin B. Podgoršak
Licensed Content Date	Jan 1, 2016
Type of Use	Thesis/Dissertation
Requestor type	academic/university or research institute
Format	print and electronic
Portion	figures/tables/illustrations
Number of figures/tables/illustrations	1
Will you be translating?	no

Circulation/distribution	100 - 199
Author of this Springer Nature content	no
Title of new work	A 3D Printed Patient Specific In-Vivo Dosimetry System
Institution name	Dalhousie Univeristy
Expected presentation date	May 2024
Portions	Figure 6.13, page 261
Requestor Location	Dalhousie University 5511 Bloomfield St. Unit 505 Halifax, NS B3K 0H3 Canada Attn: Dalhousie University
Total	0.00 CAD

A.6 PERMISSION FOR: REPRODUCTION AND MODIFICATION OF FIGURE 2.12

CCC Marketplace

This is a License Agreement between Nicholas Lynch ("User") and Copyright Clearance Center, Inc. ("CCC") on behalf of the Rightsholder identified in the order details below. The license consists of the order details, the Marketplace Permissions General Terms and Conditions below, and any Rightsholder Terms and Conditions which are included below.

All payments must be made in full to CCC in accordance with the Marketplace Permissions General Terms and Conditions below.

Order Date	23-Apr-2024	Type of Use	Republish in a thesis/dissertation
Order License ID	1476371-1		
ISSN	0031-9155	Publisher	IOP Publishing
		Portion	Image/photo/illustration

LICENSED CONTENT

Publication Title	Physics in Medicine & Biology	Country	United Kingdom of Great Britain and Northern Ireland
Author/Editor	American Association of Physicists in Medicine, Canadian Association of Physicists.Medical and Biological Physics Division, Institute of Physics (Great Britain), Hospital Physicists' Association, Deutsche Gesellschaft für Medizinische Physik., International Organization for Medical Physics	Rightsholder	IOP Publishing, Ltd
		Publication Type	Journal
Date	01/01/1956		
Language	English		

REQUEST DETAILS

Portion Type	Image/photo/illustration	Distribution	United States and Canada
Number of Images / Photos / Illustrations	1	Translation	Original language of publication
Format (select all that apply)	Print, Electronic	Copies for the Disabled?	No
		Minor Editing Privileges?	Yes
Who Will Republish the Content?	Academic institution	Incidental Promotional Use?	No
Duration of Use	Life of current edition	Currency	CAD
Lifetime Unit Quantity	Up to 499		
Rights Requested	Main product		

NEW WORK DETAILS

Title	A 3D PRINTED PATIENT SPECIFIC IN-VIVO DOSIMETRY SYSTEM	Institution Name	Dalhousie University
		Expected Presentation Date	2024-05-20

Instructor Name	Dr. James Robar

ADDITIONAL DETAILS

Order Reference Number	N/A	**The Requesting Person / Organization to Appear on the License**	Nicholas Lynch

REQUESTED CONTENT DETAILS

Title, Description or Numeric Reference of the Portion(s)	Figure 4 D)	**Title of the Article / Chapter the Portion Is From**	Monte-Carlo-derived insights into dose–kerma–collision kerma inter-relationships for 50 keV–25 MeV photon beams in water, aluminum and copper
Editor of Portion(s)	Nicholas Lynch		
Volume / Edition	Volume 60, Number 2		
Page or Page Range of Portion	Page 2623	**Author of Portion(s)**	Sudhir Kumar, Deepak D Deshpande, Alan E Nahum
		Issue, if Republishing an Article From a Serial	N/A
		Publication Date of Portion	2014-12-30

RIGHTSHOLDER TERMS AND CONDITIONS

A.7 PERMISSION FOR: REPRODUCTION AND MODIFICATION OF FIGURE 2.13

SPRINGER NATURE LICENSE
TERMS AND CONDITIONS

Apr 25, 2024

This Agreement between Dalhousie University -- Nicholas Lynch ("You") and Springer Nature ("Springer Nature") consists of your license details and the terms and conditions provided by Springer Nature and Copyright Clearance Center.

License Number	5776000881106
License date	Apr 25, 2024
Licensed Content Publisher	Springer Nature
Licensed Content Publication	Springer eBook
Licensed Content Title	Fundamentals of Radiation Dosimetry
Licensed Content Author	Ervin B. Podgoršak
Licensed Content Date	Jan 1, 2016
Type of Use	Thesis/Dissertation
Requestor type	academic/university or research institute
Format	print and electronic
Portion	figures/tables/illustrations
Number of figures/tables/illustrations	1

Will you be translating?	no
Circulation/distribution	100 - 199
Author of this Springer Nature content	no
Title of new work	A 3D Printed Patient Specific In-Vivo Dosimetry System
Institution name	Dalhousie Univeristy
Expected presentation date	May 2024
Portions	Chapter 15 Fundamentals of Radiation Dosimetry, Section 15.7 Cavity Theories for Radiation Dosimetry, Figure 15.4, Page 662
Requestor Location	Dalhousie University 5511 Bloomfield St. Unit 505 Halifax, NS B3K 0H3 Canada Attn: Dalhousie University
Total	0.00 CAD

Terms and Conditions

Springer Nature Customer Service Centre GmbH Terms and Conditions

The following terms and conditions ("Terms and Conditions") together with the terms specified in your [RightsLink] constitute the License ("License") between you as Licensee and Springer Nature Customer Service Centre GmbH as Licensor. By clicking 'accept' and completing the transaction for your use of the material ("Licensed Material"), you confirm your acceptance of and obligation to be bound by these Terms and Conditions.

A.8 PERMISSION FOR: REPRODUCTION AND MODIFICATION OF FIGURE 2.15

This is a License Agreement between Nicholas Lynch ("User") and Copyright Clearance Center, Inc. ("CCC") on behalf of the Rightsholder identified in the order details below. The license consists of the order details, the Marketplace Permissions General Terms and Conditions below, and any Rightsholder Terms and Conditions which are included below.

All payments must be made in full to CCC in accordance with the Marketplace Permissions General Terms and Conditions below.

Order Date	29-Apr-2024	Type of Use	Republish in a thesis/dissertation
Order License ID	1478350-1		
ISBN-13	978-1-4822-0899-3	Publisher	CRC Press
		Portion	Image/photo/illustration

LICENSED CONTENT

Publication Title	Scintillation Dosimetry	Country	United States of America
Author/Editor	Beddar, Sam, Beaulieu, Luc	Rightsholder	Taylor & Francis Group LLC - Books
Date	03/29/2016	Publication Type	Book
Language	English	URL	http://www.crcnetbase.com/doi/book/10.1201/b19491

REQUEST DETAILS

Portion Type	Image/photo/illustration	Distribution	United States and Canada
Number of Images / Photos / Illustrations	1	Translation	Original language of publication
Format (select all that apply)	Print, Electronic	Copies for the Disabled?	No
		Minor Editing Privileges?	Yes
Who Will Republish the Content?	Academic institution	Incidental Promotional Use?	No
Duration of Use	Life of current edition	Currency	CAD
Lifetime Unit Quantity	Up to 999		
Rights Requested	Main product		

NEW WORK DETAILS

Title	A 3D Printed Patient Specific In-Vivo Dosimetry System	Institution Name	Dalhousie University
		Expected Presentation Date	2024-05-10
Instructor Name	Dr. James Robar		

ADDITIONAL DETAILS

Order Reference Number	N/A	The Requesting Person / Organization to Appear on the License	Nicholas Lynch

REQUESTED CONTENT DETAILS

Title, Description or Numeric Reference of the Portion(s)	Figure 5.2: Production of Cerenkov in a transparent medium.	**Title of the Article / Chapter the Portion Is From**	Chapter 5 Cerenkov and its solutions, Section 5.2 Physics of Cerenkov Radiation,
Editor of Portion(s)	Nicholas Lynch	**Author of Portion(s)**	Beddar, Sam; Beaulieu, Luc
Volume / Edition	1st Edition	**Issue, if Republishing an Article From a Serial**	N/A
Page or Page Range of Portion	75	**Publication Date of Portion**	2016-03-29

SPECIAL RIGHTSHOLDER TERMS AND CONDITIONS

Each copy containing our material must bear a credit line in the following format: Copyright (Insert © Year) From (Insert Title) by (Insert Author/Editor Name). Reproduced by permission of Taylor and Francis Group, LLC, a division of Informa plc. This permission does not cover any third party copyrighted work which may appear in the material requested. User is responsible for obtaining permission for such material separately from this grant.

Marketplace Permissions General Terms and Conditions

The following terms and conditions ("General Terms"), together with any applicable Publisher Terms and Conditions, govern User's use of Works pursuant to the Licenses granted by Copyright Clearance Center, Inc. ("CCC") on behalf of the applicable Rightsholders of such Works through CCC's applicable Marketplace transactional licensing services (each, a "Service").

1) **Definitions.** For purposes of these General Terms, the following definitions apply:

"License" is the licensed use the User obtains via the Marketplace platform in a particular licensing transaction, as set forth in the Order Confirmation.

"Order Confirmation" is the confirmation CCC provides to the User at the conclusion of each Marketplace transaction. "Order Confirmation Terms" are additional terms set forth on specific Order Confirmations not set forth in the General Terms that can include terms applicable to a particular CCC transactional licensing service and/or any Rightsholder-specific terms.

"Rightsholder(s)" are the holders of copyright rights in the Works for which a User obtains licenses via the Marketplace platform, which are displayed on specific Order Confirmations.

"Terms" means the terms and conditions set forth in these General Terms and any additional Order Confirmation Terms collectively.

"User" or "you" is the person or entity making the use granted under the relevant License. Where the person accepting the Terms on behalf of a User is a freelancer or other third party who the User authorized to accept the General Terms on the User's behalf, such person shall be deemed jointly a User for purposes of such Terms.

"Work(s)" are the copyright protected works described in relevant Order Confirmations.

2) **Description of Service.** CCC's Marketplace enables Users to obtain Licenses to use one or more Works in accordance with all relevant Terms. CCC grants Licenses as an agent on behalf of the copyright rightsholder identified in the relevant Order Confirmation.

3) **Applicability of Terms.** The Terms govern User's use of Works in connection with the relevant License. In the event of any conflict between General Terms and Order Confirmation Terms, the latter shall govern. User acknowledges that Rightsholders have complete discretion whether to grant any permission, and whether to place any limitations on any grant, and that CCC has no right to supersede or to modify any such discretionary act by a Rightsholder.

A.9 PERMISSION FOR: REPRODUCTION OF FIGURE 2.26

Dear Nicolas,

sure! Please go ahead and include the QE-Curve graph in your thesis. Please find attached according graph as PDF.

With kind regards,
Mit freundlichen Grüßen,

PCO Support Team
Alexander Dietz
--
+49 (0) 9441 2005 55
Excelitas PCO GmbH | Donaupark 11 | 93309 Kelheim | Germany | www.pco.de
Geschäftsführer / Managing Directors: Ronald Keating, Benedict Stas, Alexander Grünig, Luitpold Kaspar
USt. ID-Nr. / VAT: DE128590843, Registergericht / Register Court: Amtsgericht Regensburg HRB 18850
Sitz der Gesellschaft / Registered Office: Kelheim
--

> Am Montag, 15. April 2024 um 21:00:39, schrieb Nick Lynch:
>
> > You don't often get email from nc828332@dal.ca. Learn why this is important
>
> Hello,
>
> My name is Nicholas Lynch, I am a PhD Candidate at the Dalhousie University Department of Physics and Atmospheric Science. My research focuses on the development of a patient specific radiation detector for use in cancer radiotherapy treatment. The novel detector developed as part of my thesis uses two PCO panada 4.2 sCMOS cameras as its primary optical photon detectors. Please see attached for our previous publication.
>
> I am currently in the process of writing my thesis and I would like to seek permission to include the monochrome quantum efficiency curve presented on page 4 of the attached technical data sheet.
>
> I am unsure if this contact is the appropriate channel, if not could you please direct me to the correct department?
>
> Best regards,
>
> Nicholas Lynch
>
> PhD Candidate
> Dalhousie University
> Department of Physics and Atmospheric Science
> QEII Health Sciences Centre
> Centennial Building Office 4-066

A.10 PERMISSION FOR: REPRODUCTION OF "CHARACTERIZATION OF NOVEL 3D PRINTED SCINTILLATION DOSIMETERS"

Dear Nick Lynch,

Thank you for your email and for taking the time to seek this permission.

When you transferred the copyright in your article to IOP, we granted back to you certain rights, including the right to include all or part of the Final Published Version of the article within any thesis or dissertation provided it is not then shared or deposited online. Full details can be found in our Author Rights Policy.

If you are required by your institution to share your thesis/dissertation publicly (such as in an institutional repository), the Final Published Version would need to be removed prior to publication online or in print. Your institution should be able to withhold the IOP article section of your thesis from this version. However, you should still reference the article, include the abstract and provide a DOI link to it on IOPscience so that people know that it has been published.

Please include citation details, "© IOP Publishing. Reproduced with permission. All rights reserved" and for online use, a link to the Version of Record.

Please note you may need to obtain separate permission for any third party content you included within your article.

If you do not wish to remove the IOP article section of your thesis, you also have the following alternative options:

1) Our Author Rights Policy allows authors to post the Accepted Manuscript in certain places **after** the embargo period has elapsed. This includes your institutional repository, subject to certain restrictions (please see the full terms and conditions in our Author Rights Policy linked in the signature of this email.). Therefore, an option may be to include your Accepted Manuscript article version in your thesis or dissertation, as it would allow you to place the unaltered dissertation onto your repository after the embargo period.
Please note that your article is outside of its embargo period. An Embargo Period is 'a period of 12 months from the Date of Publication'.

2) A further option would be to include the Author's Original or Preprint version of the article, provided that you do so in line with our Preprint pre-publication policy.

I wish you the best of luck with the completion of your thesis/dissertation.

Kind regards,

Sophie
Copyright & Permissions Team
Sophie Brittain - Rights & Permissions Assistant
Cameron Wood - Legal & Rights Adviser
Contact Details
E-mail: permissions@ioppublishing.org

A.11 PERMISSION FOR: REPRODUCTION OF "CAMERA-BASED RADIOTHERAPY DOSIMETERY USING DUAL-MATERIAL 3D PRINTED SCINTILLATOR ARRAYS"

JOHN WILEY AND SONS LICENSE
TERMS AND CONDITIONS

Mar 07, 2024

This Agreement between Dalhousie University -- Nicholas Lynch ("You") and John Wiley and Sons ("John Wiley and Sons") consists of your license details and the terms and conditions provided by John Wiley and Sons and Copyright Clearance Center.

License Number	5743691242987
License date	Mar 07, 2024
Licensed Content Publisher	John Wiley and Sons
Licensed Content Publication	Medical Physics
Licensed Content Title	Camera-based radiotherapy dosimetry using dual-material 3D printed scintillator arrays
Licensed Content Author	Thalat Monajemi, James L. Robar, Nicholas Lynch
Licensed Content Date	Jan 11, 2023
Licensed Content Volume	50
Licensed Content Issue	3
Licensed Content Pages	19
Type of use	Dissertation/Thesis
Requestor type	Author of this Wiley article

Format	Print and electronic
Portion	Full article
Will you be translating?	No
Title of new work	A 3D Printed Patient Specific In-Vivo Dosimetry System
Institution name	Dalhousie Univeristy
Expected presentation date	May 2024
Order reference number	3445
Requestor Location	Dalhousie University 5511 Bloomfield St. Unit 505 Halifax, NS B3K 0H3 Canada Attn: Dalhousie University
Publisher Tax ID	EU826007151
Total	0.00 USD
Terms and Conditions	